Co-Evolution in Complex Adaptive Water Systems

from Long-Term Planning to Short-Term Responses

by

Chung-Yi Lin

A Dissertation

Presented to the Graduate and Research Committee

of Lehigh University

in Candidacy for the Degree of

Doctor of Philosophy

in

Civil Engineering

Lehigh University

January 2023

Approval of the Doctoral Committee

Approved and recommended for acceptance as a dissertation in partial fulfillment of the requirements for the degree of Doctor of Philosophy in Environmental Engineering on this date of_____.

_____

Paolo Bocchini, Ph.D.
Committee Chairperson
Department of Civil and Environmental Engineering
Lehigh University

_____

Y. C. Ethan Yang, Ph.D.
Dissertation Advisor
Department of Civil and Environmental Engineering
Lehigh University

_____

Faegheh Moazeni, Ph.D.
Committee Member
Department of Civil and Environmental Engineering
Lehigh University

_____

Brian D. Davison, Ph.D.
Committee Member
Department of Computer Science and Engineering
Lehigh University

Date Accepted:_____

Acknowledgments

The journey of becoming a doctor is with too much appreciation that this one-page acknowledgment is certainly not sufficient to reveal them all. I treasure all those moments deep in my heart as I carry this doctoral title.

I would like to first give my deepest gratitude to my advisor of the thesis, Dr. Y. C. Ethan Yang, who guided and supported my Ph.D. study over the past few years. His rigorous research experience and constructive suggestions elevate this work to a higher level. He also mentors my professional development and directs me along the path of the transformation from a student to an independent researcher.

I would extend my special thanks to the rest of my committee members: Dr. Brian D. Davison, Dr. Faegheh Moazeni, and Dr. Paolo Bocchini, who witnessed my growth and provided me with invaluable assistance in my research topics. To that end, I also want to thank my other collaborators: Dr. Jennifer C. Adam, Dr. Keyvan Malek, and Dr. Sungwook Wi, who provide valuable data and advice on drafting manuscripts.

I want to thank my research group members: Dr. Feng-Wei Hung, Jiaorui Zhang, Qiaochu Sun, and all others, for their help and mental support. I will remember the road trip we had in the summer of 2021. I also appreciate the friendship and help received from the Lehigh community.

Finally, I wish to show my appreciation to my parents. Their love is the reason why I can be who I am. Without their support, this journey might not be possible. I will use the rest of my life to return their love and support to the best of my ability.

Table of Contents

Acknowledgments iv
Table of Contents v
List of Tables viii
List of Figures ix
Abstract 1
Chapter 1: Introduction 3
Chapter 2: An Investigation of Coupled Natural Human Systems Using a Two-Way Coupled Agent-Based Modeling Framework 10
2.1 Introduction 10
2.2 Background 13
2.2.1 RiverWare 13
2.2.2 Agent-based modeling 14
2.2.3 Model coupling 15
2.3 Case study - the Yakima River Basin 16
2.4 Model and experimental setup 18
2.4.1 Models and simulation schema 18
2.4.2 Models' calibration and validation 25
2.4.3 Experimental setup 26
2.5 Results 28
2.5.1 Model comparison and adaptive capacity 28
2.5.2 LSA of social network structure 31
2.5.3 Impact of policy rules on the human behavior 34
2.6 Discussion 37
2.6.1 Cross-scale CNHS modeling for multi-level governance application 37
2.6.2 Limitations 38
2.7 Conclusions 41
Chapter 3: HydroCNHS: A Python Package of Hydrological Model for Coupled Natural–Human Systems 42
3.1 Introduction 43
3.2 Methods 45
3.2.1 Structure of the HydroCNHS Model 45
3.2.2 Module components 47
3.2.3 Routing Scheme 51
3.2.4 Coupling APIs 51
3.3 Case Study – Tualatin River Basin 54
3.4 Results 58
3.5 Conclusions 61
Chapter 4: The Effects of Model Complexity on Model Output Uncertainty in Co-Evolved Coupled Natural-Human Systems 63
4.1 Introduction 64
4.2 Study area and materials 67
4.2.1 Yakima River Basin 67

4.2.2 Data and climate change scenarios 71
4.3 Methods 73
4.3.1 Hydrological model 73
4.3.2 Human Model 76
4.3.3 Model uncertainty decomposition 81
4.4 Results 85
4.4.1 Calibration and validation of EMRs 85
4.4.2 Comparing model complexity and uncertainty 87
4.4.3 Model uncertainty and co-evolution in CNHS 93
4.5 Discussion 96
4.5.1 Other sources of uncertainty in CNHS 96
4.5.2 Limitations 97
4.6 Conclusions 98
Chapter 5: Compounding Risks of Natural Hazards and Cyber-physical Attacks in a Smart Storm Water System 100
5.1 Introduction 101
5.2 Methods 104
5.2.1 Mathematical Framework for Smart Stormwater Systems 104
5.2.2 Compounding Impact Evaluation 110
5.2.3 Compounding Risk Quantification 114
5.3 Materials 116
5.3.1 Study Area 116
5.3.2 Numerical Experiment Setup 118
5.4 Results 120
5.4.1 Water Levels under Uncontrolled, Controlled, and FDI scenarios 120
5.4.2 Flooding Risks under Sensor Noises, Forecast Uncertainties, and FDI 122
5.4.3 Compounding Flooding Risks 124
5.5 Discussion 126
5.5.1 The Missing Piece of Compounding Risks Quantification 126
5.5.2 Application in Network-based Systems 127
5.5.3 Limitations 128
5.6 Conclusions 129
Chapter 6: Conclusions 131
6.1 Research Findings 131
6.2 Limitations and Future Research 134
Reference 138
Appendix A: Supplementary Materials for Chapter 2 154
A.1 Py-RAMID technical details 154
A.2 ODD+D Protocol of Agent-Based Model 157
A.3 Agent's decision-making algorithm for diversion request 161
A.4 Supplementary figures and tables 165
Appendix B: Supplementary Materials for Chapter 3 169
B.1 Agents' design for the Tualatin River Basin (TRB) 169
B.2 Calibration setting for the TRB 172
Appendix C: Supplementary Materials for Chapter 4 175

C.1 Derivation of the law of total variance 175
C.2 Derivation of the law of total variance with two conditioning random variables 175
C.3 Supplementary figures and tables 176
Appendix D: Supplementary Materials for Chapter 5 190
D.1 Construction of a state-space model for a given pond network 190
D.2 Time-invariant linear quadratic gaussian (LQG) controller 193
D.2.1 LQE and Kalman gain (L): 194
D.2.2 LQR and $\boldsymbol{K}$ 194
D.2.3 Feedforward control for reference tracking, $\boldsymbol{Kr}$ 195
D.2.4 Feedforward control for disturbance cancelation, $\boldsymbol{Kw}$ 196
D.2.5 Linear combination of $\boldsymbol{K}$, $\boldsymbol{Kr}$, and $\boldsymbol{Kw}$ 197
D.3 MIQCP problem for solving FDI in a smart stormwater system 199
D.4 Supplementary figures and tables 200
Vita 202

List of Tables

Table 2-1. Canal gauges, water rights, average water diversion, and district area of six irrigation districts. 18
Table 2-2. Agent attributes that affect their decision-making processes. 22
Table 2-3. NSE values of YAKRW, Coupled-YAKRW, and Coupled-YAKRW w/o S. models. 29
Table 2-4. Percentage of difference between Coupled-YAKRW and Coupled-YAKRW w/o S. regarding each parameter's calibrated range. Raw parameter values of Coupled-YAKRW and Coupled-YAKRW w/o S. are given in Table A1 and Table A2, respectively. 32
Table 3-1. Calibration parameter bounds for the hydrological model and the ABM model..... 58
Table 3-2. KGE comparison for the calibration and validation results of two models..... 60
Table 4-1. Calibration Parameter Bounds for Hydrological and ABM Models. 74
Table 4-2. Summary of diversion agent type setup of five YRB coupled models..... 80
Table 4-3. Monthly Calibration and Validation Results of Hydrological Models..... 86

List of Figures

Figure 1-1. Linkages of Chapters 2 to 5 toward co-evolution exploration in CAWS from long-term planning to short-term responses. 7
Figure 2-1. Yakima River Basin. The map shows five major reservoirs, six major irrigation districts with corresponding canal flow gauges, and streamflow gauges used as model calibration targets. 17
Figure 2-2. Coupled-YAKRW simulation schema. Yellow boxes are agent decision-making processes (dotted thin arrows), which output the ratio (Rg, yi) that is used to adjust the mean annual diversion request (circle number 6) and to simulate the next year by RW. Annual mean diversion request is computed using all historical annual diversion request records before the current year. Solid arrows connecting diversion requests (green boxes) and the RW model (blues boxes) show information flow in the coupling process. 19
Figure 2-3. (a) is a social network matrix. Each row of the matrix is the social network of the agent in that row, which is affected by the agent in the column with cell's value 1. (b) Sw is a weight vector to balance between neighbor opinions and the agent's own beliefs. (c) Pyt is a collection of agent's evaluations of water supply conditions in yt. 23
Figure 2-4. Model comparison of annual diversions. Grey lines are the observed annual irrigation diversions. Green dashed lines are outputs of the original YAKRW model. Blue and red dotted lines are simulated results from coupled-YAKRW and coupled-YAKRW w/o S., respectively. 29
Figure 2-5. Timeseries plot of the state variable, Center (C), for six agents in the Coupled-YAKRW model. Colored regions have negative perceived beliefs about water supply conditions. Note: higher C values indicate agents will divert less water. 31
Figure 2-6. NSE of irrigation diversions in LSA. The weight of the social norm effect of each agent is shown by brackets. The red cross indicates calibrated Coupled-YAKRW model results, and the orange lines are median values. Black circles are NSE values outside the range of 25% and 75% quantiles shown as boxes. 33
Figure 2-7. Standard deviations of 465 LSA simulation results with respect to calibrated Coupled-YAKRW outputs. The x-axis is the weight inside the social norm effect. Blue circles represent actual diversion (RW output), and orange triangles indicate diversion requests sent from ABM to RW (RW input). 34
Figure 2-8. Prospect functions (e.g., mapping agents' risk attitudes; Equation 2-5) under original (solid lines) and all-proratable (dotted lines) water right scenarios. The upper right corners are the risk attitudes toward the beliefs of positive water supply conditions, while the lower left corners are of negative conditions (e.g., droughts). 36
Figure 3-1. Structure of the HydroCNHS model structure (blue box) and three user inputs (yellow box), including climate data (temperature and precipitation), model configuration file (*.yaml*), and ABM modules (*.py*; green box). User-provided ABM modules will be integrated into the HydroCNHS through four APIs. 46

Figure 3-2. A generic example of HydroCNHS coupling APIs and water system description. Note that agents R1, R2, D1, C1, C2, and I1, are programmed in ABM modules (*.py*) and integrated into HydroCNHS through APIs. 53
Figure 3-3. The Tualatin River Basin system. TRTR, $Hagg_{In}$, DLLO, TRGC, DAIRY, RCTV, and WSLO are seven subbasins. PipeAgt, ResAgt, and DivAgt are trans-basin aqueduct, Hagg reservoir, and TVID agents, respectively. DrainAgt1 and DrainAgt2 are two drainage system agents for the runoff-changing scenario..... 55
Figure 3-4. Four monthly time series plots for calibrated M_{gwlf} and M_{abcd}. DLLO and WSLO are the calibrated streamflow. Release and diversion are simulated by ResAgt and DivAgt, respectively. Grey vertical lines separate the calibration (1981-2005) and validation (2006-2013) periods. Black dotted lines are the observations.60
Figure 3-5. Two scenarios of the M_{gwlf} model. (a) Standard deviation difference between $M_{gwlf,endog}$ and $M_{gwlf,fixed}$ in annual mean values. (b) The annual WSLO streamflow for with (solid line)/without (dashed line) urbanization using calibrated..... 61
Figure 4-1. System diagram of Yakima River Basin (YRB). S1, S2, and S3 and R1, R2, and R3 are reservoir inflow and release models, respectively. YRB coupled natural-human model (yellow-colored area), which consists of three subbasins (yellow circles are their outlets) and five irrigation diversion districts (green boxes), is the focus of uncertainty analysis..... 69
Figure 4-2. (a) Precipitation ratios and (b) temperature deltas sampled from five quantile values over the range of 20 GCMs (boxplots) under RCP 2.6 (left column) and RCP 8.5 (right column), respectively, in the 2030s, 2050s, 2070s, and 2090s. Future weather time series were generated by adjusting annually bootstrapped time series with climate change scenarios, combinations of linearly interpolated ratios, and deltas. 72
Figure 4-3. Conceptual diagram of EMRs and model uncertainty decomposition. Blue lines indicate model uncertainty caused by different model configurations. Light blue zones represent model uncertainty introduced by uncertain input data (e.g., climate uncertainty). 82
Figure 4-4. Modeling schema for the numerical experiment. Schema begins by calibrating the hydrological model and identifying HydroEMRs through the K-means algorithm; then, HydroEMRs drive ABM calibration and ABMEMRs identification. Identified EMRs are then applied to exploratory application and uncertainty analysis..... 84
Figure 4-5. Calibration and validation results (separated by vertical lines) of five diversion irrigation districts (columns) for five coupled models (rows). Each EMR result is one of the four ABMEMRs driven by HydroEMR1 (blue lines) or HydroEMR2 (orange lines) that were averaged over 10 simulations. Red lines are observed data, and gray areas are 95% confidence intervals..... 88
Figure 4-6. (a) Model uncertainty decomposition of QM for five coupled models (columns). (b) Fractional contribution percentage of decomposed variances. (c) Boxplot time series of SM with mean values (blue lines) and outliers (black dots). Three uncertainty sources were climate scenario uncertainty, internal climate variability, and different model configurations. 89

Figure 4-7. (a) Model uncertainty decomposition of DM for five coupled models (columns). (b) Fractional contribution percentage of decomposed variances. (c) Total model uncertainty of QM. Three uncertainty sources are climate scenario uncertainty, internal climate variability, and different model configurations. 92
Figure 4-8. Factors showing co-evolution, particularly with the learning mechanism, leading to overall lower model uncertainty. $Qdown$, Qup, and Div are streamflow before diversion, streamflow after diversion, and diversion at Parker gauge, respectively. (a) Averaged (co)variances of five coupled models from 2030 to 2100. (b) Differences between averaged (co)variance from 2066 to 2100 and from 2030 to 2065..... 94
Figure 5-1. A mathematical framework for smart stormwater systems consists of a stormwater (drainage) system representative, a control system, and a bad data detector. The red-colored variables indicate the polluted path to the outflow control ($\boldsymbol{u}$), where $\boldsymbol{y}\acute{}$ is the contaminated measurements from FDI. 105
Figure 5-2. $\chi 2$ distributions for operator (yellow lines) and attacker (blue lines) to determine corresponding thresholds, ε and εa, based on their operation and attack strategy. The attackable range ($Erra$) decreases as the number of attacking time steps (Ta) increases. 110
Figure 5-3. Disclosure of potential FDI consequences with Pond 1 as the flooding target. (a) A smart stormwater system with three ponds. (b) Water level impact of Pond 1 from enlarging inflow caused by FDI. (c) Water level impact of Pond 1 from reducing outflow caused by FDI. (d) The water level time series of Pond 1 under "uncontrolled," "controlled," and "FDI" scenarios. 113
Figure 5-4. Probability estimation concepts for (a) PE, (b) $PFDI$, and (c) PWs, where PE is estimated by DDF curve, $PFDI$ (blue area) is calculated from $\chi dof = n - na2$ distribution, and PWs is computed by Monte Carlo simulations over realizations of sensor noises and forecasted runoffs (grey lines). 116
Figure 5-5. A designed stormwater system with the network layout referenced from a residential area in Bethlehem township, PA, US. Ponds' capacities are indicated by circle size in a log scale. 117
Figure 5-6. A control rule for desired water level ($\boldsymbol{rt}$). $t5\%$ (cross) and tp (star) are two control time points determined by the simulated water level reaching 5% pond capacity and the peak under an uncontrolled scenario. The desired water level linearly increases from 0 to 80% pond capacity and maintains for five hours before decreasing. 119
Figure 5-7. Water level comparisons of uncontrolled (dotted blue line), controlled (dashed brown line), $FDIS$ (orange line), and $FDIM$ (green line) with 25-year storm and 30-minute attack. The nested stem plots indicate relative maximum water level differences between controlled and two FDI scenarios of nine ponds. The star signs in the subtitle indicate the flooded ponds under FDI. The pond-conduit network is visualized in the upper left corner. 122
Figure 5-8. Water level variations under sensor noises and forecasted runoffs with a 25-year storm. Water levels in uncontrolled, controlled, and $FDIS$ scenarios are shown in dotted blue lines, dashed brown lines, and solid orange lines, respectively. Each

plot is one independent experiment differing in attacking targets. The pond-conduit network is visualized in the upper left corner. 124
Figure 5-9. Heatmap of compounding flooding risks over different attacking lengths and return periods of 24-hour design storms. Grey color indicates zero in compounding risk of flooding. Each plot is one independent experiment differing in attacking targets of $FDIs$ scenario. The pond-conduit network is visualized inside the Pond 8 subplot. 126

Abstract

Water system planning and management is the science between the natural environment and human society. This dissertation explores the coevolution in complex adaptive water systems from long-term planning to short-term responses to advance our understanding of interactions between natural and human systems using computational modeling approaches. This dissertation investigates the effect of the social norm on farmers' water diversion behaviors interacting with the hydrological environment through a two-way coupling model. Coupled models bidirectionally bridge the information flow between RiverWare, a commonly adopted water planning model, and an agent-based model (ABM), a human model constructed from a bottom-up modeling logic. ABM can capture the heterogeneity of human actors (farmers) and reveal the emergence of collective patterns. The coupled models are applied to show how the changing water allocation policy impact agents' characteristics (e.g., risk attitudes). To further explore the coupled models' characteristics, an open-source Python package, Hydrological model for Coupled Natural-Human Systems, is developed to facilitate the complex adaptive water systems (CAWS) modeling process and conduct an uncertainty analysis. This dissertation analyzes how the model output uncertainty in nature and human systems vary with different ABM complexities concerning uncertainty sources like climate change scenarios uncertainty, internal climate variability, and different model configurations with parameter sets or model structures that are equally capable of producing similar outcomes using the law of total variance. The last research topic shifts the focus from long-term planning to short-term responses. Those responses are viewed as the drivers accumulating to form the trend of long-term changes. This dissertation quantifies the compounding risks of flood caused by storms and cyber-physical

attacks in a smart stormwater system, a pond-conduit network that has water level sensors and outflow gate actuators to be remotely controlled by a real-time control system modeled by a linear quadratic Gaussian controller. The numerical experiments illustrate how the maliciously injected data impact the system operation and the pattern of flooding risks in the urban area. The results serve as an initial step to discussing the potential human responses toward compounding risks that might trigger the long-term evolution of CAWS. In sum, this dissertation contributes to advancing the understanding of coevolution in CAWS and encourages future work to develop a holistic framework linking the perspectives of long-term planning and short-term responses in CAWS modeling.

Chapter 1: Introduction

Initiated by the Harvard Water Program in the 1960s (Maass et al., 1962; Reuss, 2003), complex water resources management problems have been addressed by combining operations research, statistics, and economics methods under the stationary assumption in the early days. However, the ignorance of the changing climate and adaptability of human behaviors, such as reservoir operations, off-stream water diversions, and urbanization, might deviate modeling results from the time-variant reality and bias the associated policy decisions (Milly et al., 2008). For example, while farmers' annual water diversions amount for irrigation may rely on the economic status of growing crop types and the overall condition of the hydrological regime, the water supply limitation, affected by the changing climate and the total water demands of individual water users, could alter farmers water use decisions. Such interactions could lead to a long-term regime shift in both natural and human systems. This feedback cycle highlights the significance of advancing our understanding of the co-evolution (i.e., bidirectional interactions; Brown et al., 2015; Sivapalan and Blöschl, 2015) between natural and human systems, so-called coupled natural human systems (CNHS; Bauch et al., 2016; Liu et al., 2007; Wada et al., 2017) or socio-environmental systems (SES; Elsawah et al., 2020), and the corresponding short-term responses that drive long-term co-evolutions. Here, we refer CNHS to complex adaptive water systems (CAWS; Yang et al., 2009; Yang et al., 2020).

Projecting or modeling characteristic changes of human behavior like risk attitudes is challenging, despite the fact that the co-evolution mechanism has been used to explain the offsetting behavior (Campbell et al., 2004; Fielding et al., 2012), where the feedback of human behaviors toward the changing policy jeopardizes the original intention or the

effectiveness of the newly introduced policy. Similarly, due to the modeling challenge, the well-recognized psychological factor driving human behaviors, the social norm effect (i.e., the informal rules that govern behavior in groups and societies; Ajzen, 1991; Bicchieri and Muldoon, 2014; Cedeno-Mieles et al., 2020; Chen et al., 2012, Niles and Mueller, 2016), has not yet been thoroughly investigated in the CAWS model (Groeneveld et al., 2017; Kremmydas et al., 2018). The underlying question that interests the water system community is whether the social norm structure affects the model on results and is worth the extra model complexity and data acquisition costs. Such issues indicate the need for a modeling method that can identify potential behavior characteristic changes (e.g., risk attitudes) and test human actors' interactions (e.g., social norms) to better inform policy for long-term planning.

Two-way coupling is one of the techniques to bidirectionally link natural and human models (Hyun et al., 2019; Lin et al., 2022), whereas agent-based modeling (ABM) is commonly used in describing heterogeneous human actors (i.e., agents) from a bottom-up point of view. Each agent has a unique set of attributes governing its behaviors and interactions with other agents and the environment. However, the integrity of the coupled model is often constrained by the original software. While some existing hydrological model software like Neitsch et al. (2011) and Liang et al. (1996) can incorporate human decision units, the option that allows users to choose among exogenous or endogenous human components is often not supported. For example, reservoir releases can be modeled by exogenous inputs like historical daily time series records or represented by a decision-making model to endogenously and dynamically simulate water releases. Such freedom is critical when we face a lack of data or other limitations in CAWS modeling. Another

limitation of two-way coupling is modelers often need to reconstruct the model (structure) for every study area, namely, lack of generality. These highlight the need for new modeling tools targeting code integrity so that modelers can focus more on the science instead of the technical challenges, especially when dealing with more complex CAWS research.

When more complex models have been built to address human behaviors in CAWS (Zellner, 2008), the model uncertainty issue has become a concern. With more sophisticated modeling methods and the growing number of parameters, handling model uncertainty becomes increasingly challenging (Srikrishnan and Keller, 2021), which could significantly affect the confidence of model results' inference and interpretation (Allison et al., 2018; Kelly et al., 2013; Sun et al., 2016). The growing model complexity in CAWS modeling directs us to focus on parameter and structural uncertainties, so-called equifinality. Equifinality, first introduced into hydrological modeling by Beven (1993), describes a situation where multiple model structures and/or parameter sets are equally capable of reproducing a similar/acceptable (not necessarily identical) hydrological outcome given a set of observed data (Beven, 2006). Namely, a more complex model may suffer a more severe equifinality with limited data (Srikrishnan and Keller, 2021). While a few recent studies (Ekblad and Herman, 2021; Khatami et al., 2019; Williams et al., 2020) try to partially solve this puzzle, uncertainty studies and equifinality issues of coupled natural human models in CAWS are still in their infant stage (Elsawah et al., 2020). Furthermore, how different coupled models' structural assumptions impact the simulation uncertainty, which directly links to informing planning and management, remains almost unexplored.

In addition to long-term planning purposes, coupled models in CAWS can also simulate various short-term human responses (Thonicke et al., 2020) and help researchers understand the co-evolution caused by natural-hazard-induced disasters. For example, it will be helpful for disaster adaptation policy if a model can simulate the process of how the flooding impact of Hurricane Sandy in 2012 triggered New York City to build barriers to protect its critical infrastructures from floodwater, storms, and other impacts of a changing climate. Furthermore, natural hazards are not the only factor that could cause a disaster and potentially trigger co-evolution (Adamo et al., 2021). For example, Bowman Avenue Dam, 30 miles north of Manhattan, was detected to be cyber-attacked in 2013 (Hassanzadeh et al., 2020). Although no damages resulted from the incident, this event raises awareness of the potential impact of human interventions, where the such impact could be even worse when accompanied by natural hazards. However, the "compounding impacts" from natural hazards and human interventions are not well-studied. We argue that these compounding impacts involving natural and human factors play an important role in proposing strategies for short-term responses; or, broadly, driving the long-term planning for the future human society under the umbrella of the co-evolution concept.

In sum, we identify several knowledge gaps in understanding co-evolution in CAWS. The gaps include (1) insufficient understanding of behavioral change modeling and the role of social norm modeling structure, (2) insufficient coupled ABM modeling tools for CAWS, (3) unclear uncertainty properties in CAWS modeling, and (4) unclear short-term responses toward compounding impacts of natural hazards and human interventions. These gaps lead to the overarching goal of this dissertation to **advance the understanding of co-evolution in CAWS modeling and quantify CAWS modeling**

uncertainty via case studies in different applications, from long-term planning to short-term responses. We broke down the overarching dissertation goal into Chapters 2 to 5 (Figure 1-1) to address the four identified gaps respectively. These chapters are self-contained and are formulated as individual scientific papers that can be read separately. Altogether, they advance the understanding of co-evolution in CAWS modeling and quantify CAWS modeling uncertainty via case studies in different applications, from long-term planning to short-term responses. The contents of these chapters are condensed into the following paragraphs.

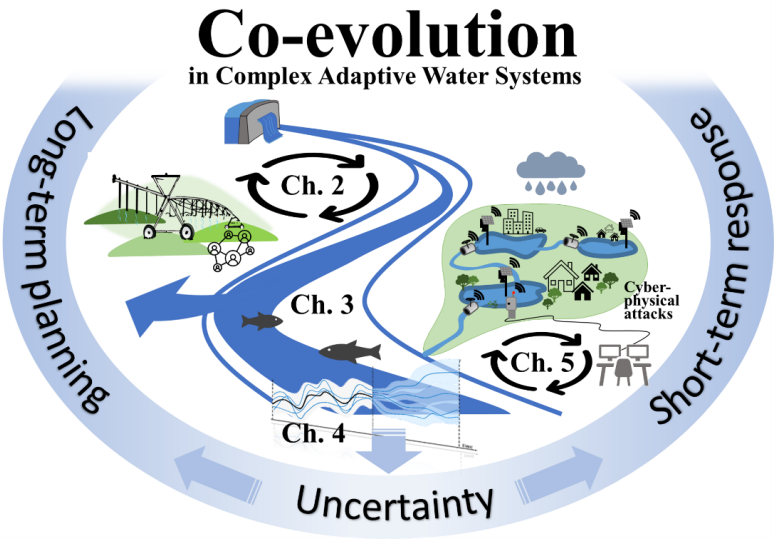

Figure 1-1. Linkages of Chapters 2 to 5 toward co-evolution exploration in CAWS from long-term planning to short-term responses.

Chapter 2 investigates the co-evolution issues of social norms and changing human behavior characteristics in water resources allocation in agricultural water systems via two-way coupling RiverWare (a river-reservoir routing model) with a water diversion ABM (i.e., a human decision model) in the Yakima River Basin, Washington, US. Using this two-way-coupled model, we demonstrate the effect of social norms among farmers (i.e., the influence on irrigation decisions from neighbors) by local sensitivity analysis and test

a “what-if” water reallocation scenario to evaluate the influence of changing water policies on human behavior characteristics (e.g., risk attitudes). Finally, we discuss the potential benefits of coupled models in informing multi-level water resources governance. For example, how to address co-management (e.g., collaboration) issues across power-imbalanced governance levels or human actors.

Chapter 3 addresses the gap of insufficient CAWS modeling tools that allow users to freely integrate exogenous or endogenous human components into a process-based hydrological model. To achieve this, we developed a semi-distributed Hydrological model for Coupled Natural–Human Systems, HydroCNHS. The HydroCNHS is an open-source Python package supporting four Application Programming Interfaces (APIs), including Dam API, RiverDiv API, Conveying API, and InSitu API, for integrating, respectively, customized man-made infrastructures such as reservoirs, off-stream diversions, trans-basin aqueducts, and drainage systems that abstract human behaviors (e.g., operator and farmers’ water use decisions). Namely, users have complete freedom in designing human decision models programmed with the ABM concept. They can easily plug “agents” into HydroCNHS using APIs, where within-subbasin and inter-subbasin (i.e., river) routing logics for maintaining the water balance are handled by HydroCNHS internally. In addition, HydroCNHS uses a single model configuration file to organize input features for the hydrological model and case-specific human systems models. Also, HydroCNHS supports model calibration using parallel computing power.

Chapter 4 contributes to a better understanding of CAWS modeling properties through an uncertainty analysis of coupled hydrological and water diversion ABMs built by HydroCNHS (Chapter2) in an exploratory analysis. We propose five coupled model

types that have different model complexities of human behavior settings (i.e., model structure and the number of calibrated parameters): one static, two adaptive, and two learning adaptive. Learning adaptive models (the most complex) have both the learning component (capturing long-term trends) and the adaptive component (capturing short-term variations), while adaptive models omit the learning component. The static model is the simplest model without learning and adaptive components. Applying the law of total variance, the model output uncertainty is decomposed into three sources: (1) climate change scenario uncertainty, (2) climate internal variability, and (3) equifinality (defined as parameter sets or model structures that are equally capable of producing similar model outcomes).

Chapter 5 explores the compounding impacts of floods from storms and cyber-physical attacks in a smart stormwater system, standing for a pond-conduit network that has water level sensors and outflow gate actuators at each pond for real-time control. We develop a cyber-attacker mathematical framework considering sensor noises and weather forecast uncertainties to inform system planning and investments and discuss how the growing usage of Internet-of-Thing-based infrastructures drives long-term co-evolution. The framework contains a state-space model to describe the pond-conduit network, a linear quadratic Gaussian controller to control ponds' outflows in real-time, and a bad data detector to prevent bad/false data from entering the control system.

Finally, Chapter 6 concludes this dissertation with each chapter's major findings and points out future works that may further advance the understanding of co-evolution in complex adaptive water systems.

Chapter 2: An Investigation of Coupled Natural Human Systems Using a Two-Way Coupled Agent-Based Modeling Framework

Abstract

Improving the understanding of coupled natural human systems (CNHS) can better inform environmental policymaking. We investigated the co-evolution (i.e., bidirectional interactions) issues in CNHS via two-way coupling RiverWare (RW; a river-reservoir routing model) with agent-based models (ABMs, human decision models) in the Yakima River Basin in Washington, US. Results show that coupled models can better capture the historical irrigation diversion (human) and streamflow (nature) dynamics. We further demonstrated the effect of social norms (i.e., the influence of neighbors) among farmers and tested a "water reallocation" scenario to evaluate the influence of water policies on irrigation diversion behaviors. Detailed model structure and parameter uncertainty analysis are suggested to further quantify the benefit of CNHS models in multi-level water resources governance.

2.1 Introduction

Most of the major basins involve some degree of human activity in this anthropogenic era, indicating the significance of investigating the co-evolution (i.e., bidirectional interactions) between natural and human systems, so-called the coupled natural human systems (CNHS; An, 2012; Giuliani et al., 2016; Hyun et al., 2019; Liu et al., 2007; Yang et al., 2020) or socio-environmental systems (SES; Elsawah et al., 2020). While the social-hydrology

communities (Sivapalan and Blöschl, 2015) actively study the co-evolution mechanism emphasizing human influences on the water cycle, we focus more on the water resources management problem from a CNHS point of view, where the hydrological response is one of the indicators for making decisions (Brown et al., 2015; Reuss, 2003).

An additional human complexity layer has been claimed can improve environmental planning and policy (Zellner, 2008). To that, the co-evolution mechanism is the foundation to generate more holistic information for policymaking, especially for revealing the offsetting behavior (Campbell et al., 2004; Fielding et al., 2012), where the feedback of human behaviors toward the changing policy jeopardizes the original intention or the effectiveness of that newly introduced policy, and multi-level governance application (Cash et al., 2006; Di Gregorio et al., 2019), which tend to address co-management issues across power-imbalanced governance levels (or human actors). This chapter aims to tackle the abovementioned management issues by improving the understanding of the co-evolution mechanism in CNHS modeling. More specifically, we would like to explore the influence of policy rules (e.g., water reallocation; Du et al., 2021; Hillman et al., 2012; Yang et al., 2012) on human behaviors (e.g., irrigation diversions and risk attitudes) and discuss how CNHS model can potentially benefit multi-level water resources governance.

To model the co-evolution mechanism in CNHS, a human layer is required in addition to the natural systems (e.g., hydrological model). For constructing the human system, agent-based modeling (ABM) is often used for its capability of describing emergent and heterogeneous human behaviors. The flexibility of the ABM framework allows various designs of decision-making processes, including factors such as people's

past experiences, future expectations, risk attitudes, availability of resources, and interaction with the environment and neighbors (Hu et al., 2006; Niles and Mueller, 2016). However, the social norm effect, defined as the informal rules that govern behavior in groups and societies (Bicchieri and Muldoon, 2014), are often missing in CNHS models with only a few exceptions (Abebe et al., 2020; Nhim et al., 2019). Groeneveld et al. (2017) pointed out social influences are one of the least considered factors among 134 agent-based land-use change models' literature. Kremmydas et al. (2018) also indicated that over 70% of concerned agents' interactions in the review of ABM for agricultural policy evaluation studies referred to a land market that the agents' interactions are a shared database for sending/getting bidding information instead of agent-to-agent interactions. The theoretical foundation of the social norm effect is still actively developing (Gelfand et al., 2017), and many studies have shown the social norm effect is an essential factor influencing human behavior (Ajzen, 1991; Bicchieri and Muldoon, 2014; Cedeno-Mieles et al., 2020; Chen et al., 2012; Epstein, 2012). For example, studies of groundwater management (Castilla-Rho et al., 2017), adoption of field practice innovation (Baba et al., 2021), and weather forecast utilization (Hu et al., 2006) have shown farmers' behaviors can be significantly affected by neighbors' opinions. These motivate us to explore how the social norm effect influences the CNHS modeling results.

Consequently, this chapter aims to improve our understanding of the co-evolution mechanism in CNHS through a case study. We adopt the Yakima River Basin (YRB) in Washington, US, as our study area, where the RiverWare model (a river system model), YAKRW, developed by the U.S. Bureau of Reclamation (USBR), is available (Malek et al., 2018; USBR, 2011) to us. For the human model, we develop two diversion ABMs to

represent farmers' heterogeneous irrigation diversion behaviors with and without the social norm effect. The objectives of this chapter are (1) coupling YAKRW (natural model) and diversion ABMs (human model), (2) comparing coupled models with the original YAKRW (baseline) to explore streamflow and irrigation diversion dynamics in CNHS, (3) investigating the social norm effect with a local sensitivity analysis (LSA) on a directed social network (i.e., information flow among human actors), and (4) demonstrating the impact of changing policy rules (e.g., water reallocation) on human behaviors (e.g., diversion and calibrated ABM parameters).

The chapter is structured as follows. We introduce the technical background of RiverWare, ABM, and the coupling technique in Section 2.2 . Then, Section 2.3 describes the case study information for the YRB. After that, we show the detailed coupled model design and experimental setup in Section 2.4 . The results are presented in Section 2.5 . Next, we discuss the multi-level governance application and model limitations in Section 2.6 , which is followed by the conclusions in Section 2.7 .

2.2 Background

2.2.1 RiverWare

RiverWare (RW) is a licensed water resource engineering model developed in 1986 by the University of Colorado, Boulder. It is a process-based model that simulates river and reservoir routing (e.g., reservoir operational scheduling) and other natural processes (e.g., return flow) in a basin with policy rules, such as water rights and canal capacity, to fit the legal and physical constraints. The graphical interface enables modelers to build the model using a node-link structure. Each node is defined as an object (e.g., storage reservoir or water diversion district) with a unique set of attributes. It contains various slots to store

data (e.g., series slots for storing time-series data). Each link connects different objects to facilitate information flow. We refer to Zagona et al. (2001) and their official website: http://www.riverware.org/for more technical details of the RW model. RiverWare has been used internationally to evaluate real-world water allocation issues and assist reservoir operation (Abudu et al., 2018; Basheer et al., 2020; Biddle, 2001; Everitt, 2020; USBR, 2011, USBR, 2012; U.S. DOE, 2019; Wheeler et al., 2020; Witt et al., 2017). Its popularity in academia and public sectors is one reason that RiverWare is adopted as our coupling target despite its being a licensed standalone software. In addition, we would like to leverage existing RW models' credibility for our case study area (i.e., YAKRW).

2.2.2 Agent-based modeling

Agent-based modeling (ABM) is a bottom-up modeling approach known for its capability of describing the emergent and heterogeneous agents' behaviors, where an agent is a decision-making unit of actors. Each agent is controlled by a set of rules and attributes, and they can interact with other agents in a shared physical environment. Moreover, the adaptive learning mechanism of agents, defined as the adaptive capacity herein, enables agents' decision rules to co-evolve with a changing environment (Axelrod and Tesfatsion, 2006; Epstein, 2012; Miller and Page, 2007). Many fields have successfully adopted the ABM framework to explore CNHS, such as land-use change (Brown et al., 2004; Groeneveld et al., 2017; Zellner and Reeves, 2010), groundwater management (Al-Amin et al., 2018; Castilla-Rho et al., 2015; Reeves and Zellner, 2010), and water resources allocation (Li et al., 2017; Tesfatsion et al., 2017; Yang et al., 2009; Zhou et al., 2015).

2.2.3 Model coupling

Studies have adopted a two-way coupling technique, a technique to create feedback loops among models, to organize information flow (e.g., real-time information exchange) and illustrate potential system responses between natural models and ABM (Giuliani et al., 2016; Hyun et al., 2019; Jaxa-Rozen et al., 2019; Khan et al., 2017; Reeves and Zellner, 2010). With a more extensive scope, modeling frameworks have been developed to alleviate potential technical barriers (Robinson et al., 2018). For example, some studies emulated nature models (e.g., groundwater model or land-use decision model) into well-developed ABM platforms (e.g., NetLogo) (Castilla-Rho et al., 2015; Sun and Müller, 2013), some established a new modularized ABM framework integrating vegetation models (Murray-Rust et al., 2014; Schreinemachers and Berger, 2011), and some developed a two-way coupling Python package to fully utilized an external simulation model with NetLogo (Jaxa-Rozen and Kwakkel, 2018). More broadly speaking, several communities (e.g., CSDMS, CoMSES Net, AIMES, etc.) have initiated generic coupling/integrating frameworks and model development standards to advance open science and system-of-systems research. Some examples include OpenMI (Gregersen et al., 2007; Moore and Tindall, 2005), Basic Model Interface (BMI; Hutton et al., 2020; Peckham et al., 2013), Earth System Modeling Framework (ESMF; Hill et al., 2004), and Object Modeling System (OMS; David et al., 2013).

We attempt to follow the same coupling philosophy. However, the abovementioned frameworks might not be applicable in this chapter due to the licensed (closed source) RiverWare software that has limited modifiability. Therefore, we developed a Python package of RiverWare and Agent-based Modeling Interface for Developers (Py-RAMID)

to achieve two-way coupling between RiverWare and ABMs for our numerical experiments. The technical details for the Py-RAMID coupling framework are provided in the supplementary materials (Appendix A.1). Py-RAMID and its user manual are available at https://github.com/philip928lin/Py-RAMID.

2.3 Case study - the Yakima River Basin

The Yakima River Basin (YRB, Figure 2-1) is located in central Washington, US, where agriculture significantly contributes to the economy (USBR, 2010). According to the 2017 agriculture census from the USDA, the main crops are orchards (127,934 acres, 29.6%), small grains (67,434 acres, 15.6%), and corns (63,163 acres, 14.6%). The basin-wide annual precipitation is approximately 680 mm, and most precipitation accumulates in the mountain area as snow (Mastin and Vaccaro, 2002). Therefore, the irrigation water supply for downstream croplands relies heavily on five major reservoirs, Keechelus, Kachess, Cle Elum, Bumping, and Rimrock (Figure 2-1). These reservoirs capture melting snow in the spring and redistribute water across the growing season (April to October; USBR, 2002). The six major irrigation districts in the YRB are Kittitas, Yakima-Tieton (Tieton), Wapato, Sunnyside Valley (Sunnyside), Roza, and Kennewick. They have different compositions of water rights (e.g., junior and senior water rights). Allocated by the priority order (first in time, first in right) (USBR, 2002), proratable (receive a reduced or prorated portion of their entitlements during droughts period) and nonproratable (receive full entitlements during droughts period) water rights are given to junior and senior water right holders, separated by the date of May 10, 1905 (USBR, 2002), respectively. The six districts' water rights, average water diversion, district area, and corresponding canal gauges are summarized in Table 2-1.

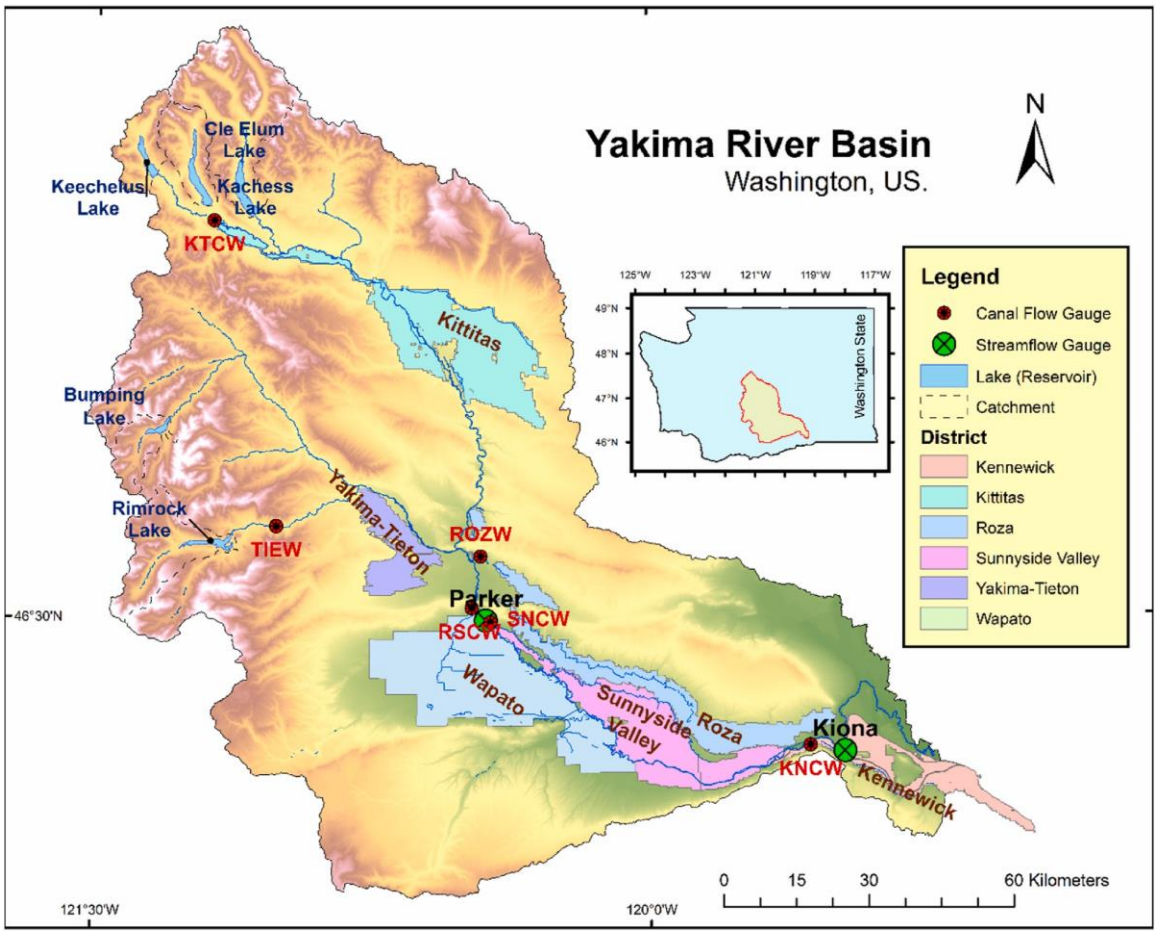

Figure 2-1. Yakima River Basin. The map shows five major reservoirs, six major irrigation districts with corresponding canal flow gauges, and streamflow gauges used as model calibration targets.

Building on previous local studies (Givens et al., 2018; Malek et al., 2018; Qiu et al., 2019), we further explored the YRB from a CNHS's viewpoint by two-way coupling diversion ABMs with the existing Yakima RiverWare model (YAKRW; Malek et al., 2018; USBR, 2011).

Table 2-1. Canal gauges, water rights, average water diversion, and district area of six irrigation districts.

District	Gauge	Water rights (acre-feet)[a]			Avg. diversion in 2001–2010 (cfs)[b]	District area (acre)
		Non-proratable[c]	Prorata ble[c]	Total		
Wapato	RSCW	305613	350000	655613	705.22	190862
Sunnyside	SNCW	289646	157776	447422	549.03	111067
Roza	ROZW	0	393000	393000	371.56	94876
Kittitas	KTCW	0	336000	336000	411.67	143383
Tieton	TIEW	75865	30425	106290	103.46	42150
Kennewick	KNCW	18000	84674	102674	128.00	54386

[a] (USBR, 2012); [b] Hydromet; [c] Proratable water right holders will receive a reduced or prorated entitlement during the droughts period, while nonproratable water right holders will receive full entitlements all the time.

2.4 Model and experimental setup

2.4.1 Models and simulation schema

To start the numerical experiments exploring CNHS in the YRB, we first constructed the coupled model, Coupled-YAKRW, by coupling YAKRW and a diversion ABM. Then, we applied Coupled-YAKRW to simulate the dynamics of historical river discharge and irrigation diversions in the six major water use districts. Each irrigation district was defined as a decision-making agent to make annual diversion requests. The general simulation schema is shown in Figure 2-2.

First, we used observed irrigation diversions as agent diversion requests and sent them to the RW model in the initial year (y_{to}). Then, the RW model outputs the simulated diversion and river discharge. Next, the simulated river discharge was sent to the ABM model (grey boxes in Figure 2-2) to update agents' decision rules. Then, ABM used the new observations (e.g., precipitation or reservoir storage) to evaluate the water supply conditions of the coming year (y_t) and calculate diversion-request-adjustment ratios (R_{g,y_t}) through the updated decision rules (yellow boxes in Figure 2-2; formulation

details are shown in Section 2.4.1.2). Finally, the diversion-request-adjustment ratios were applied to update the annual mean diversion request values, which were calculated by the annual diversion request records from y_{to} to y_{t-1} for each agent and then disaggregated into daily irrigation diversion requests for y_t simulation.

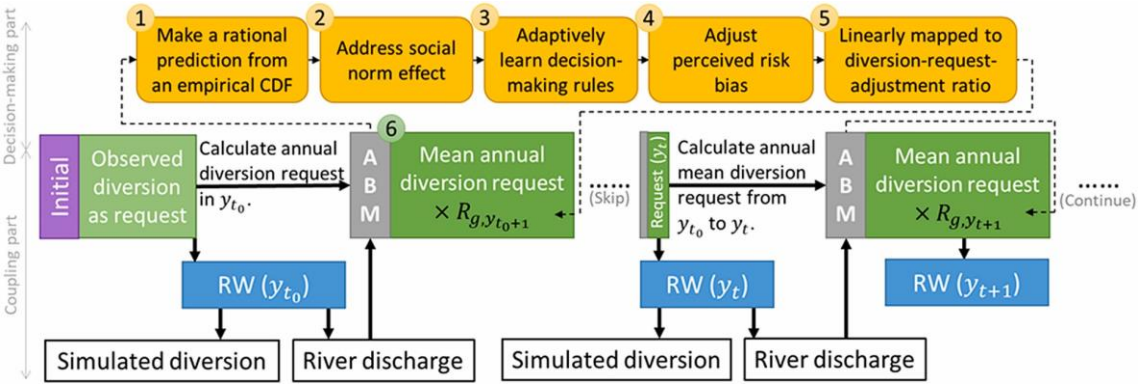

Figure 2-2. Coupled-YAKRW simulation schema. Yellow boxes are agent decision-making processes (dotted thin arrows), which output the ratio (R_{g,y_i}) that is used to adjust the mean annual diversion request (circle number 6) and to simulate the next year by RW. Annual mean diversion request is computed using all historical annual diversion request records before the current year. Solid arrows connecting diversion requests (green boxes) and the RW model (blues boxes) show information flow in the coupling process.

2.4.1.1 The baseline model – YAKRW

We use the original YAKRW (Malek et al., 2018; USBR, 2011) as our baseline model. All the input data, such as initial reservoir storages, historical reservoir inflows, water rights information, etc., are embedded inside YAKRW. YAKRW runs on a daily scale, and we can output time-series data (e.g., daily streamflow and diversions) of any given RW objects (i.e., water users or reservoirs). The diversion requests of six irrigation districts are calculated using both water entitlement and fixed values computed by historical diversion measurements. YAKRW will first compute conventional diversion requests by combining dry-year (the 50th percentile diversion from historical dry years in 1991–2010) and wet-

year (the 50th percentile diversion from historical wet years in 1991–2010) historical diversion sequences for a 365-day period based on the flow conditions at Parker gauge on a daily basis. Then, YAKRW picks the minimum of conventional diversion requests and prorated entitlement calculated according to their water rights (Table 2-1) to determine the final diversion requests.

We substitute conventional diversion requests with our diversion ABM outputs for coupling purposes. Namely, the diversion decisions made by the ABM are still constrained by water rights. Note that there is an additional policy rule further updates the diversion requests for the Kennewick agent. To that, Kennewick's diversion requests can be dominated by this highly customized policy rule. We refer readers to USBR (2011) for more details about the baseline model's settings.

2.4.1.2 Diversion ABM

For the ABM model (yellow boxes in Figure 2-2), we adopted the Theory of Planned Behavior (TPB, Ajzen, 1991) as a guideline. TPB states that the behavior of an actor (e.g., agent) is built upon its intention (e.g., diversion requests), the social norm it experienced, and reality constraints (e.g., water rights, canal capacity). In this case study, every district acquires the attributes of two state variables and eight parameters, which must be calibrated (Table 2-2). The decision-making process includes six steps, shown as numbered circles in Figure 2-2. In **step 1**, agents will evaluate water supply conditions based on the Empirical Cumulative Distribution Function (ECDF) value of the observation of the coming year (y_t) on the selected $InfoSource$ (Table 2-2, Equation A-1). The ECDF is constructed from the historical records of selected $InfoSource$ from y_{t0} to y_{t-1}. In **step 2**, agents adjust their

perceived beliefs of water supply based on neighbor opinions, so-called the social norm effect (Figure 2-3) quantified by Equation 2-1,

$$p_{g,y_t}^{adj} = \left(1 - Sw_{g,g}\right) \times P_{g,y_t} + Sw_{g,g} \sum_{i=1,i\neq g}^{N_{agents}} S_{g,i} \times P_{i,y_t} \quad (2\text{-}1)$$

where p_{g,y_t}^{adj} is the adjusted perceived belief on the water supply conditions considering the social norm effect, P_{g,y_t} is the original perceived belief of the agent at year y_t, and N_{agents} denotes the total number of agents. The social network matrix (S, Figure 2-3a) that represents agents' interaction networks, and the weight vector (Sw, Figure 2-3b) that balances neighbor opinions and the agent's evaluation are used to describe the impact of neighbor opinions on their decision, which we label the social norm effect in this chapter. In the social network matrix, each row of the matrix is a social network connection of an agent. "0" means the agent in that row is not affected by the opinion of the agent in that column. "1" indicates an influence from the opinion of the agent in that column. Also, the social network is directed. For example, agent 2 is affected by agent 1, but agent 1 is not affected by agent 2, as shown in Figure 2-3a. Lastly, *P* is a vector collecting all agents' perceived beliefs on water supply conditions (Figure 2-3c). Note that all perceived beliefs mentioned in this chapter are represented as probabilities, where values closer to 1 indicate an agent is more likely to have a positive belief in water supply conditions. The subscript g is the index of an agent.

In **step 3**, agents will update their decision rules by updating a state variable, Center (C_{g,y_t}), which will minimize the average difference between the simulated and observed river discharges (v_{g,y_t}) at their downstream area. We adopted a generalized form of the Bush-Mosteller model (Brenner, 2006), a type of reinforcement learning model, to achieve

Table 2-2. Agent attributes that affect their decision-making processes.

Attribute	Name	Type	Description
N	Record's length	State	The length of the agent's memory record, where we set it to be the length from the initial year (y_{t_0}) to y_{t-1} in this chapter.
C	Center	State	C is a state variable distinguishing the positive and negative perceived beliefs on the water supply conditions that result in increasing or decreasing irrigation diversion requests, respectively. It is updated annually using the RL algorithm (Equation 2-2).
$InfoSource$[a]	Information source	Parameter	Information that a particular agent uses to evaluate the coming year's water supply conditions. Sources include the deviation of (1) winter (Oct-Mar) precipitation in each of five reservoir catchments, (2) storage in each of five reservoirs in March, (3) total winter precipitation (Oct-Mar), and (4) total reservoir storage in March. The deviation is the difference between the current value of the selected $InfoSource$ and its historical average.
γ[a]	Learning rate	Parameter	γ is the learning rate for reinforcement learning (RL) algorithm (Equation 2-2) to update the state variable, C, based on the average difference between the simulated and observed river discharges.
Sc[a]	Scale	Parameter	Sc is a scale factor to scale the average difference between the simulated and observed river discharges. It is used to adjust the agent's sensitivity to this difference. (Equation 2-3).
α[a]	Alpha	Parameter	α is a prospect function parameter to adjust for positive beliefs about water supply conditions.
β[a]	Beta	Parameter	β is a prospect function parameter to adjust for negative beliefs about water supply conditions.
R_{max}[a]	maximum diversion-request-adjustment ratio	Parameter	R_{max} is the maximum diversion-request-adjustment ratio.
S*	social network matrix	Parameter	S is the social network matrix (Figure 2-3a), which defines the directed social network

			among agents. Each row of the matrix is the social network of the agent in that row.
Sw*	weight vector	Parameter	Sw is a weight vector for the social norm effect (Figure 2-3b), showing the proportion of each agent's belief to the neighbors' opinions.

[a] denotes parameters involved in the calibration.

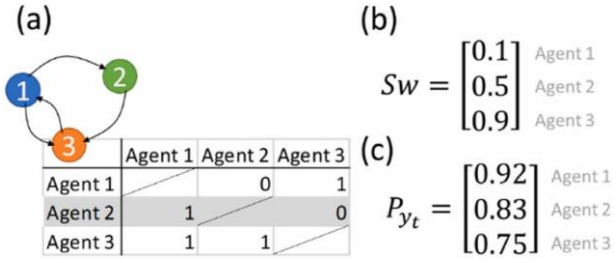

Figure 2-3. (a) is a social network matrix. Each row of the matrix is the social network of the agent in that row, which is affected by the agent in the column with cell's value 1. (b) Sw is a weight vector to balance between neighbor opinions and the agent's own beliefs. (c) P_{y_t} is a collection of agent's evaluations of water supply conditions in y_t.

the agent's adaptive learning behavior shown in the following equations:

$$C_{g,y_t} = \begin{cases} C_{g,y_{t-1}} + h_{g,y_t} \times \gamma_g \times \left(1 - C_{g,y_{t-1}}\right) & if\ h_{g,y_t} \geq 0 \\ C_{g,y_{t-1}} + h_{g,y_t} \times \gamma_g \times C_{g,y_{t-1}} & if\ h_{g,y_t} < 0 \end{cases} \quad (2\text{-}2)$$

where the strength (h_{g,y_t}) defining the updating magnitude of C is calculated by Equation 2-3. In Equation 2-3, v_{g,y_t} is equal to the observed river discharges minus the simulated discharges. v_{g,y_t} is scaled by a scale factor (Sc_g) and then transformed into a value between 0 and 1 through a sigmoid function (Equation 2-4). A "0.5" downshift defines the strength as positive or negative. The range of the strength becomes –0.5 to 0.5.

$$h_{g,y_t} = \begin{cases} \sigma\left(\frac{v_{g,y_t}}{Sc_g}\right) - 0.5 & if\ v_{g,y_t} \geq 0 \\ 1 - \sigma\left(-\frac{v_{g,y_t}}{Sc_g}\right) - 0.5 & if\ v_{g,y_t} < 0 \end{cases} \quad (2\text{-}3)$$

$$\sigma(x) = \frac{1}{1+e^{-x}} \quad (2\text{-}4)$$

The logic of Equation 2-2 and Equation 2-3 is that if we have a positive strength (positive v_{g,y_t}), which implies the observed river discharge is greater than the simulated discharge; then the agent will divert less water achieved by increasing C_{g,y_t}. The state variable C_{g,y_t} is used in **step 4** and **step 5** to distinguish the positive and negative perceived beliefs about water supply conditions, resulting in increasing or decreasing irrigation diversion requests, respectively. Therefore, higher C_{g,y_t} indicates a greater chance the agent will divert less water. This enhancement in C_{g,y_t} will result in attenuating the positive v_{g,y_t} mentioned above. In **step 4**, we address the agent's personal bias according to their risk attitude through a prospect function (Kahneman et al., 2013) with a small modification. The modified prospect function includes two nonlinear convex or concave curves split by C_{g,y_t}. These curves represent the agent's risk attitude toward positive belief (more available water) and negative belief (less available water). For a positive belief (larger than C_{g,y_t}), the convex function indicates the agent is risk-seeking, while the concave function indicates a risk-averse attitude. On the contrary, the convex function indicates risk-seeking, and the concave function means risk-averse for the agent's attitude toward negative beliefs. The agent's perceived belief (P_{g,y_t}^{bias}) is then updated by Equation 2-5,

$$P_{g,y_t}^{bias} = \begin{cases} \left(\frac{p-C_{g,y_t}}{1-C_{g,y_t}}\right)^{\alpha_g} \times \left(1-C_{g,y_t}\right) + C_{g,y_t} & if \;\; p \in P_{g,y_t}^{adj},\; p \geq C_{g,y_t} \\ \left(\frac{p-C_{g,y_t}}{C_{g,y_t}}\right)^{\beta_g} \times C_{g,y_t} + C_{g,y_t} & if \;\; p \in P_{g,y_t}^{adj},\; p < C_{g,y_t} \end{cases} \quad (2\text{-}5)$$

where α_g and β_g are the curvatures of nonlinear curves for the positive and negative beliefs, respectively, and P_{g,y_t}^{adj} is a vector of values of a discretized beta probability distribution computed from p_{g,y_t}^{adj} and N (Table 2-2, Equation A-6). In **step 5**, the diversion-request-

adjustment ratios are generated by mapping perceived beliefs (P_{g,y_t}^{bias}) into diversion-request-adjustment ratios (R_{g,y_t}) through a linear mapping function (Equation 2-6).

$$R_{g,y_t} = \left(\left(\mathrm{ECDF}_{P_{g,y_t}^{bias}}^{-1}\left(u_{g,y_t}\right) \times 2 - 1\right) - \left(C_{g,y_t} - 0.5\right) \times 2\right) \times R_{g,max} \quad (2\text{-}6)$$

where u_g is a random number from a $\mathrm{Uniform}(0,1)$ distribution.

In this chapter, the R_{g,y_t} is represented by the expected value (R_g^{Exp}) for enhancing the calibration converging speed.

$$R_{g,y_t}^{Exp} = E_u\left[R_{g,y_t}\right] \quad (2\text{-}7)$$

In addition, to prevent the numerical error, the R_{g,y_t}^{Exp} is forced to be greater than -0.9. If it is below -0.9, the algorithm will replace it with -0.9. Finally, we complete the decision-making process by using the ratios to update mean annual diversion requests and disaggregate them into daily diversion requests (**step 6,** Equation A-10). The ODD+D description (Müller et al., 2013) for the ABM model (Appendix A.2) and a complete mathematical description of the decision-making algorithm (Appendix A.3) are provided in Appendix A.

2.4.2 Models' calibration and validation

To calibrate the model, we separated a single simulation into three periods: (1) warm-up period (1960–1965), (2) calibration period (1966–1995), and (3) validation period (1996–2005). The objective function for the calibration is to maximize the mean annual Nash-Sutcliffe efficiency (NSE; Nash and Sutcliffe, 1970) of six diversions (i.e., Kittitas, Tieton, Wapato, Sunnyside, Roza, and Kennewick) and two river discharges (i.e., Parker and Kiona) as the RW is updated by the diversion ABM with an annual frequency (Section 2.4.1).

Coupled-YAKRW contains 72 parameters that require calibration, including six parameters (Table 2-2) for each district, a social network matrix, and a weight vector. To reduce the searching space, we first calibrate Coupled-YAKRW without a social network matrix (Coupled-YAKRW w/o S.); namely, 36 parameters from the social network matrix and the weight vector are removed. Then, we calibrate Coupled-YAKRW with a fixed $InfoSource$ parameter from the calibrated Coupled-YAKRW w/o S. model for each agent.

2.4.3 Experimental setup

We design the following numerical experiments to compare coupled models with the YAKRW (baseline), investigate the social norm effect, and assess the impact of changing policy rules on human irrigation behaviors.

2.4.3.1 Model comparison for testing different ABM structures

We first calibrate and validate two coupled models (Coupled-YAKRW and Coupled-YAKRW w/o S.). Then, we compare them with the baseline model (YAKRW) to examine whether coupled models can better capture both the hydrological responses (system viewpoint) and irrigation diversion dynamics (the local viewpoint).

2.4.3.2 LSA on a directed social network

The social norm effect is argued to be a significant factor affecting farmer decisions in the western U.S. (Hu et al., 2006). Therefore, in addition to the model comparison in Section 2.4.3.1, we further explored the sensitivity of social network structure to local or system-wide model performance (i.e., NSE) using local sensitivity analysis (LSA) on the directed social network. In the experiment, we slightly perturbed connections inside the network of the calibrated network of Coupled-YAKRW. This means we randomly selected one or two agent pairs and reversed their calibrated network connections. For example, if the pair of

agents had no connection (e.g., cells in the social network matrix (Figure 2-3a) with value 0), then we added a connection (changed 0 to 1) or vice versa. For a single perturbation, we had 30 combinations in social networks. For two perturbations, we had 435 combinations. Consequently, we ran a total of 465 simulations in the LSA.

2.4.3.3 Water-reallocation-induced behavior changes

The third experiment is performed as a proof-of-concept to demonstrate how the two-way coupled model can be applied to inform potential human behavior changes through a "what-if" water reallocation scenario. We would like to show how agents' risk attitudes will change if their water rights are all proratable, meaning they share the water deficiency during the drought years. To clarify, we are not proposing the implementation of such top-down water rights changes. Instead, we want to use the scenario to test the hypothesis that agents originally with nonproratable water rights will be more sensitive to environmental changes (i.e., toward risk-averse) as there is no guaranteed water supply during drought years. In reality, water rights change is an extremely complicated issue involving political debate, government negotiation, and multiple-level stakeholder engagements, which is out of this chapter's scope and beyond the limit of our current ABM structure. Therefore, we can only show the results of "what will happen" if water can be reallocated in the YRB, but we will not explore "how it might happen" in this chapter. To test the abovementioned changing behavior hypothesis, we recalibrated the coupled model with the all-proratable water rights setup and compared the recalibrated agents' parameters with the original one.

2.5 Results

2.5.1 Model comparison and adaptive capacity

We show how coupled models can better capture both long-term (overall trends) and short-term (year-to-year variations) hydrological and irrigation diversion dynamics in this section. We also discuss the impacts of the social norm effect, namely, the impact of the ABM model structure as well. In this case study, the NSEs resulting from the annual diversion of six major irrigation districts are considered as local level model performances. In contrast, the NSEs from the annual discharge of the Parker and Kiona flow gauges near the basin outlet represent system-wide performances.

Table 2-3 shows both Coupled-YAKRW and Coupled-YAKRW w/o S. can better capture local and system-wide dynamics of the observed data compared to the baseline model (YAKRW) in terms of NSE values. For system mean NSEs, the two coupled models and the baseline model are similar. However, the coupled models show significantly better local NSEs (Table 2-3). Kennewick's performances are dominated by RW's policy rule (Section 2.4.1.1), as we can also see in Figure 2-4. Figure 2-4 reveals the annual diversion time series data for six agents. The grey lines are the observed data. The validation results (after the vertical dashed lines in Figure 2-4) indicate the calibrated models are not overfitted. Similar results are provided for Parker and Kiona flow gauges in Figure A4. These results suggest that coupled models better catch diversion dynamics induced by human activities through adaptive decision-making.

Table 2-3. NSE values of YAKRW, Coupled-YAKRW, and Coupled-YAKRW w/o S. models.

Models	Local NSEs						System NSEs	
	Roza	Sunnyside	Tieton	Kennewick	Kittitas	Wapato	Kiona	Parker
YAKRW	-0.08	-5.87	-1.66	-0.69	-2.78	-0.12	0.97	0.91
Coupled YAKRW	0.60	0.34	-0.42	-0.68	0.55	-0.16	0.95	0.98
Coupled-YAKRW w/o S.	0.56	-0.60	0.54	-0.73	0.81	0.13	0.96	0.99

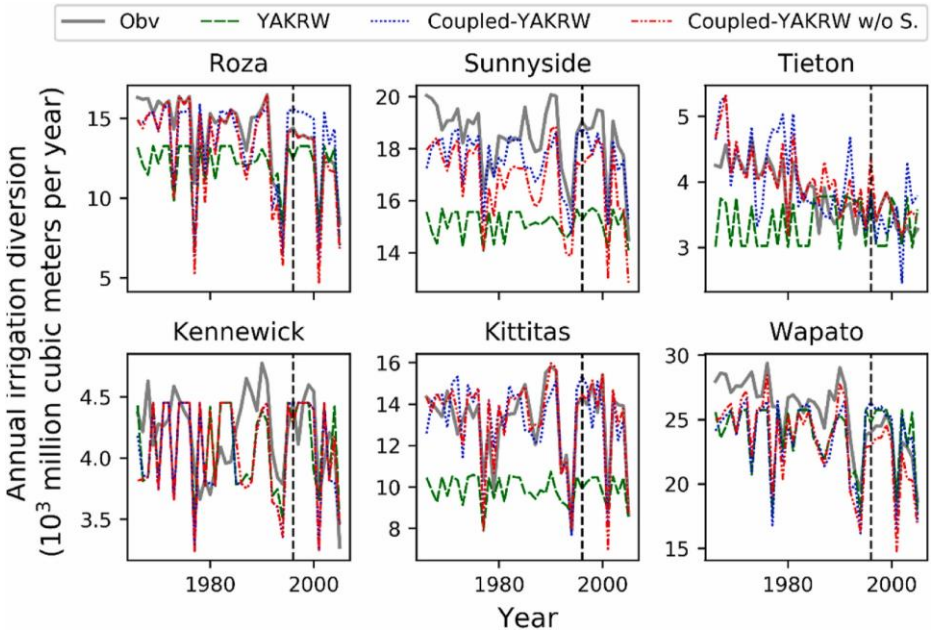

Figure 2-4. Model comparison of annual diversions. Grey lines are the observed annual irrigation diversions. Green dashed lines are outputs of the original YAKRW model. Blue and red dotted lines are simulated results from coupled-YAKRW and coupled-YAKRW w/o S., respectively.

We quantify how adaptive capacity benefits by capturing long-term trends in irrigation diversions with the state variable C in Figure 2-5. State variable C contributes to steps 3, 4, and 5 of the agent's decision-making process as a parameter in decision rules (Figure 2-2). As mentioned in Section 2.4.1.2, C distinguishes the positive and negative perceived beliefs about water supply conditions, leading to increasing (above C) or

decreasing (below C) irrigation diversion requests, respectively. Therefore, although a bit counterintuitive, if we observe C value is continuously higher than 0.5, then we can anticipate a long-term decreasing diversion trend and vice versa. For the Roza, Wapato, and Tieton districts in Figure 2-5, the C value fluctuates at approximately 0.5 before 1980 and remains greater than 0.5 after 1980. This corresponds to an observed decreasing diversion trend after 1980 (Figure 2-4). Following the YRB's history, there was only one major drought between 1960 and 1980, which provided fewer incentives to alter diversion behaviors. However, the YRB experienced about one drought every five years after 1980 (Malek et al., 2018; Pellicciotto et al., 2012), which may have influenced the competition dynamics of water. This affected the overall cooperative or defective structure in the basin, which motivates some districts to initiate water conservation measures (e.g., changing crop types and improving irrigation efficiency). These long-term changes in diversion behavior can be combined and implicitly captured by state variable C. For Sunnyside and Kittitas, C values remained approximately 0.5 during the entire simulation period, suggesting no noticeable long-term trend in diversions. These results also corresponded to the observations in Figure 2-4. For the Kennewick agent, due to dominant policy rules inside the YAKRW model (Section 2.4.1.1), our ABM model showed a minor influence on Kennewick's behavior. Therefore, neither the simulated diversion value nor the C value captured the observed dynamic.

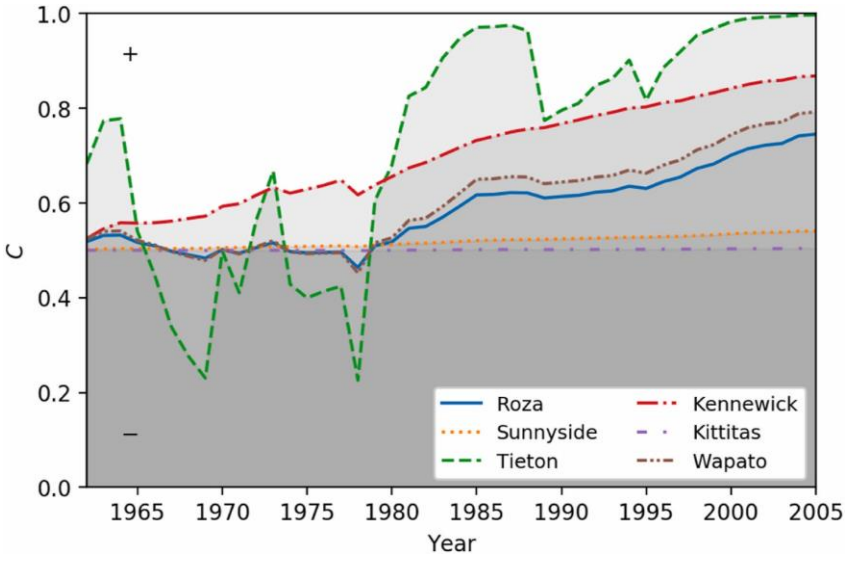

Figure 2-5. Timeseries plot of the state variable, Center (C), for six agents in the Coupled-YAKRW model. Colored regions have negative perceived beliefs about water supply conditions. Note: higher C values indicate agents will divert less water.

2.5.2 LSA of social network structure

The social norm effect is suggested as a significant factor in farmer decision-making processes in the western U.S. (Hu et al., 2006). However, in this case study, both Coupled-YAKRW and Coupled-YAKRW w/o S. models provided a similar level of mean NSE, where Coupled-YAKRW w/o S. generated a slightly higher mean NSE (Table 2-3). One explanation is model equifinality, where the over-parameterized model obtains a set of parameters (Figure A6) or structures that result in similar model performance. In Table 2-4, we show how calibrated agent-unique parameters (i.e., agent attributes) were changed from Coupled-YAKRW to Coupled-YAKRW w/o S to compensate for the absence of the social norm effect (S and Sw). Although judging the correctness of different model settings is not the target of this chapter, a further investigation can advance our understanding of the role of the social norm effect and help us evaluate model equifinality issues in the coupled models for future CNHS studies.

Table 2-4. Percentage of difference between Coupled-YAKRW and Coupled-YAKRW w/o S. regarding each parameter's calibrated range. Raw parameter values of Coupled-YAKRW and Coupled-YAKRW w/o S. are given in Table A1 and Table A2, respectively.

Parameter	Roza	Sunnyside	Tieton	Kennewick	Kittitas	Wapato
γ	-17%	-96%	21%	-7%	-63%	18%
Sc	31%	30%	20%	-12%	34%	4%
α	-29%	-24%	-64%	29%	-80%	45%
β	-15%	-54%	23%	21%	-81%	14%
R_{max}	-48%	-74%	28%	-7%	-17%	-31%

To further examine the impact of the social network structure on model performance, local sensitivity analysis (LSA) was performed by perturbing the calibrated social network matrix (Table A3) as described in Section 2.4.1.2. The LSA results (Figure 2-6) show that the mean diversion NSE over six agents was similar to the calibrated Coupled-YAKRW model (red cross). However, perturbation of the social network could affect the local performance of individual agents (e.g., Tieton, Kittitas, and Sunnyside). Our original hypothesis is that agents with larger weights for the social norm effect will be more sensitive to social network perturbations. However, the Tieton district, with a lower weight value (0.09), showed a more significant variation in NSE values compared to other agents with higher weights (e.g., Roza and Wapato). This was due to predefined policy rules inside the YAKRW model, described in the next paragraph. For the Kittitas district, the perturbation results had higher NSE values in the irrigation diversion outputs. This phenomenon was caused by the system-wide calibration objective function, in which local parameters might not be optimized for each agent. For the Sunnyside district, the variance among LSA simulations was small (i.e., insensitive), but there was a noticeable decrease in NSE values. One possible reason is that Sunnyside has the highest calibrated learning rate (γ; Table A1) and maximum diversion-request-adjustment ratio (R_{max}; Table A1), meaning its decisions may be greatly influenced by the environment feedback (e.g.,

streamflow, v). Therefore, other agents' behaviors may implicitly affect Sunnyside's diversion decisions through changing the streamflow (e.g., upstream diversions) during the social network perturbation.

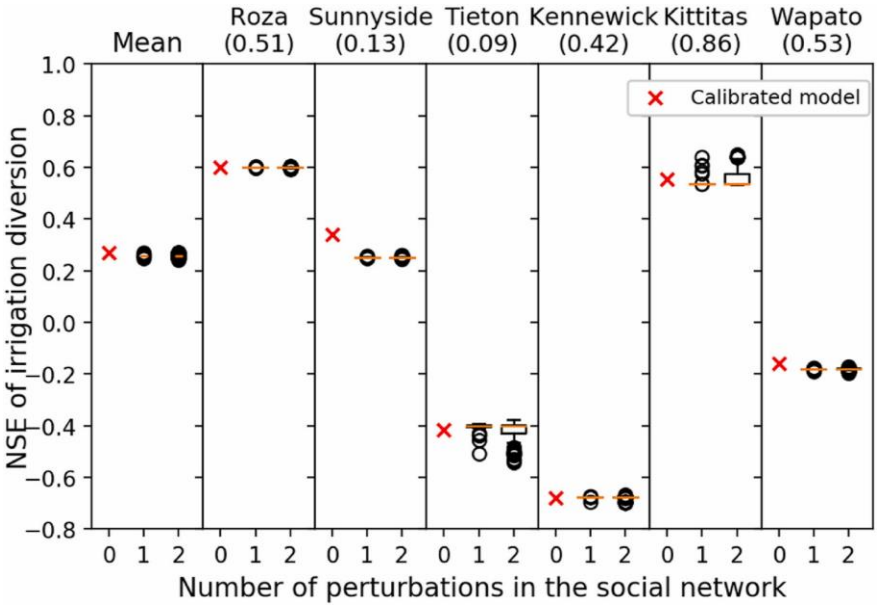

Figure 2-6. NSE of irrigation diversions in LSA. The weight of the social norm effect of each agent is shown by brackets. The red cross indicates calibrated Coupled-YAKRW model results, and the orange lines are median values. Black circles are NSE values outside the range of 25% and 75% quantiles shown as boxes.

Agents such as Roza, Sunnyside, Kennewick, and Wapato were not sensitive to the social network structure. However, those insensitive results do not imply that the social norm effect is not essential, where the predefined policy rules in the YAKRW might cause such results. Policy rules, including water rights or maximum/minimum diversion constraints (Section 2.4.1.1), could limit the utility of ABM outputs. Therefore, the social norm effect might seem limited using RW outputs. To illustrate this complexity, we plotted the standard deviation of 465 simulations with respect to calibrated Couple-YAKRW results in Figure 2-7, where blue circles represent actual diversion (RW output) and orange

triangles indicate the diversion requests sent from ABM to RW (RW input). In general, larger *Sw* values have greater standard deviations since the agent relies more on the neighbor's opinions. However, those trends are limited by RW policy rules (Section 2.4.1.1), where the standard deviations of RW outputs are less than RW inputs. This phenomenon becomes clear at larger *Sw*. Such a limitation is acceptable because individual human behaviors are indeed restricted by policy rules (e.g., water rights) in the real world.

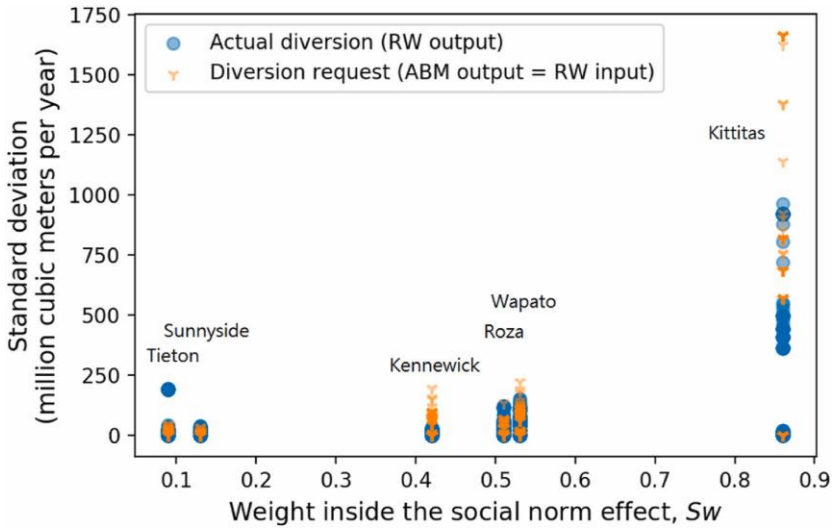

Figure 2-7. Standard deviations of 465 LSA simulation results with respect to calibrated Coupled-YAKRW outputs. The x-axis is the weight inside the social norm effect. Blue circles represent actual diversion (RW output), and orange triangles indicate diversion requests sent from ABM to RW (RW input).

2.5.3 Impact of policy rules on the human behavior

Studies have shown evidence in offsetting behaviors (Campbell et al., 2004; Fielding et al., 2012), where the feedback of human behaviors toward the changing policy jeopardizes the original intention or the effectiveness of that newly introduced policy. For example, Fielding et al. (2012) indicated that the policy of giving people water-saving hardware might result in higher water consumption, which was opposite to the goal of their water

conservation programs. This offsetting behavior motivates us to explore the impact of changing policy rules (e.g., water reallocation) on human behavior (e.g., diversions and risk attitudes).

In the comparison of Coupled-YAKRW w/o S. between original and all-proratable water rights, we found that Wapato, Sunnyside, and Tieton divert much less water during the drought years since their original non-proratable water rights are set to all-proratable water rights. Then, when those senior water rights holders divert less water, more water becomes available to junior holders. This is more obvious in normal and wet years. Therefore, we observed larger diversion fluctuations in those agents (Figure A5). We ignore Kennewick in the latter analysis due to dominant policy rules in the YAKRW (Section 2.4.1.1), leading to minor influence from the diversion ABM.

To further investigate the potential changes in human behaviors, we recalibrated the Coupled-YAKRW w/o S. (with fixed $InfoSource$) under the all-proratable water rights setup. The results indicate that agents become more sensitive to the changing environment (i.e., toward risk-averse), as shown in Figure 2-8. Figure 2-8 presents the prospect functions (Equation 2-5) of agents' perceived beliefs on the water supply conditions. The curvatures (α and β in Equation 2-5) are agents' risk attitudes. For example, concave shapes in the upright corner in each subplot of Figure 2-8 mean that agents are risk-seeking and insensitive to the belief of the positive water supply conditions (e.g., more available water), while convex shapes represent risk-averse attitudes and sensitive characteristics to the belief of the positive water supply conditions. On the contrary, the concave and convex shapes have opposite meanings for the lower-left corner in the subplots (Figure 2-8), which indicates the agents' risk attitudes to the belief of the negative water supply conditions (e.g.,

droughts). The prospect functions of the recalibrated Coupled-YAKRW w/o S. are shown in dotted lines, where the solid lines are from the original model. Comparing solid and dotted lines, we can see that most of the lines curve toward risk-averse regions (blue area) in Figure 2-8 except parts of Tieton and Wapato. Namely, agents become more willing to adjust their diversion behaviors according to the changing environment. This flexibility could potentially benefit the instream flow control (e.g., adjusting their diversions to meet target flow) and enhance the efficiency in water uses, where efficiency is defined as maximizing productivity without wasting. It has been shown that the value associated with instream flow (e.g., recreational and esthetic uses) are greater than the value made from irrigation of low-value crops (Watts et al., 2001). However, the unstable irrigation supply could also impact the investment in high-value perennial crops such as orchards and grapes (Feinerman and Tsur, 2014), which requires several preparation years before making profits.

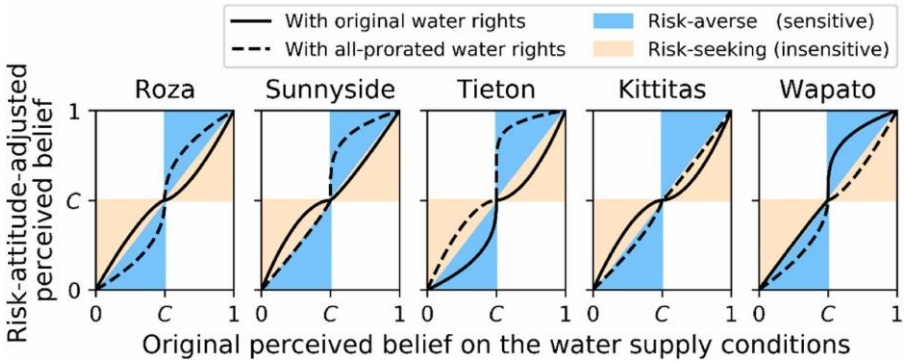

Figure 2-8. Prospect functions (e.g., mapping agents' risk attitudes; Equation 2-5) under original (solid lines) and all-proratable (dotted lines) water right scenarios. The upper right corners are the risk attitudes toward the beliefs of positive water supply conditions, while the lower left corners are of negative conditions (e.g., droughts).

2.6 Discussion

2.6.1 Cross-scale CNHS modeling for multi-level governance application

This chapter investigates the co-evolution mechanism in CNHS modeling via a case study in the YRB. The results show that the coupled models can better capture both system (e.g., streamflow) and local (e.g., irrigation diversions) dynamics. Also, we demonstrate the influences of the social norm effects and the impact of the changing water allocation policy. We would like to further discuss how to link the coupled models proposed in this chapter to potential multi-level water resources governance applications.

Multi-level water resources governance naturally occurs in many managements problem in solving water conflicts. For example, the Yakima River Basin Integrated Water Management Plan (Office of Columbia River, 2020) began in the 1980s, involving federal (e.g., USBR), Washington state, Yakama Nation, counties, cities, and farmers to collaboratively offer a long-term vision and a management plan for water allocation under the changing climate and environment. To that, the coupled model provides a quantification method to model the cross-scale responses supported by individually customized actors' behaviors and interactions (e.g., federal policy to the reservoir operations, water allocation policy to the farmers' behaviors, and ecological conditions to the drought responses) under a decentralized modeling framework (e.g., ABM). Such properties of coupled models create a unique niche for informing multi-level water resources governance via modeling results. Furthermore, according to an entire Columbia River Basin (CRB)-wide survey results (Zhang et al., 2021), reservoir operations in the CRB gradually shifted to improve the aquatic environment (USBR, 2020) and people were most supportive of sustainability policies impacting the food and water sectors instead of

energy sectors. The YRB situations and our modeling results align with the survey findings. This implies that the model structure of Coupled-YAKRW (e.g., reservoir operation rules in the RW and the diversion ABM) has the potential to be scaled up and applied to the entire CRB.

More importantly, we would like to discuss the motivation of how water agencies might consider adopting coupled models, which could help them resolve possible water conflicts under different policy scenarios (with explicit human decisions quantified). Here are some historical events for water conflicts associated with water resources multi-level governance in the CRB region. In 2006, a water rights fight between a power company and the Idaho State government occurred at the Snake River, US, where ongoing water rights dispute with the Nez Perce Indians has been last for decades (Miller, 2006). In 2016, the armed fights over the water rights and land resources in the Malheur National Wildlife Refuge, Oregon, US, between the federal government and the local people led to several casualties (Wiles, 2016). We vision that coupled models can analyze and broaden policies and management strategies, which provide a higher chance of finding a smoother path to ease those water conflicts. However, such a hypothesis cannot be solely proved by our current modeling experiments. It requires vigorous involvement of social science to establish the theoretical foundation for model setup and continuous communication among stakeholders.

2.6.2 Limitations

To explore water management challenges in CNHS, we tested different ABM models for different human behavior assumptions and built the coupled model on top of existing process-based models (e.g., YAKRW in our case study), which were developed by USBR.

These existing models are used by authorities to assist in real-world operations. Therefore, policy constraints are included in the modeling structure to reflect reality as much as possible. These inclusions are most likely present due to legal issues around water rights and minimum stream flow constraints, as examples. Therefore, our case study might not fully demonstrate the utility of the ABM. As shown in the Result section, we encountered limited flexibility in the YAKRW model. Nonetheless, these results do not mean we should not couple with these existing models; we would like to leverage their credibility and use the coupled model to demonstrate potential policy changes via modeling results.

Also, the current ABM model design limits our capability to further explore the water reallocation experiment. As a result, we only demonstrate "what will happen" but not "how it will happen." In reality, a possible way to facilitate the discussion of water reallocation is through water banking or water market mechanisms (Du et al., 2021; Yang et al., 2012). For example, with economic incentives, Du et al. (2021) and Yang et al. (2012) showed the possible transition of a nonproratable water right holder might become a proratable water right holder in a water market. Note that the water market setting will drive farmers' behaviors in a different way, as we presented in this chapter and require a different ABM model design (i.e., a decentralized optimization algorithm to drive agent's behavior is needed in the water market setup). Nevertheless, this topic will be a perfect future study applying the two-way coupled model.

Another limitation is the model equifinality issues (e.g., multiple models result in similar calibrated outcomes) along with the potentially over-parameterized coupled models. Namely, due to the unknown of the true process, modelers will encounter trade-offs between narrative complexity (e.g., how detail is the human behavior modeling design?)

and model complexity (Grimm and Railsback, 2012a), which leads to greater equifinality (Figure A6). We further refer readers to Beven (2006), Khatami et al. (2019), and Lin and Yang (2022) for a more comprehensive introduction to equifinality issues. To address this limitation, we plan to conduct uncertainty and sensitivity analysis (Yen et al., 2014) and add these features in the next version of Py-RAMID to help modelers identify dominant policy rules in the RW and model equifinal parameter sets of coupled models. Also, instead of a single mean NSE value, we can calibrate the coupled models with pattern-oriented modeling (Grimm and Railsback, 2012b; Wiegand et al., 2003), which focuses more on the adaptive capacity of the system. For example, the adaptation of an agent's behaviors (e.g., crop types and crop area) as responses to the changing environment or extreme events (e.g., droughts).

Finally, even though we put effort of developing a python-based Py-RAMID package for embracing the Open Science by Design concept (NASEM, 2018; U.S. DOE, 2019) through improving coupled models' reproducibility (Goodman et al., 2016) and extensibility (Lacroix and Critchlow, 2003), we understand Py-RAMID has its limitation to fully meet the idea due to the licensed RiverWare. Moreover, similar coupling concepts like co-simulation, multi-modeling, multi-formalism modeling, and multi-model ecologies have also been explored in energy and system control domains (Bollinger et al., 2018; Gomes et al., 2018; Plessis et al., 2014; Vangheluwe, 2000; Vaubourg et al., 2015), as well as the integration frameworks like High-Level Architecture (HLA; Dahmann et al., 1997) in the technology context. Therefore, we do not claim that Py-RAMID is a novel contribution to the Open Science by Design concept. Instead, we hope the study in this

chapter can help our readers to be aware of this concept and further contribute to it in the future.

2.7 Conclusions

This chapter aims to improve our understanding of CNHS, which has been shown to ameliorate environmental planning and policy (Zellner, 2008), through the YRB case study. We designed three numerical experiments investigating different facets of CNHS. First, we compare coupled models (e.g., Coupled-YAKRW and Coupled-YAKRW w/o S.) with the baseline model (e.g., YAKRW) and demonstrate that coupled models can better capture both irrigation diversion (human behaviors) and streamflow dynamic. Second, we analyzed the role of the social norm effect through a local sensitivity analysis. The similar simulation results between coupled models with or without social norm effect are caused by the dominant RW policy rules and the potential model equifinality issue. Separate research on quantifying the model complexity and equifinality is required before further demonstrating the effect of the social norm in CNHS modeling. Third, we show human behaviors (e.g., diversions and risk attitudes) could be affected by policy rules, where agents become more sensitive (i.e., risk-averse) to the changing environment under the all-proratable-water-rights scenario in the YRB. In sum, this chapter explores the co-evolution in CNHS from different facets, such as model structures (e.g., social norm effect) and the reciprocate influence between policy rules (e.g., water allocation) and human behaviors (e.g., diversions and risk attitudes). However, a more detailed model uncertainty analysis is needed to further quantify the benefit of CNHS in informing policymaking for future multi-level water resources governance applications.

Chapter 3: HydroCNHS: A Python Package of Hydrological Model for Coupled Natural–Human Systems

Abstract

Modeling Coupled Natural–Human Systems (CNHS) to inform comprehensive water resources management policies or describe hydrological cycles in the Anthropocene has become popular in recent years. To fulfill this need, we developed a semi-distributed Hydrological model for Coupled Natural–Human Systems, HydroCNHS. The HydroCNHS is an open-source Python package supporting four Application Programming Interfaces (APIs) that enable users to integrate their human decision models, which can be programmed with the agent-based modeling concept, into the HydroCNHS. Specifically, we design Dam API, RiverDiv API, Conveying API, and InSitu API to integrate, respectively, customized man-made infrastructures such as reservoirs, off-stream diversions, trans-basin aqueducts, and drainage systems that abstract human behaviors (e.g., operator and farmers' water use decisions). Each of the HydroCNHS APIs has a unique plug-in structure that respects within-subbasin and inter-subbasin (i.e., river) routing logic for maintaining the water balance. In addition, the HydroCNHS uses a single model configuration file to organize input features for the hydrological model and case-specific human systems models. Also, HydroCNHS enables model calibration using parallel computing power. We demonstrate the functionalities of the HydroCNHS package through a case study in the Northwest United States. Given the integrity of the modeling framework,

HydroCNHS can benefit water resources planning and management in various aspects, including uncertainty analysis in CNHS modeling and more complex agent design.

3.1 Introduction

Recently, many studies have explored the coevolution of natural and human water systems with coupled natural–human systems (CNHS) modeling approach, e.g., Faust et al. (2017) and Wada et al. (2017), for a comprehensive evaluation of water resources management policies (Yang et al., 2020) and near-surface water cycles (Sivapalan et al., 2015). The coupled modeling approach often consists of a process-based hydrological model and a human infrastructure model. Agent-based modeling (ABM) is commonly adopted to describe heterogeneous human behaviors and their impacts on water systems that significantly vary at various spatial and temporal scales, e.g., Hu et al. (2019), Lin et al. (2022), and Lin and Yang (2022). Each agent represents a decision-making unit defined by a set of attributes and behavior rules. In general, man-made infrastructures such as reservoirs, diversions, trans-basin aqueducts, and drainage systems can be represented as an agent and coupled with hydrological models with desired bidirectional information exchange frequency.

However, developing a sophisticated human model is not always possible for CNHS modeling/modelers due to the lack of data or other limitations. For example, when modeling reservoir releases, modelers can use historical records (e.g., daily time series) as exogenous inputs or use a decision-making model to endogenously and dynamically simulate water releases. While some existing hydrological model software, e.g., Neitsch et al. (2011) and Liang et al. (1996), can incorporate human decision units, the option that allows users to choose among exogenous or endogenous human components is often not

supported. Knox et al. (2018) developed a generic network-based multi-agent framework to link natural models and human models, which is one of the earlier efforts to address this gap. Following Knox et al. (2018) and trying to specifically target the water system, this technical note aims to develop a semi-distributed Hydrological model for Coupled Natural–Human Systems (hereafter HydroCNHS) that facilitates integrating hydrologic models with agent-based human system models through a generalizable coupling procedure with four Application Programming Interfaces (APIs). The four APIs are Dam API, RiverDiv API, Conveying API, and InSitu API, which have distinct plug-in structures that respect within-subbasin and inter-subbasin (i.e., river) routing logic for maintaining the water balance. They can integrate human models, where heterogeneous human agents can be modeled with different decision-making process complexity and data intensity (e.g., exogenous input data or endogenous rules) from a bottom-up viewpoint. Essentially, the HydroCNHS is a Python package simulating natural and human-induced water cycles within a or multiple watershed system(s) on a daily scale. The package features a single model configuration file to organize input settings for hydrological models and case-specific human models. In addition, the HydroCNHS supports a parallel calibration module using a genetic algorithm (GA; Whitley, 1994). The package is published with GPL-3.0 License to follow the concept of Open Science (NASEM, 2021). We demonstrate the functionalities of the HydroCNHS in a case study with the Tualatin River Basin (TRB) in the Northwest United States.

3.2 Methods

3.2.1 Structure of the HydroCNHS Model

The HydroCNHS Python package is a semi-distributed hydrological model for CNHS that simulates natural and human-induced water cycles on a daily scale. The subbasin delineation is based on the agent design and user-desired distributing resolution. Figure 3-1 shows the HydroCNHS model structure (blue box) and user inputs (yellow box). Three inputs are required: (1) daily climate data (precipitation and temperature), (2) a model configuration file (*.yaml*; setting for the HydroCNHS and ABM modules), and (3) ABM modules (*.py*; green box). HydroCNHS APIs handle the logic to integrate ABM modules.

In the "Initialization" step (Figure 3-1), the HydroCNHS form the routing scheme based on the stream orders associated with outlets (i.e., routing order of outlets). Then, agent instances/objects are created according to user-defined agent classes in ABM modules (*.py*). A "class" is a data structure in object-oriented Python defined by "attributes" and "methods." Once initialized, each agent is an instance of an assigned agent class. For example, two reservoir agents can be created by a single reservoir agent class. After that, the HydroCNHS simulates the initial subbasin runoffs independently using a rainfall-runoff module, for which we provide two options: (1) the General Water Loading Function (GWLF; Haith et al., 1987) with nine parameters and (2) the ABCD model (Thomas, 1981) with five parameters. Next, we use the Lohmann routing model (Lohmann et al., 1998) to trace the runoff from subbasins through the river channel (i.e., inter-subbasin routing) and the unit hydrograph parameterization described in Wi et al. (2015) to account for the within-subbasin routing process. A detailed description of the GWLF, ABCD, and Lohmann routing models is provided in the next section. The runoff from each subbasin is

sent to the "Coupling Simulation" step (Figure 3-1), and its contribution to the basin outlet is determined by the three factors: (1) the simulation period, (2) the routing scheme for routing outlets, and (3) agents linked to outlets. Forming a routing scheme with four APIs in the HydroCNHS will be further explained in the following sections.

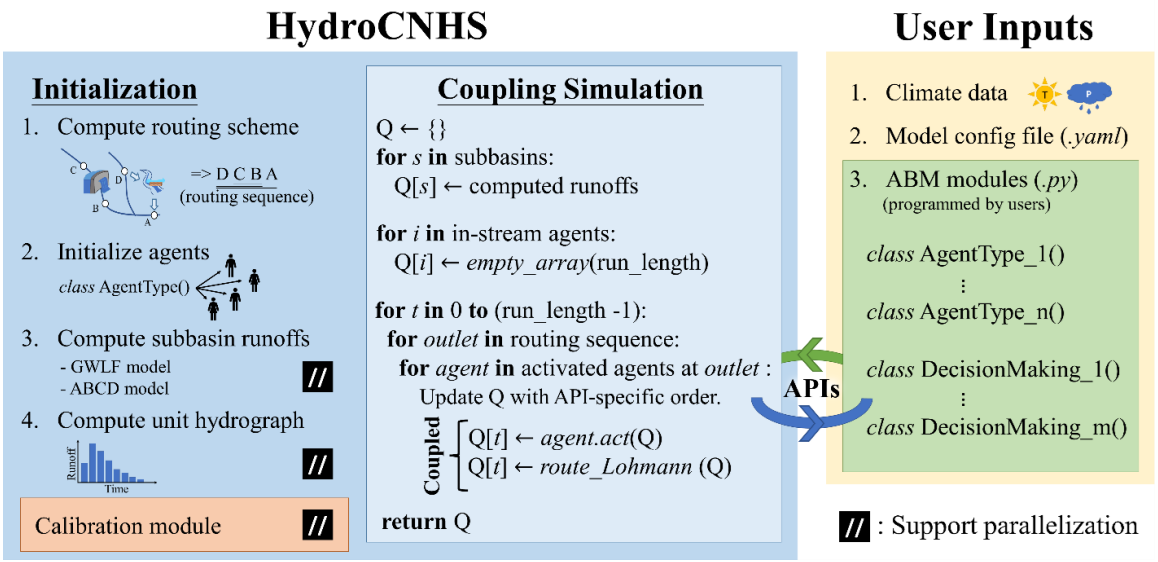

Figure 3-1. Structure of the HydroCNHS model structure (blue box) and three user inputs (yellow box), including climate data (temperature and precipitation), model configuration file (*.yaml*), and ABM modules (*.py*; green box). User-provided ABM modules will be integrated into the HydroCNHS through four APIs.

The GA "Calibration module," powered by the Distributed Evolutionary Algorithms in Python (DEAP) Python package (Fortin et al., 2012; De Rainville et al., 2012), facilitates calibrating the entire CNHS model in a parallel computing mode. We refer our readers to the HydroCNHS user manual for more details and coding examples (https://hydrocnhs.readthedocs.io).

3.2.2 Module components

3.2.2.1 Snow module

HydroCNHS is embedded with a simple snow module (Haith, 1985) to separate rainfall (R_t [cm]) from the precipitation (P_t [cm]) and updated rainfall by the snowmelt, as shown below.

$$Sn_t = \begin{cases} Sn_{t-1} - \min(Sn_{t-1}, Df * T_{t-1}), & T_{t-1} > 0 \\ Sn_{t-1} + P_{t-1}, & T_{t-1} \leq 0 \end{cases} \quad (3\text{-}1)$$

$$R_t = \begin{cases} P_t + \min(Sn_t, Df * T_t), & T_t > 0 \\ 0, & T_t \leq 0 \end{cases} \quad (3\text{-}2)$$

where Sn_t [cm] is the accumulated snow at time t. Df [cm/°C] is the degree-day coefficient for snowmelt. This module will be used in GWLF and ABCD models.

3.2.2.2 Modified General Water Loading Function (GWLF) module

The hydrologic module of the GWLF (Haith et al., 1987) is a lumped rainfall-runoff model, which simulates the daily outlet runoff (F_t [m^3/sec]) by

$$F_t = (SF_t + G_t + BF_t) \times \frac{A}{864} \quad (3\text{-}3)$$

where SF_t [cm] is surface quick flow, G_t [cm] is subsurface flow, and BF_t [cm] is newly introduced baseflow component (Luo et al., 2012) to depict low flow patterns in the modified version. Subscript t denotes the value at time step t. This will continuously apply to the rest of the content. A [ha] is the catchment area.

The **surface quick flow** is calculated by the SCS-curve-number method.

$$SF_t = \begin{cases} \left(R_t - (IS \times DS_t)\right)^2 / \left(R_t + \left((1 - IS) \times DS_t\right)\right), & R_t > IS \times DS_t \\ 0, & Otherwise \end{cases} \quad (3\text{-}4)$$

where IS is an interception coefficient. DS_t [cm] is the potential maximum detention after runoff begin, which can be estimated by

$$DS_t = 2540/CN_t - 25.4 \tag{3-5}$$

where CN_t is computed at time t by

$$CN_t = \begin{cases} CN_1 + ((CN - CN_1)/AM_1) \times AM_t, & AM_t < AM_1 \\ CN + ((CN_3 - CN)/(AM_2 - AM_1)) \times (AM_t - AM_1), & AM_1 \le AM_t \le AM_2 \\ CN_3, & AM_2 < AM_t \end{cases} \tag{3-6}$$

$$CN_1 = (4.2 \times CN)/(10 - 0.058 \times CN) \tag{3-7}$$

$$CN_3 = (23 \times CN)/(10 + 0.13 \times CN) \tag{3-8}$$

where CN is a curve number parameter. AM_t [cm] is the five-day antecedent moisture. AM_1 and AM_2 are equal to 3.6 and 5.3 [cm], respectively, if the monthly mean temperature is higher the 10 degrees Celsius (growing season). Otherwise, AM_1 and AM_2 are equal to 1.3 and 2.8 [cm], respectively.

The **subsurface flow** is calculated by

$$G_t = RC \times S_t \tag{3-9}$$

where RC is a recession coefficient and S_t [cm] is shallow saturated zone soil moistures. S_t is updated every time step by

$$S_{t+1} = S_t + PC_t - G_t - D_t \tag{3-10}$$

where PC_t [cm] and D_t [cm] are percolation from the unsaturated zone (U_t [cm]) and deep seepage out of S_t, respectively. These two values are calculated by

$$PC_t = max\big((U_t + R_t - SF_t - E_t - Ur), 0\big) \tag{3-11}$$

$$D_t = Sep \times S_t \tag{3-12}$$

where Ur [cm] is available soil water capacity at the root zone and Sep is a deep seepage coefficient. The evapotranspiration (E_t [cm]) is calculated by

$$E_t = min\big((U_t + R_t - SF_t), Ks \times Kc \times PE_t\big) \tag{3-13}$$

where Ks and Kc are water stress and land cover coefficients, respective. PE_t [cm] is the potential evapotranspiration given by users or calculated by the Horton method (Horton, 1941). Ks is computed by

$$Ks = \begin{cases} 1, & U_t \geq Ur \times 0.5 \\ U_t/(Ur \times 0.5), & otherwise \end{cases} \quad (3\text{-}14)$$

According to Luo et al. (2012), the **baseflow** is calculated by

$$BF_t = BF_{t-1} \times e^{-\alpha} + Re_t \times (1 - e^{-\alpha}) \quad (3\text{-}15)$$

$$Re_t = D_t - Ds_t \quad (3\text{-}16)$$

$$Ds_t = \beta \times D_t \quad (3\text{-}17)$$

where α and β are two baseflow coefficients. Re_t [cm] is recharge amount and Ds_t [cm] is the deep seepage loss.

3.2.2.3 ABCD module

The ABCD model (Thomas, 1981; Martinez et al., 2010) is a simple hydrologic model comprised of two storage compartments, soil moisture zone (XU_t [cm]) and groundwater zone (XL_t [cm]). Four parameters, a, b, c, and d, are used to compute the daily outlet runoff (F_t [m^3/sec]) as shown in the following equations.

$$F_t = (QL_t + QU_t) \times \frac{A}{864} \quad (3\text{-}18)$$

Where QL_t [cm] and QU_t [cm] are groundwater discharge and runoff contributed by the soil moisture zone. QL_t is calculated by

$$QL_t = d \times XL_t \quad (3\text{-}19)$$

where XL_t is updated by

$$XL_t = (XL_{t-1} + c \times AW_t)/(1 + d) \quad (3\text{-}20)$$

QU_t is computed by

$$QU_t = (1 - c) \times WA_t \tag{3-21}$$

where WA_t is the water available for runoff available water calculated by the (AW_t [cm]) and evapotranspiration opportunity (EO_t) as shown below.

$$WA_t = AW_t - EO_t \tag{3-22}$$

AW_t and EO_t are calculated by Equations 3-23 and 3-24, respectively.

$$AW_t = R_t + XU_{t-1} \tag{3-23}$$

$$EO_t = \frac{AW_t+b}{2\times a} - \sqrt{\left(\frac{AW_t+b}{2\times a}\right)^2 - \frac{AW_t+b}{a}} \tag{3-24}$$

where XU_{t-1} [cm] will be updated by

$$XU_t = EO_t - Ea_t \tag{3-25}$$

where Ea_t [cm] is the actual evapotranspiration estimated by

$$Ea_t = \min\left(PE_t, max\left(0, EO_t \times \left(1 - e^{-PE_t/b}\right)\right)\right) \tag{3-26}$$

3.2.2.4 Lohmann routing module

The Lohmann routing module (Lohmann et al., 1998; Wi et al., 2015) consists of two parts, (1) within-subbasin routing and (2) inter-subbasin (i.e., river) routing. Each of them is represented by an impulse response function (IRF). Within-subbasin routing IRF is represented by a discrete Gamma distribution with shape (G_{Shape}) and scale (G_{Scale}) parameters. River routing IRF (or Green's function) is linearized from the Saint-Venant equation (Equation 3-27) parameterized by diffusion wave celerity ($Velo$ [m/s]) and diffusive coefficient ($Diff$ [m^2/s]) and solved with its convolution integral.

$$\frac{\partial Q}{\partial t} = Diff\ \frac{\partial^2 Q}{\partial x^2} - Velo\ \frac{\partial Q}{\partial x} \tag{3-27}$$

After computing IRFs, a unit hydrograph describing water traveling time between a subbasin outlet and a downstream routing outlet can be formed by convoluting within-

subbasin routing IRF and River routing IRF. Finally, the streamflow at the routing outlet is calculated by convoluting the unit hydrograph with its corresponding outlet's runoff.

3.2.3 Routing Scheme

The routing scheme assigns an order to each routing outlet. The routing modules are executed in orders from upstream to downstream basins to ensure that the effects of upstream agent properties propagate further downstream explicitly. Note that the topographical network of outlets is pre-defined in the model configuration file by users. The routing outlets are where the streamflow information is required for calibration or agents' decisions (e.g., reservoir release rules). The backtracking process automatically generates the routing scheme starting from the basin outlet (e.g., N1 in Figure 3-2). Moreover, the HydroCNHS supports multi-basin simulation (e.g., N1 and n1 in Figure 3-2) for transboundary analysis. The routing scheme in Figure 3-2 is expressed as [N4, N5, **R2**, R1, N3, **N2**, N1, n1]. This sequence will be adjusted accordingly if users add specific "node groups" in the model configuration file. For instance, if the release rule of reservoir R2 is influenced by the streamflow at N2, we need to acquire streamflow at the location before making a decision on the release from R2. This sequence can be refined by assigning a "node group" to N2 and R2 in the model configuration file. After that, the output routing scheme will be automatically updated in the HydroCNHS as [N4, R1, N5, **N2**, **R2**, N3, N1, n1].

3.2.4 Coupling APIs

APIs, herein, are the communication interface between HydroCNHS and user-defined ABM modules. The four APIs in the HydroCNHS (Figure 3-2) are (1) Dam API, (2) RiverDiv API, (3) Conveying API, and (4) InSitu API. **Dam API** is designed for

integrating in-stream agents like reservoirs (e.g., R1 and R2 in Figure 3-2) that could significantly alter the streamflow regime. Agents with Dam API will be considered as pseudo routing outlets (no routing is needed) involved in the routing scheme. Namely, streamflow is directly defined by agents' water releases decision. **RiverDiv API** is created for agents that divert water from rivers and may have return flows to other outlets, e.g., diversion agent D1 diverts water from N3 and return water to N1 in Figure 3-2. This API ensures the diverted outlet is routed before agents' diversions. At the outlet receiving return flow, the subbasin runoff and returned flow are combined and enter the within-subbasin routing process since return flows often have no explicit return locations. **Conveying API** is designed to transfer water to another outlet from a routing outlet where the routing process has already been executed. The transferred water has no within-subbasin routing (no within-subbasin delay like runoff). Therefore, they will be routed separately from the subbasin's runoffs. If an agent wants to convey water from the downstream outlet to the upstream outlet (e.g., pump stations), the water will be delivered with delays (e.g., C2 diverts water from N3 first and delivers it to S2 at a later time step). **InSitu API** is developed for agents that directly affect runoffs via "within subbasin activities" (e.g., I1 in Figure 3-2). For example, those runoff changes may come from land-use changes due to urbanization or exploiting groundwater through wells. Such adjustments will be made before any routing process at each time step.

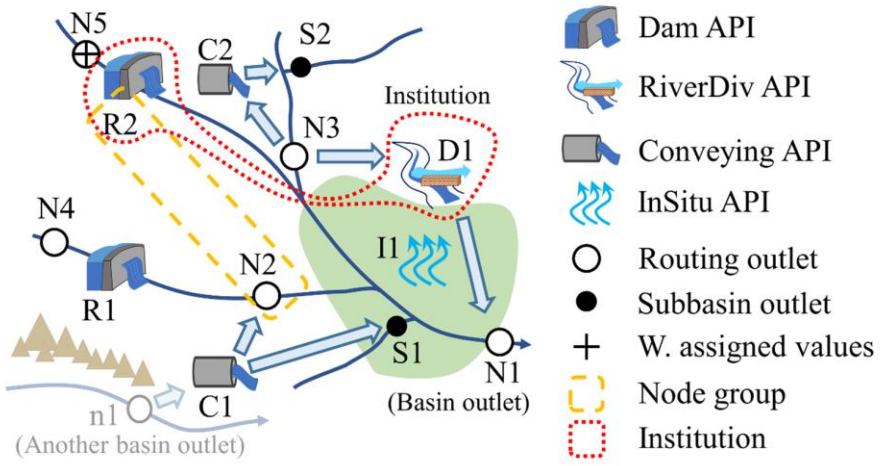

Figure 3-2. A generic example of HydroCNHS coupling APIs and water system description. Note that agents R1, R2, D1, C1, C2, and I1, are programmed in ABM modules (*.py*) and integrated into HydroCNHS through APIs.

We mathematically formalize the coupled model simulation with these four APIs at each time step. Equation 3-28 shows all runoff components within a subbasin before routing.

$$F_s' = F_s + \sum_{g \in Agt_I(s)} Eu_g^+ + \sum_{g \in Agt_I(s)} Eu_g^- + \sum_{g \in Agt_R(s)} Re_g^+, \quad \text{for all } s \in \{\text{subbasins}\} \tag{3-28}$$

where F_s and F_s' are the initial and updated runoff in subbasin s, respectively. Eu represents runoff changes with symbols of plus (gain) and minus (loss) for InSitu agents $Agt_I(s)$ activated at outlet s. $Agt_R(s)$ are RiverDiv agents activated at outlet s, and Re is the return flow.

The node-to-node routing is simulated using Equations 3-29 and 3-30. Equation 3-29 represents the streamflow replacement by in-stream agents like reservoirs.

$$Q_g = f_{release}(g), \quad \text{for all } g \in \{\text{agents using Dam API}\} \tag{3-29}$$

where Q_g is the streamflow expressed as a function $f_{release}(\cdot)$, taking the Dam agent g as inputs. Equation 3-30 computes all other routing processes and streamflow changes resulting from conveying flow and diversions.

$$Q_r = \sum_{\substack{s\in F_u,\\ u\in U(r)}} f_{rout}(F_s') + f_{rout}^{I}(F_r') + \sum_{a\in A(r)} f_{rout}^{R}(F_a') + \sum_{g\in Agt_C(r)} f_{rout}^{R}\left(C_g^{+}\right)$$

$$+ \sum_{g\in Agt_C(r)} C_g^{-} + \sum_{g\in Agt_R(r)} D_g^{-}, \text{ for all } r \in \{\text{routing outlets}\}\backslash\{\text{agents using Dam API}\} \quad (3\text{-}30)$$

where Q_r is the routed streamflow at routing outlet r. $f_{rout}(\cdot)$ represents the Lohmann routing function. $f_{rout}^{I}(\cdot)$ and $f_{rout}^{R}(\cdot)$ are the routing functions considering only within-subbasin routing and inter-subbasin (i.e., river) routing, respectively. $U(r)$ are the upstream outlets contributing to the streamflow at r. $A(r)$ are the routing outlets with assigned streamflow time series for which within-subbasin routing is not required. $Agt_C(r)$ and $Agt_R(r)$ are the Conveying agents and RiverDiv agents activated at routing outlet r, respectively. C is the conveying water, and D is the diversion. The plus and minus signs indicate flow changes due to adjustments. Each agent has a priority input for the simulation order in case conflicts occur (e.g., diversions at an outlet by multiple agents). Also, HydroCNHS supports the institution feature in which multiple agents share a decision-making instance/object allowing them to make decisions together. For example, R1 and D1 in Figure 3-2 coordinate on the release and diversion decisions.

3.3 Case Study – Tualatin River Basin

We select the TRB as a study area (Figure 3-3) to demonstrate the four APIs in the HydroCNHS. The TRB, located in northwest Oregon, United States, with a drainage area of 1844.07 km^2, is covered by densely populated areas (20%), agricultural area (30%), and forests (50%) (Tualatin River Watershed Council, 2021). Its agriculture heavily relies on

the irrigation scheme accounting for high seasonal rainfall variability because rainfall in the area concentrates during the winter season (November–February). The Spring Hill Pumping Plant is the largest diversion facility in the TRB for supporting the Tualatin Valley Irrigation District (TVID; **DivAgt**), where the Hagg reservoir (**ResAgt**) is the primary water source. During the summer period, water is transferred from the Barney reservoir (outside of the TRB) through a trans-basin aqueduct (**PipeAgt**) to augment the low flow for ecosystem conservation.

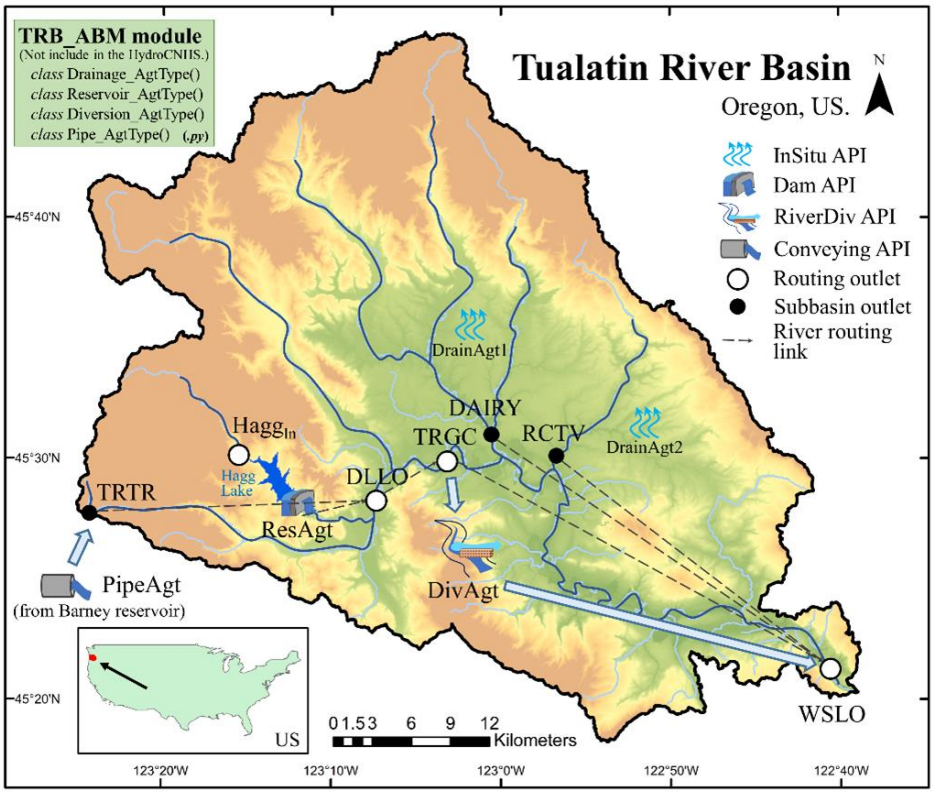

Figure 3-3. The Tualatin River Basin system. TRTR, $Hagg_{In}$, DLLO, TRGC, DAIRY, RCTV, and WSLO are seven subbasins. PipeAgt, ResAgt, and DivAgt are trans-basin aqueduct, Hagg reservoir, and TVID agents, respectively. DrainAgt1 and DrainAgt2 are two drainage system agents for the runoff-changing scenario.

We model seven TRB subbasins (in HydroCNHS) and three agents (in an externally programmed TRB_ABM module). The seven outlets of subbasins are denoted as TRTR, $Hagg_{In}$, DLLO, TRGC, DAIRY, RCTV, and WSLO (Figure 3-3). Three agents are PipeAgt, ResAgt, and DivAgt, integrated through Conveying, Dam, and RiverDiv APIs, respectively (Figure 3-3). PipeAgt (i.e., a water manager) assigns conveying water to TRTR with observed median monthly values (Bonn, 2020). ResAgt (i.e., a reservoir operator) determines reservoir releases with generic operational rules, where target storages and target releases are adopted for flood control (October–May) and storage control (June–September) periods. DivAgt (i.e., a group of farmers) diverts water from TRGC with monthly-diversion-request decisions at the beginning of each month and has return flow to WSLO. The diversion-request decisions from June to September are governed by linear functions, where the observed monthly precipitation is the predictor. Minor diversions in other months are filled with historical mean values. Details of this TRB_ABM module and agents' decision rules are provided in Appendix B.1.

We test the simulation from 1981 to 2013, where the climate data is obtained from Livneh et al. (2015). We aggregate the 1/16 degree climate grids for each subbasin and agent. The HydroCNHS GA module conducts the calibration (1981–2005) with Kling-Gupta efficiency (KGE; Gupta et al., 2009) as a target performance metric. We compare two models, M_{gwlf} and M_{abcd}, in which the same ABM model is coupled with two rainfall-runoff modules, GWLF and ABCD, respectively. We show the calibration parameters and their bounds in Table 3-1. Other detailed calibration settings, including calibration objective and data sources, are provided in Appendix B.2. In addition, we run a scenario with fixed diversion behavior of DivAgt using a monthly mean (i.e., a conventional method

to handle human decision exogenously) to compare with endogenous adaptive behavioral rules. Such differences in human behavior assumptions may lead to distinct modeling outcomes and impact the exploratory analysis of changing environments. To demonstrate the usage of InSitu API, we run runoff-changing scenarios with the calibrated M_{gwlf} model to test how the changes in upstream runoff affect the streamflow at the basin outlet. One possible cause of runoff changes is urbanization. Therefore, we model runoff changes by adding two agents, **DrainAgt1** at DAIRY and **DrainAgt2** at RCTV, and assume a linear growth of the urbanized area in DAIRY and RCTV subbasins from 5% to 50%, where such urbanization is assumed to increase unit runoff by 75% according to a local study (Gwenzi et al., 2014).

Table 3-1. Calibration parameter bounds for the hydrological model and the ABM model.

Model	Module	Parameter name	Unit	Parameter	Bound
Hydrological model	GWLF	Curve number	--	$CN2$	[25, 100]
		Interception coefficient	--	IS	[0, 0.5]
		Recession coefficient	--	Res	[10^{-3}, 0.5]
		Deep seepage coefficient	--	Sep	[0, 0.5]
		Baseflow coefficient	--	α	[0, 1]
		Percolation coefficient	--	β	[0, 1]
		Available/soil water capacity	cm	U_r	[1, 15]
		Degree-day coefficient for snowmelt	cm/° C	D_f	[0, 1]
		Land cover coefficient	--	K_c	[0.5, 1.5]
	ABCD	Controls the amount of runoff and recharge during unsaturated soil	--	a	[0, 1]
		Controls the saturation level of the soils	--	b	[0, 400]
		Ratio of groundwater recharge to runoff	--	c	[0, 1]
		Controls the groundwater discharge rate	--	d	[0, 1]
		Degree-day coefficient for snowmelt	cm/° C	D_f	[0, 1]
	Lohmann routing	Subbasin unit hydrograph shape parameter	--	G_{Shape}	[1, 100]
		Subbasin unit hydrograph rate parameter	--	G_{Scale}	[10^{-2}, 150]
		Wave velocity in the linearized Saint–Venant equation	m/s	$Velo$	[0.5, 100]
		Diffusivity in the linearized Saint–Venant equation	m^2/s	$Diff$	[200, 5000]
ABM		Return flow factor	--	Fa_{re}	[0, 0.5]
		The slope of a linear function	m^3/s/ cm	l_a	[0, 3]
		Interception of a linear function	m^3/s	l_b	[-2, 2]

3.4 Results

We compare KGEs between two calibrated models (M_{gwlf} and M_{abcd}) in Table 3-2 and Figure 3-4. The two values in parenthesis are KGEs for calibration (1981–2005) and validation (2006–2013) periods, respectively. Both models can capture streamflow dynamics and agent behaviors (i.e., reservoir releases and water diversions) on a monthly

scale. M_{gwlf} has better performance in general since the GWLF model uses a nine-parameter for each subbasin compared to the five-parameter ABCD model. One advantage of endogenous behavioral rules is that they can capture the dynamic interactions between natural and human systems and more realistically present the variances of two systems under the changing environment. For example, Figure 3-5a shows the difference in the annual outputs' variance between M_{gwlf} with the calibrated endogenous diversion behavioral rules ($M_{gwlf,endog}$) and M_{gwlf} with fixed diversion ($M_{gwlf,fixed}$). $M_{gwlf,endog}$ has a larger variance in DivAgt's diversion, reflecting DivAgt (farmers) can adjust its (their) water diversion according to the weather forecast. Such adaptive diversion behaviors counteract the streamflow downstream, leading to lower streamflow variance at WSLO (Figure 3-5a) compared to $M_{gwlf,fixed}$. $M_{gwlf,endog}$ may benefit exploratory analysis where the environment gradually changes and static behavioral rules (e.g., $M_{gwlf,fixed}$) are no longer appropriate. To demonstrate the last API (i.e., InSitu API), Figure 3-5b exhibits the gradual annual streamflow increment (gaps between two lines) at WSLO resulting from the runoff changes at DAIRY and RCTV subbasins.

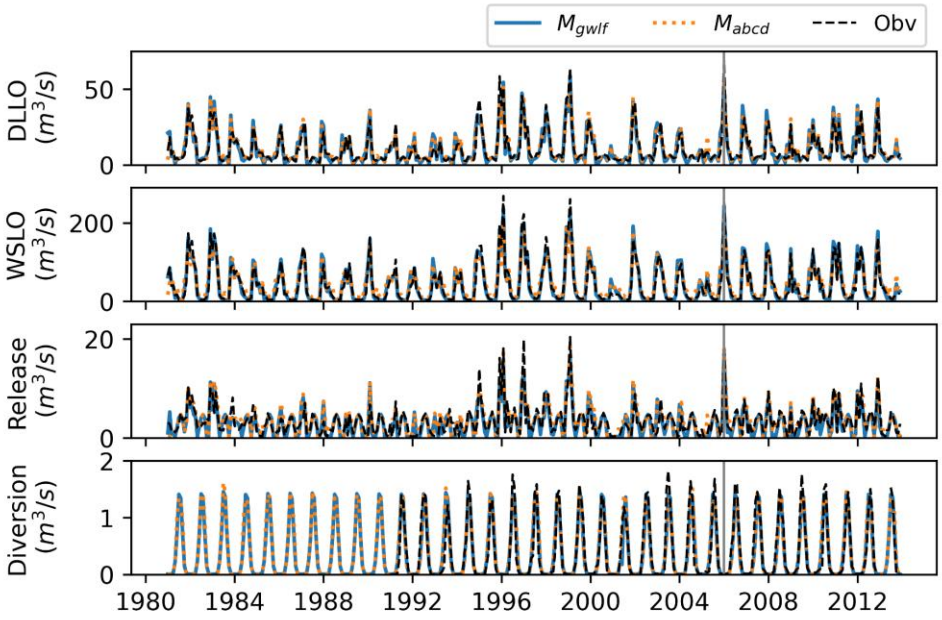

Figure 3-4. Four monthly time series plots for calibrated M_{gwlf} and M_{abcd}. DLLO and WSLO are the calibrated streamflow. Release and diversion are simulated by ResAgt and DivAgt, respectively. Grey vertical lines separate the calibration (1981-2005) and validation (2006-2013) periods. Black dotted lines are the observations.

Table 3-2. KGE comparison for the calibration and validation results of two models

Model	ResAgt	DLLO	DivAgt	WSLO
Monthly observed data	Reservoir releases	Streamflow	Diversion	Streamflow
M_{gwlf}	(0.783, 0.811)	(0.916, 0.865)	(0.917, 0.898)	(0.958, 0.894)
M_{abcd}	(0.776, 0.893)	(0.905, 0.889)	(0.905, 0.885)	(0.777, 0.836)

Note: calibration 1981–2005, validation 2006–2013, on a monthly scale.

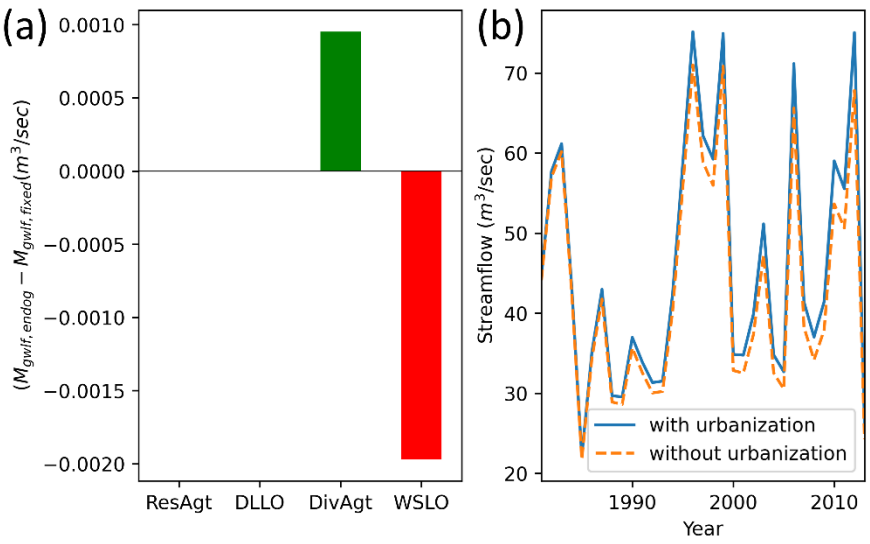

Figure 3-5. Two scenarios of the M_{gwlf} model. (a) Standard deviation difference between $M_{gwlf,endog}$ and $M_{gwlf,fixed}$ in annual mean values. (b) The annual WSLO streamflow for with (solid line)/without (dashed line) urbanization using calibrated.

3.5 Conclusions

This technical note presents a semi-distributed Hydrological model for Coupled Natural–Human Systems, HydroCNHS, an open-source Python package. We demonstrate the functionalities of the HydroCNHS through a case study in the Tualatin River Basin, Northwest United States, where we couple a trans-basin aqueduct, a reservoir, an irrigation diversion, and two drainage system agents accounting for runoff changes with four coupling APIs linked to two different rainfall-runoff models, GWLF and ABCD. The KGE comparison results indicate that coupled models could capture monthly streamflow, irrigation diversion, and reservoir release patterns. We also show that the model with endogenous diversion behavioral rule better reflects the interaction between natural and human systems and may benefit exploratory analysis. Also, the results of the runoff-changing scenario show the capability of HydroCNHS in modeling the effects of gradual environmental changes on streamflow. With the coding language integrity, flexibility in

designing agents, and parallel computing ability, the HydroCNHS can potentially benefit future studies in CNHS like uncertainty analysis or coupling with more diverse (e.g., hydropower plants and cooling plants) and complex (e.g., interactions among agents and hydrological environment) agent designs.

Chapter 4: The Effects of Model Complexity on Model Output Uncertainty in Co-Evolved Coupled Natural-Human Systems

Abstract

Studies have recently focused on using coupled natural-human systems (CNHS) to inform policymaking. However, model uncertainty can increase with model complexity and affect the variance of the model outcomes. Therefore, this chapter explores an uncertainty analysis of coupled hydrological and human decision models to better evaluate CNHS modeling properties. Five coupled models are proposed with different model complexities for human behavior settings (i.e., model structure and the number of calibrated parameters): one static, two adaptive, and two learning adaptive. Learning adaptive models (the most complex) have both a learning component (capturing long-term trends) and an adaptive component (capturing short-term variations), while adaptive models omit the learning component. The static model is the simplest, without learning or adaptive components. Applying the law of total variance, the model output uncertainty is decomposed into three sources: (a) climate change scenario uncertainty, (b) climate internal variability, and (c) different model configurations with parameter sets or model structures that are equally capable of producing similar outcomes. Our exploratory analysis demonstrated that model uncertainty would likely increase with model complexity given uncertain input data (e.g., climate forcing) and different model configurations; the inclusion of a learning mechanism in the human system can potentially offset the impact of the natural system on uncertainty through coupling natural and human systems. We also discuss other uncertainty sources,

such as assumptions about model structure due to incomplete knowledge and metrics for calibration target selection for future studies.

4.1 Introduction

In the anthropogenic era, most major basins experience human activity, requiring an understanding of interactions between human society and the natural environment, that is, co-evolution in coupled natural-human systems (CNHS; Bauch et al., 2016; Wada et al., 2017). With the recognition of the socio-physical nature of emerging water challenges, many methods and modeling techniques, including system dynamics modeling, agent-based modeling, Bayesian networks, and so on (Blair & Buytaert, 2016; Kelly et al., 2013), have been proposed to address complex water management issues, often in the style of the Harvard Water Program (Brown et al., 2015; Milly et al., 2008; Reuss, 2003). Among them, coupling an agent-based model (ABM) with a process-based model (e.g., hydrological model) is a promising method to investigate emerging phenomena and heterogeneous human behaviors in CNHS (Berglund, 2015; Giuliani et al., 2016; Yang et al., 2020). In this coupling framework, each agent (e.g., irrigation district or reservoir) serves as a decision-making unit with a set of rules and attributes governing its behavior (e.g., diversion request or release) and interacts with other agents in a shared physical environment (e.g., river basin). As a result, various ABMs have been developed with agents that have different complexities (e.g., model structure and number of calibrated parameters) to capture nonlinearity and non-stationarity in CNHS. For example, agent behaviors have been governed by a deterministic decentralized optimization model (Yang et al., 2009) or more sophisticated designs that consider adaptive (short-term) and learning (long-term)

behaviors with respect to other agent decisions and the changing environment (Giuliani et al., 2016; Hyun et al., 2019).

Many case studies (Elshafei et al., 2014; Kandasamy et al., 2014; Marston & Konar, 2017; Song & Zhang, 2015; Xu et al., 2014; Yang et al., 2020) have suggested that an additional human complexity layer in the model will improve environmental planning and policy (Zellner, 2008). Yang et al. (2020) showed that the potential tipping point of farmer behavioral changes could be identified by the bottom-up nature of the coupled model. Hung and Yang (2021) argued that the learning adaptive agent design of a coupled model could assist water managers in developing soft policies. As the complexity of a method and the number of parameters increase, the challenge of handling model uncertainty and variability increases (McLean & McAuley, 2012; Srikrishnan & Keller, 2021). This challenge is aggravated in CHNS modeling since there is often interest in both natural (e.g., streamflow) and human (e.g., water diversions) system outputs, and the co-evolved natural and human dynamics in the complex system heavily rely on structural assumptions of the model (e.g., how humans react to environmental changes; Karthe et al., 2021; Messina et al., 2008). These model parameters and structural uncertainties significantly affect confidence in the inference and interpretation of model results (Allen & Gunderson, 2011; Allison et al., 2018; Kelly et al., 2013; Sun et al., 2016).

In the modeling literature, uncertainty is often ascribed to input data, model resolution level, model structure, and parameters (Saltelli et al., 2019); in addition, problem framing, perceptions of uncertainty, inappropriate assumptions, and epistemic uncertainty are also deeply embedded in model uncertainty (Beven, 2016; Di Baldassarre et al., 2016; Moallemi et al., 2020; Westerberg et al., 2017). However, uncertainty studies of coupled

models in CNHS are still emerging (Elsawah et al., 2020). In this chapter, we focused on parameter and structural uncertainties, that is, different model configurations that can produce similar/acceptable model outcomes, in CNHS modeling. A more complex model may suffer more severe uncertainty issues from a potentially wide range of behavioral model configurations (Arendt et al., 2012; Srikrishnan & Keller, 2021). In the hydrology field, this is also known as equifinality (Beven, 1993), and many studies have demonstrated the impact of equifinality in their analysis (Arsenault & Brissette, 2014; Beven, 2006; Ekblad & Herman, 2021; Khatami et al., 2019; Williams et al., 2020).

Generalized likelihood uncertainty estimation (GLUE; Beven & Binley, 1992) and Differential Evolution Adaptive Metropolis (DREAM; Vrugt et al., 2009) are two popular Bayesian methods to address different model configurations' issues. GLUE weights model outputs based on data-fitting performance and then uses behavioral sampled models for ensemble forecasting. DREAM, on the other hand, is a more advanced formal Bayesian methods sampling model from the posterior. Instead of proposing new methods, this chapter compares model output uncertainties (both natural and human systems) under different model configurations (e.g., number of parameters and model structures). We quantify the model uncertainty brought by different model configurations using a variance-based uncertainty decomposition to evaluate uncertainty properties under different model structural assumptions in CNHS. We introduce the term "equifinal model representatives" (EMRs) to describe the selected model configurations that represent the range of model variability over the equifinal space (i.e., space of model configurations that produce similar model outcomes), and we refer to model output uncertainty as simply "model uncertainty" throughout the rest of the chapter for simplicity.

This chapter aims to capture natural and human system model uncertainty given the available data with two hypotheses. First, model uncertainty in an exploratory analysis would likely increase with model complexity, given uncertain input data (e.g., climate forcing) and different model configurations. Second, the inclusion of a learning mechanism in the human system model can potentially offset the impact of the natural system's variability on model uncertainty. The Yakima River Basin (YRB) in the Northwest United States, an agriculture-dominated basin that heavily relies on irrigation, was selected as the study area to test these hypotheses. We presented four tasks: (a) quantify model uncertainty of CNHS in exploratory simulations, (b) decompose model uncertainty into different model configurations, and input data uncertainty (e.g., climate scenario uncertainty and internal climate variability) using the law of total variance, (c) compare model uncertainty and model complexity, and (d) observe the uncertainty offsetting relationship between natural and human systems in CNHS modeling.

The chapter is structured as follows. Section 4.2 introduces the YRB study area and the climate change scenario design. The identification of EMRs, the uncertainty decomposition method, and the modeling schema are presented in Section 4.3 . Section 4.4 compares the decomposition from coupled models with different model complexities. Discussion of additional uncertainty sources in CNHS modeling and limitations of the models is presented in Section 4.5 , followed by the conclusions in Section 4.6 .

4.2 Study area and materials

4.2.1 Yakima River Basin

The YRB is selected as the study area and is shown in Figure 4-1. The YRB is a basin dominated by agriculture. Orchards (127,934 acres, 29.6%), small grains (67,434 acres,

15.6%), and corn (63,163 acres, 14.6%) (USDA, 2017 agriculture census) are the primary crops in the area. The precipitation in the YRB is concentrated in the mountains during the winter season (November–February). Agriculture heavily relies on irrigation; however, irrigation demands vary with the uncertain climate and the vicissitude of crop types across the growing season (late March to early October). Irrigation is facilitated by five major reservoirs (Keechelus, Kachess, Cle Elum, Bumping, and Rimrock), which are jointly operated by the U.S. Bureau of Reclamation (USBR). The irrigation operation (i.e., storage control) usually starts in July and continues through September to fulfill downstream demands (USBR, 2002). During this major storage control period, the streamflow at Parker gauge is tightly maintained by USBR to meet flow targets that range from 8.5–16.99 m^3/s (300 to 600 ft^3/s), based on available water (USBR, 2002). The streamflow in this period is a policy concern for USBR. Therefore, we adopt the median value of mean monthly streamflow from July to September at the Parker gauge over a given period (Q_M; Equation 4-1) as the natural system indicator for the model uncertainty analysis:

$$Q_M = median\left(\left\{\frac{1}{3}\sum_{m=7}^{9} Q_{y,m}\,; y = 1, \dots, p\right\}\right) \quad (4\text{-}1)$$

where $Q_{y,m}$ is the monthly streamflow of month m in year y and p is the number of years. Note that the flow target standard is not static. The flow target standard of the Parker gauge is affected by district conservation programs. Based on historical data, we set the flow targets equal to 9.4 m^3/s (1960–1984) and 14.4 m^3/s (1985–2013) for the model calibration, where we use the flow deviation from the target as a driving force for the learning process of the water diversion model (Section 4.3.2).

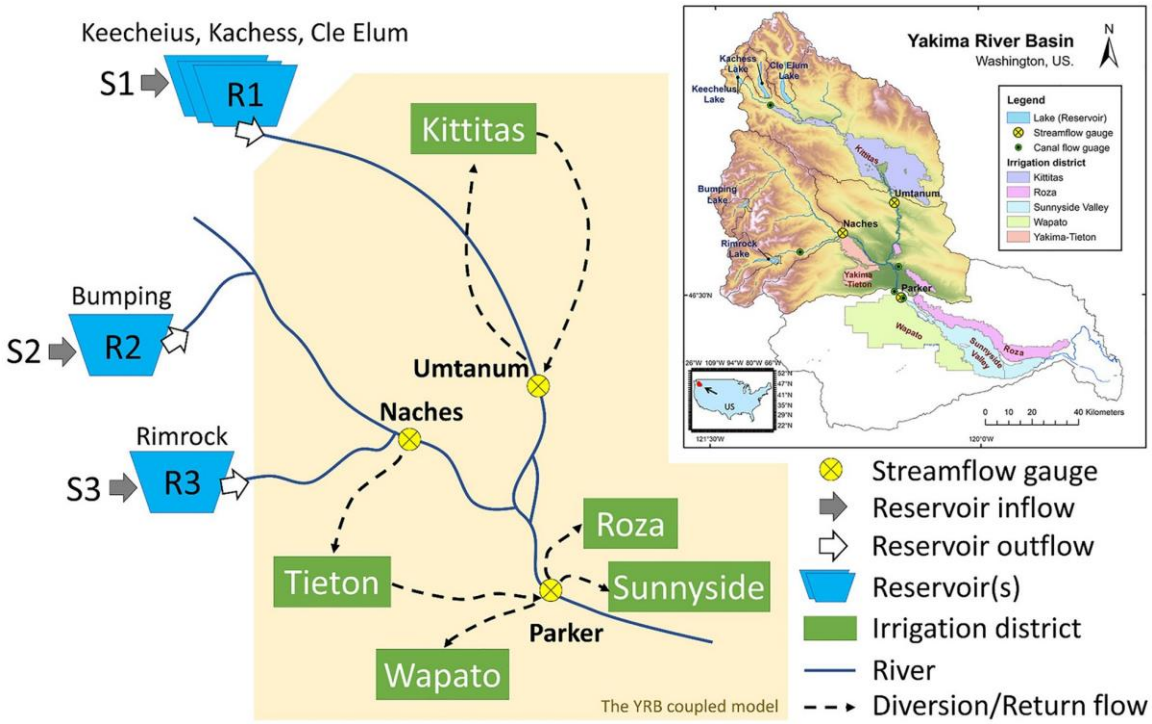

Figure 4-1. System diagram of Yakima River Basin (YRB). S1, S2, and S3 and R1, R2, and R3 are reservoir inflow and release models, respectively. YRB coupled natural-human model (yellow-colored area), which consists of three subbasins (yellow circles are their outlets) and five irrigation diversion districts (green boxes), is the focus of uncertainty analysis.

In addition, we define the median value of the annual diversion of five districts over a given period (D_M; Equation 4-2) as the human system indicator that abstracts farmers' behaviors (e.g., crop selection and irrigation measures) for the model uncertainty analysis:

$$D_M = median\left(\left\{\sum_{ag \in districts} D_{y,ag}\,; y = 1, \dots, p\right\}\right) \quad (4\text{-}2)$$

where $D_{y,ag}$ is the annual diversion of agent ag in year y. We also define the median value of shortage frequency (S_M; Equation 4-3) as an auxiliary indicator that represents the potential crop losses that farmers tend to avoid:

$$S_M = median\left(\left\{\sum_{r=1}^{20} S_{y,r}\,; y = 1, \dots, p\right\}\right) \quad (4\text{-}3)$$

where $S_{y,r}$ is a shortage index experienced in internal climate variability realization r. $S_{y,r}$ is equal to 1 if the total diversion request of five agents is not fulfilled in that year; otherwise, $S_{y,r}$ is equal to 0. Higher S_M implies a lower variation in Q_M, since the streamflow is likely to approximate minimum flow requirements.

The YRB coupled natural-human model (Figure 4-1) includes hydrological and water diversion models. The hydrological model contains three subbasins, Umtanum (328,818.70 ha), Naches (203,799.79 ha), and Parker (291,203.80 ha), and the diversion model includes five irrigation districts: Kittitas, Yakima-Tieton (Tieton), Roza, Wapato, and Sunnyside Valley (Sunnyside). Their diversion points are all above the Parker gauge. The details of these five districts, such as water rights, average annual diversions, and district areas, are summarized in Table C1 in Appendix C.3. We define five major irrigation districts in the basin as agents that make annual diversion requests. The inclusion of these five irrigation districts in the water diversion model abstracts possible causes of changes in diversions (land use, conservation programs, climate, and farmers' subjective decisions) into the empirical equations presented in Section 4.3.2 .

Reservoirs are another human component in the YRB. The reservoir model uses the simulated inflows of S1, S2, and S3 (whose drainage areas are equal to 83,014.25, 11,601.47, and 28,016.20 ha, respectively); storage status; and pre-defined fixed operational rules to simulate the reservoir releases. These releases are then used as input data for the YRB coupled model for simplicity. Namely, the reservoir releases constrain the downstream water users' choices. For readers interested in finding optimal reservoir operating rules or interactions between reservoirs and diversion agents, we refer them to Giuliani et al. (2016) and Madani and Hooshyar (2014), respectively.

In sum, the Q_M and D_M uncertainties under an exploratory analysis accumulate the input data uncertainty (e.g., reservoir releases and climate) and the errors of simplification (i.e., the conceptualization of physical mechanisms) in both the natural process (e.g., hydrological model) and human behaviors (e.g., water diversion model).

4.2.2 Data and climate change scenarios

We use data from 1960 to 2013 as the diagnostic period to develop the model. The data are separated into calibration (1960–1999) and validation (2000–2013) periods. The weather data (i.e., precipitation and temperature) are collected from Livneh et al. (2015), and the reservoir storage and release, streamflow, and diversion data are downloaded from the USBR website. The precipitation data are bias-corrected through a simple annual water balance method to solve the temporal inconsistency issue mentioned in the limitation section in Livneh et al. (2015).

The weather inputs for the exploratory analysis (2021–2100) are generated by adjusting annually bootstrapped historical time series to different climate change scenarios (Figure 4-2). The climate change scenarios are defined as combinations of linearly interpolated precipitation ratios (PF_{ratio}; average annual precipitation in future periods to the baseline; lines in Figure 4-2a) and temperature deltas (TF_{delta}; average annual temperature in future periods minus the baseline; lines in Figure 4-2b) that are selected from five quantile values (q0.1, q0.3, q0.5, q0.7, and q0.9) over the range of 20 general circulation models (GCMs; Taylor et al., 2012; boxplots in Figure 4-2; Table C2 in Appendix C.3) in the 2030s, 2050s, 2070s, and 2090s. Such a climate change scenario setting is similar to the climate stress test in Decision Scaling (Brown et al., 2012); however, the climate changes we tested are limited within the range of GCMs.

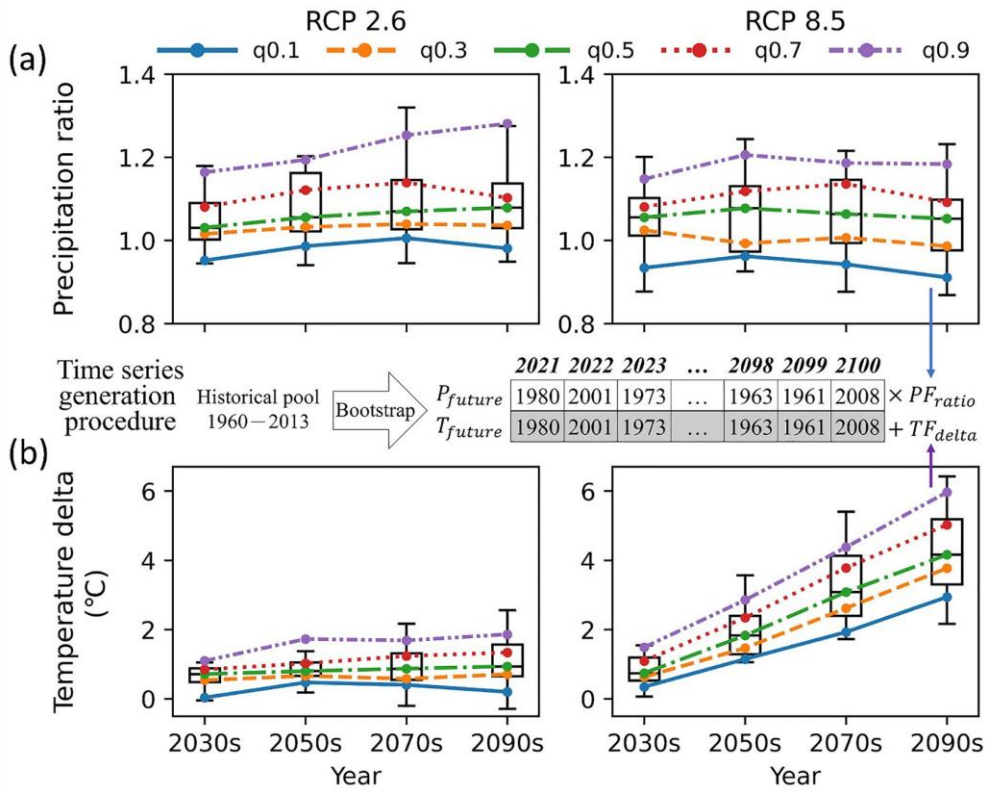

Figure 4-2. (a) Precipitation ratios and (b) temperature deltas sampled from five quantile values over the range of 20 GCMs (boxplots) under RCP 2.6 (left column) and RCP 8.5 (right column), respectively, in the 2030s, 2050s, 2070s, and 2090s. Future weather time series were generated by adjusting annually bootstrapped time series with climate change scenarios, combinations of linearly interpolated ratios, and deltas.

This chapter adopts two representative concentration pathways (RCPs), RCP 2.6 and RCP 8.5, which represent mild and severe future climate projections, respectively. By selecting two distinct climate change scenarios, we could potentially maximize the ability to separate climate change signals from noises. As a result, we generate 25 climate change combinations (5 PF_{ratio}× 5 TF_{delta}) per RCP. For exploratory simulations, the climate change scenarios are statistically downscaled by the delta method (Walsh et al., 2018), to which we apply PF_{ratio} and TF_{delta} to 20 annually bootstrapped time series sampled from 1960 to 2013 in historical annual slices (daily precipitation and temperature time series of

the entire year). This enables us to incorporate internal climate variability and output future weather time series (P_{future} and T_{future}; Equation 4-4):

$$\begin{cases} P_{future,y} = P_{bootstrap,y} \times PF_{ratio,y} \\ T_{future,y} = T_{bootstrap,y} + TF_{delta,y} \end{cases}, y \in [2021,2100], y \in \mathbb{Z} \quad (4\text{-}4)$$

where P and T are annually bootstrapped daily precipitation and temperature time series, respectively. Subscript y denotes the year. In sum, we generate 1,000 realizations (25 climate change combinations × 2 RCPs × 20 bootstrapped time series) for the exploratory analysis. Note that we only consider a subset of climate input data uncertainty in this chapter; other uncertainties, like single GCM outputs and different downscaling methods, are not included.

4.3 Methods

4.3.1 Hydrological model

The semi-distributed hydrological model developed for the YRB is made of the modified hydrological module of the Generalized Watershed Loading Functions (GWLF; Haith & Shoemaker, 1987; Tung & Haith, 1995) and the Lohmann routing model (Lohmann et al., 1998; Wi et al., 2015). The hydrological module of the GWLF is a lumped rainfall-runoff model, which simulates daily streamflow by summing the surface quick flow, which is computed by the NRCS curve number method and subsurface flow (Haith et al., 1996). The modified version further includes a baseflow component (Luo et al., 2012) to depict low flow patterns. The Lohmann routing model is a simple linear transfer function model that considers routing both within the subbasin (concentration time of subbasin runoff to reach the outlet) and in rivers (from one upstream subbasin outlet to a lower subbasin outlet). The Lohmann routing model can be derived independently from the GWLF, and

connecting its results with GWLF-simulated streamflow forms the semi-distributed hydrological model for the YRB.

Table 4-1. Calibration Parameter Bounds for Hydrological and ABM Models.

Model	Sub-model	Parameter name	Unit	Code	Bound
Hydrological model	GWLF	Curve number	--	$CN2$	[25, 100]
		Interception coefficient	--	IS	[0, 0.5]
		Recession coefficient	--	Res	[10^{-3}, 0.5]
		Deep seepage coefficient	--	Sep	[0, 0.5]
		Baseflow coefficient	--	α	[0, 1]
		Percolation coefficient	--	β	[0, 1]
		Available/soil water capacity	cm	U_r	[1, 15]
		Degree-day coefficient for snowmelt	cm/°C	D_f	[0, 1]
		Land cover coefficient	--	K_c	[0.5, 1.5]
	Lohmann routing	Subbasin unit hydrograph shape parameter	--	G_S	[1, 100]
		Subbasin unit hydrograph rate parameter	--	G_R	[10^{-4}, 100]
		Wave velocity in the linearized Saint–Venant equation	m/s	Ve	[0.5, 100]
		Diffusivity in the linearized Saint–Venant equation	m^2/s	Di	[200, 5000]
ABM model		Return flow factor	--	R_f	[0, 0.5]
		Upper flow deviation threshold	m^3/s	L_U	[25, 50]
		Lower flow deviation threshold	m^3/s	L_L	[0, 15]
		Learning rate	--	γ	[0, 1]
		Standard deviation modifier	m^3/s	Sig	[0, 2][a]
		Prorated ratio	--	R	[0.4, 1]
		Slope of linear model	$m^3/s/cm$	a_L	[0, 0.5]
		Intercept of linear model	m^3/s	b_L	[-2, 2][a]
		Quadratic coefficient of quadratic model	$m^3/s/cm^2$	a_Q	[-27, 11.5][a]
		Slope of quadratic model	$m^3/s/cm$	b_Q	[-12, 42][a]
		Intercept of quadratic model	m^3/s	c_Q	[-24, 10][a]

[a] Union bound over five diversion agents. Each has customized bound estimated according to historical diversion data.

The hydrological model in the YRB coupled model (Figure 4-1) contains 47 parameters that must be calibrated (27 GWLF + 20 Lohmann), where each subbasin has a unique parameterization. The S1, S2, and S3 subbasin models used to simulate reservoir inflows each have 11 parameters involved in the calibration process (9 GWLF + 2 Lohmann, GS and GR). In sum, the four hydrological models (S1, S2, and S3 subbasin models and the YRB coupled model) are independently calibrated. The calibrated parameters, abbreviations, and bounds are summarized in Table 4-1.

The calibration is performed by a genetic algorithm (GA) with an objective function that differs for each calibration (Table C3 in Appendix C.3). For each subbasin model, the objective is to maximize the Kling-Gupta efficiency (KGE; Gupta et al., 2009; Equation 4-5), which comprehensively takes correlation, variability bias, and mean bias into account. For the integrated model, the objective is to maximize a penalized KGE in which $1 - \overline{D}$, the mean annual diversion shortage, is added to the KGE as a penalty factor (Table C3 in Appendix C.3):

$$\mathrm{KGE} = 1 - \sqrt{(r-1)^2 + \left(\frac{\sigma_{sim}}{\sigma_{obs}} - 1\right)^2 + \left(\frac{\mu_{sim}}{\mu_{obs}} - 1\right)^2} \tag{4-5}$$

where r is the Pearson correlation coefficient, and μ and σ denote the mean and standard deviation of flows, respectively. The subscripts obs and sim refer to observed and simulated streamflow time series, respectively. In the GA setup, we use roulette wheel selection, uniform crossover (crossover probability = 0.5), and uniform mutation (mutation probability = 0.1), which are coded under the Distributed Evolutionary Algorithms in Python (DEAP; Fortin et al., 2012) framework. Theoretically, the global optimum can be found with the mutation mechanism involved if the GA runs long enough, but it is still likely to be trapped in the local optima given limited computational resources, especially

with highly nonlinear problems. Hence, we do not aim to find the global optima. Instead, we consider multiple local optima with similar performance (i.e., above a certain threshold) as a form of model configuration uncertainty. The detailed GA calibration settings are provided in Table C3.

4.3.2 Human Model

4.3.2.1 Water Diversion Model

For the water diversion model in the YRB coupled model, we define each of the five irrigation districts as agents. These five agents made their annual irrigation requests on March 1st every year. In our design, the annual pattern of the historical diversion is described by three deterministic components and one stochastic component. The three deterministic components are learning, adaptive, and emergency response components.

The **learning component** enables agents to adjust their diversion request references ($Div_{req,ref}$) to achieve a goal (i.e., flow target at the Parker gauge) in the long run by learning from the flow deviation of the flow target through a set of empirical Equations 4-6 to 4-9:

$$Div_{req,ref,y} = Div_{req,ref,y-1} + V_{avg,y} \times \gamma \tag{4-6}$$

$$V_{avg,y} = \frac{1}{10}\sum_{i=1}^{10} V_{y-i} \tag{4-7}$$

where γ is the learning rate, subscript y denotes the year, and V_{avg} is the average strength value, with a ten-year rolling window indicating the magnitude and learning direction (e.g., increase $Div_{req,ref,y}$ if $V_{avg,y}$ is positive, or decrease $Div_{req,ref,y}$ if $V_{avg,y}$ is negative). This ten-year rolling window also creates learning momentum in the learning direction of $Div_{req,ref}$, where V_{avg} needs several (consecutive) counter events (e.g., $V = 1$ when

$V_{avg} < 0$ or $V = -1$ when $V_{avg} > 0$) to reverse its sign (i.e., the learning direction of $Div_{req,ref}$). The events are denoted as V and calculated by Equation 4-8:

$$V_y = \begin{cases} 1 \; if \; |De_y| > L_u \;\; if \; De_y > 0 \\ -1 \; if \; |De_y| < L_l \;\; if \; De_y < 0 \\ 0 \; otherwise \end{cases} \tag{4-8}$$

$$De = Q_{789} - Q_{target} \tag{4-9}$$

where L_u and L_l are the upper and lower flow deviation thresholds, respectively. These two parameters control how sensitive an agent is to wet or dry hydrological conditions. De is the deviation of the average flow from July to September (Q_{789}) relative to the flow target (Q_{target}), as shown in Equation 4-9. We provide an example of this learning process in Figure C1. To maintain a rational value for $Div_{req,ref}$, we subjectively bound $Div_{req,ref}$ in a range of 1.2× the historical maximum and 0.8× the historical minimum from 1960 to 2013 because it is unlikely that diversion will be less than 80% of the historical minimum, given continuous economic growth and associated water use. Also, it is unlikely that the diversion can be greater than 120% of the historical maximum for the years of the simulation, even with technology improvement (e.g., irrigation efficiency), given the physical constraints of available water and canal capacities.

The **adaptive component** is designed to capture short-term variation in diversion requests, which are believed to be induced by different weather conditions. We consider two alternative functional forms governing agent adaptive diversion behavior: linear (Equation 4-10) or quadratic (Equation 4-11) functions.

$$Div_{req,mu,y} = Div_{req,ref,y} + a_L \times P_{11-6,y} + b_L \tag{4-10}$$

$$Div_{req,mu,y} = Div_{req,ref,y} + a_Q \times P_{11-6,y}^2 + b_Q \times P_{11-6,y} + c_Q \tag{4-11}$$

where a_L and b_L are parameters for a linear function, and subscript y denotes the year. a_Q, b_Q, and c_Q are parameters for a quadratic function. The linear function assumes farmers will strictly divert more water in wet years. The quadratic function can capture the more complex phenomenon. For example, farmers start to divert less water when precipitation reaches a certain level because irrigation is not needed to maintain soil moisture (Figure C2). $Div_{req,mu}$ is the mean of the annual diversion request. P_{11-6} is the total precipitation from November to June in the reservoir catchments. P_{11-6} abstracts the water storage conditions above the reservoirs (e.g., snowpack and reservoir storage; November to February) prior to a decision and a perfect precipitation forecast in the first half of the growing season (March to June). Precipitation in the latter half of the growing season (July to October) may not affect diversion requests because this decision is often made before the growing season; thus, it is not as informative in deciding $Div_{req,mu}$.

P_{11-6} is also used as an indicator to trigger the emergency response component. If $P_{11-6,y}$ is lower than a given threshold (i.e., drought year), then the **emergency response component** will take the place of the adaptive component and prorate $Div_{req,ref,y}$ according to a calibrated constant ratio (R) in Equation 4-12:

$$Div_{req,mu,y} = Div_{req,ref,y} \times R \tag{4-12}$$

Next, the **stochastic component** of agent behavior is computed by:

$$Div_{req,y} = Div_{req,mu,y} + Rn \times Sig \tag{4-13}$$

where Div_{req} is the annual diversion request, and subscript y denotes the year. We use a matrix to represent the covariance coefficient among historical agent diversion decisions to mimic the "social norm" effect (i.e., farmer diversion decisions will correlate to some degree with neighbor decisions; Bicchieri and Muldoon, 2014), and Rn is a random vector

sampled from a multivariate normal distribution with this covariance matrix (i.e., social norm effect matrix). Sig is the calibrated standard deviation modifier, representing the modification of the randomness level. Finally, Div_{req} is disaggregated into a daily scale based on historical monthly reduction proportions to continue the simulation. Note that the return flow (Q_r) is computed from the actual diversion (Div) shown below:

$$Q_{r,d} = f_{rout}(R_f \times Div_d) \tag{4-14}$$

where $f_{rout}(\cdot)$ represents the routing process within the subbasin of the returned outlet, R_f is the return flow factor, and the subscript d is the day.

We simulate five different diversion agent types in the YRB coupled models. The five coupled models are, from simple to complex, (1) static model, M_s, (2) adaptive model with linear functions, $M_{A,L}$, (3) adaptive model with quadratic functions, $M_{A,Q}$, (4) learning adaptive model with linear functions, $M_{L,L}$, and (5) learning adaptive model with quadratic functions, $M_{L,Q}$. The complexities of the coupled models depend on how we simulate agent diversion behaviors. Agents in $M_{L,L}$ and $M_{L,Q}$ have all components, enabling them to learn to capture long-term trends and adapt to short-term shocks, with the difference in the selected adaptive function mentioned above. The learning component is omitted in the adaptive models (i.e., $M_{A,L}$ and $M_{A,Q}$), which enables agents to capture short-term variations without learning (constant $Div_{req,ref}$). M_s is a deterministic model that only has the emergency response component, which is designed to mimic a traditional method that considers the diversion demand as a constant/deterministic input. The actual diversion variation from an agent only comes from physical constraints (e.g., minimum flow requirements) and prorated water rights during a drought year, represented by the

emergency response component. Table 4-2 summarizes the diversion agent setup for these five YRB coupled models.

Table 4-2. Summary of diversion agent type setup of five YRB coupled models.

Component	Coupled model				
	M_S	$M_{A,L}$	$M_{A,Q}$	$M_{L,L}$	$M_{L,Q}$
Emergency response component	✓	✓	✓	✓	✓
Adaptive component	--	✓	✓	✓	✓
Learning component	--	--	--	✓	✓
Stochastic component	--	✓	✓	✓	✓
Number of parameters per agent	2	4	5	7	8
Calibrated parameters	b_L, R, R_f	a_L, b_L, R, Sig, R_f	a_Q, b_Q, c_Q, R, Sig, R_f	γ, L_u, L_l, a_L, b_L, R, Sig, R_f	γ, L_u, L_l, a_Q, b_Q, c_Q, R, Sig, R_f

Similar to the hydrological model calibration, we maximize a penalized KGE, where the penalty here is $10 \times (1 - \overline{D})$ (Table C3). Note that we use the mean of ten model simulations in an evaluation of the GA algorithm to address the model stochasticity issue. The detailed calibration settings and calibration parameter bounds are provided in Table C3 and Table 4-1, respectively. The ODD+D description (Müller et al., 2013) for the ABM is shown in Table C4.

4.3.2.2 Reservoir model

Reservoirs are another human component in the YRB that we consider as input data. To build the reservoir release simulation model for exploratory analysis, we empirically set up monthly operational rules based on the monthly simulated inflows forecast (S1, S2, and S3), storage status, and control periods (flood or storage). Then, the simulated monthly releases are uniformly disaggregated into daily values. This has no effect on our results, which are presented on an annual scale. We group the adjacent Keechelus, Kachess, and

Cle Elum reservoirs into one representative for simplicity, as shown in Figure 4-1. Consequently, we have three reservoir models (R1, R2, and R3). The pseudo-code of reservoir models is provided in Figure C3 in Appendix C.3.

4.3.3 Model uncertainty decomposition

Model uncertainty is attributed to various uncertainty sources. We adopt a variance-based uncertainty decomposition to isolate model uncertainty caused by different model configurations and input data. Figure 4-3 shows this concept. Using GA, or any other calibration methods (e.g., dynamically dimensioned search algorithm; Tolson & Shoemaker, 2007), to calibrate nonlinear models often result in multiple model configurations with similar outcomes (because most methods cannot guarantee the global optimum in a nonlinear solution space). We call such models as "equifinal models" (i.e., different model configurations) in this chapter. An infinite number of equifinal models (gray area) could be found within a continuous (e.g., real number) or unbounded equifinal space. For example, infinite parameter combinations are within the given calibration bounds (Table 4-1). It is impossible to evaluate or identify this infinite number of equifinal models. Therefore, we define an EMRs identification step (orange box in Figure 4-3) to identify a finite number of EMRs (blue lines in Figure 4-3) to represent the range of model variability over the equifinal space for the uncertainty evaluation. This chapter separately analyzes the uncertainty of five coupled model structures with different diversion agent types.

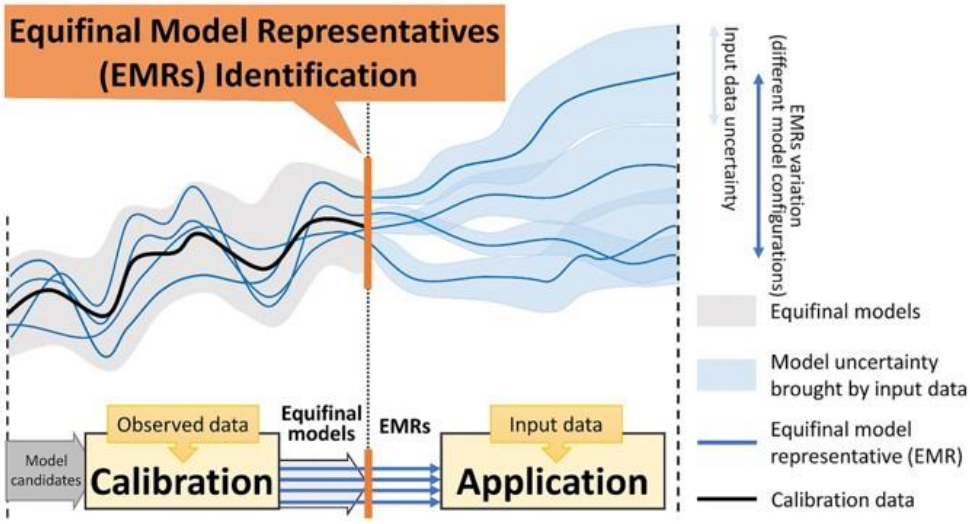

Figure 4-3. Conceptual diagram of EMRs and model uncertainty decomposition. Blue lines indicate model uncertainty caused by different model configurations. Light blue zones represent model uncertainty introduced by uncertain input data (e.g., climate uncertainty).

In application, model uncertainty is composed of the different model configurations from EMRs (e.g., variation of blue lines in Figure 4-3) and the input data (e.g., blue zone in Figure 4-3). To decompose the model uncertainty, we apply the law of total variance. In the first step, we isolate the uncertainty of the different model configurations (e.g., different parameter sets producing similar outcomes) by:

$$\mathrm{Var}(I) = \mathrm{E}[\mathrm{Var}(I|EMR)] + \mathrm{Var}(\mathrm{E}[I|EMR]) \tag{4-15}$$

The total model uncertainty, $\mathrm{Var}(I)$, of an output indicator (I; e.g., Q_M and D_M) is decomposed into two parts: uncertainty caused by the input data, $\mathrm{E}[\mathrm{Var}(I|EMR)]$ and uncertainty caused by the variation of EMRs, $\mathrm{Var}(\mathrm{E}[I|EMR])$. In an exploratory application, input data uncertainty is often related to climate uncertainty. In this chapter, the climate uncertainty is further decomposed into climate change scenario uncertainty (e.g., different combinations of PF_{ratio} and TF_{delta}) and internal climate variability (e.g.,

different realizations under a given climate scenario). We can apply the law of total variance again to E[Var($I|EMR$)] to have

$$E[Var(I|EMR)] = \mathrm{E}[\mathrm{Var}(I|EMR, ICR\ )] + \mathrm{E}[\mathrm{Var}(\mathrm{E}[I|EMR, ICR\ ])|EMR)] \quad (4\text{-}16)$$

where E[Var($I|EMR, ICR$)] is the model uncertainty resulting from uncertain climate change scenarios. E[Var(E[$I|EMR, ICR$])|EMR)] represents the model uncertainty caused by internal climate variabilities, where ICR is a realization under a given climate change scenario. The derivations of Equation 4-15 and Equation 4-16 are provided in Appendix C.1 and C.2, respectively.

To explain the impact of different model structures on the uncertainty in the co-evolving CNHS, we adopt the following variance formula:

$$Var(Q_{down}) = Var\big(Q_{up} - Div\big) = Var\big(Q_{up}\big) + Var(Div) - 2 \times Cov\big(Q_{up}, Div\big) \quad (4\text{-}17)$$

Equation 4-17 indicates that if the upstream flow (Q_{up}; streamflow before diversion) and diversion (Div) are positively correlated, then the variance of downstream flow (Q_{down}; streamflow after diversion) will be lower than the sum of $Var\big(Q_{up}\big)$ and $Var(Div)$. That is, even if uncertainty in both the human and natural systems increases, i.e., $Var\big(Q_{up}\big)$ and $Var(Div)$ both increase, it is possible for uncertainty in outputs, $Var(Q_{down}$)to decrease if Q_{up} and Div are sufficiently positively correlated. This implies that learning and adaptive mechanisms, in which agents change Div in response to Q_{up}, can potentially offset streamflow uncertainty over time. Namely, the agent's action co-evolves with the changing environment after they learn from environmental feedback (Woodard et al., 2019).

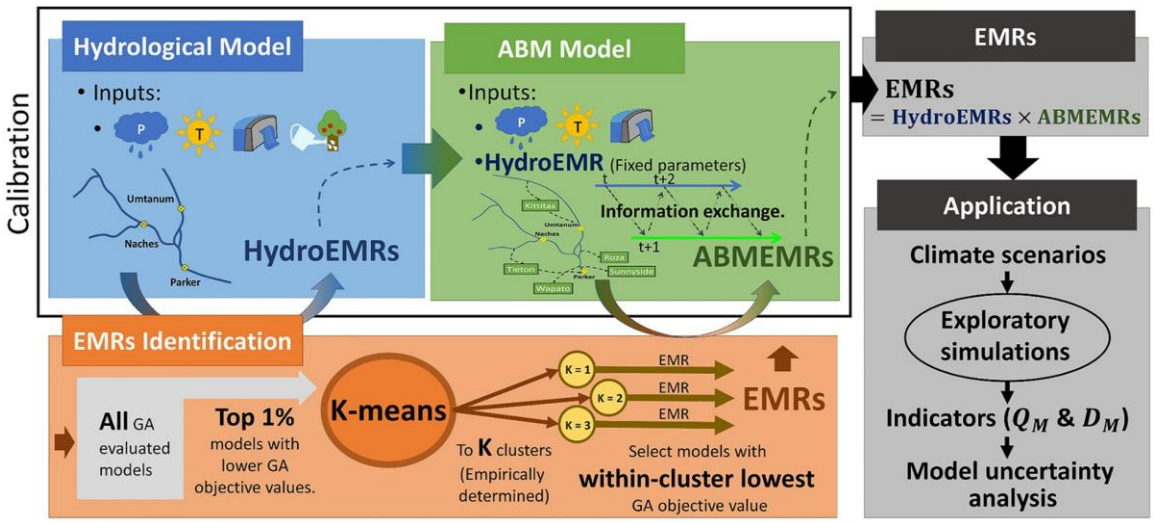

Figure 4-4. Modeling schema for the numerical experiment. Schema begins by calibrating the hydrological model and identifying HydroEMRs through the K-means algorithm; then, HydroEMRs drive ABM calibration and ABMEMRs identification. Identified EMRs are then applied to exploratory application and uncertainty analysis.

The entire numerical experiment is visualized in Figure 4-4. It consists of (a) calibration and EMRs identification and (b) exploratory simulations and model uncertainty analysis. In the first part, the calibration is separated for the hydrological model and ABM. We first calibrate the hydrological model using weather data, observed reservoir releases, and irrigation diversions. After reaching the GA termination criteria (e.g., maximum generation), we identify two HydroEMRs following the procedure shown in the orange box in Figure 4-4. The chosen maximum generation as termination criteria ensures consistency in the number of evaluations for EMRs identification. During the EMRs identification step, we collect all simulations from the GA calibration and then select the top 1% models, that is, those with better fits, as feasible models. Then, we normalize those calibrated parameters into [0,1] according to their calibration bounds (Table 4-1) and input them into the K-means algorithm (Pedregosa et al., 2011). The number of clusters/EMRs is empirically determined from the explained variance elbow plot (e.g., two clusters for the

hydrological model; Bholowalia & Kumar, 2014; Figure C4 in Appendix C.3). After that, models with the best fit are selected within each cluster as EMRs.

Next, we use these two HydroEMRs to drive ABM calibration. Following the same procedure as calibrating HydroEMRs, four ABMEMRs (elbow plot in Figure C5 in Appendix C.3) are found for each HydroEMRs. Note that the information (e.g., streamflow and diversion requests) is exchanged annually between the hydrological and water diversion models during the evaluation. We refer readers to Hyun et al. (2019) for more details about this coupling technique. Then, we repeat this calibration process for five coupled models with the different diversion agent types introduced in Section 4.3.2 . Therefore, at the end of the first part, eight EMRs (2 HydroEMRs × 4 ABMEMRs) are identified per coupled model and then applied to the second part, exploratory application. In the second part, we conduct exploratory simulations with 1,000 input realizations and then calculate indicators (Q_M and D_M) for each EMRs of the five coupled models. Then, we repeat this exploratory Experiment 30 times to address the stochastic nature of our model. Consequently, we use 1,200,000 model evaluations (1,000 climate input realizations × 5 types of diversion agents × 8 EMRs × 30 iterations) for the model uncertainty analysis.

4.4 Results

4.4.1 Calibration and validation of EMRs

This section describes the calibration and validation results of EMRs. Table 4-3 shows that both HydroEMR1 and HydroEMR2 have similar mean KGE values (0.672 and 0.675) in the calibration, and the differences are a result of different compromises in the subbasin KGE performance. For example, HydroEMR1 has a higher KGE at the Naches outlet,

while the Umtanum and Parker outlets perform better in HydroEMR2. The monthly time series plot is provided in Figure C6 in Appendix C.3, and calibration statistics are shown in (Table C6 and Figure C7 in Appendix C.3).

Table 4-3. Monthly Calibration and Validation Results of Hydrological Models.

Period	Model	Mean KGE	Subbasin	KGE
Calibration (1960–1999)	HydroEMR1	0.672	Umtanum	0.653
			Naches	0.750
			Parker	0.611
	HydroEMR2	0.675	Umtanum	0.686
			Naches	0.712
			Parker	0.628
Validation (2000–2013)	HydroEMR1	0.591	Umtanum	0.536
			Naches	0.752
			Parker	0.487
	HydroEMR2	0.599	Umtanum	0.569
			Naches	0.712
			Parker	0.517

We show the ABMEMR calibration (1960–1999) and validation (2000–2013) for annual diversion results (separated by vertical dotted lines) for five coupled models (rows), from simple to complex (top to down), in Figure 4-5. The red lines are the observed data, and the grey areas are 95% confidence intervals. Each EMR result is one of four ABMEMRs (line styles) that are driven by HydroEMR1 (blue lines) or HydroEMR2 (orange lines) and averaged over ten simulations. For example, EMR2.1 is the result of the coupled model consisting of HydroEMR2 and ABMEMR1. We show the detailed calibration statistics in Table C6 and Figure C8. In general, the EMRs of M_S show the lowest variations because it is the simplest two-parameter deterministic model type. Two adaptive models ($M_{A,L}$ and $M_{A,Q}$) recreate short-term variations (e.g., yearly fluctuations),

while two learning adaptive models ($M_{L,L}$ and $M_{L,Q}$) capture both the long-term decrease and short-term variations. Figure 4-5 also shows that coupled models with quadratic functions have greater variation than the linear function, which implies that coupled models with quadratic functions have larger equifinal space. In Figure 4-5, column 2, Tieton's diversion pattern is not well-captured, especially in $M_{A,Q}$ and $M_{L,Q}$; however, it has limited influence on the overall results due to the small diversion amount. The "spikes" in Tieton's pattern are the diversion output governed by the emergency response component and the prorated ratio during drought years instead of the adaptive component. Tieton's adaptive component output low diversions to achieve a better calibration objective value of the model. Although such diversion patterns are not realistic, we keep them in our uncertainty analysis because these EMRs satisfied our equifinal model definition (i.e., similar objective value in calibration).

4.4.2 Comparing model complexity and uncertainty

4.4.2.1 Uncertainty decomposition of natural system output (Q_M)

We run the identified EMRs under 1000 future climate realizations 30 times each to calculate the Q_M uncertainty (i.e., $\mathrm{Var}(Q_M)$). In Figure 4-6, we decompose $\mathrm{Var}(Q_M)$ into three parts that are attributed to three uncertainty sources: climate change scenario (blue areas; combinations of PF_{ratio} and TF_{delta}), internal climate variability (orange areas; bootstrapped realizations), and different model configurations (green areas; variation of EMRs) for five coupled models (columns), with mean values from 30 runs to address stochasticity in the ABM. The diversity of model configurations is contributed by variations of HydroEMRs (light green areas; $Config_{HydroEMR}$; $\mathrm{Var}(\mathrm{E}[I|EMR, HydroEMR])$) and ABMEMRs (dark green areas; $Config_{ABMEMR}$;

E[Var($I|EMR, HydroEMR$)]). Figure 4-6a shows the actual variance value of Q_M; Figure 4-6b indicates the fractional contribution percentage of three uncertainty sources; and Figure 4-6c is the S_M boxplot time series representing the shortage frequency of 20 internal climate variability realizations over climate change scenarios and EMRs.

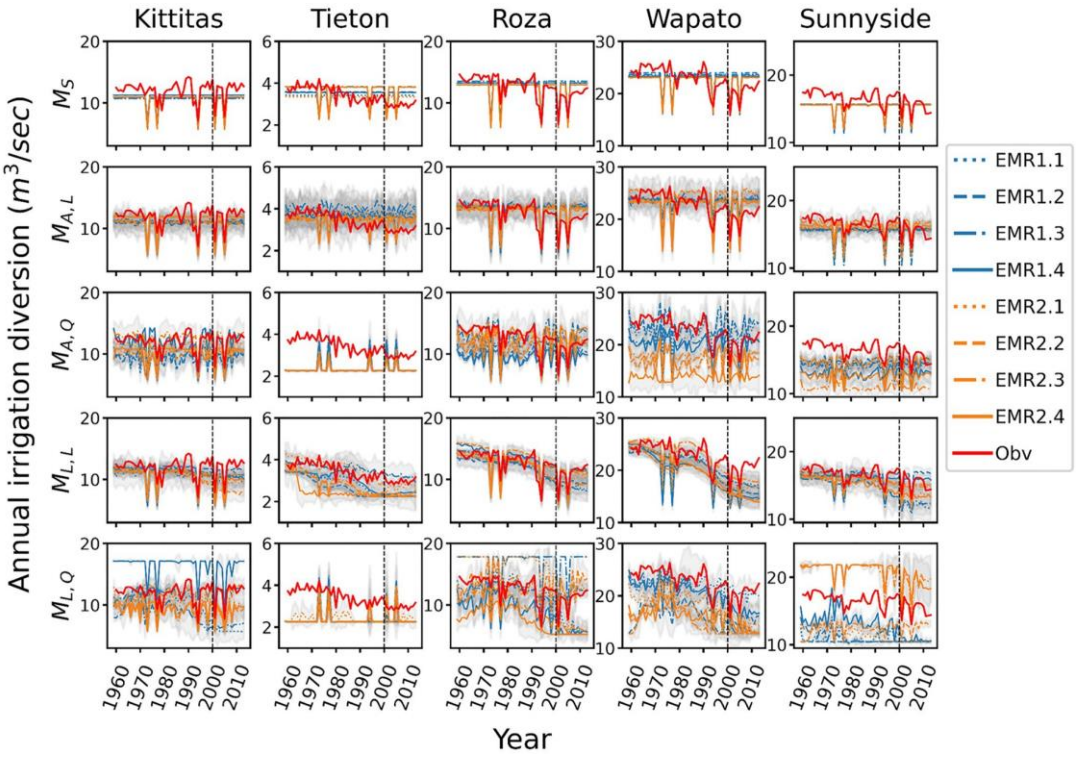

Figure 4-5. Calibration and validation results (separated by vertical lines) of five diversion irrigation districts (columns) for five coupled models (rows). Each EMR result is one of the four ABMEMRs driven by HydroEMR1 (blue lines) or HydroEMR2 (orange lines) that were averaged over 10 simulations. Red lines are observed data, and gray areas are 95% confidence intervals.

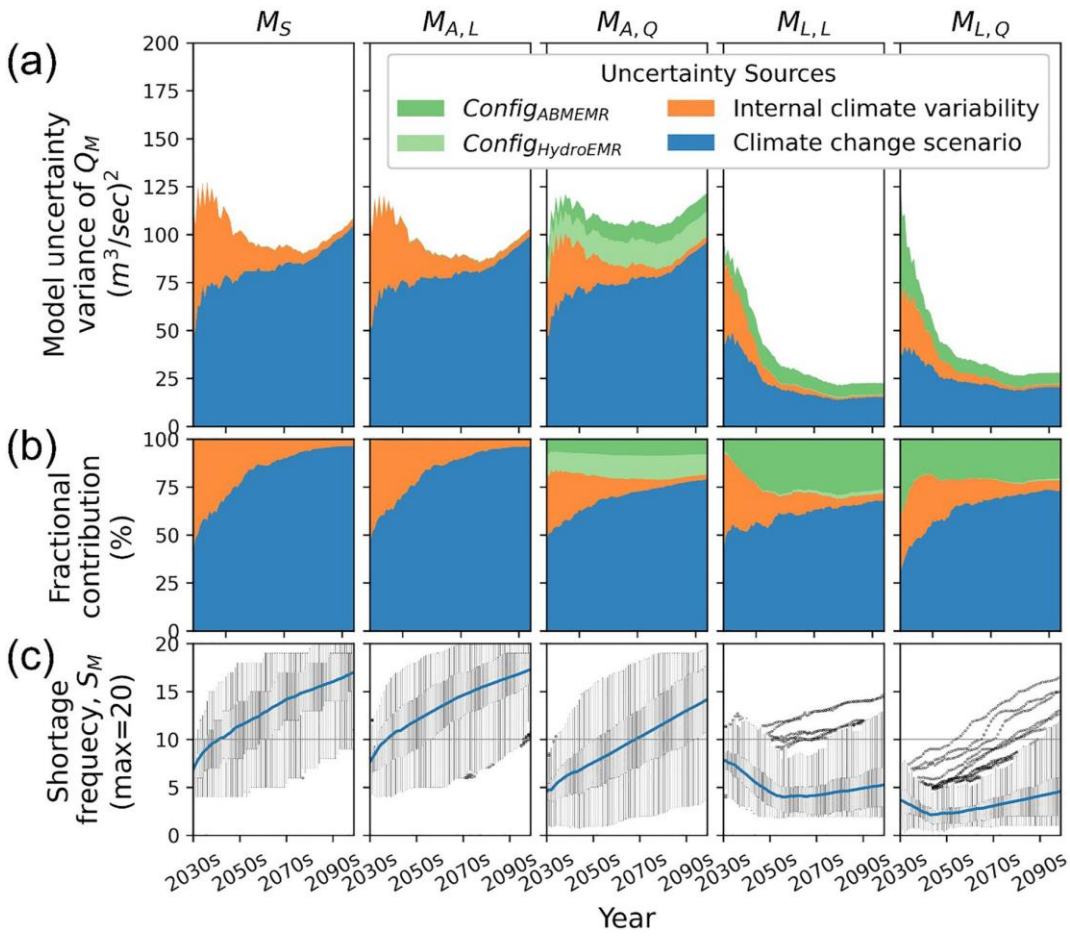

Figure 4-6. (a) Model uncertainty decomposition of Q_M for five coupled models (columns). (b) Fractional contribution percentage of decomposed variances. (c) Boxplot time series of S_M with mean values (blue lines) and outliers (black dots). Three uncertainty sources were climate scenario uncertainty, internal climate variability, and different model configurations.

For M_S, the uncertainty caused by climate change scenarios increases over the simulation period, while the uncertainty driven by internal climate variability gradually decreases. The model configuration uncertainty is almost negligible (<0.3) in M_S. A similar pattern is observed in $M_{A,L}$, where the model configuration uncertainty (<1) is only slightly larger than M_S. For the more complex model $M_{A,Q}$, we observe a significantly larger contribution from different model configurations. However, this trend is not present in models with the learning component, which we discuss later.

The increasing amount of blue areas in M_S, $M_{A,L}$, and $M_{A,Q}$ indicates the limited ability of the agents in these coupled models to address long-term trends in climate change scenarios since the ABMs are not designed to "learn" from the long-term environmental changes. The adaptive component could absorb short-term shocks caused by internal climate variability, so $M_{A,L}$ and $M_{A,Q}$ have smaller orange areas than M_S ($M_{A,Q}$<$M_{A,L}$<M_S). However, the shrinking magnitude of uncertainty from climate variability toward the end of the simulation is caused by increasing shortage frequency, S_M (Figure 4-6c). Diversion shortage implies that streamflow is at the minimum flow requirement, as no more water can be diverted to meet the demand. Therefore, increasing S_M across climate change scenarios and EMRs results in lower internal climate variability in Q_M. In addition, $M_{A,Q}$ shows the smallest uncertainty caused by input data (i.e., blue and orange areas), but it has the largest model configuration uncertainty. Therefore, ignoring possible model configurations could artificially reduce uncertainty (i.e., no green area), which may affect the interpretation of model results and bias the concluding information.

In Figure 4-6, coupled models with learning components ($M_{L,L}$ and $M_{L,Q}$) have much smaller Q_M uncertainty because agents in these models can learn to adjust their diversion requests for both long-term and short-term changes; this offsets the Q_M uncertainty contributed by input data (i.e., P_{future} and T_{future}). Furthermore, we observe that the model configuration differences of $M_{L,L}$ and $M_{L,Q}$ is primarily caused by ABMEMRs variations ($Config_{ABMEMR}$), while the model configuration differences in $M_{A,Q}$ is contributed by both HydroEMRs and ABMEMRs variations (Figure 4-6a). The negligible $Config_{HydroEMR}$ of the two learning adaptive models can again be attributed to learning abilities (i.e., achieving flow target by updating $Div_{req,ref}$). When we use learning

adaptive models to simulate irrigation requests, the driver of ABMEMR (i.e., HydroEMR1 or HydroEMR2) does not matter because agents could adjust their diversion behaviors according to feedback from different hydrological environments. Therefore, we observe smaller $Config_{HydroEMR}$ results in the exploratory simulations. Furthermore, the learning abilities of $M_{L,L}$ and $M_{L,Q}$ result in a lower frequency of encountering shortages upon diversion (Figure 4-6c).

4.4.2.2 Uncertainty decomposition of human system output (D_M)

After analyzing the model uncertainty of the nature system indicator (Q_M), we next consider how flexible agent behaviors need to be to reach the level of Q_M uncertainty revealed in Figure 4-6. Therefore, we examine similar variance decomposition plots for D_M (human-system indicator) in Figure 4-7, with the total model uncertainty of Q_M (Figure 4-7c).

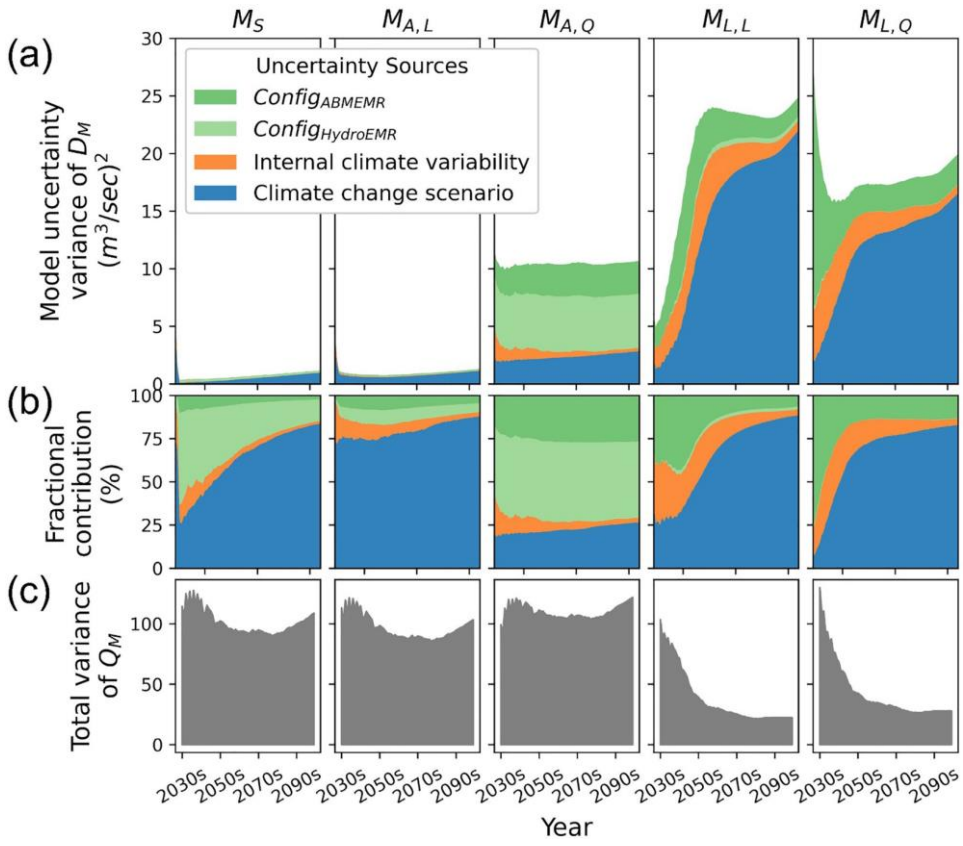

Figure 4-7. (a) Model uncertainty decomposition of D_M for five coupled models (columns). (b) Fractional contribution percentage of decomposed variances. (c) Total model uncertainty of Q_M. Three uncertainty sources are climate scenario uncertainty, internal climate variability, and different model configurations.

For M_S, the D_M uncertainty gradually increases over time due to the climate change scenario uncertainty (Figure 4-7a). As we discussed earlier, diversion shortage dominates in M_S, where the quantity of available water under different input data (i.e., P_{future} and T_{future}) determines the model uncertainty for diversion behavior. Namely, if there is no diversion shortage, the variance of D_M will be a flat line, with only the contribution of different model configurations because the diversion request is a fixed value in M_S.

The greater internal climate variability fractional contribution (orange area in Figure 4-7b) in $M_{A,L}$ and $M_{A,Q}$, compared to M_S, is contributed by agent adaptability (e.g.,

different diversion requests based on water supply conditions). Furthermore, variations caused by HydroEMR1 and HydroEMR2 play an important role in driving D_M model configuration variations in M_S, $M_{A,L}$, and $M_{A,Q}$, demonstrated by greater $Config_{HydroEMR}$ than $Config_{ABMEMR}$ in Figure 4-7b. This is because M_S, $M_{A,L}$, and $M_{A,Q}$ cannot learn. Therefore, the identified EMRs driven by different HydroEMRs show distinct patterns in calibration (Figure 4-5), leading to larger contributions from different model configurations in D_M uncertainty.

The two learning adaptive models, $M_{L,L}$ and $M_{L,Q}$, show distinct patterns from the other three models. The D_M uncertainty caused by climate change scenarios increases significantly over time, which is the opposite behavior as the Q_M shown in Figure 4-7c. This further indicates that agents can learn from environmental feedback (e.g., flow deviations) and then mitigate some environmental uncertainty through their flexibility in adjusting long-term diversion behaviors. These results visualize an opposing trend between Q_M and D_M uncertainties in CNHS. In the next section, we will mathematically explain this learning behavior.

4.4.3 Model uncertainty and co-evolution in CNHS

In the previous analysis, we show the uncertainty decomposition for both natural (Q_M) and human (D_M) system outputs. We claim that the learning mechanism limits $\mathrm{Var}(Q_M)$ with more complex model designs. Although the two learning models exhibit greater uncertainties in human system behavior, the increasing magnitude of D_M uncertainty is less than the decreasing magnitude of Q_M uncertainty. We hypothesize that co-evolution, particularly in the learning mechanism of CNHS, leads to such results. To test this hypothesis, we adopt Equation 4-17 and show the results at the Parker gauge in Figure 4-8.

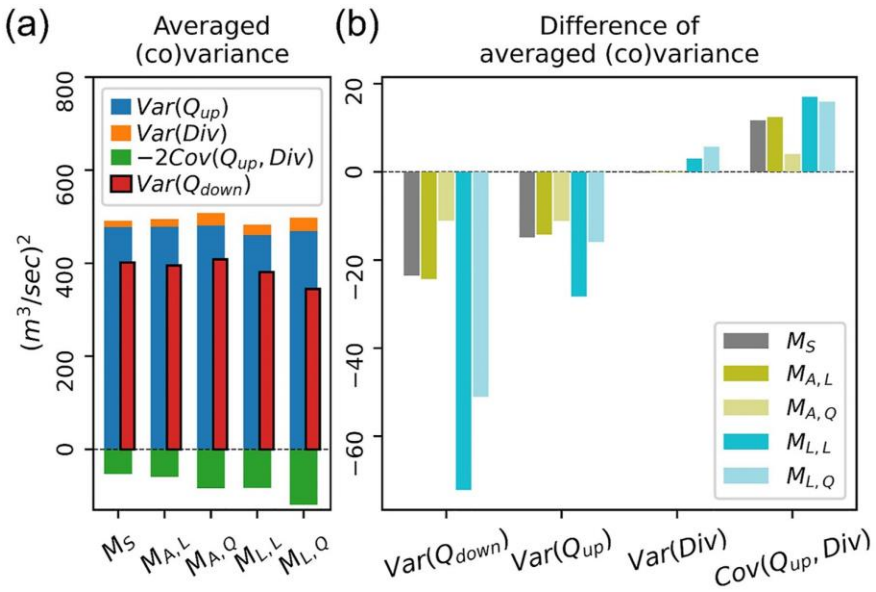

Figure 4-8. Factors showing co-evolution, particularly with the learning mechanism, leading to overall lower model uncertainty. Q_{down}, Q_{up}, and Div are streamflow before diversion, streamflow after diversion, and diversion at Parker gauge, respectively. (a) Averaged (co)variances of five coupled models from 2030 to 2100. (b) Differences between averaged (co)variance from 2066 to 2100 and from 2030 to 2065.

Figure 4-8 shows the value of each term in Equation 4-17 using the Parker gauge as an example. Q_{down}, Q_{up}, and Div are the streamflow before diversion, the streamflow after diversion, and the diversion at Parker gauge, respectively. The averaged (co)variances of five coupled models (x-axis) from 2030 to 2100 are shown in Figure 4-8a. Figure 4-8b shows differences between the averaged (co)variance from 2066 to 2100 and from 2030 to 2065.

Equation 4-17 shows that $Var(Q_{down})$ can only be less than $Var(Q_{up})$ only if $Cov(Q_{up}, Div)$ is not zero and $2 \times Cov(Q_{up}, Div)$ is greater than $Var(Div)$. Following this logic, Figure 4-8a mathematically demonstrates that our designed agents act (i.e., divert) differently (i.e., co-evolve; green bars) according to the environment and indicates a decreasing pattern in $Var(Q_{down})$ as the model becomes more complex (red bars). For

example, M_S diverts different amounts of water based on the available water (Q_{up}). $M_{A,L}$ and $M_{A,Q}$ have larger covariance values because of their adaptability to short-term shocks. $M_{L,Q}$ and $M_{L,L}$ have the highest covariance value because they have both adaptive and learning capabilities. The $Cov(Q_{up}, Div)$ pattern of models with different complexities is highly correlated with the pattern in $Var(Div)$, verifying the design of our diversion agent given how closely an agent co-evolves with the environment.

The decreasing trend in Q_M uncertainty (e.g., $M_{L,Q}$ and $M_{L,L}$ in Figure 4-6a) only occurs when the difference in the summation of $Var(Q_{up})$ and $Var(Div)$ is lower than the difference in $2 \times Cov(Q_{up}, Div)$ between the former and latter simulation periods (Figure 4-8b). The negative difference of M_S and $M_{A,L}$ in $Var(Q_{down})$ is primarily contributed by the decrease in $Var(Q_{up})$ and the shortage-induced $Cov(Q_{up}, Div)$. $M_{A,Q}$ has a similar explanation: the difference in $Var(Div)$ is almost zero (i.e., the adaptability remains the same over the entire simulation). The most interesting results are in the two learning models, $M_{L,Q}$ and $M_{L,L}$, where increasing $Var(Div)$ results in a significant increase in $Cov(Q_{up}, Div)$ that leads to a larger magnitude of decreasing $Var(Q_{down})$. This demonstrates our explanation for Q_M variance decomposition results in the previous section and supports our hypothesis: learning behaviors in a human system can potentially offset the impact of a natural system's variability on output uncertainty (i.e., $Var(Q_M)$. However, we do not extend these results to claim that the learning adaptive model is a better design. This chapter quantifies model uncertainty properties for different designs used to model CNHS. It is important to verify the existence of learning behavior or any other structural designs in a chosen case study; otherwise, uncertainty may be introduced from inappropriate structural assumptions. For this particular case study, we may argue

that $M_{L,L}$ is a more appropriate model design as it has higher objective values in calibration (Table C6).

4.5 Discussion

4.5.1 Other sources of uncertainty in CNHS

Our results, which show that learning adaptive models have less observed variance in the nature system (e.g., Q_M), align with the philosophy of "adaptive management" strategies in facing increasing climate change uncertainty (Giordano & Shah, 2014; Karthe et al., 2021). However, it is also important to consider the causes of decreasing nature system uncertainty. First, our results show that, if possible model configurations are ignored, Q_M uncertainty is only driven by input data whose uncertainty appears to be smaller in the adaptive models than in the static model. This might lead to a false conclusion that the adaptive model is more reliable (i.e., less uncertain). Second, although utilizing learning adaptive models shows a decreasing trend in Q_M uncertainty, they could be impacted by uncertainty from incomplete knowledge of proposed model structural assumptions, such as a learning structure (Karthe et al., 2021), which would not be directly revealed in the modeling results. Such introduced assumption-based uncertainty could be a barrier to interpreting modeling results and implementing adaptive management strategies (Allen & Gunderson, 2011; Lee, 2001). Therefore, continuously monitoring (i.e., acquiring data) and communicating uncertainty among modelers, policymakers, and other stakeholders is essential.

While this chapter decomposes specific uncertainties (e.g., input data and different model configurations), other uncertainty sources are not analyzed, such as indicator selection (Khatami et al., 2019), model resolution level (Saltelli et al., 2019), and coupling

structure (e.g., data exchange frequency and exchanged information). Some benchmark study cases may help the CNHS modeling community eliminate indicator selection factors when evaluating model uncertainty across different model designs (Vallario et al., 2021). However, the indicator selection procedure requires its own systematic study. For example, we choose KGE in this chapter, but other widely used indicators, like Nash-Sutcliffe efficiency (Nash & Sutcliffe, 1970) or R-squared, might lead to different uncertainty analysis results. Investigations of the uncertainty caused by the model resolution level and coupling structures will benefit the use of CNHS models in cross-scale (temporal and spatial) studies (Aburto et al., 2012; Fleischmann et al., 2019), especially when coupling to models with various simulation timesteps and frequency of information exchange. However, this requires each coupled-model component to be run over the full spectrum of temporal and spatial resolutions to set up comparable numerical experiments. This is particularly challenging when coupling to large-scale models or standalone software, which are often restricted to coarse or limited temporal or spatial resolutions.

4.5.2 Limitations

We identify several limitations in this chapter that could be improved in future studies. First, the reservoir settings are highly simplified, where reservoir releases are considered as input data. Interactions between reservoirs and water demands are ignored. Namely, the CNHS of the YRB is only partially tested. Second, we assume that calibrated agent behaviors (e.g., γ for learnability; a_L and b_L for linear adaptability; and a_Q, b_Q, and c_Q for quadratic adaptability) could be directly applied to exploratory analyses. In addition, agent learnability and adaptability might not remain the same in the future (Aburto et al., 2012) for more accessible and accurate forecast information or changing environmental

regulations. Third, we subjectively bound $Div_{req,ref}$ based on historical records. This might affect uncertainty analysis results since canal capacity is possible to increase over our assumption (e.g., 120% of the historical maximum). Fourth, our numerical experimental design ignores some uncertainty sources. For example, we only consider a subset of input data uncertainty (i.e., climate change scenarios and internal climate variability), we ignore the downscaling uncertainty, and we follow the conventional calibration and validation procedure under the stationary assumption of the natural system, which a more comprehensive study can be done to evaluate the uncertainty brought by the stationary assumption. Also, based on the equifinal model definition, our identified EMRs could be approximations of a single local optimum rather than multiple local optima. We encourage the adoption of pre-calibration methods (Tarawneh et al., 2016), alternate calibration algorithms (Tolson & Shoemaker, 2007), and carefully selected feasibility model criteria (i.e., equifinal models) for model configuration uncertainty quantification in future projects focusing on case studies.

4.6 Conclusions

A deeper understanding of CNHS modeling enables us to better use modeling results to inform policymaking. This chapter explores modeling uncertainties. We quantify and then decompose the uncertainty of a coupled natural-human model (i.e., a semi-distributed hydrological model coupled with an agent-based water diversion model) into three sources by the law of total variance: (a) climate scenario uncertainty, (b) climate internal variability, and (c) model configuration uncertainty. The YRB in the Northwest US is adopted as our study area, where irrigation districts are defined as agents. We analyze how co-evolution influences the relationship between model output uncertainty and model complexity

through five coupled models with different water diversion agent types: (a) a static model, (b) an adaptive model with linear functions, (c) an adaptive model with quadratic functions, (d) a learning adaptive model with linear functions, and (e) a learning adaptive model with quadratic functions.

Our hypotheses—(a) model uncertainty in an exploratory analysis will likely increase with model complexity, given uncertain input data (e.g., climate forcing), and different model configurations, and (b) the inclusion of a learning mechanism in a human system can potentially offset the impact of natural system's variability on output uncertainty—are accepted, according to our results. The two learning adaptive models show a decreasing trend in the natural system output because agents learn and adapt to environmental changes via co-evolution between the two subsystems. The learnability and adaptability are revealed by increased variability of the human system outputs. Although the learning adaptive models generate smaller nature system output uncertainty, the modeler should be aware of how assumptions of model structure (e.g., Is the learning assumption appropriate in the exploratory analysis of a given case study?) affect the results. Finally, additional uncertainty sources should be investigated in future work, such as indicator selection, model resolution level, and coupling structure with a more sophisticated agent setup and scale-up experiments.

Chapter 5: Compounding Risks of Natural Hazards and Cyber-physical Attacks in a Smart Storm Water System

Abstract

Risk is a piece of critical information for system planning and investments of limited recourses. With the growing usage of Internet-of-Thing-based infrastructures, new cybersecurity risks were introduced to water systems. However, the compounding risks of natural hazards and cyber-attacks have not yet been widely evaluated. This chapter explores this concept and proposes a quantification method for such compounding risks. We implement the proposed method in a smart stormwater system, a pond-conduit network that has water level sensors and outflow gate actuators at each pond and is dynamically controlled in real-time, to quantify the compounding risks of storms and false data injection (FDI) on a flooding issue while considering sensor noises and weather forecast uncertainties. We show that FDI can intensify the flooding risks by raising the controlled pond water level by injecting false data to sabotage the feedback control system and cause it to output wrong outflow control signals. In addition, we find that the flooding risk patterns of different storm intensities are significantly altered by FDI, where compounding risks tend to be higher with smaller, more frequent storms. Such results indicate the merit of the compounding risk concept in terms of planning and investments for smart stormwater systems. The proposed compounding risk quantification method can be further applied to other network-based water systems, such as irrigation canal systems, multi-reservoir systems, and water distribution systems.

5.1 Introduction

Risk plays a vital role in decision-making processes, for example, infrastructure investment with limited resources (Depoy et al., 2005; IPCC, 2022). Traditionally, risks like flooding were evaluated based on a single type of natural hazards, such as heavy storms (Tung et al., 2019). However, the absence of a correlation analysis with other natural and human factors might lead to overestimating or underestimating the concerning risks (Hillier et al., 2020). Recently, the compounding hazards concept has been proposed, where multiple natural hazards were considered in a risk evaluation (Bevacqua et al., 2021, Zscheischler et al., 2018). For instance, a stormwater system in a coastal city can be simultaneously impacted by heavy storms and sea level rises (Wahl et al., 2015). However, the compounding risks involving natural hazards and human interventions (e.g., cyber-attack) have not been well-studied (Xu et al., 2021), especially for their quantification methods.

Proper stormwater management strategies are required to address corresponding flooding, pollution, and erosion issues in urban stormwater systems (Burian et al., 2002; Fletcher et al., 2015; Jongman, 2018; Ministry of the Environment, 2003). Natural-based solutions, e.g., detention ponds, are conventionally adopted with gravity-based passive control to detain runoffs and reduce peak outflows to prevent flooding and erosions (Huang et al., 2020; Van Meter et al., 2011). Namely, the outflows of ponds are controlled by the combinations of pond capacities, conduit sizes, and components' relative invert elevations. Studies have tried to optimize the system over different combinations of the abovementioned ponds' properties (Froise & Burges, 1978; Yeh & Labadi; 1997). However, passive stormwater systems (e.g., outflow gate openings are fixed) tend to be difficult (or costly) to expand and adapt to environmental changes like weather patterns

and land use once it is built (Shishegar et al., 2018). To improve a system's flexibility and efficiency, real-time control (RTC) has the potential to enhance the utilization of existing infrastructures at a low cost, especially Internet-of-Thing (IoT) technologies, including sensors, actuators, and cloud-based data storage (Gaborit et al., 2013; Mullapudi et al., 2020; Piro et al., 2019). For example, the peak outflow at a stormwater system outlet can be reduced by controlling outflows from upstream ponds in real-time using water level measurements and weather forecasts (Sadler et al., 2020; Shishegar et al., 2021; Wong and Kerkez, 2018). We called these IoT-based stormwater systems as smart stormwater systems (Bartos et al., 2018).

However, those IoT technologies in RTC systems also introduce new cybersecurity issues (Kriaa et al., 2015; Shin et al., 2020; Yanakiev, 2020). Several cyber-attack incidents have been reported in various water systems, from water/wastewater treatment plants and pump stations to canal systems and reservoirs (Hassanzadeh et al., 2020; Tuptuk et al., 2021). Recently, the US Federal government released a water sector action plan to expand public-private cybersecurity partnership (The White House, 2022), which further indicated the sincere concern about the cyber security issue in the water sector. With various forms of cyber-attacks, including device compromise, false alarms, denial of service, and data exfiltration (Dieu, 2001; Li and Liu, 2021; Lu and Reeves, 2014), this chapter focuses on "false data injection" (Mo et al., 2010), in which stealthy attackers inject false measurements into the supervisory control and data acquisition (SCADA) system without being detected. Then, those contaminated measurements bias the decisions (e.g., outflows of ponds) in RTC and possibly lead to physical damages to the system (e.g., flooding), thus called cyber-physical attacks. While the impact of false data injection (FDI) has been

studied in water distribution systems (Ahmed et al., 2017; Moazeni et al., 2021), irrigation canals (Amin et al., 2012; Amin et al., 2013), and water treatment plants (Kumar et al., 2021), it has not yet been explored in IoT-based smart stormwater systems.

Compared to the impact analysis of cyber intrusions, relatively few studies addressed the risk assessment in cyber-physical systems (Depoy et al., 2005) and the quantification of compounding risks (Yadav et al., 2020). Depoy et al. (2005) proposed a high-level cyber-physical system risk assessment framework considering physical and cyber security in large-scale critical infrastructures, e.g., water distribution systems. Later, the framework was developed into a computer program to assist the cyber-physical systems risk assessment (DePoy et al., 2006). However, this framework focused on human factors only (i.e., infrastructure vulnerability, attacks, and defending responses). It did not specify how to consider the interactions between natural and human factors (e.g., storms and FDI) in the assessment, where the growing threats of compounding disruptions by natural hazards and cyber-attack have been shown in a transportation system study (Yadav et al., 2020). Based on the literature review, a knowledge gap emerges that new methods to quantify compounding risks seem necessary (Nurse et al., 2017).

Therefore, this chapter aims to develop a compounding risks quantification method and demonstrate its utility in a smart stormwater system, where we consider storms and FDI in flooding risk evaluation. The three tasks of this chapter are (1) developing a mathematical framework for the compounding impact analysis, (2) demonstrating disclosure of potential FDI consequences in smart stormwater systems, and (3) quantifying the additional flooding risks caused by FDI while considering sensor noises and weather forecast uncertainties. Considering that smart stormwater systems have not yet been

prevalent in practice, this chapter serves as an initial step to discuss the compounding risk through a hypothetical case based on the real-world pond network layout to assist future system development.

The article is structured as follows. Section 5.2 presents the methods used to achieve the abovementioned three tasks, and Section 5.3 introduces the study area and the experiment setup. Results are shown in Section 5.4 . A discussion of control system properties and model limitations is shown in Section 5.5 , followed by the Conclusions in Section 5.6 .

5.2 Methods

5.2.1 Mathematical Framework for Smart Stormwater Systems

This chapter abstracts a smart stormwater system into a mathematical framework (Figure 5-1) that consists of three components: (1) a stormwater (drainage) system representative, (2) an outflow control system, and (3) a bad data detector. The stormwater system is described by a linear state-space model that simulates the water balance and water level dynamics in a pond-conduit network. A time-invariant linear quadratic gaussian (LQG) controller is adopted to mimic the system control process that assimilates water level measurements into model estimates using the Kalman filter and yields outflow controls. A χ^2 detector (Mo et al., 2010) is chosen to be a bad data detector representing the SCADA system that checks the quality of the sensor measurements before passing them to the LQG controller. We explain these three components in detail in the following sections.

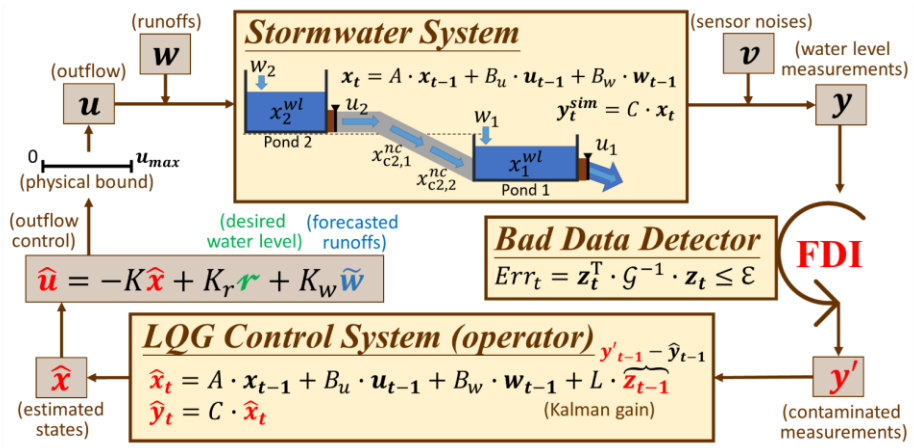

Figure 5-1. A mathematical framework for smart stormwater systems consists of a stormwater (drainage) system representative, a control system, and a bad data detector. The red-colored variables indicate the polluted path to the outflow control ($\hat{\boldsymbol{u}}$), where $\boldsymbol{y}'$ is the contaminated measurements from FDI.

5.2.1.1 State-Space Representation for the Pond-Conduit Network

The stormwater system we considered is a network of ponds and conduits (Figure 5-1) that can be further abstracted into a node-link system, where nodes are storages (i.e., ponds) and links are the network topology (i.e., conduits). The state-space model (Equation 5-1) has been successfully adopted to simulate the water balance dynamics in such network-based systems (Ahmed et al., 2017; Schuurmans, 1997; Wong and Kerkez, 2018).

$$\boldsymbol{x_t} = A \cdot \boldsymbol{x_{t-1}} + B_u \cdot \boldsymbol{u_{t-1}} + B_w \cdot \boldsymbol{w_{t-1}} \tag{5-1}$$

$$\boldsymbol{y_t^{sim}} = C \cdot \boldsymbol{x_t} \tag{5-2}$$

where $\boldsymbol{x_t}$ [cm] is a vector of states to represent the water level in ponds and the flow quantities in segments of a conduit. The flow quantities are represented by the water level change of the source pond. The term $\boldsymbol{u_{t-1}}$ [cm] is a vector of pond outflows represented by the water level change of the source pond, and $\boldsymbol{w_{t-1}}$ [cm] is a vector of runoffs represented by the water level change of the destination pond. The subscript $t \in \mathcal{T} = \{1,2,\dots,T\}$ denote the time step in a discrete simulation system, where $\mathcal{T}$ is a set of

simulation time steps, and T is the number of time steps in a simulation. The coefficients A, B_u, and B_w are state, control, and disturbance matrixes, respectively, abstracting the topology of network and unit/scale conversion. Matrix A is a square matrix with a dimension equal to the number of states in $\boldsymbol{x_t}$. The diagonal elements corresponding to water level states have the value one; otherwise, zero. The off-diagonal non-zero elements represent the routing process in conduits. Those non-zero elements have the value $\frac{a_{s,\text{source}}}{n_c \cdot a_{s,\text{destination}}}$, where n_c is the number of segments in a conduct c and $\frac{a_{s,\text{source}}}{a_{s,\text{destination}}}$ is the ratio of source pond area and destination pond area. Matrix B_u has the dimension of the number of states in $\boldsymbol{x_t}$ times the number of ponds. In the matrix B_u, pond-to-conduit-inlet elements have the value of one, and conduit-outlet-to-pond elements have the value of negative one; otherwise, zero. Matrix B_w has the same dimension as B_u. The only non-zero elements are those linking sub-catchment runoff to pond elements, which have the value of one. We expand Equation 5-1 and illustrate the water level dynamics of Pond 1 in a two-pond system (Figure 5-1) in Equation 5-3.

$$x_{1,t}^{wl} = x_{1,t-1}^{wl} + \underbrace{\overbrace{\frac{a_{s,2}}{n_{c2} a_{s,1}} \left(x_{c2,1,t-1}^{\text{nc}} + x_{c2,2,t-1}^{\text{nc}} \right)}^{\text{Conduit inflow from Pond 2}} + \overbrace{u_{1,t-1}}^{\text{Outflow}} + \overbrace{w_{1,t-1}}^{\text{Runoff}}}_{\text{Water level change of Pond 1 from different sources}} \tag{5-3}$$

where x^{wl} is pond water level states, and $x_{c,s}^{nc}$ is the water quantity state of segment s in a conduct c. The dynamic of the water level in a pond is equal to the water level at the previous time step (the first term) plus the water level changes resulting from the conduit inflows of the upstream ponds (the second term), the pond's outflow (the third term), and the runoffs (the fourth term) generated from its sub-catchments. The output matrix (C) in Equation 5-2 collects the simulated water level ($\boldsymbol{y_t^{sim}}$ [cm]) information from $\boldsymbol{x_t}$, which contains water level states and water quantity states of conduit segments. Matrix C has the

dimension of the number of ponds times the number of states in $\boldsymbol{x_t}$. We provide a more thorough example with a three-pond system in the supporting information (Appendix D.1) to demonstrate the construction of a state-space model from a given pond-conduit network.

The sensor measurements of water levels ($\boldsymbol{y_t}$ [cm]) are expressed in Equation 5-4.

$$\boldsymbol{y_t} = \Gamma_t^{\mathrm{h}} \cdot (\boldsymbol{y_t^{sim}} + \boldsymbol{v_t}) + \Gamma_t^{a} \cdot \boldsymbol{y_t^{a}} \tag{5-4}$$

where Γ^h and Γ^a are indicator matrixes (i.e., 0 or 1) showing the time steps and sensors that are healthy or being attacked (i.e., FDI), respectively. The term $\boldsymbol{v_t}$ [cm] is a vector of the Gaussian sensor white noise and $\boldsymbol{y_t^a}$ [cm] is a vector of the false data injected by an attacker at time step t.

5.2.1.2 LQG Controller for System Operation

The second component of the proposed framework is the LQG controller. The LQG controller consists of a linear quadratic estimator (LQE) and a linear quadratic regulator (LQR). LQE outputs the estimates of future states ($\hat{\boldsymbol{x}}_t$ [cm]) by assimilating model predictions ($\hat{\boldsymbol{y}}$ [cm]) and water level measurements through a Kalman filter as shown below:

$$\hat{\boldsymbol{x}}_t = A \cdot \hat{\boldsymbol{x}}_{t-1} + B_u \cdot \boldsymbol{u_{t-1}} + B_w \cdot \boldsymbol{w_{t-1}} + L \cdot \boldsymbol{z_{t-1}} \tag{5-5}$$

$$\boldsymbol{z_t} = \boldsymbol{y_t} - \hat{\boldsymbol{y}}_t \tag{5-6}$$

$$\hat{\boldsymbol{y}}_t = C \cdot \hat{\boldsymbol{x}}_t \tag{5-7}$$

In LQE (Equation 5-7), we adopt the same state-space model (Equations 5-1 and 5-2) as the prediction model. The term *L* is the Kalman gain, a coefficient matrix to adjust the current prediction using the differences between predictions and measurements at the previous time step ($\boldsymbol{z_{t-1}}$ [cm]; Equation 5-6). The Kalman gain is determined based on the level of sensor noises and the weather forecast uncertainty. The value of *L* is closer to 1 when sensor noises are smaller than the forecast uncertainty ($\hat{\boldsymbol{x}}_t$ relies more on the

measurements). In the opposite situation, L is closer to 0 ($\widehat{\boldsymbol{x}}_{\boldsymbol{t}}$ depends more on the model prediction). We show the calculation for L in (Appendix D.2).

LQR is a closed-loop feedback control method (Mo et al., 2010) that will use $\widehat{\boldsymbol{x}}_{\boldsymbol{t}}$ from LQE to determine the optimal control based on an overall objective function (Equation 5-8; J [cm^2]):

$$J = \widehat{\boldsymbol{x}}_{\boldsymbol{T}}^{\mathrm{T}} Q \widehat{\boldsymbol{x}}_{\boldsymbol{T}} + \sum_{t=1}^{T-1} (\widehat{\boldsymbol{x}}_{\boldsymbol{t}}^{\mathrm{T}} Q \widehat{\boldsymbol{x}}_{\boldsymbol{t}} + \widehat{\boldsymbol{u}}_{\boldsymbol{t}}^{\mathrm{T}} R \widehat{\boldsymbol{u}}_{\boldsymbol{t}}) \tag{5-8}$$

where T is the total time step, Q is a weight matrix for the control error (e.g., deviation of desired water level), and R is a weight matrix for the control cost (e.g., power consumption of gate controllers). The term $\widehat{\boldsymbol{x}}_{\boldsymbol{T}}^{\mathrm{T}} Q \widehat{\boldsymbol{x}}_{\boldsymbol{T}}$ is the control error at the terminal step. The analytical solution of this linear optimization problem to minimize J is $\widehat{\boldsymbol{u}}_{\boldsymbol{t}} = -K\widehat{\boldsymbol{x}}_{\boldsymbol{t}}$, where $\widehat{\boldsymbol{u}}_{\boldsymbol{t}}$ is the optimal control at the time step t, and K is the feedback gain matrix solved by the Riccati equation (Kučera, 1973). In addition to the information derived from past measurements (i.e., $\widehat{\boldsymbol{x}}_{\boldsymbol{t}}$), we further adopt future information, which is future desired water levels ($\boldsymbol{r}_{\boldsymbol{t}}$ [cm]) and forecasted runoffs ($\widetilde{\boldsymbol{w}}_{\boldsymbol{t}}$ [cm]), to adjust the outflow control ($\widehat{\boldsymbol{u}}_t$ [cm]):

$$\widehat{\boldsymbol{u}}_{\boldsymbol{t}} = -K \cdot \widehat{\boldsymbol{x}}_{\boldsymbol{t}} + K_r \cdot \boldsymbol{r}_{\boldsymbol{t}} + K_w \cdot \widetilde{\boldsymbol{w}}_{\boldsymbol{t}} \tag{5-9}$$

where K_r and K_w are two corresponding feedforward gain matrixes for $\boldsymbol{r}_{\boldsymbol{t}}$ and $\widetilde{\boldsymbol{w}}_{\boldsymbol{t}}$, respectively. For example, if the system foresees a large incoming runoff or a decrease in desired water levels (i.e., control target), outflow control ($\widehat{\boldsymbol{u}}_{\boldsymbol{t}}$) will be enlarged. We provide the detailed derivation of K, K_r, and K_w in Appendix D.2.

The actual controllable outflows (defined as a negative value), however, are limited to the available water in ponds ($\boldsymbol{u}_{\boldsymbol{t}}^{\boldsymbol{aw}}$ [cm]) and the physical properties of gravity-driven outflows ($\boldsymbol{u}_{\boldsymbol{t}}^{\boldsymbol{uc}}$ [cm]; assuming no pumps were installed) as shown in Equation 5-10.

$$\boldsymbol{u}_{\boldsymbol{t}} = \max(min(0, \widehat{\boldsymbol{u}}_{\boldsymbol{t}}), -\boldsymbol{u}_{\boldsymbol{t}}^{\boldsymbol{aw}}, -\boldsymbol{u}_{\boldsymbol{t}}^{\boldsymbol{uc}}) \tag{5-10}$$

$$\boldsymbol{u_t^{aw}} = \boldsymbol{y_t^{sim}} \tag{5-11}$$

$$\boldsymbol{u_t^{uc}} = \boldsymbol{c_g} \times \boldsymbol{\mu} \times \boldsymbol{a_g} \times \sqrt{2g\boldsymbol{y_t^{act}}} \times \left(\frac{dt}{\boldsymbol{a_s}}\right) \tag{5-12}$$

$$\boldsymbol{y_t^{act}} = \min\left(\boldsymbol{y^{max}}, max\left(0, \boldsymbol{y_t^{sim}}\right)\right) \tag{5-13}$$

The available water in ponds ($\boldsymbol{u_t^{aw}}$) is equal to $\boldsymbol{y_t^{sim}}$ (Equation 5-11). The maximum gravity-driven outflows ($\boldsymbol{u_t^{uc}}$) is computed under the assumption of full pipe flow (Equation 5-12), where $\boldsymbol{c_g}$ is a calibrated gate coefficient, $\boldsymbol{\mu}$ is the coefficient of contraction (often set to 0.65; Rossman, 2010), $\boldsymbol{a_g}$ is the cross-section area of the maximum gate opening (e.g., orifice), g is gravitational acceleration, and the actual water level in a pond ($\boldsymbol{y_t^{act}}$ [cm]; Equation 5-13) is bounded between 0 (i.e., no negative water level) and the maximum depth of ponds ($\boldsymbol{y_t^{max}}$ [cm]). The term $\frac{dt}{\boldsymbol{a_s}}$ converts the unit from flow rate to the water level change of ponds, where dt is the simulation time interval and $\boldsymbol{a_s}$ is a vector of the surface area of ponds, a function of $\boldsymbol{y_t^{act}}$.

5.2.1.3 Bad Data Detector

This chapter adopted a χ^2 detector (Mo et al., 2010) as a bad data detector in Equation 5-14.

$$Err_t = \boldsymbol{z_t}^{\mathrm{T}} \cdot \mathcal{G}^{-1} \cdot \boldsymbol{z_t} \leq \varepsilon \tag{5-14}$$

where $\boldsymbol{z}_t$ is a vector of the water level differences between predictions and measurements at the time step t as shown in Equation 5-6, $\mathcal{G}$ is a sensor weight matrix, and ε is an operator-selected threshold for measured errors tolerance (see the next section). We further denote $\boldsymbol{z_t^T} \cdot \mathcal{G}^{-1} \cdot \boldsymbol{z_t}$ as Err_t [cm^2], which can be interpreted as the sum of weighted squared independent and identically distributed Gaussian sensor noises (i.e., inter-product of $\boldsymbol{z_t}$)

such that Err_t is a χ^2 distribution with a degree of freedom equal to the number of water level sensors.

5.2.2 Compounding Impact Evaluation

5.2.2.1 Operation and FDI Strategies

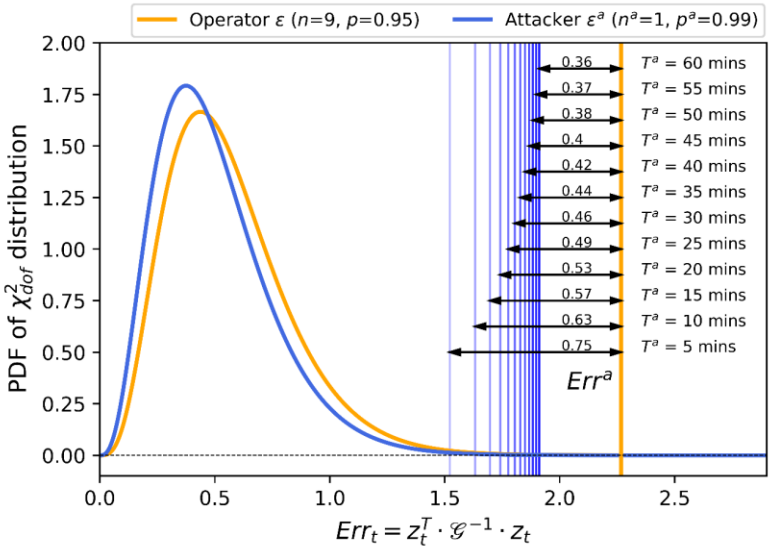

Figure 5-2. χ^2 distributions for operator (yellow lines) and attacker (blue lines) to determine corresponding thresholds, ε and ε^a, based on their operation and attack strategy. The attackable range (Err^a) decreases as the number of attacking time steps (T^a) increases.

This chapter evaluates compounding impact and quantifies compounding risk given a set of operations (e.g., outflow control rules; from the operator's perspective) and FDI strategies (e.g., the number of attacking sensors and time steps; from the attacker's perspective). The operation strategy ($\mathcal{O}$) and FDI strategy ($\mathcal{A}$) in a smart stormwater system ($\mathcal{N}$) are defined as:

$$\begin{cases} \mathcal{N} = \{A, B_u, B_w, C, \mathcal{g}, L, K, K_r, K_w\} \\ \mathcal{O} = \{\mathcal{R}, p\}, \\ \mathcal{A} = \{\Gamma^a, p^a\} \end{cases} \tag{5-15}$$

where p is the designed probability that the detector alarm will not be triggered in a healthy system during a storm event, and p^a is the designed probability of a successful FDI given attacking sensors and time steps (Γ^a) in a storm event. Next, we convert p and p^a into the corresponding single time step thresholds for an operator threshold (ε) and an attacker threshold (ε^a) in Equation 5-16.

$$\begin{cases} \varepsilon = {\chi^2_{dof=n}}^{-1}\left(p^{1/T}\right), \\ \varepsilon^a = {\chi^2_{dof=n-n^a}}^{-1}\left((p^a)^{1/T^a}\right) \end{cases} \tag{5-16}$$

where T is the total control time steps, n is the number of sensors, T^a is the total attacking time steps, and n^a is the number of attacking sensors. Degree of freedom of a χ^2 distribution is denoted as dof. The difference between ε and ε^a is defined as an attackable range (Err^a [cm^2]). Figure 5-2 visualizes the concept of ε (yellow lines) and ε^a (blue lines) and indicates Err^a with different T^a (dt is equal to 1 minute in Figure 5-2). From the operator's viewpoint, if p is set too large, it gives attacker wider Err^a; however, if p is set too low, the operator might be overwhelmed by false alarms. From the attacker's viewpoint, if p^a is set too large, decreased Err^a might limit the goal which is to flood a pond; however, if p^a is set too low, there is a higher chance the attack will be detected and blocked. Being detected might also trigger the system upgrade against future attacks that an attacker wants to avoid.

5.2.2.2 Solving FDI with Optimization

To evaluate the compounding impacts of FDI given operation ($\mathcal{O}$) and attacking ($\mathcal{A}$) strategies, we solve the injected false data ($\boldsymbol{y_t^a}$ [cm]) by formulating the proposed mathematical framework into a deterministic mixed-integer quadratically-constrained programming (MIQCP) problem. We assume a stealthy attacker who only targets to flood

one pond (s_{target}) and is well-acknowledged about the stormwater system ($\mathcal{N}$) and the operation strategy ($\mathcal{O}$). Hence, the attacker's objective function in this MIQCP problem is:

$$Obj = Max\left\{\sum y^{sim}_{s_{\text{target}},t}\right\} \tag{5-17}$$

which is subjected to Equations 5-1 to 5-13 (except Equations 5-3 and 5-8), Equation 5-18, and Equation 5-19 with no sensor noises ($\boldsymbol{v_t} = 0$) as $E[\boldsymbol{v_t}] = 0$ and a perfect weather forecast ($\widetilde{\boldsymbol{w}}_{\boldsymbol{t}} = \boldsymbol{w_t}$).

$$\boldsymbol{z}_{\boldsymbol{t}}^{\mathrm{T}} \cdot \mathcal{G}^{-1} \cdot \boldsymbol{z_t} \leq Err^{a} \tag{5-18}$$

$$\boldsymbol{x}_{\mathbf{t_s}} = \widehat{\boldsymbol{x}}_{\mathbf{t_s}} = \boldsymbol{x}^{\boldsymbol{h}}_{\mathbf{t_s}}, \boldsymbol{u}_{\mathbf{t_s}} = \boldsymbol{u}^{\boldsymbol{h}}_{\mathbf{t_s}}, t \in \mathcal{T}^{\mathrm{a}} = \{t_s + 1, t_s + 2, \dots, t_s + T^{a}\} \tag{5-19}$$

We substitute the bad data detector (Equation 5-14) with Equation 5-18 since the only source of $\boldsymbol{z_t}$ is $\boldsymbol{y}^{\boldsymbol{a}}_{\boldsymbol{t}}$ in a deterministic setup. The adoption of Err^{a} is to ensure the successful FDI rate is at least p^{a} (i.e., rate of not being detected). Since we only need to solve $\boldsymbol{y}^{\boldsymbol{a}}_{\boldsymbol{t}}$ for the time steps having FDI, the initial values of this MIQCP problem (i.e., $\boldsymbol{x}_{\mathbf{t_s}}$, $\widehat{\boldsymbol{x}}_{\mathbf{t_s}}$, and $\boldsymbol{u}_{\mathbf{t_s}}$) are equal to the values in a healthy system at the time t_s (i.e., $\boldsymbol{x}^{\boldsymbol{h}}_{\mathbf{t_s}}$ and $\boldsymbol{u}^{\boldsymbol{h}}_{\mathbf{t_s}}$; Equation 5-19). We show a complete MIQCP problem in Appendix D.3.

5.2.2.3 Consequences of FDI

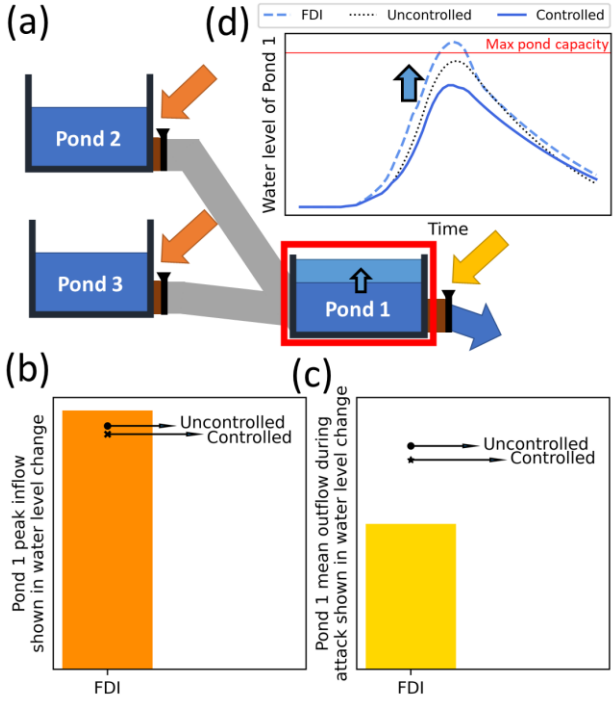

Figure 5-3. Disclosure of potential FDI consequences with Pond 1 as the flooding target. (a) A smart stormwater system with three ponds. (b) Water level impact of Pond 1 from enlarging inflow caused by FDI. (c) Water level impact of Pond 1 from reducing outflow caused by FDI. (d) The water level time series of Pond 1 under "uncontrolled," "controlled," and "FDI" scenarios.

Two potential FDI consequences are demonstrated in Figure 5-3 as a simple three-pond stormwater system where Pond 1 is under attack. The first type of FDI impact is the attacker can potentially aggregate the peak outflows of upstream ponds with peak runoffs to manually form a peak inflow of Pond 1 larger than the uncontrolled and controlled scenarios (Figure 5-3b). The second type of FDI impact is to attack the Pond 1 sensor and maliciously reduce its outflow, as shown in Figure 5-3c. Both attacking strategies can increase the water level in Pond 1. An attacker can also combine those two strategies, as shown in Figure 5-3d. Figure 5-3d indicates a higher water level peak with the FDI-to-all-sensors scenario compared to uncontrolled and controlled scenarios. Such water level rise

means a lower tolerance toward control errors from sensor noises and weather forecast uncertainties, resulting in higher flooding risk. In Figure 5-3d, the water level in the FDI scenario exceeds the maximum pond capacity, where Pond 1 is flooded.

5.2.3 Compounding Risk Quantification

In addition to the compounding impacts solving in a deterministic formulation (Section 2.2), we propose a method to quantify the compounding risks of flooding under Gaussian sensor white noises and weather forecast uncertainties in this section. Given a smart stormwater system ($\mathcal{N}$), the level of sensor noises ($\boldsymbol{\sigma_s}$), weather forecast uncertainty ($\boldsymbol{\sigma_w}$), an attacking strategy ($\mathcal{A}$), an operation strategy ($\mathcal{O}$) and $t \in \mathcal{T}^a$, the compounding risks can be quantified by Equation 5-20.

$$\underbrace{P_c(F_s)}_{P_c^s} = \underbrace{P(E)}_{P_E} \times \underbrace{P(\boldsymbol{z_t}^{\mathrm{T}} \cdot \mathcal{G}^{-1} \cdot \boldsymbol{z_t} \leq \varepsilon | \boldsymbol{y^a})}_{P_{FDI}} \times \underbrace{\left[1 - P\left(dy_{s,t}^f \leq \left(y_s^{max} - y_{s,t}^{sim,a}\right) | \boldsymbol{y^a}\right)\right]}_{P_W^s} \quad (5\text{-}20)$$

where $P_c^s = P_c(F_s)$ is the compounding risk of pond s getting flooded in $\mathcal{T}^a$, in which F_s is an indicator variable (value "1" if pond s is flooded). The occurrence probability of storm E is $P_E = P(E)$ (i.e., the return period). The successful FDI rate (i.e., not being detected) given $\boldsymbol{y^a}$ is $P_{FDI} = P(\boldsymbol{z_t}^{\mathrm{T}} \cdot \mathcal{G}^{-1} \cdot \boldsymbol{z_t} \leq \varepsilon | \boldsymbol{y^a})$. The injected false data ($\boldsymbol{y^a}$) is solved by optimization introduced in Section 2.2. $P_W^s = \left[1 - P\left(dy_{s,t}^f \leq \left(y_s^{max} - y_{s,t}^{sim,a}\right) | \boldsymbol{y^a}\right)\right]$ is the flooding probability of pond s under the water level control errors ($dy_{s,t}^f$ [cm]) caused by forecast errors given $\boldsymbol{y^a}$. The simulated water levels given $\boldsymbol{y^a}$ is denoted as $y_{s,t}^{sim,a}$, and y_s^{max} is the maximum depth of pond s. To evaluate those three terms, the storm occurrence probability (P_E) can be estimated from frequency analysis, such as a depth–duration–frequency (DDF) curve (Figure 5-4a). The successful FDI rate (P_{FDI}) is calculated by multiplying the blue area under the shifted

$\chi^2_{dof=n-n^a}$ distribution over every time step in $\mathcal{T}^a$ (Figure 5-4b), where the shift is equal to $Err_t = z_t^{\mathrm{T}} \cdot \mathcal{G}^{-1} \cdot z_t$ from Equation 5-14. The flooding probability under sensor noises and forecast uncertainties (P_W^S) is estimated by Monte Carlo simulations, in which 1000 realization sets of sensor noises and forecasted runoffs were generated to evaluate the water level variations given y^a. For example, even the water level under one single FDI experiment in a deterministic system (orange line in Figure 5-4c) does not overflow the pond, some realizations of sensor noises and forecast uncertainties might result in floods (some grey lines are over 100% pond's capacity in Figure 5-4c), where the brown dashed line references the water level in the controlled scenario. Then, P_W^S is computed by the number of flooded realizations to the total number of realizations. Finally, P_c^S is quantified by multiplying P_E, P_{FDI}, and P_W^S together.

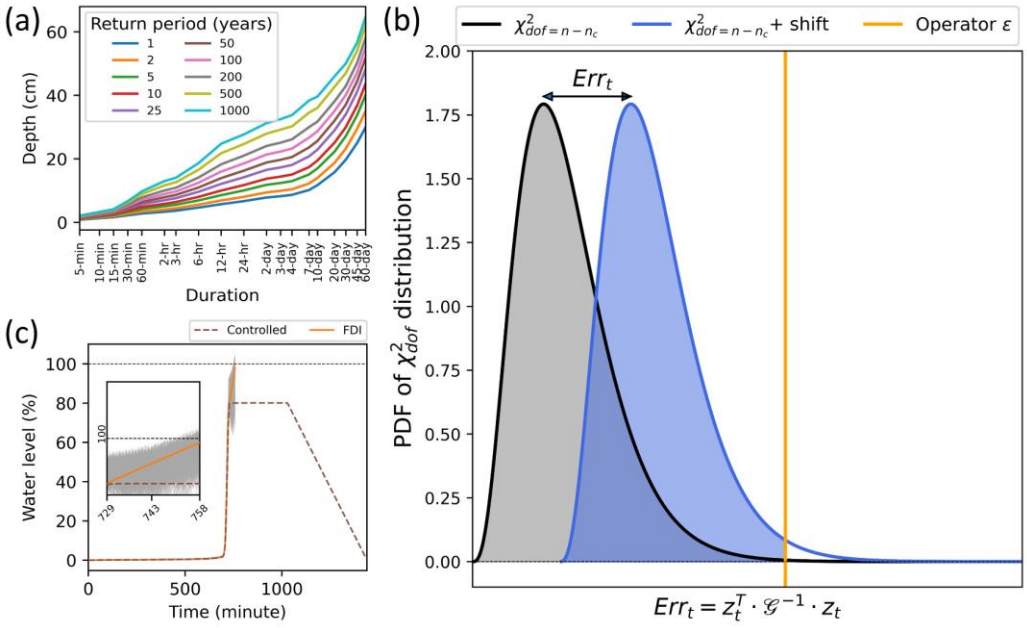

Figure 5-4. Probability estimation concepts for (a) P_E, (b) P_{FDI}, and (c) P_W^S, where P_E is estimated by DDF curve, P_{FDI} (blue area) is calculated from $\chi^2_{dof=n-n^a}$ distribution, and P_W^S is computed by Monte Carlo simulations over realizations of sensor noises and forecasted runoffs (grey lines).

5.3 Materials

5.3.1 Study Area

A designed stormwater system (Figure 5-5) with a nine-pond network layout referenced from a residential area in Bethlehem township, PA, US, is adopted in this chapter. The total basin area is 0.81 km^2. The ponds are radically connected to Pond 1 with circular conduits, where Pond 1 is the system outlet that outflows to Nancy Run Creek. We designed the stormwater system with US EPA's Storm Water Management Model (SWMM; Rossman, 2010) to have all pond outflows below 1.4 m^3/s under a 2-year-24-hour design storm (Figure D1) and all pond water levels below 85% of their storage capacities under 25-year-24-hour design storm (Figure D2) in a passive control scenario (i.e., uncontrolled) since

the designed system tend to reduce outflow peak while guaranteeing to accommodate 25-year-24-hour design storm without flooding. The synthetic design storms are based on the standard 24-hour NRCS type II rainfall distribution (NRCS, 2004) with a DDF curve from NOAA Atlas 14 Volume 2 Version 3 (Bonnin et al., 2004). This chapter only considers 24-hour storms. For simplicity, all storms mentioned in the content below are 24-hour designed storms. Without losing the generality, the ponds are set to be rectangular, in which the pond's surface area ($\boldsymbol{a_s}$) is a fixed value over depth. A square orifice is located at the bottom of each pond, and each pond has its invert elevation higher than the overflow heights of all downstream ponds to satisfy the gravity-driven outflow assumption (Equation 5-12). The detailed configurations of this design stormwater system, such as pond capacities, conduit lengths, orifice sizes, and invert elevations, are provided in Table D1. For a "smart" stormwater system, there are a water level sensor and an outflow gate actuator at each pond, communicating with a SCADA center.

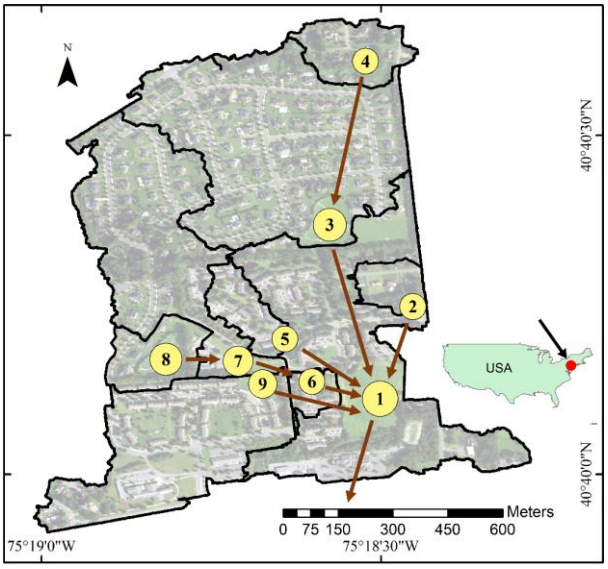

Figure 5-5. A designed stormwater system with the network layout referenced from a residential area in Bethlehem township, PA, US. Ponds' capacities are indicated by circle size in a log scale.

5.3.2 Numerical Experiment Setup

Our numerical experiment considers three scenarios: (1) uncontrolled, (2) controlled, and (3) FDI associated with the controlled system. We translate the pond-conduit network (Figure 5-5) into A, B_u, B_w, and C matrixes to establish a state-space model with discretized time step equal to 1-minute. First, for the uncontrolled scenario, we calibrate the number of segments (n_c) and gate coefficient ($\boldsymbol{c_g}$) with the SWMM-simulated data in the uncontrolled scenario, where pond outflows are governed by:

$$\boldsymbol{u_t} = \max(-\boldsymbol{u_t^{aw}}, -\boldsymbol{u_t^{uc}}) \tag{5-21}$$

For n_c, we search in [1, 4] from upstream to downstream to minimize the mean Root Mean Square Error (RMSE) of SWMM-simulated water levels under 2-year and 25-year storms ($RMSE_{n_c}$). Then, we manually tune $\boldsymbol{c_g}$ to minimize the mean RMSE of SWMM-simulated water levels and pond outflows under 2-year and 25-year storms ($RMSE_{C_g}$).

After that, we designed a simple control rule of desired water level ($\boldsymbol{r_t}$) for the controlled scenario, where the control philosophy is to detain runoffs in ponds by maintaining the water level at 80% pond capacity for five hours before decreasing. The control rule is visualized in Figure 5-6, where the two control time points $t_{5\%}$ and t_p are determined by the simulated water level in the uncontrolled scenario. The term $t_{5\%}$ is the time step that the simulated water level reaches 5% pond capacity and t_p is the time step when simulated water level reaches the peak. The idea is to gradually accumulate water to 80% of the pond's capacity during the water level rising period, defined as $t_{5\%}$ to t_p. This control rule is applied to Pond 2 to 9, but Pond 1 (system outlet) is designed to drain the water with the maximum physical capacity (Equation 5-21; i.e., desired water level is zero) for the safety issue. To achieve a better controlling result, R and Q in Equation 5-8 are

tuned to satisfy the control need (Appendix D.2). Note that searching for an optimal control rule is out of the scope of this chapter.

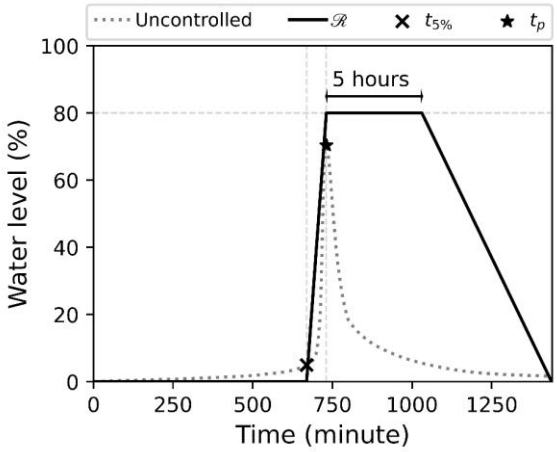

Figure 5-6. A control rule for desired water level ($\boldsymbol{r_t}$). $t_{5\%}$ (cross) and t_p (star) are two control time points determined by the simulated water level reaching 5% pond capacity and the peak under an uncontrolled scenario. The desired water level linearly increases from 0 to 80% pond capacity and maintains for five hours before decreasing.

Last, for FDI scenarios, we consider (1) attacking only the sensor at the targeted pond (FDI_S) and (2) attacking multiple sensors at the targeted pond and its upstream ponds (FDI_M) with different attacking lengths from 5 minutes to 60 minutes. The value for p and p^a in Equation 5-16 are set to be 0.95 and 0.99, respectively. We design the attack starting at t_p, in which each pond has a different attacking start time step. Also, to avoid solving a large-scale optimization problem and potential numerical issues, the MIQCP (Section 2.2.2) problem was sequentially solved every 5 minutes. For instance, the 60-minute-FDI problem is split into 12 subproblems.

For the Monte Carlo simulations (i.e., P_W^S estimation), we generate 1000 realizations of sensor noises and forecasted runoffs (i.e., $\{\boldsymbol{v_t}, \widetilde{\boldsymbol{w}}_{\boldsymbol{t}}; t \in \mathcal{T}\}$). We sampled sensor noises from

a Gaussian distribution with zero mean and standard deviation ($\boldsymbol{\sigma_s}$ [cm]) equal to 0.25 (MaxBotix MB7384, 2012) and synthesize forecasted runoffs through a multiplicative error model that is commonly used in radar forecast literature (Schleiss et al., 2020):

$$\boldsymbol{w_t} = \beta \times \widetilde{\boldsymbol{w}}_{\boldsymbol{t}} \times \boldsymbol{\varepsilon_w} \tag{5-22}$$

where β is set to 1 and $\boldsymbol{\varepsilon_w}$ is a vector of random numbers sampled from a lognormal distribution with a median of 1 and a standard deviation equal to 0.9 (Schleiss et al., 2020). Since we assume a time-invariant LQG control system (i.e., K, K_w and K_r are fixed constant over a storm event), the standard deviation of $\boldsymbol{\varepsilon_w}$ ($\boldsymbol{\sigma_w}$ [cm]) was estimated by averaging the standard deviation calculated at each time step for each pond. We simulate runoffs ($\boldsymbol{w_t}$) by the SWMM model with storms that have different return periods, i.e., 1, 2, 5, 10, 25, 50, 100, and 200 years.

5.4 Results

5.4.1 Water Levels under Uncontrolled, Controlled, and FDI scenarios

To evaluate compounding risks, the first step is to understand the impact of FDI given a design storm. We first calibrate the state-space model, where $RMSE_{n_c}$ and $RMSE_{C_g}$ are equal to 4.49 cm and 2.30 cm, respectively, to compare the water level dynamics in uncontrolled and controlled scenarios. Then, we calculate the water levels under FDI_S and FDI_M by solving MIQCP problems. Figure 5-7 shows the water level comparisons of uncontrolled (dotted blue line), controlled (dashed brown line), FDI_S (orange line), and FDI_M (green line) with 25-year storm and 30-minute attack. Each plot is one independent experiment showing a specific pond is under attack. The nested stem plots indicate relative maximum water level differences between controlled and two FDI scenarios of nine ponds in that experiment.

In the control scenario, we detain the water in the pond for 5 hours to reduce the peak outflow, where most ponds' peak outflows reduce (-0.006 to -0.218 m^3/s) except Pond 8 (+0.001 m^3/s). Among them, Pond 1 has the maximum reduction (-0.218 m^3/s). This reduction is also reflected in its lower water level in the controlled scenario (Figure 5-7). Since the desired water level of Pond 1 is set to zero, Pond 1 always has the maximum possible outflow; hence, a lower water level means a lower outflow. These results agree with previous smart stormwater system studies (Wong and Kerkez, 2018) that actively controlling a stormwater system is likely to enhance the utilization of existing infrastructures and accommodate larger storms with lower erosion impact at the downstream area (lower peak outflow).

However, the results of FDI_S show that it is possible to cause floods in a smart stormwater system through cyber-attack. In Figure 5-7, Ponds 2, 4, 5, and 6 are flooded (subtitle with *) if they are attacked. We test FDI_M scenario with the targeted pond, which has inflows from upstream ponds, namely Ponds 1, 3, 6, and 7. In Pond 1, FDI has a limited effect on reducing Pond 1's outflow gate opening. However, the water levels are slightly higher in FDI_M than FDI_S because of the larger inflows from upstream ponds (this is indicated by the lower peak water levels in the stem plot since water is released downstream). Such a phenomenon can also be observed in Pond 3, where the green dot is lower at Pond 3's upstream pond (i.e., Pond 4). In Ponds 6 and 7, their inflows are not vastly increased; however, water levels in FDI_M are higher than FDI_S. These are the results from the wider attackable range (Err^a) due to attacking multiple sensors (i.e., lower dof in χ^2 distribution; Equation 5-16). In Pond 8's stem plot, we found its downstream pond, Pond 7, has the largest increased peak water level. This is because contaminated Pond 8's

measurements also affect Pond 7's outflow control. In other words, Pond 7 is convinced that no large inflow from the upstream pond, hence, reduces its outflow. From Figure 5-7, we observed that the difference between FDI_M and FDI_S are mild (Section 2.2.3) in our case, thus, we only consider FDI_S for the following experiments.

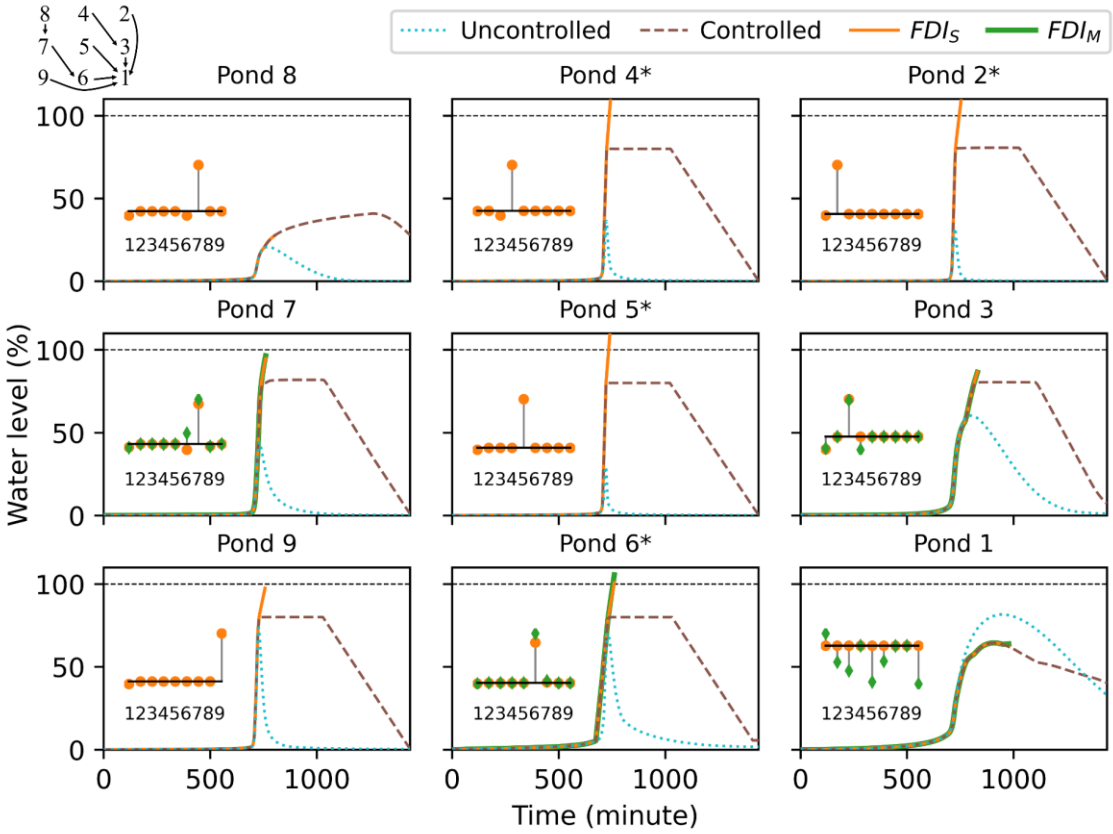

Figure 5-7. Water level comparisons of uncontrolled (dotted blue line), controlled (dashed brown line), FDI_S (orange line), and FDI_M (green line) with 25-year storm and 30-minute attack. The nested stem plots indicate relative maximum water level differences between controlled and two FDI scenarios of nine ponds. The star signs in the subtitle indicate the flooded ponds under FDI. The pond-conduit network is visualized in the upper left corner.

5.4.2 Flooding Risks under Sensor Noises, Forecast Uncertainties, and FDI

In this section, we further consider the impact of sensor noises and forecast uncertainties (i.e., $\{\boldsymbol{v}_t, \widetilde{\boldsymbol{w}}_t; t \in \mathcal{T}\}$) on flooding risks via Monte Carlo simulations. Figure 5-8 has a

similar layout as Figure 5-7; however, the nested plots are the magnified section for attacking periods, and the percentage of 1000 realizations (grey lines) that is flooded (P_W^S) is shown in the subtitle. In Ponds 4 and 6, all realizations have flood occur with or without sensor noises and forecast uncertainties. In Ponds 2 and 5, the percentage of floods is not 100% (P_W^2 = 93.3% and P_W^5 = 99.8%) compared to the deterministic scenario (Figure 5-7). A possible reason is that some realizations with overestimated runoff forecasts unintentionally neutralize the effect of FDI. While the results might look like sensor noises and forecast uncertainties reduce the flooding risk, over 90% flooding probability is still quite high. On the opposite side, the effect of sensor noises and forecast uncertainties can increase the flooding probability of Ponds 7 and 9 (P_W^7 = 1% and P_W^9 = 38.5%) compare to the deterministic scenario. In sum, when we consider the effect of sensor noises and forecast uncertainties, the overall flooding risks in our case study (i.e., the number of ponds being flooded) increase.

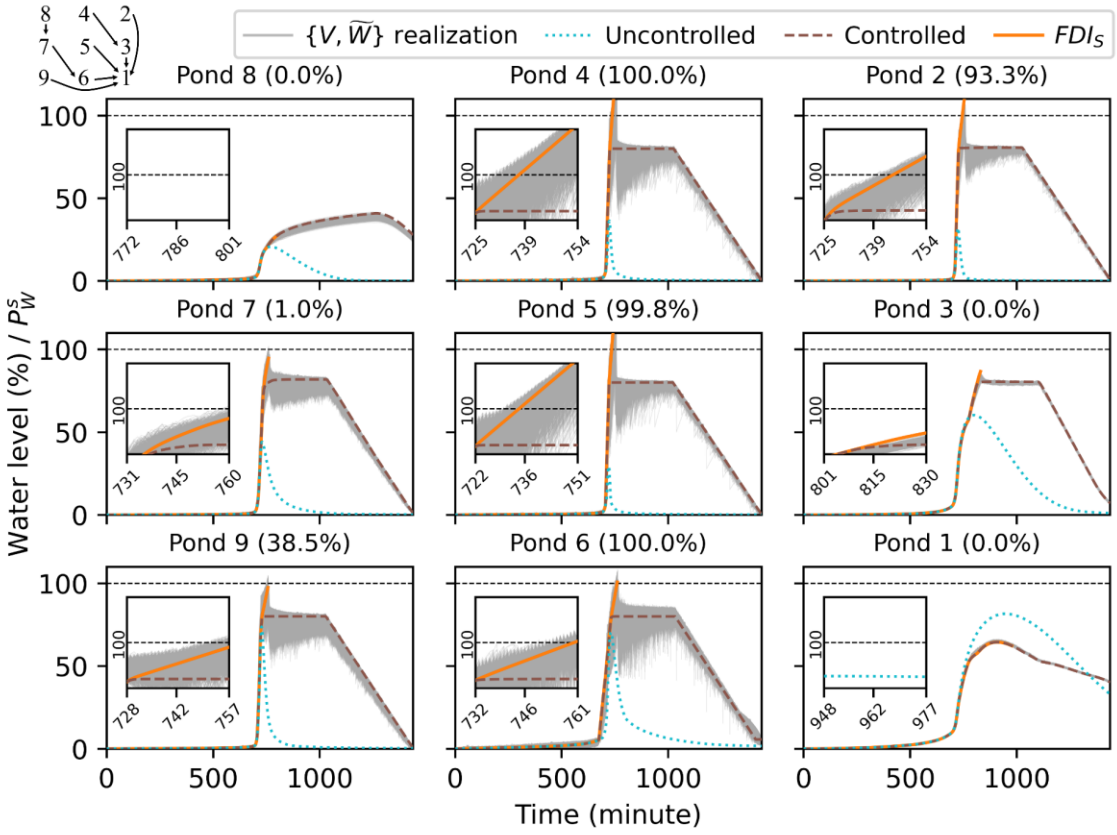

Figure 5-8. Water level variations under sensor noises and forecasted runoffs with a 25-year storm. Water levels in uncontrolled, controlled, and FDI_S scenarios are shown in dotted blue lines, dashed brown lines, and solid orange lines, respectively. Each plot is one independent experiment differing in attacking targets. The pond-conduit network is visualized in the upper left corner.

5.4.3 Compounding Flooding Risks

With the information from Figure 5-8, we can compute the compounding flooding risk using Equation 5-20. Take Pond 9 as an example, P_E is one over twenty-five (0.04) for the 25-year designed storm, The successful FDI rate (P_{FDI}) is equal to designed successful FDI rate ($p^a = 0.99$) in this particular case since the attacker use all attackable range at each attacking time step ($Err_t = Err^a$ for $t \in T^a$). Next, P_W^9 is 0.385 as we shown in the previous section. Finally, we can obtain the compounding risk $P_c^9 = 0.04 \times 0.99 \times 0.385 = 0.015$.

Following this qualification procedure, Figure 5-9 shows a heatmap of compounding risks over different consecutive attacking lengths (T^a) and return periods of design storms. Grey color indicates zero in compounding risk of flood, and each plot is one independent experiment differing in attacking targets of FDI_s scenario. Ponds 1, 3, and 8 have relatively low compounding risks. The compounding risks of Ponds 1 and 3 only occur with 100- and 200-year return period storms, implying the flooding risks are dominated by the natural factor (i.e., the intensity of storms). Pond 8 is the most upstream pond with large storage compared to its relatively small sub-catchments. As a result, FDI has a limited effect on increasing the water levels in these three ponds. On the contrary, the pattern of compounding risks is considerably influenced by FDI in other ponds. In general, compounding risks grow more prominent with longer attacking time (increasing T^a) and gradually decrease with increasing return periods due to the reducing P_E. Namely, compounding risks are higher with smaller storms. However, the highest compounding risk does not always appear in the lower right corner of each plot in our case. For example, Ponds 2 and 7 have the highest flooding risk in 2-year and 5-year return period storms, respectively. These point out different defending strategies' needs. For example, we can apply a lower desired water level for those high-compounding-risk storms to support larger control error tolerance, namely, the trade-off between control efficiency and error tolerance. Information like Figure 5-9 can assist in targeting system weak spots and identifying potential defending strategies (e.g., modify $\mathcal{O}$ and $\mathcal{N}$) to mitigate potential compounding impacts.

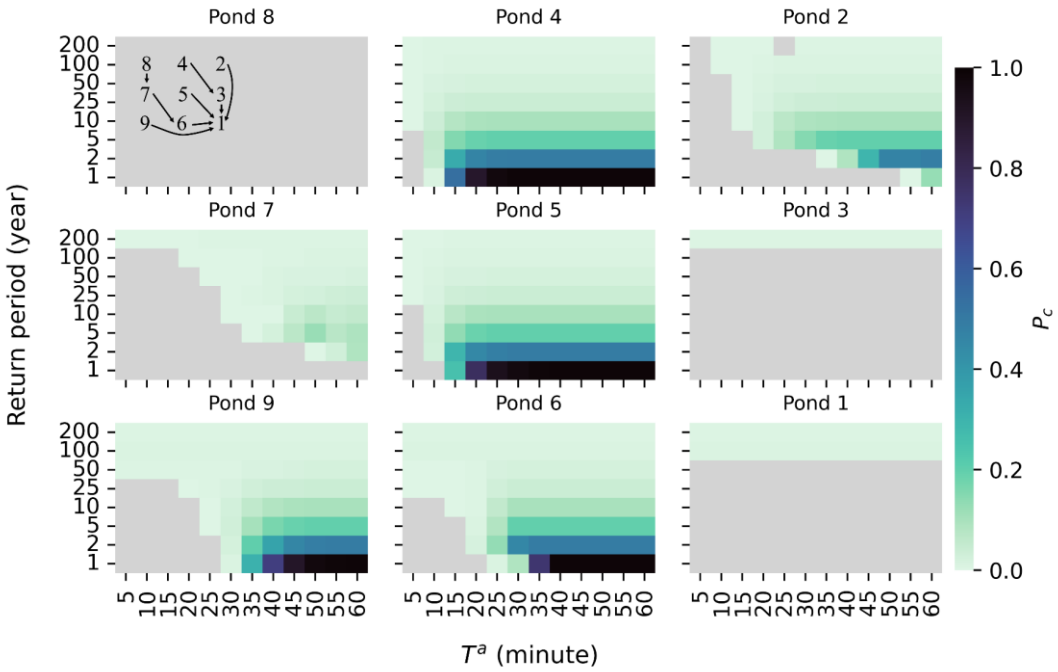

Figure 5-9. Heatmap of compounding flooding risks over different attacking lengths and return periods of 24-hour design storms. Grey color indicates zero in compounding risk of flooding. Each plot is one independent experiment differing in attacking targets of FDI_s scenario. The pond-conduit network is visualized inside the Pond 8 subplot.

5.5 Discussion

5.5.1 The Missing Piece of Compounding Risks Quantification

This chapter proposes a quantification method for evaluating compounding risks given a stormwater system ($\mathcal{N}$), level of sensor noises ($\boldsymbol{\sigma_s}$), weather forecast uncertainty ($\boldsymbol{\sigma_w}$), an attacking strategy ($\mathcal{A}$), and an operation strategy ($\mathcal{O}$). However, compounding risk (P_c) computed using Equation 5-20 is a conditional probability that conditions on a system is cyber-attacked (Depoy et al., 2005). While it is extremely difficult, if not impossible, to quantify the occurrence likelihood of a cyber-attack (P_O), we want to discuss how we can approach this missing piece. We can view this issue from two aspects: (1) to what degree the system is exposed to the public and (2) the potential motivations that attackers want to cyber-attack the system. In the first aspect, data accessibility or the cyber security level of

cyberinfrastructures may provide a qualitative way to describe P_O (Ezell et al., 2001). For example, suppose the water level measurements are easily accessible to the public. In that case, it is more likely for an attacker (assuming there is one) to learn how the system works and potentially increase the likelihood of implementing FDI. Similarly, suppose the cyber security level is low. In that case, e.g., the application programming interface to the cloud database or actuators are exposed, attackers may easily invade the system and steal data or directly control the outflow gates. The concept of privilege graph (Dacier and Deswarte, 1994) and attack graph (Lippmann and Ingols, 2005) can potentially help us identify intrusion pathways, and Hahn and Govindarasu (2011) further propose exposure graph to evaluate P_O. In the second aspect, we can conduct a motivation-based analysis (Ngafeeson, 2010) to identify the profit chain, in which we may estimate the likelihood of being cyber-attacked, given the assumption of rational attackers. However, the quantification of P_O would still be subjective to the system operator and often require confidential information to do such analysis. Therefore, we left this part for future studies and focused on the conditional compounding risks we could quantify objectively in this chapter.

5.5.2 Application in Network-based Systems

Despite the abovementioned missing piece (P_O), the proposed mathematical framework for compounding risk quantification can still provide useful information in identifying system vulnerable spots and assisting in defending strategy development. Identifying system-vulnerable spots in critical infrastructures under the threat of compounding risks becomes significant as more IoT technologies are used, and the consequences of system failure could be catastrophic (e.g., dam failure). The proposed compounding risk quantification method can be applied to network-based critical infrastructures, such as irrigation pump-canal

systems, multi-reservoir joint operation systems, and drinking water distribution systems. Systems can be represented by a state-space model similar to the stormwater drainage system presented in this chapter. For example, studies have successfully used a state-space model and LQG controller with the consideration of backwater effects (Conde et al., 2021) to operate the irrigation canal system (Amin et al., 2012; Amin et al., 2013; Durdu, 2010; Schuurmans, 1997), which allow a direct application of our proposed method. Multi-reservoir systems (Labadie, 2004) are also shown to be modeled and operated by a state-space model and LQG controller in the topic of optimal flood control (Wasimi and Kitanidis, 1983) and hydropower scheduling (Georgakakos, 1989). Lastly, Ahmed et al. (2017) adopted a state-space model and Kalman filter in a water distribution network to evaluate attack detection schemes, which led to the potential adoption of our compounding risk quantification method with the modification of bad data detectors in future work.

5.5.3 Limitations

The proposed compounding risks quantification method is currently limited to χ^2 detector when computing P_{FDI}. However, it could adapt to other detectors with different probability distributions, where the general concept remains the same. For our demonstration case of a smart stormwater system, we adopt a simple time-invariant linear control system (i.e., LQG), where L, K, K_r, and K_w are constant given a storm and rely on predefined desired water levels ($\boldsymbol{r_t}$). Such assumptions might not be sufficient for the real-world control system, where the time-variant L, K, K_r, and K_w and a more flexible $\boldsymbol{r_t}$ should be considered in a LQG controller. Despite these limitations, they will not affect the compounding risks quantification concept shown in this chapter. However, future works are required to test how the results of compounding risks evaluation are influenced by time-

variant settings. Finally, this chapter only considers a binary flooding risk. We recommend future works include the flooding quantity or depth, which may estimate potential property damages of compounding impacts.

5.6 Conclusions

With growing IoT-based infrastructures being applied to water systems, cyber risks are also introduced. However, the compounding risks involving natural hazards and cyber-attacks have not yet been well-explored. The need for a method to identify vulnerable spots in the system under the threat of compounding risks emerges. This chapter proposed a mathematical framework to address this gap. We implemented the proposed method in a nine-pond smart stormwater system, consisting of water level sensors and outflow gate actuators, on an urban flooding issue. The stormwater dynamics are represented by a state-space model, and the outflows of ponds are controlled by a LQG controller in real-time. We evaluate the compounding impacts of storms and FDI and quantify the compounding risks with combinations of different storm intensities and attacking lengths.

Our results demonstrate the potential consequences of FDI, such as creating a large inflow peak or maliciously reducing the outflow to intensify the flooding risks. We also show that the flooding risk patterns of different storm intensities are significantly changed by FDI, which indicates the merit of the compounding risks in future system planning and investment. The proposed mathematical framework can serve as a foundation to evaluate the effectiveness of different defending strategies over potential attacking strategies for future studies. While some limitations still exist (e.g., the occurrence likelihood of a cyber-attack, χ^2 detector, and time-invariant LQG controller), the proposed method can be used

in other network-based water systems, such as irrigation canal systems, multi-reservoir systems, and water distribution systems.

Chapter 6: Conclusions

This dissertation advances the knowledge of co-evolution in CAWS from the aspects of (1) investigating the co-evolution of farmers' water diversion decisions in response to environmental changes and the role of social norm structure through two-way coupling RiverWare and ABM, (2) developing open-source python package of a semi-distributed hydrological model that can freely integrate user-defined ABM for CAWS modeling, (3) implementing uncertainty analysis to quantify the effects of model complexity on model output uncertainty (i.e., equifinality) in coupled hydrological and ABM models, and (4) analyzing compounding risks of storms and cyber-physical attacks that could potentially impact people's short-term responses. We conclude the previous chapters with their major findings in the following paragraphs with respect to the four aspects listed above.

6.1 Research Findings

Chapter 2 explores the co-evolution in CAWS through a case study in the Yakima River Basin, Northwest US. Three numerical experiments were designed. First, we demonstrate that coupled models (e.g., Coupled-YAKRW and Coupled-YAKRW w/o S.) can better capture both irrigation diversion (human behaviors) and streamflow dynamic (nature system) compared to the baseline model (i.e., YAKRW), which is used for policymaking in the real world. Second, we analyzed the role of the social norm effect through a local sensitivity analysis. Although similar simulation results were found between coupled models with or without social norm effect, the evidence is insufficient to draw a conclusion due to the dominant RiverWare policy rules and the model equifinality issue (see Chapter 4). Lastly, we show farmers' diversion behaviors and risk attitudes could be affected by the changing policy rules. In this case study, agents become more sensitive (i.e., risk-averse)

to the changing environment under the all-proratable-water-rights scenario. The findings and cross-scale nature of the two-way coupling technique could benefit policymaking for future multi-level water resources governance applications, which often require cross-scale analysis.

Chapter 3 develops a semi-distributed Hydrological model for Coupled Natural–Human Systems, HydroCNHS, an open-source Python package, and demonstrates its functionalities through a case study in the Tualatin River Basin, Northwest US. We integrate a trans-basin aqueduct, a reservoir, an irrigation diversion, and two drainage system agents accounting for runoff changes with four coupling APIs linked to two different rainfall-runoff models, GWLF and ABCD. The designed APIs handle within-subbasin and inter-subbasin routings internally in HydroCNHS. Similar to Chapter 2, we show that coupled models could capture monthly streamflow, irrigation diversion, and reservoir release patterns. Results further indicate the model with endogenous diversion behavioral rule better reflects the interaction between natural and human systems. In addition, the results of the runoff-changing scenario show the capability of HydroCNHS in modeling the effects of gradual environmental changes on streamflow. With coding language integrity, flexibility in designing agents, and parallel computing ability, the HydroCNHS can facilitate uncertainty analysis in CAWS, leading to Chapter 4.

Chapter 4 targets a challenging task of uncertainty analysis in CAWS using the same study area as Chapter 2, the Yakima River Basin in Northwest US, where irrigation districts are defined as agents. We quantify and then decompose the uncertainty of a semi-distributed hydrological model coupled with an agent-based water diversion model into three sources by the law of total variance: (a) climate scenario uncertainty, (b) climate

internal variability, and (c) model configuration uncertainty. Five coupled models with different water diversion agent types are tested in the numerical experiments: (a) a static model, (b) an adaptive model with linear functions, (c) an adaptive model with quadratic functions, (d) a learning adaptive model with linear functions, and (e) a learning adaptive model with quadratic functions. Results accept our hypotheses—(i) model uncertainty in an exploratory analysis will likely increase with model complexity, given uncertain input data (e.g., climate forcing) and different model configurations, and (ii) the inclusion of a learning mechanism in a human system can potentially offset the impact of natural system's variability on output uncertainty. Co-evolution plays a major role in shaping the relationship between model output uncertainty and model complexity. For example, the learning adaptive models show a decreasing trend in the natural system output because agents learn and adapt to environmental changes, where the learnability and adaptability are revealed by increased variability of the human system outputs. Despite the smaller natural system output uncertainty in the learning adaptive models, we suggest the modeler should be aware of the assumptions of model structure, such as the appropriateness of learning assumptions in the exploratory analysis of a given case study.

Chapter 5 shifts the perspective from long-term planning to short-term responses, in which we argue that the newly introduced cyber-physical risks could change the flooding risks in a smart stormwater system and potentially alter long-term co-evolution patterns. Chapter 5 serves as the initial step of this argument. We apply a mathematical framework to quantify compounding risks of storms and FDI in a nine-pond smart stormwater system, consisting of water level sensors and outflow gate actuators, on an urban flooding issue. The stormwater dynamics are represented by a state-space model, and the ponds' outflows

are controlled by a LQG controller in real-time. The numerical experiments evaluate the compounding impacts of storms and FDI and quantify the compounding risks with different storm intensities and attacking lengths. Results show that false data injection (FDI) attacks can successfully inject false data into the control system without being detected, leading to additional flooding risks. We found that the flooding risk patterns of different storm intensities are significantly altered by FDI, where compounding risks tend to be higher with smaller, more frequent storms. Such results indicate the merit of the compounding risk concept.

6.2 Limitations and Future Research

This dissertation explores the co-evolution in CAWS through a numerical modeling approach. For long-term planning, we investigate the social norm effect, develop a semi-distributed hydrological model that can integrate human systems, and conduct an uncertainty analysis to gain insights into the trade-offs between model complexity and model output uncertainty. For short-term responses, we quantify the compounding risks of storms and human interventions (i.e., FDI) in a smart stormwater system to initiate the conversation on the potential human responses or defending strategies to address the additional flooding risks from cyber-physical attacks. However, future work is needed to evaluate assumptions and overcome the limitations of our work. We discuss limitations and point out future research directions in the following paragraphs.

Chapter 2 adopts a two-way coupling technique to couple ABM with RiverWare. Although using the existing YAKRW model developed by USBR can leverage its credibility, some RiverWare-embedded policies like water rights and drought operations may dominate the coupled models' modeling results, affecting the experiment's efficiency

in exploring the human system, such as the social norm effect. However, we are not suggesting not to couple YAKRW since those dominant policies may be enforced in the real world due to legal issues constraining people's behaviors. The water reallocation scenario experiment indicates that the changing water allocation policy can shift people's risk attitudes toward risk-averse. We suggest future studies incorporate water banking or water market mechanisms into the ABM and re-test the water reallocation scenario to see how people behave with the additional trading option.

Chapter 3 targets open-source software for CAWS modeling. The developed HydroCNHS are able to couple with more diverse (e.g., hydropower plants and cooling plants) and more complex (e.g., interactions among agents and hydrological environment) agent designs with the given coupling APIs in future studies. However, it requires a certain level of coding experience in programming ABM. We can further add a more user-friendly interface and default agent types into highly modularized and well-documented HydroCNHS as a plug-in to benefit broader communities, even for people without coding experience. Also, additional hydrological components like sediment routing, nutrients simulation, and groundwater transportation can be further developed to enrich the functionality of the current HydroCNHS version that focuses on just water balance computing.

Chapter 4 investigates components of the modeling output uncertainty in response to different agent-type complexities in CAWS modeling. In the numerical experiment design, we follow the conventional calibration and validation procedure (i.e., splitting a time series into two portions) that relies on the stationary assumption. Also, we assume agents' adaptability and learnability remain the same as in the historical period. These

limitations will need further effort to address as the world is non-stationary, and human behavioral characteristics (e.g., adaptability and learnability) could change. Combining empirical social data (e.g., surveys and behavioral experiments) may provide evidence to support model design to include the vicissitude of hyperparameters. In addition, this chapter focuses on uncertainty sources of climate change scenarios, internal climate variability, and equifinality. We suggest analyzing additional uncertainty sources, such as indicator selection, model resolution level, and coupling structure with a more sophisticated agent setup and scale-up experiments in future work.

Chapter 5 gives the initial step of quantifying the compounding risks of storms and cyber-physical attacks to discuss potential human responses and defending strategies for long-term flood planning and smart stormwater system design. The proposed quantification method is limited to χ^2 bad data detector. However, this can be addressed by adopting other detectors, in which the probability distribution of errors is available. As an initial study of this topic, we apply to a simple time-invariant linear control system (i.e., parameters in the LQG controller are fixed), where the time-variant parameters (e.g., L, K, K_r, and K_w) should be considered in future work. Also, the control targets (i.e., desired water levels) are predefined for each design storm. Future studies may design real-time-generated control targets by using, e.g., machine learning to analyze the compounding risks with actual precipitation data. Also, we recommend future works include the flooding quantity or depth in addition to a binary flooding risk. This may benefit estimating potential property damages of compounding impacts.

Lastly, this dissertation contributes to several aspects of CAWS modeling to understand the co-evolution between nature and human systems. The relationship between

long-term planning and short-term responses has not yet been thoroughly investigated. They are partially explored from different angles in this dissertation. A more high-level framework and assessment across a wide variety of application topics like water quality management, disaster risk reduction, water resources allocation, and goods/water trading markets may assist in identifying general rules governing co-evolution and risk propagations that further complete the picture of this dissertation.

Reference

1. Abebe, Y.A., Ghorbani, A., Nikolic, I., Manojlovic, N., Gruhn, A., Vojinovic, Z., (2020). The role of household adaptation measures in reducing vulnerability to flooding: a coupled agent-based and flood modelling approach. *Hydrology and Earth System Sciences*, *24*(11), 5329–5354.
2. Abudu, S., Sheng, Z., Sabzi, H.Z., King, J.P., (2018). Drought scenario analysis using RiverWare: a case study in urumqi River Basin, China. *Civil Engineering Journal*, *4*(8), 1837–1850.
3. Aburto, M. O., de los Angeles Carvajal, M., Barr, B., Barbier, E. B., Boesch, D. F., Boyd, J., et al. (2012). Ecosystem-based management for the oceans. Island Press.
4. Adamo, N., Al-Ansari, N., Sissakian, V., Laue, J., & Knutsson, S. (2021). Dam Safety: Hazards Created by Human Failings and Actions. *Journal of Earth Sciences and Geotechnical Engineering*, *11*(1), 65-107.
5. Ahmed, C. M., Murguia, C., & Ruths, J. (2017). Model-based attack detection scheme for smart water distribution networks. *In Proceedings of the 2017 ACM on Asia Conference on Computer and Communications Security* (pp. 101-113).
6. Ajzen, I., (1991). The theory of planned behavior. *Organizational behavior and human decision processes*, *50*(2), 179–211.
7. Al-Amin, S., Berglund, E.Z., Mahinthakumar, G., Larson, K.L., (2018). Assessing the effects of water restrictions on socio-hydrologic resilience for shared groundwater systems. *Journal of Hydrology*, *566*, 872–885.
8. Allen, C. R., & Gunderson, L. H. (2011). Pathology and failure in the design and implementation of adaptive management. *Journal of Environ-mental Management*, *92*(5), 1379–1384. https://doi.org/10.1016/j.jenvman.2010.10.063
9. Allison, A. E., Dickson, M. E., Fisher, K. T., & Thrush, S. F. (2018). Dilemmas of modelling and decision-making in environmental research. *Environmental Modelling & Software*, *99*, 147–155. https://doi.org/10.1016/j.envsoft.2017.09.015
10. Amin, S., Litrico, X., Sastry, S., & Bayen, A. M. (2012). Cyber security of water SCADA systems—Part I: Analysis and experimentation of stealthy deception attacks. *IEEE Transactions on Control Systems Technology*, *21*(5), 1963-1970.
11. Amin, S., Litrico, X., Sastry, S. S., & Bayen, A. M. (2013). Cyber security of water SCADA systems—Part II: Attack detection using enhanced hydrodynamic models. *IEEE Transactions on Control Systems Technology*, *21*(5), 1679-1693.
12. An, L., (2012). Modeling human decisions in coupled human and natural systems: review of agent-based models. *Ecological Modelling*, *229*, 25–36.
13. Arendt, P. D., Apley, D. W., & Chen, W. (2012). Quantification of model uncertainty: Calibration, model discrepancy, and identifiability. *Journal of Mechanical Design*, *134*(10), 100908. https://doi.org/10.1115/1.4007390
14. Arsenault, R., & Brissette, F. P. (2014). Continuous streamflow prediction in ungauged basins: The effects of equifinality and parameter set selection on uncertainty in regionalization approaches. *Water Resources Research*, *50*(7), 6135–6153. https://doi.org/10.1002/2013wr014898
15. Axelrod, R., Tesfatsion, L., (2006). Appendix AA guide for newcomers to agent-based modeling in the social sciences. *Handbook of computational economics*, *2*, 1647–1659.

16. Baba, S., Yudu, S., & Nurlelah, S. (2021). The effect of subjective norm on farmer behaviour in utilizing rice straw as feed in Barru district. In *IOP Conference Series: Earth and Environmental Science (Vol. 788, No. 1, p. 012160)*. IOP Publishing.
17. Bartos, M., Wong, B., & Kerkez, B. (2018). Open storm: a complete framework for sensing and control of urban watersheds. *Environmental Science: Water Research & Technology*, *4*(3), 346-358.
18. Basheer, M., Wheeler, K.G., Elagib, N.A., Etichia, M., Zagona, E.A., Abdo, G.M., Harou, J. J., (2020). Filling Africa's largest hydropower dam should consider engineering realities. *One Earth*, *3*(3), 277–281.
19. Bauch, C. T., Sigdel, R., Pharaon, J., & Anand, M. (2016). Early warning signals of regime shifts in coupled human-environment systems. *Proceedings of the National Academy of Sciences of the United States of America*, *113*(51), 14560–14567. https://doi.org/10.1073/pnas.1604978113
20. Berglund, E. Z. (2015). Using agent-based modeling for water resources planning and management. *Journal of Water Resources Planning and Management*, *141*(11), 04015025. https://doi.org/10.1061/(asce)wr.1943-5452.0000544
21. Bevacqua, E., De Michele, C., Manning, C., Couasnon, A., Ribeiro, A. F., Ramos, A. M., ... & Zscheischler, J. (2021). Guidelines for studying diverse types of compound weather and climate events. *Earth's Future*, *9*(11), e2021EF002340.
22. Beven, K. (1993). Prophecy, reality and uncertainty in distributed hydrological modelling. *Advances in Water Resources*, *16*(1), 41–51. https://doi.org/10.1016/0309-1708(93)90028-E
23. Beven, K., (2006). A manifesto for the equifinality thesis. *Journal of Hydrology*, *320*(1–2), 18–36.
24. Beven, K. (2016). Facets of uncertainty: Epistemic uncertainty, non-stationarity, likelihood, hypothesis testing, and communication. *Hydrological Sciences Journal*, *61*(9), 1652–1665. https://doi.org/10.1080/02626667.2015.1031761
25. Beven, K., & Binley, A. (1992). The future of distributed models: Model calibration and uncertainty prediction. *Hydrological Processes*, *6*(3), 279–298. https://doi.org/10.1002/hyp.3360060305
26. Bholowalia, P., & Kumar, A. (2014). EBK-means: A clustering technique based on elbow method and k-means in WSN. *International Journal of Computer Applications*, *105*(9).
27. Blair, P., & Buytaert, W. (2016). Socio-hydrological modelling: A review asking "why, what and how?" *Hydrology and Earth System Sciences*, *20*(1), 443–478. https://doi.org/10.5194/hess-20-443-2016
28. Bonn, B. (2020) Tualatin River Flow Management Technical Committee 2020 Annual Report.
29. Bonnin, G. M., Martin, D., Lin, B., Parzybok, T., Yekta, M., & Riley, D. (2004). Precipitation-Frequency Atlas of the United States. Volume 2 Version 3.0. Delaware, District of Columbia, Illinois, Indiana, Kentucky, Maryland, New Jersey, North Carolina, Ohio, Pennsylvania, South Carolina, Tennessee, Virginia, West Virginia.
30. Bicchieri, C., & Muldoon, R. (2014). Social norms. In E. N. Zalta (Ed.), The Stanford encyclopedia of philosophy. Retrieved from http://plato.stanford.edu/archives/spr2014/entries/social-norms/

31. Biddle, S.H., (2001). Optimizing the TVA reservoir system using RiverWare. In: *Bridging the Gap: Meeting the World's Water and Environmental Resources Challenges*, pp. 1–6.
32. Bollinger, L.A., Davis, C.B., Evins, R., Chappin, E.J.L., Nikolic, I., (2018). Multi-model ecologies for shaping future energy systems: design patterns and development paths. *Renewable and Sustainable Energy Reviews*, *82*, 3441–3451.
33. Brenner, T., (2006). Chapter 18 agent learning representation: advice on modelling economic learning. In: Tesfatsion, L., Judd, K.L. (Eds.), Handbook of Computational Economics, vol. 2. Elsevier, pp. 895–947.
34. Brown, D.G., Page, S.E., Riolo, R., Rand, W., (2004). Agent-based and analytical modeling to evaluate the effectiveness of greenbelts. *Environmental Modelling & Software*, *19*(12), 1097–1109.
35. Brown, C. M., Ghile, Y., Laverty, M., & Li, K. (2012). Decision scaling: Linking bottom-up vulnerability analysis with climate projections in the water sector. *Water Resources Research*, *48*(9). https://doi.org/10.1029/2011wr011212
36. Brown, C. M., Lund, J. R., Cai, X., Reed, P. M., Zagona, E. A., Ostfeld, A., et al. (2015). The future of water resources systems analysis: Toward a scientific framework for sustainable water management. *Water Resources Research*, *51*(8), 6110–6124. https://doi.org/10.1002/2015WR017114
37. Bureau, U.S., (2020). Federal Columbia river power system hydrosystem. https://www.usbr.gov/pn/fcrps/hydro/index.html. (Accessed 17 October 2021).
38. Burian, S. J., & Edwards, F. G. (2002). Historical perspectives of urban drainage. *Global Solutions for Urban Drainage*, pp. 1-16.
39. Campbell, H.E., Johnson, R.M., Larson, E.H., (2004). Prices, devices, people, or rules: the relative effectiveness of policy instruments in water conservation 1. *Review of policy research*, *21*(5), 637–662.
40. Cash, D.W., Adger, W.N., Berkes, F., Garden, P., Lebel, L., Olsson, P., et al., (2006). Scale and cross-scale dynamics: governance and information in a multilevel world. *Ecology and society*, *11*(2).
41. Castilla-Rho, J.C., Mariethoz, G., Rojas, R., Andersen, M.S., Kelly, B.F., (2015). An agent-based platform for simulating complex human–aquifer interactions in managed groundwater systems. *Environmental Modelling & Software*, *73*, 305–323.
42. Castilla-Rho, J.C., Rojas, R., Andersen, M.S., Holley, C., Mariethoz, G., (2017). Social tipping points in global groundwater management. *Nature Human Behaviour*, *1*(9), 640–649.
43. Cedeno-Mieles, V., Hu, Z., Ren, Y., Deng, X., Adiga, A., Barrett, C., et al., (2020). Networked experiments and modeling for producing collective identity in a group of human subjects using an iterative abduction framework. *Social Network Analysis and Mining*, *10*(1), 1–43.
44. Chen, X., Lupi, F., An, L., Sheely, R., Vina, A., Liu, J., (2012). Agent-based modeling of the effects of social norms on enrollment in payments for ecosystem services. *Ecological modelling*, *229*, 16–24.
45. Conde, G., Quijano, N., & Ocampo-Martinez, C. (2021). Modeling and control in open-channel irrigation systems: A review. *Annual Reviews in Control*, *51*, 153-171.

46. Dacier, M., & Deswarte, Y. (1994). Privilege graph: an extension to the typed access matrix model. In European Symposium on Research in Computer Security (pp. 319-334). Springer, Berlin, Heidelberg.
47. Dahmann, J.S., Fujimoto, R.M., Weatherly, R.M., (1997). The department of defense high level architecture. In: *Proceedings of the 29th Conference on Winter Simulation*, pp. 142–149.
48. David, O., Ascough II, J.C., Lloyd, W., Green, T.R., Rojas, K.W., Leavesley, G.H., Ahuja, L. R., (2013). A software engineering perspective on environmental modeling framework design: the Object Modeling System. *Environmental Modelling & Software*, *39*, 201–213.
49. DePoy, J., Phelan, J., Sholander, P., Smith, B. J., Varnado, G. B., Wyss, G. D., ... & Walter, A. (2006). Critical infrastructure systems of systems assessment methodology. Sandia report.
50. Depoy, J., Phelan, J., Sholander, P., Smith, B., Varnado, G. B., & Wyss, G. (2005). Risk assessment for physical and cyber attacks on critical infrastructures. In MILCOM 2005-2005 IEEE Military Communications Conference (pp. 1961-1969). IEEE.
51. De Rainville, F. M., Fortin, F. A., Gardner, M. A., Parizeau, M., & Gagné, C. (2012). Deap: A python framework for evolutionary algorithms. In *Proceedings of the 14th annual conference companion on Genetic and evolutionary computation* (pp. 85-92).
52. Di Baldassarre, G., Brandimarte, L., & Beven, K. (2016). The seventh facet of uncertainty: Wrong assumptions, unknowns and surprises in the dynamics of human–water systems. *Hydrological Sciences Journal*, *61*(9), 1748–1758. https://doi.org/10.1080/02626667.2015.1091460
53. Dieu, B. (2001). Application of the SCADA system in wastewater treatment plants. *ISA transactions*, *40*(3), 267-281.
54. Di Gregorio, M., Fatorelli, L., Paavola, J., Locatelli, B., Pramova, E., Nurrochmat, D.R., et al., (2019). Multi-level governance and power in climate change policy networks. *Global Environmental Change*, *54*, 64–77.
55. Du, E., Cai, X., Wu, F., Foster, T., Zheng, C., (2021). Exploring the impacts of the inequality of water permit allocation and farmers' behaviors on the performance of an agricultural water market. *Journal of Hydrology*, *599*, 126303.
56. Durdu, Ö. F. (2010). Fuzzy logic adaptive Kalman filtering in the control of irrigation canals. *International journal for numerical methods in fluids*, *64*(2), 187-208.
57. Ekblad, L., & Herman, J. D. (2021). Toward data-driven generation and evaluation of model structure for integrated representations of human behavior in water resources systems. *Water Resources Research*, *57*(2), e2020WR028148. https://doi.org/10.1029/2020wr028148
58. Elsawah, S., Filatova, T., Jakeman, A. J., Kettner, A. J., Zellner, M. L., Athanasiadis, I. N., et al. (2020). Eight grand challenges in socio-environ-mental systems modeling. *Socio-Environmental Systems Modelling*, *2*, 16226. https://doi.org/10.18174/sesmo.2020a16226
59. Elshafei, Y., Sivapalan, M., Tonts, M., & Hipsey, M. R. (2014). A prototype framework for models of socio-hydrology: Identification of key feedback loops and parameterisation approach. *Hydrology and Earth System Sciences*, *18*(6), 2141–2166. https://doi.org/10.5194/hess-18-2141-2014

60. Epstein, J.M., (2012). Generative Social Science: Studies in Agent-Based Computational Modeling, second ed. Princeton University Press.
61. Everitt, J., (2020). Weber Basin Water Conservancy District Bottom-Up Climate Vulnerability Study Using RiverWare.
62. Ezell, B. C., Haimes, Y. Y., & Lambert, J. H. (2001). Risks of cyber attack to water utility supervisory control and data acquisition systems. *Military Operations Research*, 23-33.
63. Faust, K. M., Abraham, D. M., & DeLaurentis, D. (2017). Coupled human and water infrastructure systems sector interdependencies: Framework evaluating the impact of cities experiencing urban decline. *Journal of Water Resources Planning and Management*, *143*(8), 04017043.
64. Feinerman, E., Tsur, Y., (2014). Perennial crops under stochastic water supply. *Agricultural economics*, *45*(6), 757–766.
65. Fielding, K.S., Russell, S., Spinks, A., Mankad, A., (2012). Determinants of household water conservation: the role of demographic, infrastructure, behavior, and psychosocial variables. *Water Resources Research*, *48*(10).
66. Fleischmann, A., Paiva, R., & Collischonn, W. (2019). Can regional to continental river hydrodynamic models be locally relevant? A cross-scale comparison. *Journal of Hydrology*, *3*, 100027. https://doi.org/10.1016/j.hydroa.2019.100027
67. Fletcher, T. D., Shuster, W., Hunt, W. F., Ashley, R., Butler, D., Arthur, S., ... & Viklander, M. (2015). SUDS, LID, BMPs, WSUD and more–The evolution and application of terminology surrounding urban drainage. *Urban water journal*, *12*(7), 525-542.
68. Fortin, F. A., De Rainville, F. M., Gardner, M. A. G., Parizeau, M., & Gagné, C. (2012). DEAP: Evolutionary algorithms made easy. *Journal of Machine Learning Research*, *13*(1), 2171–2175.
69. Froise, S., & Burges, S. J. (1978). Least-cost design of urban-drainage networks. *Journal of the Water Resources Planning and Management Division*, *104*(1), 75-92.
70. Gaborit, E., Muschalla, D., Vallet, B., Vanrolleghem, P. A., & Anctil, F. (2013). Improving the performance of stormwater detention basins by real-time control using rainfall forecasts. *Urban water journal*, *10*(4), 230-246.
71. Gelfand, M.J., Harrington, J.R., Jackson, J.C., (2017). The strength of social norms across human groups. *Perspectives on Psychological Science*, *12*(5), 800–809.
72. Georgakakos, A. P. (1989). Extended linear quadratic Gaussian control: Further extensions. *Water Resources Research*, *25*(2), 191-201.
73. Giordano, M., & Shah, T. (2014). From IWRM back to integrated water resources management. *International Journal of Water Resources Development*, *30*(3), 364–376. https://doi.org/10.1080/07900627.2013.851521
74. Giuliani, M., Li, Y., Castelletti, A., & Gandolfi, C. (2016). A coupled human-natural systems analysis of irrigated agriculture under changing climate. *Water Resources Research*, *52*(9), 6928–6947. https://doi.org/10.1002/2016WR019363
75. Givens, J.E., Padowski, J., Guzman, C.D., Malek, K., Witinok-Huber, R., Cosens, B., et al., (2018). Incorporating social system dynamics in the Columbia River basin: food-energy-water resilience and sustainability modeling in the Yakima River basin. *Frontiers in Environmental Science*, *6*, 104.

76. Gomes, C., Thule, C., Broman, D., Larsen, P.G., Vangheluwe, H., (2018). Co-simulation: a survey. *ACM Computing Surveys (CSUR)*, *51*(3), 1–33.
77. Goodman, S.N., Fanelli, D., Ioannidis, J.P., (2016). What does research reproducibility mean? *Science translational medicine*, *8*(341).
78. Gregersen, J.B., Gijsbers, P.J.A., Westen, S.J.P., (2007). OpenMI: open modelling interface. *Journal of hydroinformatics*, *9*(3), 175–191.
79. Grimm, V., Railsback, S.F., (2012a). Designing, formulating, and communicating agent-based models. In: *Agent-based Models of Geographical Systems*. Springer, Dordrecht, pp. 361–377.
80. Grimm, V., Railsback, S.F., (2012b). Pattern-oriented modelling: a 'multi-scope' for predictive systems ecology. *Philosophical Transactions of the Royal Society B: Biological Sciences*, *367*(1586), 298–310.
81. Groeneveld, J., Müller, B., Buchmann, C.M., Dressler, G., Guo, C., Hase, N., et al., (2017). Theoretical foundations of human decision-making in agent-based land use models–A review. *Environmental modelling & software*, *87*, 39–48.
82. Gupta, H. V., Kling, H., Yilmaz, K. K., & Martinez, G. F. (2009). Decomposition of the mean squared error and NSE performance criteria: Implications for improving hydrological modelling. *Journal of Hydrology*, *377*(1–2), 80–91. https://doi.org/10.1016/j.jhydrol.2009.08.003
83. Gwenzi, W., & Nyamadzawo, G. (2014). Hydrological impacts of urbanization and urban roof water harvesting in water-limited catchments: a review. *Environmental Processes*, *1*(4), 573-593.
84. Hahn, A., & Govindarasu, M. (2011). Cyber attack exposure evaluation framework for the smart grid. *IEEE Transactions on Smart Grid*, *2*(4), 835-843.
85. Haith, D. A., (1985). An Event-based Procedure for Estimating Monthly Sediment Yields. *Transactions of the ASAE*, *28*(6), 1916–1920. doi:10.13031/2013.32541
86. Haith, D. A., Mandel, R., & Wu, R. S. (1996). Generalized watershed loading functions version 2.0 user's manual. Cornell University.
87. Haith, D. A., & Shoemaker, L. L. (1987). Generalized watershed loading functions for stream flow nutrients. *Journal of the American Water Resources Association*, *23*(3), 471–478. https://doi.org/10.1111/j.1752-1688.1987.tb00825.x
88. Hassanzadeh, A., Rasekh, A., Galelli, S., Aghashahi, M., Taormina, R., Ostfeld, A., & Banks, M. K. (2020). A review of cybersecurity incidents in the water sector. *Journal of Environmental Engineering*, *146*(5), 03120003.
89. Hill, C., DeLuca, C., Suarez, M., Da Silva, A.R., (2004). The architecture of the earth system modeling framework. *Computing in Science & Engineering*, *6*(1), 18–28.
90. Hillier, J. K., Matthews, T., Wilby, R. L., & Murphy, C. (2020). Multi-hazard dependencies can increase or decrease risk. *Nature Climate Change*, *10*(7), 595-598.
91. Hillman, B., Douglas, E.M., Terkla, D., (2012). An analysis of the allocation of Yakima River water in terms of sustainability and economic efficiency. *Journal of environmental management*, *103*, 102–112.
92. Horton R. E. 1941 An approach toward a physical interpretation of infiltration-capacity. *Soil Science Society of America Journal*, *5*, 399. doi:10.2136/sssaj1941.036159950005000C0075x.

93. Huang, Y., Tian, Z., Ke, Q., Liu, J., Irannezhad, M., Fan, D., ... & Sun, L. (2020). Nature-based solutions for urban pluvial flood risk management. *Wiley Interdisciplinary Reviews: Water*, *7*(3), e1421.
94. Hu, Q., Zillig, L.M.P., Lynne, G.D., Tomkins, A.J., Waltman, W.J., Hayes, M.J., et al., (2006). Understanding farmers' forecast use from their beliefs, values, social norms, and perceived obstacles. *Journal of applied meteorology and climatology*, *45*(9), 1190–1201.
95. Hutton, E.W., Piper, M.D., Tucker, G.E., (2020). The Basic Model Interface 2.0: a standard interface for coupling numerical models in the geosciences. *Journal of Open Source Software*, *5*(51), 2317.
96. Hung, F., & Yang, Y. E. (2021). Assessing adaptive irrigation impacts on water scarcity in nonstationary environments—A multi-agent reinforcement learning approach. *Water Resources Research*, *57*(9), e2020WR029262. https://doi.org/10.1029/2020wr029262
97. Hu, Y., & Beattie, S. (2019). Role of heterogeneous behavioral factors in an agent-based model of crop choice and groundwater irrigation. *Journal of Water Resources Planning and Management*, *145*(2), 04018100.
98. Hyun, J. Y., Huang, S. Y., Yang, Y. C. E., Tidwell, V., & Macknick, J. (2019). Using a coupled agent-based modeling approach to analyze the role of risk perception in water management decisions. *Hydrology and Earth System Sciences*, *23*(5), 2261–2278. https://doi.org/10.5194/hess-23-2261-2019
99. IPCC, 2022: Summary for Policymakers [H.-O. Pörtner, D.C. Roberts, E.S. Poloczanska, K. Mintenbeck, M. Tignor, A. Alegría, M. Craig, S. Langsdorf, S. Löschke, V. Möller, A. Okem (eds.)]. In: Climate Change 2022: Impacts, Adaptation, and Vulnerability. Contribution of Working Group II to the Sixth Assessment Report of the Intergovernmental Panel on Climate Change [H.-O. Pörtner, D.C. Roberts, M. Tignor, E.S. Poloczanska, K. Mintenbeck, A. Alegría, M. Craig, S. Langsdorf, S. Löschke, V. Möller, A. Okem, B. Rama (eds.)]. Cambridge University Press. In Press.
100. Jaxa-Rozen, M., Kwakkel, J.H., (2018). Pynetlogo: linking netlogo with python. *Journal of Artificial Societies and Social Simulation*, *21*(2).
101. Jaxa-Rozen, M., Kwakkel, J.H., Bloemendal, M., (2019). A coupled simulation architecture for agent-based/geohydrological modelling with NetLogo and MODFLOW. *Environmental Modelling & Software*, *115*, 19–37.
102. Jongman, B. (2018). Effective adaptation to rising flood risk. *Nature communications*, *9*(1), 1-3.
103. Kahneman, D., Tversky, A., (2013). Prospect theory: an analysis of decision under risk. In: Handbook of the Fundamentals of Financial Decision Making: Part I, pp. 99–127.
104. Kandasamy, J., Sounthararajah, D., Sivabalan, P., Chanan, A., Vigneswaran, S., & Sivapalan, M. (2014). Socio-hydrologic drivers of the pendulum swing between agricultural development and environmental health: A case study from Murrumbidgee River Basin, Australia. *Hydrology and Earth System Sciences*, *18*(3), 1027–1041. https://doi.org/10.5194/hess-18-1027-2014
105. Karthe, D., Bogardi, J. J., & Borchardt, D. (2021). Water resources management: Integrated and adaptive decision making. In Handbook of water resources

management: Discourses, concepts and examples (pp. 365–381). Springer. https://doi.org/10.1007/978-3-030-60147-8_12
106. Kelly, R. A., Jakeman, A. J., Barreteau, O., Borsuk, M. E., ElSawah, S., Hamilton, S. H., et al. (2013). Selecting among five common model-ling approaches for integrated environmental assessment and management. *Environmental Modelling & Software*, *47*, 159–181. https://doi.org/10.1016/j.envsoft.2013.05.005
107. Khan, H.F., Yang, Y.C.E., Xie, H., Ringler, C., (2017). A coupled modeling framework for sustainable watershed management in transboundary river basins. *Hydrology and Earth System Sciences*, *21*(12), 6275.
108. Khatami, S., Peel, M. C., Peterson, T. J., & Western, A. W. (2019). Equifinality and flux mapping: A new approach to model evaluation and process representation under uncertainty. *Water Resources Research*, *55*(11), 8922–8941. https://doi.org/10.1029/2018wr023750
109. Knox, S., Meier, P., Yoon, J., & Harou, J. J. (2018). A python framework for multi-agent simulation of networked resource systems. *Environmental modelling & software*, *103*, 16-28.
110. Kremmydas, D., Athanasiadis, I.N., Rozakis, S., (2018). A review of agent based modeling for agricultural policy evaluation. *Agricultural systems*, *164*, 95–106.
111. Kriaa, S., Pietre-Cambacedes, L., Bouissou, M., & Halgand, Y. (2015). A survey of approaches combining safety and security for industrial control systems. *Reliability engineering & system safety*, 139, 156-178.
112. Kučera, V. (1973). A review of the matrix Riccati equation. *Kybernetika*, *9*(1), 42-61.
113. Kumar, A., Saxena, N., Jung, S., & Choi, B. J. (2021). Improving detection of false data injection attacks using machine learning with feature selection and oversampling. *Energies*, *15*(1), 212.
114. Labadie, J. W. (2004). Optimal operation of multireservoir systems: State-of-the-art review. *Journal of water resources planning and management*, *130*(2), 93-111.
115. Lacroix, Z., Critchlow, T., (2003). Compared evaluation of scientific data management systems. *Bioinformatics*, 371–391. https://doi.org/10.1016/B978-155860829-0/50015-2.
116. Lee, K. N. (2001). Appraising adaptive management. In *Biological diversity* (pp. 3–26). CRC Press. https://doi.org/10.1201/9781420042597.sec1
117. Liang, X., Wood, E. F., & Lettenmaier, D. P. (1996). Surface soil moisture parameterization of the VIC-2L model: Evaluation and modification. *Global and Planetary Change*, *13*(1-4), 195-206.
118. Lin, C. Y., Yang, Y.C.E., (2022). The effects of model complexity on model output uncertainty in co-evolved coupled natural-human systems. *Earth's Future*, *10*(6). https://doi.org/10.1029/2021EF002403 e2021EF002403.
119. Lin, C. Y., & Ethan Yang, Y. C. (2022). Code: The effects of model complexity on model output uncertainty in co-evolved coupled natural–human systems (v0.0.1). [Dataset]. *Zenodo*. https://doi.org/10.5281/zenodo.6564777
120. Lin, C. Y., Yang, Y. E., Malek, K., & Adam, J. C. (2022). An investigation of coupled natural human systems using a two-way coupled agent-based modeling framework. *Environmental Modelling & Software*, *155*, 105451.
121. Lippmann, R. P., & Ingols, K. W. (2005). An annotated review of past papers on attack graphs.

122. Liu, J., Dietz, T., Carpenter, S.R., Alberti, M., Folke, C., Moran, E., Pell, A.N., Deadman, P., Kratz, T., Lubchenco, J., Ostrom, E., Ouyang, Z., Provencher, W., Redman, C.L., Schneider, S.H., Taylor, W.W., (2007). Complexity of coupled human and natural systems. *Science*, *317*, 1513–1516. https://doi.org/10.1126/science.1144004.
123. Livneh, B., Bohn, T. J., Pierce, D. W., Muñoz-Arriola, F., Nijssen, B., Vose, R., et al. (2015). A spatially comprehensive, meteorological data set for Mexico, the U.S., and southern Canada (NCEI Accession 0129374). NOAA National Centers for Environmental Information. Dataset. https://doi.org/10.7289/v5x34vf6. Accessed June 4, 2021.
124. Livneh, B., & National Center for Atmospheric Research Staff (Eds). Last modified 12 Dec 2019. "The Climate Data Guide: Livneh gridded precipitation and other meteorological variables for continental US, Mexico and southern Canada." Retrieved from https://climatedataguide.ucar.edu/climate-data/livneh-gridded-precipitation-and-other-meteorological-variables-continental-us-mexico
125. Li, Y., Giuliani, M., Castelletti, A., (2017). A coupled human-natural system to assess the operational value of weather and climate services for agriculture. *Hydrology and Earth System Sciences*, *21*, 4693–4709.
126. Li, Y., & Liu, Q. (2021). A comprehensive review study of cyber-attacks and cyber security; Emerging trends and recent developments. *Energy Reports*, 7, 8176-8186.
127. Lohmann, D., Raschke, E., Nijssen, B., & Lettenmaier, D. P. (1998). Regional scale hydrology: I. Formulation of the VIC-2L model coupled to a routing model. *Hydrological Sciences Journal*, *43*(1), 131–141. https://doi.org/10.1080/02626669809492107
128. Lu, M., & Reeves, J. (2014). Types of cyber attacks. *Trustworthy Cyber Infrastructure For The Power Grid*, 18, 2017.
129. Luo, Y., Arnold, J., Allen, P., & Chen, X. (2012). Baseflow simulation using SWAT model in an inland river basin in Tianshan Mountains, North-west China. *Hydrology and Earth System Sciences*, *16*(4), 1259–1267. https://doi.org/10.5194/hess-16-1259-2012
130. Maass, A., Hufschmidt, M., Dorfman, R., Thomas, Jr., H., Marglin, S. & Fair, G. (1962). Design of Water-Resource Systems: New Techniques for Relating Economic Objectives, Engineering Analysis, and Governmental Planning. Cambridge, MA and London, England: Harvard University Press. https://doi.org/10.4159/harvard.9780674421042
131. Madani, K., & Hooshyar, M. (2014). A game theory–reinforcement learning (GT–RL) method to develop optimal operation policies for multi-operator reservoir systems. *Journal of Hydrology*, *519*, 732–742. https://doi.org/10.1016/j.jhydrol.2014.07.061
132. Malek, K., Adam, J., Stockle, C., Brady, M., Rajagopalan, K., (2018). When should irrigators invest in more water-efficient technologies as an adaptation to climate change? *Water Resources Research*, *54*(11), 8999–9032.
133. Marston, L., & Konar, M. (2017). Drought impacts to water footprints and virtual water transfers of the Central Valley of California. *Water Resources Research*, *53*(7), 5756–5773.

134. Martinez, G. F., & Gupta, H. V. (2010). Toward improved identification of hydrological models: A diagnostic evaluation of the "abcd" monthly water balance model for the conterminous United States. *Water Resources Research*, *46*(8).
135. Mastin, M.C., Vaccaro, J.J., (2002). Watershed models for decision support in the Yakima River basin, Washington. Wash. U.S. Geol. Surv. Open-file rep. 02–404 Tacoma WA.
136. Maurer, E.P., A.W. Wood, J.C. Adam, D.P. Lettenmaier, and B. Nijssen, (2002). A Long-Term Hydrologically-Based Data Set of Land Surface Fluxes and States for the Conterminous United States, *J. Climate*, *15*, 3237-3251.
137. MB7384 (2012). Retrieved from http://www.maxbotix.com/Ultrasonic_Sensors/MB7384-Ultrasonic_Snow_Depth_Sensor.htm
138. McLean, K. A., & McAuley, K. B. (2012). Mathematical modelling of chemical processes—Obtaining the best model predictions and parameter estimates using identifiability and estimability procedures. *Canadian Journal of Chemical Engineering*, *90*(2), 351–366. https://doi.org/10.1002/cjce.20660
139. Messina, J. P., Evans, T. P., Manson, S. M., Shortridge, A. M., Deadman, P. J., & Verburg, P. H. (2008). Complex systems models and the management of error and uncertainty. *Journal of Land Use Science*, *3*(1), 11–25. https://doi.org/10.1080/17474230802047989
140. Miller, J., (2006). "State, power company fight over Snake River." the spokesman-review, March 16. https://www.spokesman.com/stories/2006/mar/16/state-power-company-fight-over-snake-river/. (Accessed 18 October 2021).
141. Miller, J.H., Page, S.E., (2007). Complex Adaptive Systems: an Introduction to Computational Models of Social Life. Princeton University Press, Princeton, NJ.
142. Milly, P. C., Betancourt, J., Falkenmark, M., Hirsch, R. M., Kundzewicz, Z. W., Lettenmaier, D. P., & Stouffer, R. J. (2008). Stationarity is dead: Whither water management? *Science*, *319*(5863), 573–574. https://doi.org/10.1126/science.1151915
143. Ministry of the Environment. (2003). Stormwater Management Planning and Design Manual. Water Resources. Ministry of the Environment, Toronto, Ontario.
144. Moallemi, E. A., Kwakkel, J., de Haan, F. J., & Bryan, B. A. (2020). Exploratory modeling for analyzing coupled human-natural systems under uncertainty. *Global Environmental Change*, *65*, 102186. https://doi.org/10.1016/j.gloenvcha.2020.102186
145. Moore, R.V., Tindall, C.I., (2005). An overview of the open modelling interface and environment (the OpenMI). *Environmental Science & Policy*, *8*(3), 279–286.
146. Mullapudi, A., Wong, B. P., & Kerkez, B. (2017). Emerging investigators series: building a theory for smart stormwater systems. *Environmental Science: Water Research & Technology*, *3*(1), 66-77.
147. Müller, B., Bohn, F., Dreßler, G., Groeneveld, J., Klassert, C., Martin, R., et al. (2013). Describing human decisions in agent-based models–ODD+ D, an extension of the ODD protocol. *Environmental Modelling & Software*, *48*, 37–48.
148. Murray-Rust, D., Robinson, D.T., Guillem, E., Karali, E., Rounsevell, M., (2014). An open framework for agent based modelling of agricultural land use change. *Environmental modelling & software*, *61*, 19–38.

149. Nash, J. E., & Sutcliffe, J. V. (1970). River flow forecasting through conceptual models part I—A discussion of principles. *Journal of Hydrology*, *10*(3), 282–290. https://doi.org/10.1016/0022-1694(70)90255-6
150. National Academies of Sciences, Engineering, and Medicine, (2018). Open Science by Design: Realizing a Vision for 21st Century Research. The National Academies Press, Washington, DC. https://doi.org/10.17226/25116.
151. National Academies of Sciences, Engineering, and Medicine. (2021). Developing a Toolkit for Fostering Open Science Practices: Proceedings of a Workshop.
152. National Center for Atmospheric Research Staff (Eds). Last modified 06 Jul 2016. "The Climate Data Guide: CMIP (Climate Model Intercomparison Project) overview. "Retrieved from https://climatedataguide.ucar.edu/climate-model-evaluation/cmip-climate-model-intercomparison-project-overview
153. Natural Resources Conservation Service (NRCS). (2004). National engineering handbook, Part 630-Hydrology, U.S. Dept. of Agriculture, Washington, D.C.
154. Neitsch, S. L., Arnold, J. G., Kiniry, J. R., & Williams, J. R. (2011). Soil and water assessment tool theoretical documentation version 2009. Texas Water Resources Institute.
155. Ngafeeson, M. (2010). Cybercrime classification: a motivational model. College of Business Administration, The University of Texas-Pan American, 1201.
156. Nhim, T., Richter, A., Zhu, X., (2019). The resilience of social norms of cooperation under resource scarcity and inequality—an agent-based model on sharing water over two harvesting seasons. *Ecological Complexity*, *40*, 100709.
157. Niles, M.T., Mueller, N.D., (2016). Farmer perceptions of climate change: associations with observed temperature and precipitation trends, irrigation, and climate beliefs. *Global Environmental Change*, *39*, 133–142.
158. Nurse, J. R., Creese, S., & De Roure, D. (2017). Security risk assessment in Internet of Things systems. *IT professional*, *19*(5), 20-26.
159. Office of Columbia River, (2020). Yakima River Basin Integrated 2019 Implementation Status Report. Washington State Department of Ecology.
160. Peckham, S.D., Hutton, E.W., Norris, B., (2013). A component-based approach to integrated modeling in the geosciences: the design of CSDMS. *Computers & Geosciences*, *53*, 3–12.
161. Pedregosa, F., Varoquaux, G., Gramfort, A., Michel, V., Thirion, B., Grisel, O., et al. (2011). Scikit-learn: Machine learning in Python. *The Journal of machine Learning Research*, *12*, 2825–2830.
162. Pellicciotto, J., Andrejko, G., Design, A., (2012). National Fish, Wildlife and Plants Climate Adaptation Strategy Copyright© 2012.
163. Piro, P., Turco, M., Palermo, S. A., Principato, F., & Brunetti, G. (2019). A comprehensive approach to stormwater management problems in the next generation drainage networks. *The Internet of Things for Smart Urban Ecosystems*, pp. 275-304, Springer, Cham.
164. Plessis, G., Amouroux, ́E., Haradji, Y., (2014), March. Coupling occupant behaviour with a building energy model-A FMI application. In: *Proceedings of the 10 Th International Modelica Conference*; March 10-12; 2014. Link ̈oping University Electronic Press, Lund; Sweden, pp. 321–326, 096.

165. Qiu, J., Yang, Q., Zhang, X., Huang, M., Adam, J.C., Malek, K., (2019). Implications of water management representations for watershed hydrologic modeling in the Yakima River basin. *Hydrology and Earth System Sciences* (Online), *23* (PNNL-SA-135306).
166. Reeves, H. W., & Zellner, M. L. (2010). Linking MODFLOW with an agent-based land-use model to support decision making. *Groundwater*, *48*(5), 649-660.
167. Reuss, M. (2003). Is it time to resurrect the Harvard water program? *Journal of Water Resources Planning and Management*, *129*(5), 357–360. https://doi.org/10.1061/(asce)0733-9496(2003)129:5(357)
168. Robinson, D.T., Di Vittorio, A., Alexander, P., Arneth, A., Barton, C.M., Brown, D.G., et al., (2018). Modelling feedbacks between human and natural processes in the land system. *Earth System Dynamics*, *9*(2), 895–914.
169. Rossman, L. A. (2010). Storm water management model user's manual, version 5.0 (p. 276). Cincinnati: National Risk Management Research Laboratory, Office of Research and Development, US Environmental Protection Agency.
170. Sadler, J. M., Goodall, J. L., Behl, M., Bowes, B. D., & Morsy, M. M. (2020). Exploring real-time control of stormwater systems for mitigating flood risk due to sea level rise. *Journal of Hydrology*, 583, 124571.
171. Saltelli, A., Aleksankina, K.,Becker, W., Fennell, P., Ferretti, F., Holst, N., et al. (2019). Why so many published sensitivity analyses are false: A systematic review of sensitivity analysis practices. *Environmental Modelling & Software*, *114*, 29–39. https://doi.org/10.1016/j.envsoft.2019.01.012
172. Schleiss, M., Olsson, J., Berg, P., Niemi, T., Kokkonen, T., Thorndahl, S., ... & Pulkkinen, S. (2020). The accuracy of weather radar in heavy rain: a comparative study for Denmark, the Netherlands, Finland and Sweden. *Hydrology and Earth System Sciences*, *24*(6), 3157-3188.
173. Schreinemachers, P., Berger, T., (2011). An agent-based simulation model of human–environment interactions in agricultural systems. *Environmental Modelling & Software*, *26*(7), 845–859.
174. Schuurmans, J. (1997). Control of water levels in open-channels.
175. Shin, S., Lee, S., Burian, S. J., Judi, D. R., & McPherson, T. (2020). Evaluating resilience of water distribution networks to operational failures from cyber-physical attacks. *Journal of Environmental Engineering*, *146*(3), 04020003.
176. Shishegar, S., Duchesne, S., & Pelletier, G. (2018). Optimization methods applied to stormwater management problems: a review. *Urban Water Journal*, *15*(3), 276-286.
177. Shishegar, S., Duchesne, S., Pelletier, G., & Ghorbani, R. (2021). A smart predictive framework for system-level stormwater management optimization. *Journal of Environmental Management*, 278, 111505.
178. Sivapalan, M., Bl¨oschl, G., (2015). Time scale interactions and the coevolution of humans and water. *Water Resources Research*, *51*(9), 6988–7022.
179. Song, W., & Zhang, Y. (2015). Expansion of agricultural oasis in the Heihe River Basin of China: Patterns, reasons and policy implications. *Physics and Chemistry of the Earth*, Parts A/B/C, *89*, 46–55. https://doi.org/10.1016/j.pce.2015.08.006
180. Srikrishnan, V., & Keller, K. (2021). Small increases in agent-based model complexity can result in large increases in required calibration data. *Environmental Modelling & Software*, *138*, 104978. https://doi.org/10.1016/j.envsoft.2021.104978

181. Sun, Z., Müller, D., (2013). A framework for modeling payments for ecosystem services with agent-based models, Bayesian belief networks and opinion dynamics models. *Environmental modelling & software*, *45*, 15–28.
182. Sun, Z., Lorscheid, I., Millington, J. D., Lauf, S., Magliocca, N. R., Groeneveld, J., et al. (2016). Simple or complicated agent-based models? A complicated issue. *Environmental Modelling & Software*, *86*, 56–67. https://doi.org/10.1016/j.envsoft.2016.09.006
183. Tarawneh, E., Bridge, J., & Macdonald, N. (2016). A pre-calibration approach to select optimum inputs for hydrological models in data-scarce regions. *Hydrology and Earth System Sciences*, *20*(10), 4391–4407. https://doi.org/10.5194/hess-20-4391-2016
184. Taylor, K. E., Stouffer, R. J., & Meehl, G. A. (2012). An overview of CMIP5 and the experiment design. *Bulletin of the American Meteorological Society*, *93*(4), 485–498. https://doi.org/10.1175/bams-d-11-00094.1
185. Tesfatsion, L., Rehmann, C.R., Cardoso, D.S., Jie, Y., Gutowski, W.J., (2017). An agent-based platform for the study of watersheds as coupled natural and human systems. *Environmental Modelling & Software*, *89*, 40–60.
186. The White House. (2022). "Fact Sheet: Biden-Harris Administration Expands Public-Private Cybersecurity Partnership to Water Sector." https://www.whitehouse.gov/briefing-room/statements-releases/2022/01/27/fact-sheet-biden-harris-administration-expands-public-private-cybersecurity-partnership-to-water-sector.
187. Thomas, H. A. (1981). Improved Methods for National Water Assessment. Report, Contract: WR15249270. Washington, D.C.: US Water Resource Council.
188. Thonicke, K., Bahn, M., Lavorel, S., Bardgett, R. D., Erb, K., Giamberini, M., ... & Rammig, A. (2020). Advancing the understanding of adaptive capacity of social-ecological systems to absorb climate extremes. *Earth's Future*, *8*(2), e2019EF001221.
189. Tolson, B. A., & Shoemaker, C. A. (2007). Dynamically dimensioned search algorithm for computationally efficient watershed model calibration. *Water Resources Research*, *43*(1). https://doi.org/10.1029/2005wr004723
190. Tualatin River Watershed Council (2021). Tualatin Basin Information. http://trwc.org/tualatin-basin-information/ Accessed [Nov 19 2021]
191. Tuptuk, N., Hazell, P., Watson, J., & Hailes, S. (2021). A systematic review of the state of cyber-security in water systems. *Water*, *13*(1), 81.
192. Tung, C. P., & Haith, D. A. (1995). Global-warming effects on New York streamflows. *Journal of Water Resources Planning and Management*, *121*(2), 216–225. https://doi.org/10.1061/(asce)0733-9496(1995)121:2(216)
193. Tung, C. P., Tsao, J. H., Tien, Y. C., Lin, C. Y., & Jhong, B. C. (2019). Development of a novel climate adaptation algorithm for climate risk assessment. *Water*, *11*(3), 497.
194. U.S. DOE, (2019). Open Watershed Science by Design: Leveraging Distributed Research Networks to Understand Watershed Systems Workshop Report, DOE/SC-0200. U.S. Department of Energy Office of Science (doesbr.org/openwatersheds/).
195. USBR, (2002). Interim Comprehensive Basin Operating Plan for the Yakima Project Washington.

196. USBR, (2010). Technical memorandum Yakima River basin study – WaterSMART program subtask 2.1. Tech. Memo. Yakima River Basin Study – WaterSMART Program Subtask 21.
197. USBR, (2011). Technical Memorandum Yakima River Basin Study – Modeling of Reliability and Flows Technical Memorandum Task 6 Tech. Memo. Yakima River Basin Study – Modeling of Reliability and Flows. Technical Memorandum task 6.
198. USBR, (2012). Environmental Assessment Development and Implementation of a Protocol for High-Flow Experimental Releases from Glen Canyon Dam, Arizona, 2011 – 2020.
199. USDA. (2017). National Agricultural Statistics Service, 2017 Census of Agriculture. Retrieved from www.nass.usda.gov/AgCensus
200. Vallario, B., Arnold, J., Weyant, J., Scheetz, A., Lipschultz, F., Arrigo, J., et al. (2021). Coastal integrated HydroTerrestrial modeling: A multi-agency invited workshop. U.S. Global Change Research Program. Retrieved from https://downloads.globalchange.gov/coasts-IG/workshop-report/C-IHTM_Workshop_Report_Nov2020.pdf
201. Vangheluwe, H., (2000). Multi-formalism Modelling and Simulation. Doctoral dissertation, Ghent University.
202. Van Meter, R. J., Swan, C. M., & Snodgrass, J. W. (2011). Salinization alters ecosystem structure in urban stormwater detention ponds. *Urban Ecosystems*, *14*(4), 723-736.
203. Vaubourg, J., Presse, Y., Camus, B., Bourjot, C., Ciarletta, L., Chevrier, V., et al., (2015). Multi-agent multi-model simulation of smart grids in the MS4SG project. In: *International Conference on Practical Applications of Agents and Multi-Agent Systems*. Springer, Cham, pp. 240–251.
204. Vrugt, J. A., Ter Braak, C. J. F., Gupta, H. V., & Robinson, B. A. (2009). Equifinality of formal (DREAM) and informal (GLUE) Bayesian approaches in hydrologic modeling? *Stochastic Environmental Research and Risk Assessment*, *23*(7), 1011–1026. https://doi.org/10.1007/s00477-008-0274-y
205. Wada, Y., Bierkens, M. F., Roo, A. D., Dirmeyer, P. A., Famiglietti, J. S., Hanasaki, N., et al. (2017). Human–water interface in hydrological modelling: Current status and future directions. *Hydrology and Earth System Sciences*, *21*(8), 4169–4193. https://doi.org/10.5194/hess-21-4169-2017
206. Wahl, T., Jain, S., Bender, J., Meyers, S. D., & Luther, M. E. (2015). Increasing risk of compound flooding from storm surge and rainfall for major US cities. *Nature Climate Change*, *5*(12), 1093-1097.
207. Walsh, J. E., Bhatt, U. S., Littell, J. S., Leonawicz, M., Lindgren, M., Kurkowski, T. A., et al. (2018). Downscaling of climate model output for Alaskan stakeholders. *Environmental Modelling & Software*, *110*, 38–51. https://doi.org/10.1016/j.envsoft.2018.03.021
208. Wasimi, S. A., & Kitanidis, P. K. (1983). Real-time forecasting and daily operation of a multireservoir system during floods by linear quadratic Gaussian control. *Water Resources Research*, *19*(6), 1511-1522.
209. Watts, G., Noonan, W.R., Maddux, H., Brookshire, D.S., (2001). The Endangered Species Act and critical habitat designation: economic consequences for the Colorado

River basin. Protecting Endangered Species in the United States: Biological Needs, Political Realities, *Economic Choices* 177–199.
210. Westerberg, I. K., Di Baldassarre, G., Beven, K. J., Coxon, G., & Krueger, T. (2017). Perceptual models of uncertainty for socio-hydrological systems: A flood risk change example. *Hydrological Sciences Journal*, *62*(11), 1705–1713. https://doi.org/10.1080/02626667.2017.1356926
211. Wheeler, K.G., Jeuland, M., Hall, J.W., Zagona, E., Whittington, D., (2020). Understanding and managing new risks on the nile with the grand Ethiopian renaissance dam. *Nature Communications*, *11*(1), 1–9.
212. Whitley, D. (1994). A genetic algorithm tutorial. *Statistics and computing*, *4*(2), 65-85.
213. Wiegand, T., Jeltsch, F., Hanski, I., Grimm, V., (2003). Using pattern-oriented modeling for revealing hidden information: a key for reconciling ecological theory and application. *Oikos*, *100*(2), 209–222.
214. Wiles, J., (2016). "Malheur occupation, explained." high country news, january 4. http://www.hcn.org/articles/oregon-occupation-at-wildlife-refuge. (Accessed 18 October 2021).
215. Williams, T. G., Guikema, S. D., Brown, D. G., & Agrawal, A. (2020). Assessing model equifinality for robust policy analysis in complex socio-environmental systems. *Environmental Modelling & Software*, *134*(8). https://doi.org/10.1016/j.envsoft.2020.104831
216. Wi, S., Yang, Y. C. E., Steinschneider, S., Khalil, A., & Brown, C. M. (2015). Calibration approaches for distributed hydrologic models in poorly gaged basins: Implication for streamflow projections under climate change. *Hydrology and Earth System Sciences*, *19*(2), 857–876. https://doi.org/10.5194/hess-19-857-2015
217. Witt, A., Magee, T., Stewart, K., Hadjerioua, B., Neumann, D., Zagona, E., Politano, M., (2017). Development and implementation of an optimization model for hydropower and Total dissolved gas in the mid-Columbia River System. *Journal of Water Resources Planning and Management*, *143*(10), 04017063.
218. Wong, B. P., & Kerkez, B. (2018). Real-Time Control of Urban Headwater Catchments Through Linear Feedback: Performance, Analysis, and Site Selection. *Water Resources Research*, *54*(10), 7309-7330.
219. Woodard, D. L., Davis, S. J., & Randerson, J. T. (2019). Economic carbon cycle feedbacks may offset additional warming from natural feedbacks. *Proceedings of the National Academy of Sciences*, *116*(3), 759–764. https://doi.org/10.1073/pnas.1805187115
220. Xu, W. D., Burns, M. J., Cherqui, F., & Fletcher, T. D. (2021). Enhancing stormwater control measures using real-time control technology: a review. *Urban Water Journal*, *18*(2), 101-114.
221. Xu, W., Lowe, S. E., & Adams, R. M. (2014). Climate change, water rights, and water supply: The case of irrigated agriculture in Idaho. *Water Resources Research*, *50*(12), 9675–9695. https://doi.org/10.1002/2013wr014696
222. Yadav, N., Chatterjee, S., & Ganguly, A. R. (2020). Resilience of urban transport network-of-networks under intense flood hazards exacerbated by targeted attacks. *Scientific reports*, *10*(1), 1-14.

223. Yanakiev, Y. (2020). –Introduction to nato sto task group hfm-259: human systems integration approach to cyber security. Human Systems Integration Approach to Cyber Security.
224. Yang, Y. C. E., Cai, X., & Stipanović, D. M. (2009). A decentralized optimization algorithm for multiagent system-based watershed management. *Water Resources Research*, *45*(8), 8430. https://doi.org/10.1029/2008WR007634
225. Yang, Y.C.E., Zhao, J., Cai, X., (2012). Decentralized optimization method for water allocation management in the Yellow River Basin. *Journal of Water Resources Planning and Management*, *138*(4), 313–325.
226. Yang, Y. C. E., Son, K., Hung, F., & Tidwell, V. (2020). Impact of climate change on adaptive management decisions in the face of water scarcity. *Journal of Hydrology*, *588*, 125015. https://doi.org/10.1016/j.jhydrol.2020.125015
227. Yeh, C. H., & Labadie, J. W. (1997). Multiobjective watershed-level planning of storm water detention systems. *Journal of Water Resources Planning and Management*, *123*(6), 336-343.
228. Yen, H., Wang, X., Fontane, D.G., Harmel, R.D., Arabi, M., (2014). A framework for propagation of uncertainty contributed by parameterization, input data, model structure, and calibration/validation data in watershed modeling. *Environmental Modelling & Software*, *54*, 211–221.
229. Zagona, E.A., Fulp, T.J., Shane, R., Magee, T., Goranflo, H.M., (2001). Riverware: a generalized tool for complex reservoir system modeling 1. *Journal of the American Water Resources Association*, *37*(4), 913–929.
230. Zellner, M. L. (2008). Embracing complexity and uncertainty: The potential of agent-based modeling for environmental planning and policy. *Planning Theory & Practice*, *9*(4), 437–457. https://doi.org/10.1080/14649350802481470
231. Zellner, M.L., Reeves, H.W., (2010). Integrating land-use and groundwater modeling: opportunities, challenges and implications for policy analysis. *International Journal of Operations and Quantitative Management*, Special Issue on Decision Making in Complex Systems, *16*(4), 389–414.
232. Zhang, J., Yang, Y.C.E., Li, H., Shittu, E., (2021). Examining the food-energy-water-environment nexus in transboundary river basins through a human dimension lens: Columbia River basin. *Journal of Water Resources Planning and Management*, *147*(10), 05021019.
233. Zhou, Y., Guo, S., Xu, C.Y., Liu, D., Chen, L., Ye, Y., (2015). Integrated optimal allocation model for complex adaptive system of water resources management (I): methodologies. *Journal of Hydrology*, *531*, 964–976.
234. Zscheischler, J., Westra, S., Van Den Hurk, B. J., Seneviratne, S. I., Ward, P. J., Pitman, A., ... & Zhang, X. (2018). Future climate risk from compound events. *Nature Climate Change*, *8*(6), 469-477.

Appendix A: Supplementary Materials for Chapter 2

A.1 Py-RAMID technical details

In this section, the file-based two-way coupling technical details of Py-RAMID will be provided. For the instruction on Py-RAMID, please see the user manual at https://github.com/philip928lin/Py-RAMID.

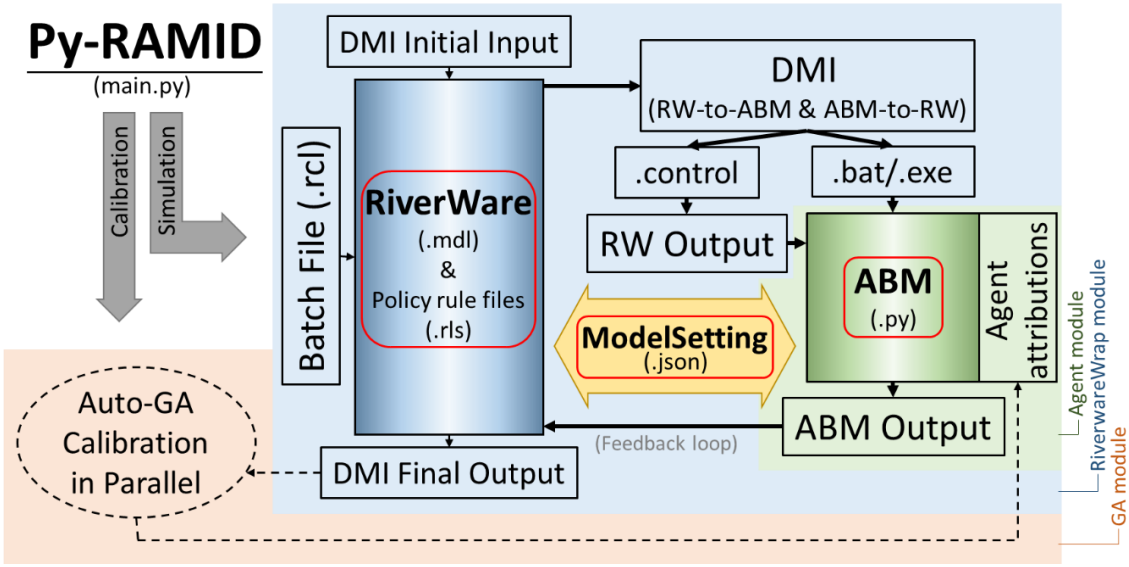

Figure A1. Py-RAMID framework and calibration structure. Two grey arrows indicate primary tasks performed by the Py-RAMID framework. Three background colors distinguish three modules in the Py-RAMID. Three user-prepared items are highlighted in red boxes. The feedback loop is shown with thick solid arrows.

Inside Py-RAMID, the coupling mechanism between RW and ABM is achieved by utilizing the RW model's data management interface (DMI), which can import and export data from and to text files as well as trigger outside executable programs (e.g., *.bat* or *.exe*). In a feedback loop (Figure A1), the RW-to-ABM DMI will be first activated by the RW; output corresponding to RW simulated data is defined in *.control* files. The RW-to-ABM DMI will then trigger the ABM model (must be an executable program), which is designed to intake RW outputs and generate updated data. In Py-RAMID, we allow ABM models

that are python files (e.g., ABM.py) or executable files (e.g., ABM.exe). If ABM.py is provided, Py-RAMID will wrap ABM.py with a *.bat* file, which is executable in the Windows operating system. Finally, the feedback loop is closed by re-importing ABM outputs into the RW model through the ABM-to-RW DMI. Without Py-RAMID, modelers need to manually prepare these files for each experiment.

With the assistance of Py-RAMID, modelers only need to prepare three items, with some modifications, in the original RW model. The three user-prepared items are (1) ModelSetting (*.json*) file (Figure A3), (2) the modified RW model, and (3) the ABM model (*.py*), which are all highlighted by red rectangles in Figure A1. In the ModelSetting (*.json*) file, modelers define the information flow for data exchange between RW and ABM (import/export slots of the RW), the RW simulation periods, and other RW actions using RW command language (e.g., LoadRules). Using the information in ModelSetting (*.json*), Py-RAMID will create control (*.control*) and batch (*.rcl*) files. DMI uses control files to determine the imported/exported slots. A batch file is used to execute the RW model with predefined action orders (e.g., OpenWorkspace, LoadRules, and SetRunInfo). Therefore, Py-RAMID serves as a wrapper to help modelers form all required coupling files. However, modelers must add two additional policies that are associated with the RW-to-ABM and ABM-to-RW DMIs into the original RW policy rules (*.rls*) for the very first time. Inside those two additional policies, modelers can define data exchange frequency; for example, to export the RW data on 31 December of a year and re-import the data on 1 January of a year. Finally, modelers have complete freedom to define agents and their interactions using any ABM frameworks for ABM.py.

As the original RW model can involve a tremendous amount of policy rules and initial settings, modelers must be aware of errors, such as invalid initial values (e.g., invalid reservoir storage) or other logically incorrect-but-not-erroneous values. For example, river discharge might be adjusted by other irregular inflows through policy rules to fit the observed data, which causes river discharge to become unrepresentative of different water diversion values. Py-RAMID cannot automatically correct RW issues, which should be aware of by modelers.

To calibrate the coupled model, especially the ABM model, modelers need to load parameters that must be calibrated from separated files, such as Par.csv. Then, our GA module will update parameters in Par.csv during the calibration process according to a user-defined minimization objective value (e.g., -NSE). In the GA module, we developed an auto-calibration process in parallel using a genetic algorithm. Our GA is built on the geneticalgorithm package (https://github.com/rmsolgi/geneticalgorithm), and parallelization is achieved by utilizing the joblib package (https://github.com/joblib/joblib). In addition to the joblib package, the GA module will replicate and modify necessary coupled model files into an isolated working space to overcome the file exchange conflicts in parallel computing. The GA module also provides options to remove replicated simulation space for storage control. Additionally, the GA module supports an auto-save mechanism to prevent accidental interruption (e.g., computer shut down or model crash) and allows to continue of previous unfinished calibration.

A.2 ODD+D Protocol of Agent-Based Model

1. Overview

1.1. Purpose

Coupled-YAKRW aims to demonstrate the modularized two-way coupling framework using Py-RAMID. From the perspective of a case study, Coupled-YAKRW is built for decision-makers. Coupled-YAKRW can simulate district diversion request decisions and their reciprocal interaction with the external environment, simulated by a physical hydrological model, RiverWare.

1.2. Entities, state variables, and scales

Coupled-YAKRW has six agents representing six major water use districts in the YRB. Namely, the space characteristics are implied in each agent's diverted location (e.g., district). Each agent has ten attributions, including two state variables and eight parameters, as shown in Table 2-2. The simulation period is from 1960 to 2005, which is separated into (1) warm-up period (1960－1965), (2) calibration period (1966－1995), and (3) validation period (1996-2005). The agent's decision (e.g., diversion requests) is made annually.

1.3. Process overview and scheduling

The interaction between agents and the environment in Coupled-YAKRW is triggered at the beginning of each year. The state variables will be updated, and the updated diversion requests for each district will be imported into the RiverWare (e.g., YAKRW).

2. Design Concepts

2.1. Theoretical and Empirical Background

For the decision-making process in the ABM model (yellow boxes in Figure A2), we followed the Theory of Planned Behavior (Ajzen, 1991) as a guideline, which states that

the behavior is built upon intention (e.g., diversion requests) and reality constraints (e.g., water rights, canal capacity).

2.2. Individual Decision-Making

The agent's objective is to decide the amount of requested diversion according to historical diversion records and external information (e.g., precipitation and reservoirs' storage). The basic rationality is that agents will make their predictions based on current and historical observations. These predictions are adjusted by the social norm effect and the agent's risk attitude in the later decision-making process. The Coupled-YAKRW is a single-agent level model. The details of the agent's decision-making process and its calculation are presented in Appendix A.3.

2.3. Learning

The agent's decision rules (e.g., state variable C) will be updated by learning the difference in the simulated and observed river discharges using reinforcement learning (Equation A-3).

2.4. Individual Sensing

In Coupled-YAKRW, agents can sense external states (e.g., winter precipitation, reservoir storages, and differences in the simulated and observed river discharges) and neighbors' evaluation of the water supply conditions (social norm effect). There are no costs and time lags to acquire the abovementioned information.

2.5. Individual Prediction

According to the agent's selected InfoSource, the agent will evaluate the water supply conditions based on the Empirical Cumulative Distribution Function (ECDF) value of the

current year's (y_t) observation. The ECDF is constructed by the historical records of selected InfoSource from the initial year (y_{t_o}) to y_{t-1}.

2.6. Interaction

The Coupled-YAKRW has direct interaction among agents defined by the social norm effect and indirect interaction through the feedback from the RiverWare simulation.

2.7. Collectives

No collectives (or single collectives) are in our case study area.

2.8. Heterogeneity

Each agent will have a unique set of attributions (Table 2-2) to represent their heterogeneity.

2.9. Stochasticity

According to their perceived beliefs, Coupled-YAKRW has a stochastic simulation option in which the agent randomly decides a diversion-request-adjustment ratio according to a probability distribution. However, during the model calibration and the experiment in Chapter 2, this stochastic option is replaced by the expected value to enhance the convergent speed in GA calibration.

2.10. Observation

We evaluate Coupled-YAKRW performance using observations of six diversions (agent level) and observations of two river discharges (basin level). The observed data is collected from the Hydromet platform operated by the U.S. Bureau of Reclamation.

3. Details

3.1. Implementation Details

Coupled-YAKRW, constructed by Py-RAMID package, is designed to run under Python 3.7 in the Windows system. Coupled-YAKRW is accessible at the request of the corresponding author.

3.2. Initialization

We have a fixed initialization in Coupled-YAKRW. For the ABM part, initial diversion request records are defined by observations of the previous year's diversion. RiverWare (e.g., YAKRW) initializes the model before simulation with predefined input values, such as input flows, policies, and initial reservoirs' storage, on 31 October 1960.

3.3. Input Data

All required input data to run RiverWare has been stored in YAKRW. For the ABM part, the grid-based precipitation data from Maurer et al. (2002) are used. The observed reservoir storage and observed diversion data are from the Hydromet platform.

3.4. Sub-models

There are no sub-models in Coupled-YAKRW.

A.3 Agent's decision-making algorithm for diversion request

The ABM part of Coupled-YAKRW describes the decision-making process of six major water use districts' diversion requests. The decision-making process is composed of six steps. Each step is described below.

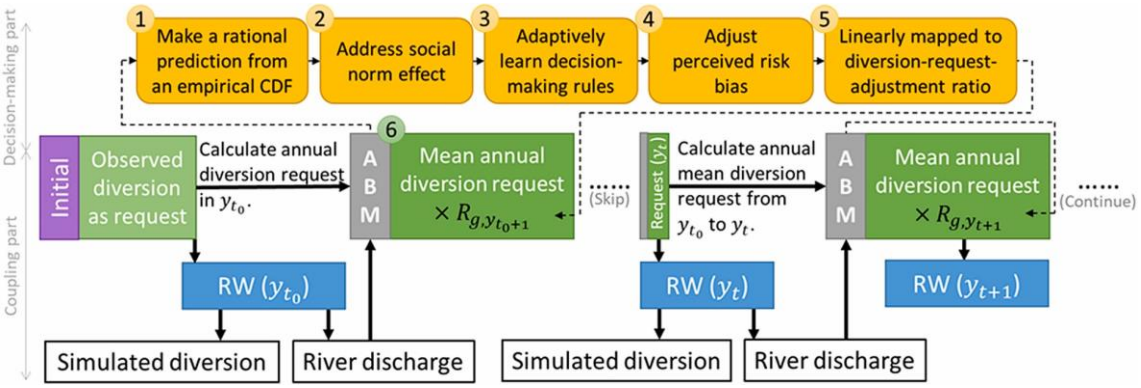

Figure A2. Coupled-YAKRW simulation schema. Yellow boxes are agent decision-making processes (dotted thin arrows), which output the ratio (R_{g,y_t}) that is used to adjust the mean annual diversion request (circle number 6) and to simulate the next year by RW. Annual mean diversion request is computed using all historical annual diversion request records before the current year. Solid arrows connecting diversion requests (green boxes) and the RW model (blues boxes) show information flow in the coupling process.

Step 1: Making a rational prediction from ECDF constructed by historical records.

The agent will first evaluate the water supply conditions (p_{g,y_t}) based on the ECDF value of the current year's (y_t) observation (x_{g,y_t}) on the selected $InfoSource$. The ECDF is constructed by the historical records of selected $InfoSource$ from the initial year (y_{t_0}) to y_{t-1}. The formula is shown in Equation A-1.

$$p_{g,y_t} = \mathrm{ECDF}_{InfoSource,N}\left(x_{g,y_t}\right) \tag{A-1}$$

where g is an agent's index, t is the current year, and N is the memory length of an agent, defined as the number of years from y_{t_0} to y_{t-1}.

Step 2: Social norm effect

Given a social network matrix (S), a weight vector (Sw), and a vector of agents' own evaluation of water supply conditions in y_t (P), the adjusted perceived belief (p_{g,y_t}^{adj}) is calculated by Equation A-2.

$$p_{g,y_t}^{adj} = \left(1 - Sw_{g,g}\right) \times P_{g,y_t} + Sw_{g,g} \sum_{i=1,i\neq g}^{N_{agents}} S_{g,i} \times P_{i,y_t} \quad \text{(A-2)}$$

where N_{agents} denotes the total number of agents.

Step 3: Adaptive learning

In step 3, agents will adaptively update their decision rules by updating a state variable, Center (C_{g,y_t}), to reinforce the average difference between the simulated and observed river discharges (v_{g,y_t}) at their downstream area to be minimized. We adopted a generalized form of the Bush-Mosteller model (Brenner, 2006), a type of reinforcement learning model, to achieve the agent's adaptive learning behavior shown in the following equations.

$$C_{g,y_t} = \begin{cases} C_{g,y_{t-1}} + h_{g,t} \times \gamma_g \times \left(1 - C_{g,y_{t-1}}\right) & if\ h_{g,t} \geq 0 \\ C_{g,y_{t-1}} + h_{g,t} \times \gamma_g \times C_{g,y_{t-1}} & if\ h_{g,t} < 0 \end{cases} \quad \text{(A-3)}$$

where the strength ($h_{g,t}$) is calculated by Equation A-4. In Equation A-4, $v_{g,t}$ is equal to the observed river discharges minus the simulated discharges. v_{g,y_t} scaled by a scale factor (Sc_g) is then transformed into a value between 0 and 1 through a sigmoid function (Equation A-5). A "0.5" downshift defines the strength as positive or negative. The range of the strength becomes –0.5 to 0.5.

$$h_{g,y_t} = \begin{cases} \sigma\left(\frac{v_{g,y_t}}{Sc_g}\right) - 0.5 & if\ v_{g,y_t} \geq 0 \\ 1 - \sigma\left(-\frac{v_{g,y_t}}{Sc_g}\right) - 0.5 & if\ v_{g,y_t} < 0 \end{cases} \quad \text{(A-4)}$$

$$\sigma(x) = \frac{1}{1+e^{-x}} \quad \text{(A-5)}$$

Step 4: Perceived risk bias adjustment

Before the adjustment, p_{g,y_t}^{adj} is converted into a vector of values of a discretized beta probability distribution computed from p_{g,y_t}^{adj} and N (Equation A-6).

$$P_{g,y_t}^{adj} \sim \text{Beta}(a, b) \tag{A-6}$$

where $a = p_{g,y_t}^{adj} \times N$, $b = (1 - p_{g,y_t}^{adj}) \times N$, and Beta is a beta distribution.

Then, we address the agent's personal bias according to their risk attitude through a prospect function (Kahneman & Tversky, 2013) with a small modification. The modified prospect function comprises two nonlinear convex or concave curves splitting by C_{g,y_t}, which represents the agent's risk attitude toward positive belief (more available water) and negative belief (less available water). For a positive belief (larger than C_{g,y_t}), the convex function indicates the agent is risk-seeking in positive belief, while the concave function indicates a risk-averse attitude. On the contrary, for negative beliefs, the convex function indicates risk-seeking and the concave function means risk-averse for the agents' attitude. The agent's perceived belief (P_{g,y_t}^{bias}) is then calculated by Equation A-7

$$P_{g,y_t}^{bias} = \begin{cases} \left(\frac{p - C_{g,y_t}}{1 - C_{g,y_t}}\right)^{\alpha_{ag}} \times \left(1 - C_{g,y_t}\right) + C_{g,y_t} & if \;\; p \in P_{g,y_t}^{adj}, p \geq C_{g,y_t} \\ \left(\frac{p - C_{g,y_t}}{C_{g,t}}\right)^{\beta_{ag}} \times C_{g,y_t} + C_{g,y_t} & if \;\; p \in P_{g,y_t}^{adj}, p < C_{g,y_t} \end{cases} \tag{A-7}$$

where α_g and β_g are curvatures of the nonlinear curves for the positive and negative beliefs, respectively.

Step 5: Linear mapping for generating a diversion-request-adjustment ratio

To map the perceived belief into a diversion-request-adjustment ratio (R_{ag,y_t}), a linear mapping function (Equation A-8) is applied.

$$R_{g,y_t} = \left(\left(\mathrm{ECDF}^{-1}_{P^{bias}_{g,y_t}}(u_{g,y_t}) \times 2 - 1\right) - \left(C_{g,y_t} - 0.5\right) \times 2\right) \times R_{g,max} \quad \text{(A-8)}$$

where u_g is a random number from a $\mathrm{Uniform}(0,1)$ distribution.

In Chapter 2, the R_{g,y_t} is represented by the expected value (R_g^{Exp}) for enhancing the calibration converging speed.

$$R^{Exp}_{g,y_t} = E_u\left[R_{g,y_t}\right] \quad \text{(A-9)}$$

In addition, to prevent the numerical error, the R^{Exp}_{g,y_t} is forced to be greater than -0.9. If it is below -0.9, the algorithm will replace it with -0.9.

Step 6: Disaggregate to daily diversion request input

The annual diversion request (Div_{g,y_t}) is first calculated by Equation A-10, then it is disaggregated into a daily scale by a fixed averaged daily diversion proportions computed by each district's observed diversion data from 1960 to 2005.

$$Div_{g,y_t} = R^{Exp}_{g,y_t} \times \frac{1}{N}\sum_{i=1}^{N} Div_{g,i} \quad \text{(A-10)}$$

A.4 Supplementary figures and tables

```
{"AgentName": ["ROZW", "SNCW", "TIEW", "KNCW", "KTCW", "RSCW"],
 "AgentSlots": {
    "KNCW": {"DivSlots": ["DIVERSION Kennewick.Diversion"],
             "FlowSlots": ["Yakima_River_at_Kiona.Gage_Inflow"]},
    "KTCW": {"DivSlots": ["DIVERSION Kittitas.Diversion"],
             "FlowSlots": ["Yakima_River_at_Parker_PARW.Gage_Inflow",
                           "Yakima_River_at_Kiona.Gage_Inflow"]},
    "ROZW": {"DivSlots": ["DIVERSION Roza Irrigation.Diversion"],
             "FlowSlots": ["Yakima_River_at_Parker_PARW.Gage_Inflow",
                           "Yakima_River_at_Kiona.Gage_Inflow"]},
    "RSCW": {"DivSlots": ["DIVERSION Reservation New.Diversion"],
             "FlowSlots": ["Yakima_River_at_Parker_PARW.Gage_Inflow",
                           "Yakima_River_at_Kiona.Gage_Inflow"]},
    "SNCW": {"DivSlots": ["DIVERSION Sunnyside.Diversion",
                          "Sunnyside 3:DistributionCanal0.Return Flow",
                          "Sunnyside 4:DistributionCanal0.Return Flow",
                          "Sunnyside 5:DistributionCanal0.Return Flow",
                          "Sunnyside 6:DistributionCanal0.Return Flow"],
             "FlowSlots": ["Yakima_River_at_Kiona.Gage_Inflow"]},
    "TIEW": {"DivSlots": ["DIVERSION Tieton.Diversion"],
             "FlowSlots": ["Yakima_River_at_Parker_PARW.Gage_Inflow",
                           "Yakima_River_at_Kiona.Gage_Inflow"]}},
 "FileContentDict": {
    "BatchFile": {
        "YAKRW2BatchFile.rcl": {
            "OtherActionList":
                ["SetRunInfo #RunInfo !InitDate {10-31-1960 24:00} !EndDate {12-31-2005 24:00}",
                 "StartController",
                 "InvokeDMI CYLin_FinalOutput"],
            "RWModelName": "YAKRW2_CYLin.mdl",
            "RWModelRuleName": "YAKRW2_CYLin_Final.rls"}},
    "ControlFile": {
        "DMIControlFile_ABM2RW.control": {
            "DataFolder": "ABM_Output_toRW",
            "ObjectList": ["ABM_Diversion.ABM_KNCW",
                           "ABM_Diversion.ABM_KTCW",
                           "ABM_Diversion.ABM_ROZW",
                           "ABM_Diversion.ABM_RSCW",
                           "ABM_Diversion.ABM_SNCW",
                           "ABM_Diversion.ABM_TIEW"],
            "Scales": "1.0",
            "Units": "cfs"},
        "DMIControlFile_RW2ABM.control": {
            "DataFolder": "RW_Output_toABM",
            "ObjectList": [
                "Yakima River at Parker PARW.Gage Inflow",
                "Yakima 202_0 at Easton EASW.Gage Inflow",
                "Yakima River at Kiona.Gage Inflow",
                "Naches 16_8 at Naches NACW.Gage Inflow",
                "Yakima 127_98 at Roza Dam RBDW.Gage Inflow",
                "DIVERSION Roza Irrigation.Diversion",
                "DIVERSION Sunnyside.Diversion",
                "Sunnyside 3:DistributionCanal0.Return Flow",
                "Sunnyside 4:DistributionCanal0.Return Flow",
                "Sunnyside 5:DistributionCanal0.Return Flow",
                "Sunnyside 6:DistributionCanal0.Return Flow",
                "DIVERSION Tieton.Diversion",
                "DIVERSION Kennewick.Diversion",
                "DIVERSION Kittitas.Diversion",
                "DIVERSION Reservation New.Diversion"],
            "Scales": "1.0",
            "Units": "cfs"},
        "DMIControlFile_FinalOutput.control": <Same as "DMIControlFile_RW2ABM.control">},
    "Simulation": {"ABMoffsetYear": 2,
                   "EndYear": 2005,
                   "StartYear": 1960}}}
```

Figure A3. *ModelSetting.json* of Coupled-YAKRW.

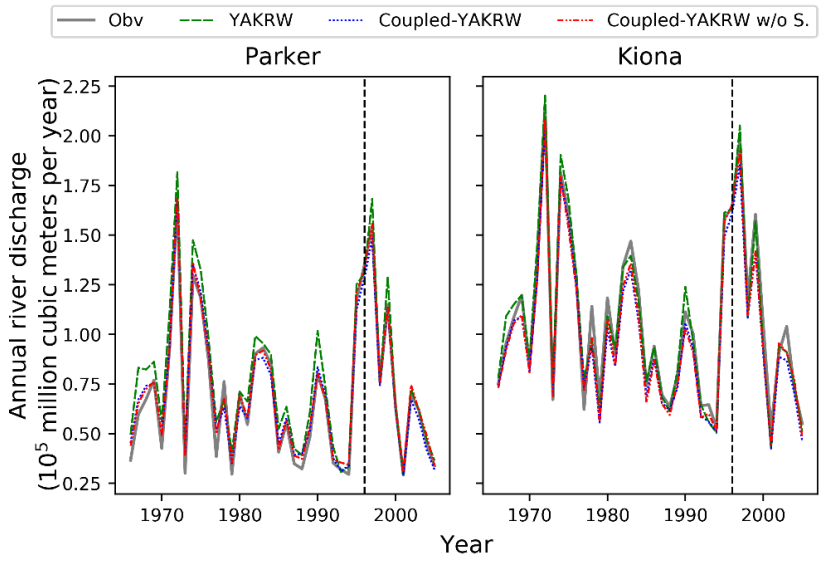

Figure A4. Model comparison of annual river discharges. Grey lines are the observed annual river discharges. Green dashed lines are the outputs of the original YAKRW model. Blue and red dotted lines are simulated results from coupled-YAKRW and coupled-YAKRW w/o S., respectively.

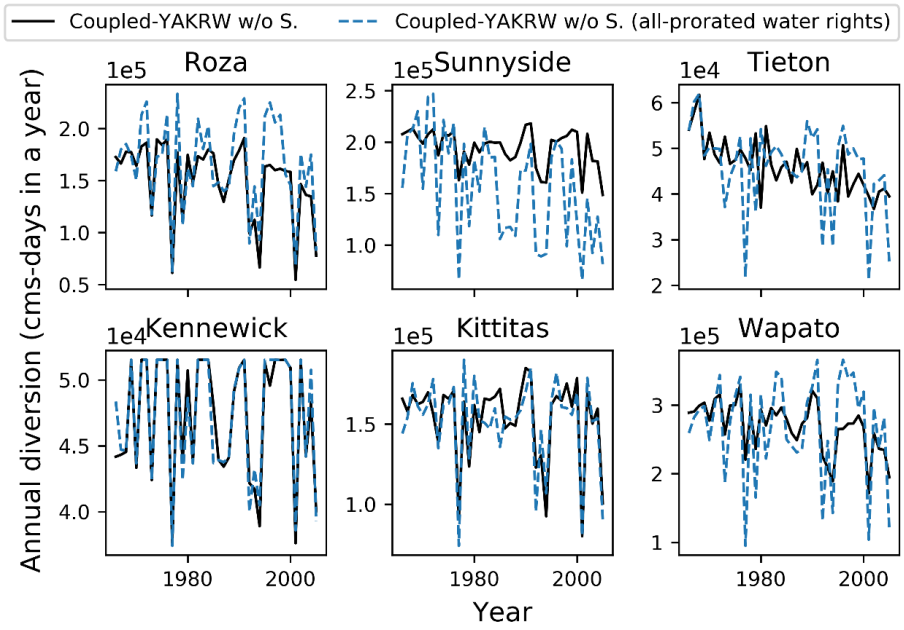

Figure A5. Model comparison of annual diversions with two water allocation setups (e.g., water rights) in Coupled-YAKRW w/o S. Black solid lines are the original Coupled-YAKRW w/o S. simulation results, while blue dotted lines are with an all-proratable-water-rights scenario.

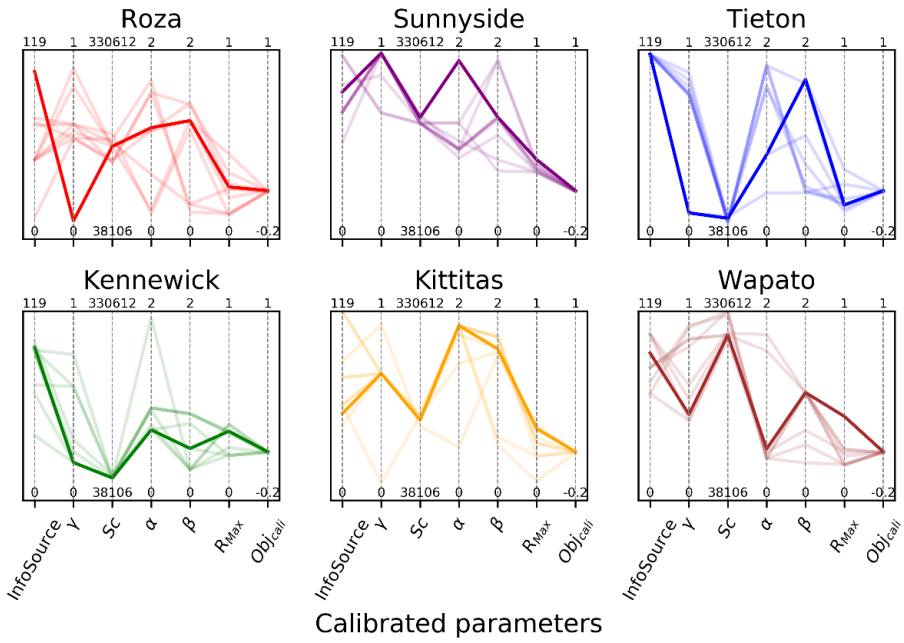

Figure A6. Equifinal parameter sets in Coupled-YAKRW w/o S. The equifinal parameter sets are selected by the top 1% of model performance (mean NSE) in the calibration period (Obj_{cali}). Darker lines represent the optimal parameter set.

Table A1. Calibrated parameters of Coupled-YAKRW.

Parameter	Roza	Sunnyside	Tieton	Kennewick	Kittitas	Wapato
γ	0.49	0.98	0.78	0.18	0.64	0.57
Sc	140300	205753	38107	47453	145720	296022
α	1.50	1.15	1.82	0.87	1.83	0.29
β	1.37	1.88	0.37	0.81	1.70	1.05
R_{max}	0.22	0.34	0.10	0.29	0.23	0.16

Table A2. Calibrated parameters of Coupled-YAKRW w/o S.

Parameter	Roza	Sunnyside	Tieton	Kennewick	Kittitas	Wapato
γ	0.32	0.02	1.00	0.11	0.00	0.75
Sc	160206	218155	41270	46129	167101	299637
α	0.93	0.68	0.55	1.46	0.24	1.18
β	1.06	0.80	0.83	1.22	0.07	1.33
R_{max}	0.03	0.04	0.21	0.26	0.17	0.03

Table A3. (a) Calibrated social network matrix and (b) the weight vector of the social norm.

(a)	Roza	Sunnyside	Tieton	Kennewick	Kittitas	Wapato
Roza		1	0	1	1	0
Sunnyside	0		1	1	1	1
Tieton	1	1		1	1	1
Kennewick	1	0	1		1	0
Kittitas	0	1	0	0		0
Wapato	1	0	1	1	0	

(b)	*Sw*
	0.51
	0.13
	0.09
	0.42
	0.86
	0.53

Appendix B: Supplementary Materials for Chapter 3

B.1 Agents' design for the Tualatin River Basin (TRB)

In this study, we design four types of agents (i.e., DivAgt, ResAgt, PipeAgt, and DrainAgt) to run the numerical experiment. These agents are programmed in the TRB_ABM module (*.py*), which is not included in the HydroCNHS package. Namely, users can integrate their human models (ABMs) with more sophisticated agent behaviors following the basic example in the TRB case study. Below are the simple behavior rules of the four agent types that we used in this study.

DivAgt

The diversion agent (DivAgt) makes monthly-diversion-request decisions at the beginning of each month and has a return flow back to the river. For this example, we design the diversion-request decisions from June to September to be governed by a linear function (i.e., y = ax + b), where the perfect forecast of monthly precipitation (Pr_m). Minor diversions in other months are filled with monthly mean values (Div_m [m^3/sec]) is the predictor. Note that we bound the monthly-diversion-request decision by the historical maximum ($Div_{max,m}$ [m^3/sec]) and minimum ($Div_{min,m}$ [m^3/sec]) monthly diversion values to prevent unrealistic decisions. The monthly-diversion-request decisions ($Div_{req,m}$) is calculated by

$$Div_{req,m} = \begin{cases} \min\left(max\left(Div_m + l_a \times Pr_m + l_b, Div_{min,m}\right), Div_{max,m}\right), & m \in 6\sim9 \\ Div_m, & otherwise \end{cases} \quad \text{(B-1)}$$

The actual daily diversion (Div_t [m^3/sec]; shown below) is constrained by the available water. We simply assume the available water equal to the streamflow ($Q_{r,t}$ [m^3/sec]) at the diversion outlet. l_a and l_b are the parameters for the linear function.

$$Div_t = \min\left(Q_{r,t}, Div_{req,m}\right), \quad \text{for all } t \in \text{timestep in } m \tag{B-2}$$

The return flow (Re_t [m^3/sec]) is determined by a calibrated factor (Fa_{re}).

$$Re_t = Fa_{re} \times Div_t \tag{B-3}$$

The historical diversion data source is shown in Table B2 (station code is SHPP).

ResAgt

The reservoir agent (ResAgt) determines reservoir releases (Res_t [m^3/sec]) by a generic operational rule modified from Neitsch et al. (2011), where target storages (Ts_t [m^3]) and target releases (Tr_t [m^3/sec]) are adopted for flood control (October - May) and storage control (June - September) period.

For the flood control period, releases are computed by

$$Res_t = \begin{cases} \max\left(\frac{S_{t-1}+I_t-Ts_t}{86400}, Res_{min}\right), & S_{t-1} + I_t \geq S_{min} \\ 0, & otherwise \end{cases} \tag{B-4}$$

$$S_t = S_{t-1} + I_t - Res_t \times 86400 \tag{B-5}$$

where S_t [m^3] is storage at time t and S_{min} [m^3] is the inactive (dead) storage. Res_{min} [m^3/sec] is a constant minimum release. I_t [m^3/sec] is the inflow. We adopted daily values interpolated over 95% quantile of historical monthly storage from 1981 to 2013 as our target storage.

For the storage control period, releases are computed by

$$Res_t = \begin{cases} \frac{S_{t-1}+I_t-S_{max,t}}{86400}, & S_{temp,t} \geq S_{max,t} \\ \frac{S_{t-1}+I_t-S_{q5,t}}{86400}, & S_{temp,t} \leq S_{q5,t} \\ Tr_t, & otherwise \end{cases} \tag{B-6}$$

$$S_{temp,t} = S_{t-1} + I_t - Tr_t \times 86400 \quad \text{(B-7)}$$

where the target releases are constrained by the $S_{max,t}$ [m^3] and $S_{q5,t}$ [m^3] that are calculated by the daily values interpolated over the maximum and 5% quantile of historical monthly storages from 1981 to 2013, respectively. The target releases are the daily values interpolated over 50% quantile of historical monthly releases from 1981 to 2013. The data sources of historical storage (station code is SCO) and release (station code is SCOO) values are in Table B2.

PipeAgt

The trans-basin aqueduct (PipeAgt) conveys water from the Barney reservoir (outside the TRB) to the outlet TRTR. For simplicity, we didn't model the Barney reservoir (i.e., diversion outside of the TRB) and assigned the amount of conveying water (C_t [m^3/sec]) to TRTR with observed median values of each month, where the data source is shown in Table B2 with station code TRTR.

$$C_t = C_m \qquad \text{for all } t \in \text{timesteps in } m \quad \text{(B-8)}$$

DrainAgt

DrainAgt is coupled through InSitu API, which is used to test the runoff-changing scenario. One of the possible reasons for altering the runoff in a subbasin is urbanization (Gwenzi et al., 2014). Therefore, in this scenario, we assume a linear change of the urbanized area in the DAIRY and RCTV subbasins from 5% to 50% ($ratio_t$), where each unit of urbanization increases unit runoff by 75% (Gwenzi et al., 2014).

$$Eu_t = ratio_t \times 0.75 \times F_t \quad \text{(B-9)}$$

where Eu_t is the runoffs change and F_t is the original subbasin runoff.

B.2 Calibration setting for the TRB

In the TRB case study, we calibrate two coupled models (M_{gwlf} and M_{abcd}) with two different LSMs, GWLF and ABCD. The calibration information, including the number of calibrating parameters and the calibration targets for these two models, is shown in Table B1. The calibrating parameters' boundaries are shown in

Table 3-1. The calibration objective is the mean KGE of calibration targets (Table B1). KGE (Gupta et al., 2009) is calculated by

$$\mathrm{KGE} = 1 - \sqrt{(r-1)^2 + \left(\frac{\sigma_{sim}}{\sigma_{obs}} - 1\right)^2 + \left(\frac{\mu_{sim}}{\mu_{obs}} - 1\right)^2} \quad \text{(B-10)}$$

where r is the Pearson correlation coefficient. μ and σ denote the mean and the standard deviation of flows, respectively. The subscripts obs and sim refer to observed and simulated time series of streamflow, respectively. The calibration targets are compared with monthly observations from stations with codes SHPP, SCOO, DLLO, and WSLO (Table B2). SHPP is used to calibrate the diversions of DivAgt. SCOO streamflow station located below the Hagg reservoir is used to calibrate water releases of ResAgt. Streamflow stations, DLLO and WSLO, are used to calibrate simulated streamflow at DLLO and WSLO routing outlets.

Table B1. Calibration information for two coupled models with GWLF and ABCD, respectively.

Model	M_{gwlf}	M_{abcd}
Number of parameters	92	64
Random seeds	5, 10, 13	5, 10, 13
Population size	200	200
Maximum generation	100	100
Initial population sampling method	Latin hypercube	Latin hypercube
Number of elites	1	1
Mutation probability	0.1	0.1
Crossover probability (uniform)	0.5	0.5
Indicator	KGE	KGE
Calibrate targets	ResAg, DLLO, DivAg, and WSLO	ResAg, DLLO, DivAg, and WSLO

Table B2. Stations' information and data sources of observed data

Code	Full station name	Station number	Data source
SCOO	Scoggins Creek below Henry Hagg Lake, Oregon	14202980	USBR[a]
DLLO	Tualatin River near Dilley, Oregon	14203500	USBR[a]
WSLO	Tualatin River near West Linn, Oregon	14207500	USBR[a]
TRTR	Barney Reservoir (Trask River) Release to Tualatin River	--	(Bonn, 2020)[b]
SHPP	TVID–Withdrawal at Spring Hill Pump Plant	14204650	(Bonn, 2020)[b]
SCO	Scoggins Dam & Henry Hagg Lake nr Forest Grove, Oregon	--	USBR[a]

[a] The US Bureau of Reclamation (USBR) Hydromet platform: https://www.usbr.gov/pn/hydromet/tuatea.html

[b] Monthly median of instantaneous flows is provided in the PDF file.

Appendix C: Supplementary Materials for Chapter 4

C.1 Derivation of the law of total variance

$$\mathrm{Var}(I) = \mathrm{E}[\mathrm{Var}(I|EMR)] + \mathrm{Var}(\mathrm{E}[I|EMR]) \quad \text{(C-1)}$$

To derive the law of total variance (Equation C-1), we first expand $\mathrm{Var}(I)$ following the definition of variance as shown below.

$$\mathrm{Var}(I) = \mathrm{E}[I^2] - \mathrm{E}[I]^2 \quad \text{(C-2)}$$

Then, by applying the law of total expectation (e.g., $\mathrm{E}[X] = \mathrm{E}[\mathrm{E}[X|Y]]$), we can get

$$\mathrm{Var}(I) = \mathrm{E}\big[\mathrm{E}[I^2|EMR]\big] - \mathrm{E}\big[\mathrm{E}[I|EMR]\big]^2 \quad \text{(C-3)}$$

Next, expand the first term again by the definition of variance.

$$\mathrm{Var}(I) = \mathrm{E}[\mathrm{Var}(I|EMR) + \mathrm{E}[I|EMR]^2] - \mathrm{E}\big[\mathrm{E}[I|EMR]\big]^2 \quad \text{(C-4)}$$

Reordering the equation, we then derive the law of total variance.

$$\begin{aligned}\mathrm{Var}(I) &= \mathrm{E}[\mathrm{Var}(I|EMR) + \mathrm{E}[I|EMR]^2] - \mathrm{E}\big[\mathrm{E}[I|EMR]\big]^2 \\ &= \mathrm{E}[\mathrm{Var}(I|EMR)] + \mathrm{E}[\mathrm{E}[I|EMR]^2] - \mathrm{E}\big[\mathrm{E}[I|EMR]\big]^2 \\ &= \mathrm{E}[\mathrm{Var}(I|EMR)] + \mathrm{Var}(\mathrm{E}[I|EMR]) \quad \text{(C-5)}\end{aligned}$$

C.2 Derivation of the law of total variance with two conditioning random variables

$$E[Var(I|EMR)] = \mathrm{E}[\mathrm{Var}(I|EMR, ICR\ )] + \mathrm{E}[\mathrm{Var}(\mathrm{E}[I|EMR, ICR\ ])|EMR)] \quad \text{(C-6)}$$

The law of total variance (Equation C-1) can be applied to two conditioning random variables as shown in Equation C-6.

From Equation C-1, we know

$$\mathrm{Var}(I) = \mathrm{E}[\mathrm{Var}(I|EMR)] + \mathrm{Var}(\mathrm{E}[I|EMR]) \quad \text{(C-7)}$$

where $\mathrm{Var}(I|EMR)$ can be further decomposed into:

$$\mathrm{Var}(I|EMR) = \mathrm{E}[\mathrm{Var}(I|EMR, ICR)] + \mathrm{Var}(\mathrm{E}[I|EMR, ICR]) \quad \text{(C-8)}$$

by applying the law of total variance. Therefore, we can get

$$\mathrm{E}[\mathrm{Var}(I|EMR)] = \mathrm{E}[\mathrm{E}[\mathrm{Var}(I|EMR, ICR)] + \mathrm{Var}(\mathrm{E}[I|EMR, ICR])]$$

$$= \mathrm{E}\big[\mathrm{E}[\mathrm{Var}(I|EMR, ICR)]\big] + \mathrm{E}[\mathrm{Var}(\mathrm{E}[I|EMR, ICR])] \quad \text{(C-9)}$$

From the law of total expectation, we can further remove the double expectation in the first term and get

$$\mathrm{E}[\mathrm{Var}(I|EMR)] = \mathrm{E}[\mathrm{Var}(I|EMR, ICR)] + \mathrm{E}[\mathrm{Var}(\mathrm{E}[I|EMR, ICR])] \quad \text{(C-10)}$$

Finally, put back the above equation to Equation C-1.

$$\mathrm{Var}(I) = \mathrm{E}[\mathrm{Var}(I|EMR, ICR)] + \mathrm{E}[\mathrm{Var}(\mathrm{E}[I|EMR, ICR])] + \mathrm{Var}(\mathrm{E}[I|EMR]) \quad \text{(C-11)}$$

C.3 Supplementary figures and tables

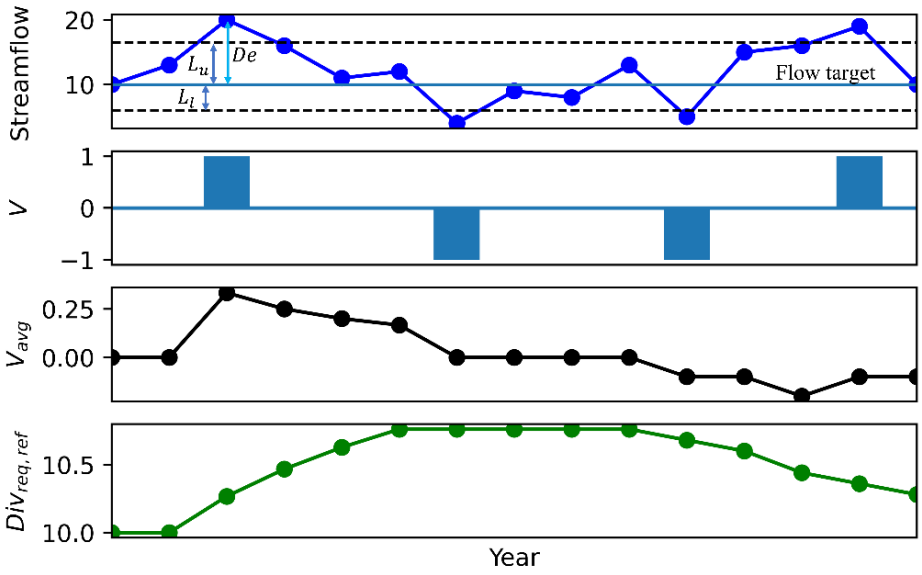

Figure C1. An example for the learning component. First, if the flow deviation (De) is greater than L_u, V is equal to 1. If De is less than L_l, V is equal to -1. Otherwise, V is equal to 0. Next, we use a ten-year moving window to calculate V_{avg}, which serves as a strength to drive the changes in diversion reference ($Div_{req,ref}$).

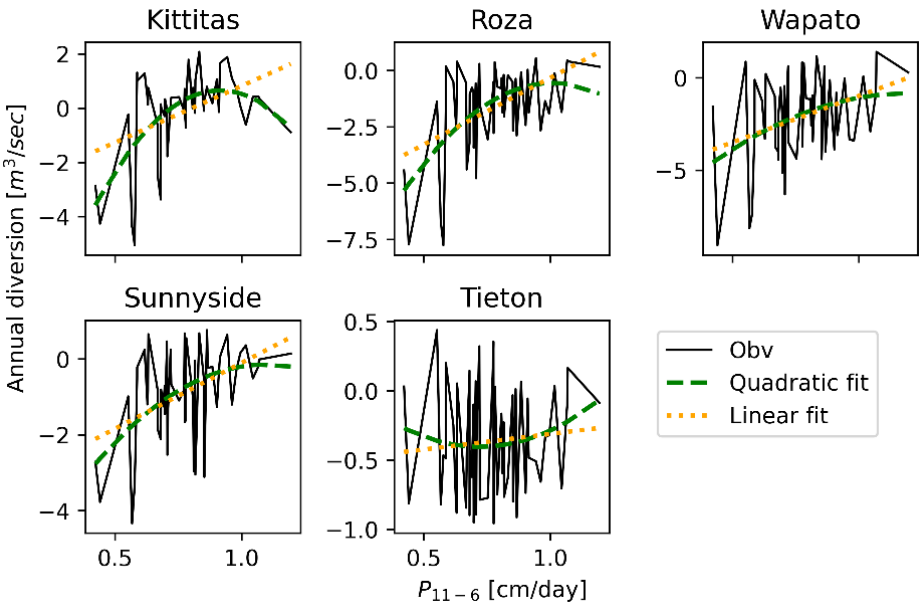

Figure C2. The relationship between precipitation from November to June vs. annual diversion for adaptive behavior curve fitting using quadratic (green dashed line) and linear (yellow dotted) functions.

```
Initialize release_output = []
Initialize previous_storage
Input forecast_inflow
For y in range(number of years):
  For m in range(12 months):
    monthly_release = f(forecast_inflow, previous_storage)
    storage = f(forecast_inflow, previous_storage, monthly_release)
    If check storage with maximum and minimum criteria fail:
      Update monthly_release
      Update storage
    daily_release = uniformly convert monthly_release
    release_output.append(daily_release)
    previous_storage = storage
```

Figure C3. Pseudo-code for the reservoir release model.

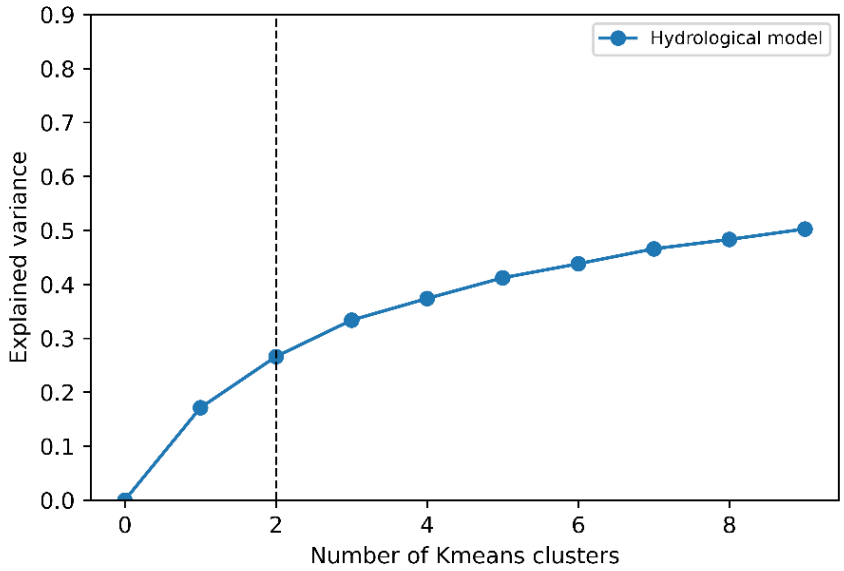

Figure C4. Elbow plot for determining the number of HydroEMRs.

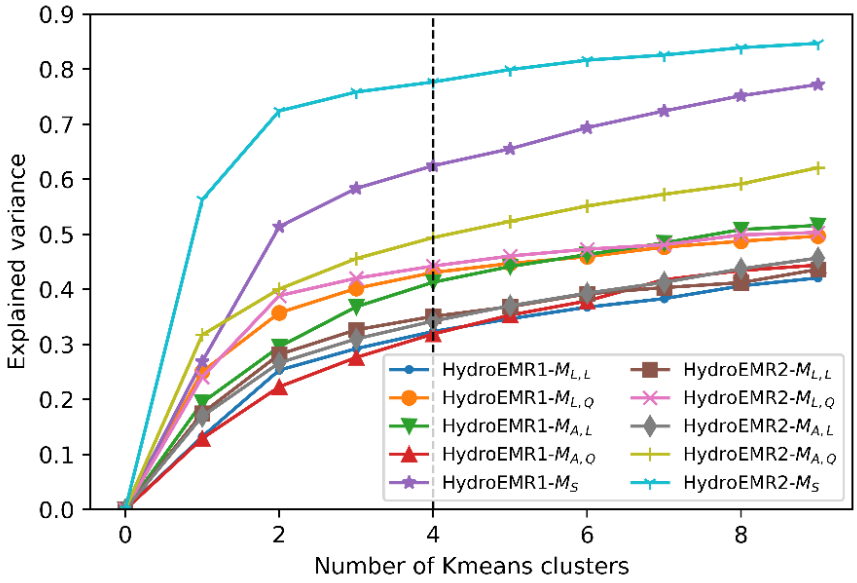

Figure C5. Elbow plot for determining the number of ABMEMRs. Note the goal is to represent the range of model variability. Therefore, the selected cluster number should include the elbow.

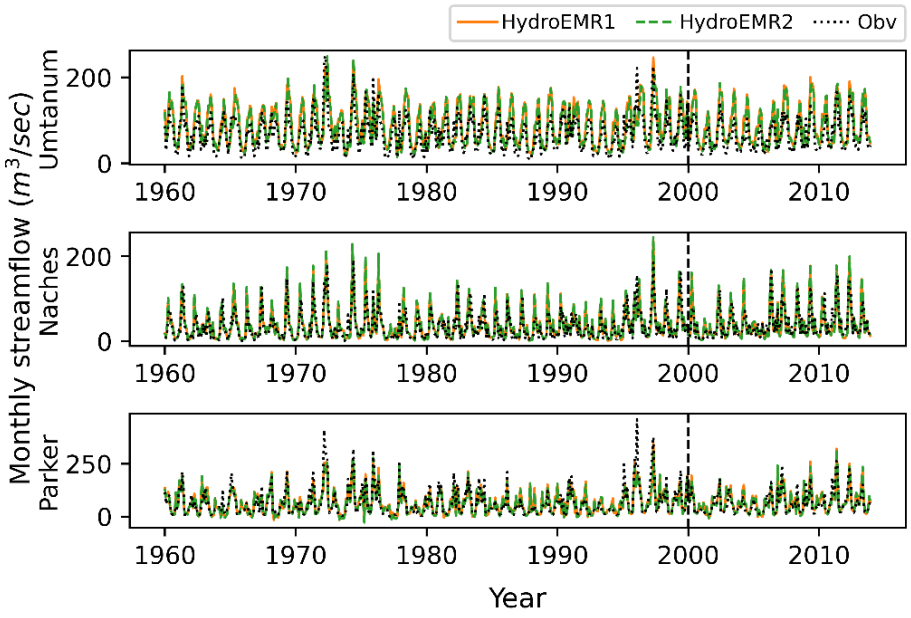

Figure C6. Calibration (1960 – 1999) and validation (2000 – 2013) monthly time series streamflow of two HydroEMRs for three sub-basins, Umtanum, Naches, and Parker. We have considered the calibrated minor diversions (Table C5) for the Parker gauge in this figure.

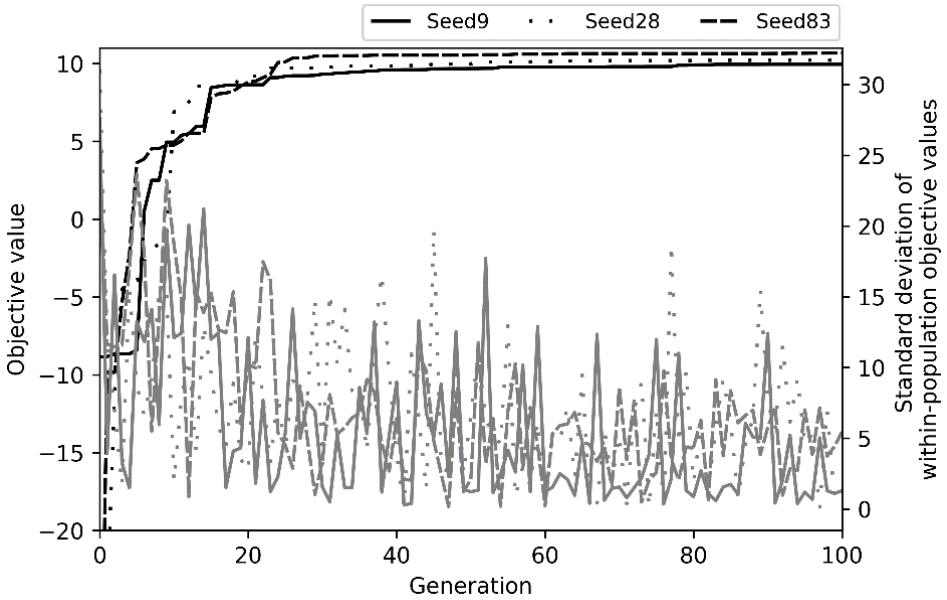

Figure C7. Performance of GA for hydrological model calibration. Black lines are objective values of three random seeds. Grey lines are the standard deviation of within-population objective values.

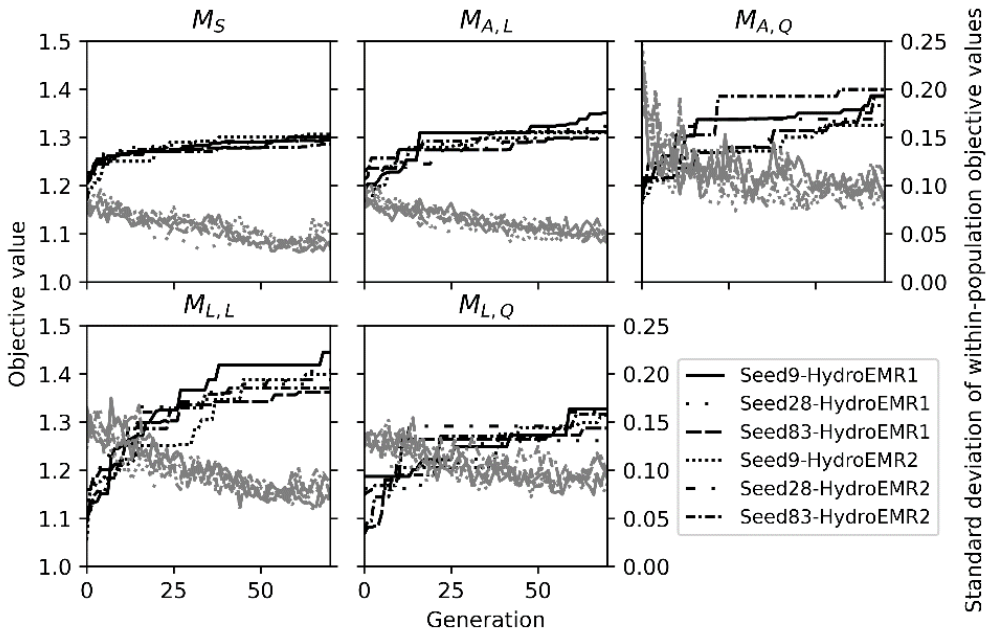

Figure C8. Performance of GA for the calibration of five coupled models. Black lines are objective values of three random seeds and two HydroEMRs. Grey lines are the standard deviation of within-population objective values.

Table C1. District area, water rights, and average water diversion of five irrigation districts.

District	Area (ha)	Water rights ($m^3/sec \times 10^6$)[a]			Avg. diversion in 2001–2010 (m^3/sec)
		Non-proratable[b]	Proratable[b]	Total	
Wapato	77239.11	376.97	431.72	808.69	20.31
Sunnyside	44947.22	357.27	194.61	551.89	15.26
Roza	38394.95	0	484.76	484.76	10.88
Kittitas	58025.04	0	414.45	414.45	11.91
Tieton	17057.5	93.58	37.53	131.11	2.96

[a] (USBR, 2012)

[b] Proratable water right holders will receive a prorated entitlement during the droughts period, while non-proratable water right holders will receive full entitlements.

Table C2. Selected GCMs for the climate change scenario setup.

Selected GCMs			
GISS-E2-H	NorESM1-ME	HadGEM2-ES	GFDL-ESM2G
CSIRO-Mk3-6-0	NorESM1-M	GISS-E2-R	IPSL-CM5A-LR
CCSM4	MIROC5	CESM1-CAM5	FIO-ESM
MIROC-ESM-CHEM	IPSL-CM5A-MR	bcc-csm1-1-m	MIROC-ESM
HadGEM2-AO	GFDL-CM3	bcc-csm1-1	MRI-CGCM3

Table C3. Genetic algorithm setting for calibrating reservoir inflow models, hydrological model, and ABM models.

Items	S1, S2, and S3	Hydrological model[1]	ABM models[2] $-M_S, M_{A,L}, M_{A,Q}, M_{L,L}, M_{L,Q}$ (coupled with a HydroEMR identified from the hydrological model calibration)
Population size	100	100	100
Maximum generation	100	100	70
Number of simulations per evaluation	--	--	10 (due to stochastic components)
Initial seeds	9, 28, 83	9, 28, 83	9, 28, 83
Initial population sampling method	Latin hypercube	Latin hypercube	Latin hypercube
Number of elites	1	1	1
Mutation probability	0.1	0.1	0.1
Crossover probability (uniform)	0.5	0.5	0.5
Objective function	$\mathrm{Max}\{\mathrm{KGE}\}$	$\mathrm{Max}\{\overline{\mathrm{KGE_F}} + 10 \times (1 - \overline{D})\}$	$\mathrm{Max}\{\overline{\mathrm{KGE_{F\&D}}} + (1 - \overline{D})\}$
Number of parameters	11 per S	47 + two R_f[3]	10, 20, 25, 35, and 40 for five agent types, respectively.

[1] Include three subbasins, Umtanum, Naches, and Parker.
[2] Include five diversion agents, Kittitas, Tieton, Roza, Wapato, and Sunnyside.
[3]Return flow factors (R_f) of ABM models are calibrated beforehand with the hydrological model.
$\overline{D}$ is the average annual diversion shortage of five diversion agent over the simulation period.
$\overline{\mathrm{KGE_F}}$ is the average KGE value of three subbasins monthly streamflow[1].
$\overline{\mathrm{KGE_{F\&D}}}$ is the average KGE value of three subbasins monthly streamflow[1] and five annual diversions[2].

Table C4. ODD+D description for ABM model.

Guiding questions			ODD+D model description
Overview	I.i Purpose	I.i.a What is the purpose of the study?	To test the hypothesis of the relationship between decomposed model uncertainty and model complexity.
		I.ii.b For whom is the model designed?	Scientists, decision-makers, and students/teachers
	I.ii Entities, state variables, and scales	I.ii.a What kinds of entities are in the model?	We design five types of irrigation diversion agents. An agent represents one of the five irrigation districts in the Yakima River Basin.
		I.ii.b By what attributes (i.e., state variables and parameters) are these entities characterized?	We design four components: (1) learning, (2) adaptive with linear or quadratic functions, (3) emergency response, and (4) stochastic components, where five types of agents have different components (Table 4-2)
		I.ii.c What are the exogenous factors / drivers of the model?	Climate, weather, reservoir releases, and streamflow.
		I.ii.d If applicable, how is space included in the model?	Agents are defined based on irrigation districts' geolocation and space.
		I.ii.e What are the temporal and spatial resolutions and extents of the model?	Model runs on a daily scale and the decision is made annually. Each agent represents one irrigation district.
	I.iii Process overview and scheduling	I.iii.a What entity does what, and in what order?	If the given agent type has the components, the order of the process is learning, adaptive or emergency response, and stochastic components.
Design Concepts	II.i Theoretical and Empirical Background	II.i.a Which general concepts, theories or hypotheses are underlying the model's design at the system level or at the level(s) of the submodel(s) (apart from the decision model)? What is the link to	None. The model is empirically designed for testing the hypothesis.

		complexity and the purpose of the model?	
		II.i.b On what assumptions is/are the agents' decision model(s) based?	The decision-making mechanism is derived from historical observations.
		II.i.c Why is a/are certain decision model(s) chosen?	The model is designed to compare the uncertainty impact of different model complexities.
		II.i.d If the model / a submodel (e.g., the decision model) is based on empirical data, where does the data come from?	Hydromet platform.
		II.i.e At which level of aggregation were the data available?	No aggregation. The data is at the irrigation district's level.
	II.ii Individual Decision Making	II.ii.a What are the subjects and objects of decision-making? On which level of aggregation is decision-making modeled? Are multiple levels of decision-making included?	Single level.
		II.ii.b What is the basic rationality behind agents' decision-making in the model? Do agents pursue an explicit objective or have other success criteria?	The learning process is bounded by some expansion of the range calculated by the historical data.
		II.ii.c How do agents make their decisions?	Random choice but based on the procedure in I.iii.a.
		II.ii.d Do the agents adapt their behavior to changing endogenous and exogenous state variables? And if yes, how?	Yes, through learning and adaptive components.
		II.ii.e Do social norms or cultural values play a role in the decision-making process?	Yes. We consider social norms derived from historical diversion data.

		II.ii.f Do spatial aspects play a role in the decision process?	The spatial aspects are not explicitly designed.
		II.ii.g Do temporal aspects play a role in the decision process?	Yes. A ten-year window is used in the learning process.
		II.ii.h To which extent and how is uncertainty included in the agents' decision rules?	The uncertainty of an agent's decision is based on the calibrated parameters in the stochastic component.
	II.iii Learning	II.iii.a Is individual learning included in the decision process? How do individuals change their decision rules over time as consequence of their experience?	Yes, by the learning component.
		II.iii.b Is collective learning implemented in the model?	No
	II.iv Individual Sensing	II.iv.a What endogenous and exogenous state variables are individuals assumed to sense and consider in their decisions? Is the sensing process erroneous?	Precipitation forecast and streamflow deviation from the flow target.
		II.iv.b What state variables of which other individuals can an individual perceive? Is the sensing process erroneous?	The interaction is implicitly defined by a multivariate normal distribution with the covariance matrix calculated historical diversion data among irrigation districts.
		II.iv.c What is the spatial scale of sensing?	The entire model spaces.
		II.iv.d Are the mechanisms by which agents obtain information modeled explicitly, or are individuals simply assumed to know these variables?	Individuals are simply assumed to know these variables.
		II.iv.e Are costs for cognition and costs for	No.

		gathering information included in the model?	
	II.v Individual Prediction	II.v.a Which data uses the agent to predict future conditions?	Precipitation forecast and their experience.
		II.v.b What internal models are agents assumed to use to estimate future conditions or consequences of their decisions?	Four components mentioned in I.iii.a.
		II.v.c Might agents be erroneous in the prediction process, and how is it implemented?	False predict for drought years and irrational (stochastic) decision-making process.
	II.vi Interaction	II.vi.a Are interactions among agents and entities assumed as direct or indirect?	Indirect through streamflow and multivariate normal distribution.
		II.vi.b On what do the interactions depend?	Interaction depends on the covariance estimated by the historical data.
		II.vi.c If the interactions involve communication, how are such communications represented?	Not applicable.
		II.vi.d If a coordination network exists, how does it affect the agent behaviour? Is the structure of the network imposed or emergent?	Agents will share the irrigation deficiency based on their water rights.
	II.vii Collectives	II.vii.a Do the individuals form or belong to aggregations that affect, and are affected by, the individuals? Are these aggregations imposed by the modeller or do they emerge during the simulation?	No.

		II.vii.b How are collectives represented?	The streamflow at the Parker gauge.
	II.viii Heterogeneity	II.viii.a Are the agents heterogeneous? If yes, which state variables and/or processes differ between the agents?	Yes. Each agent has its own parameter set.
		II.viii.b Are the agents heterogeneous in their decision-making? If yes, which decision models or decision objects differ between the agents?	Yes. Their decision-making process depends on their unique parameter set.
	II.ix Stochasticity	II.ix.a What processes (including initialization) are modeled by assuming they are random or partly random?	Show in the stochastic component, where the random number is sampled from a multivariate normal distribution.
	II.x Observation	II.x.a What data are collected from the ABM for testing, understanding, and analyzing it, and how and when are they collected?	Diversion data from the Hydromet platform.
		II.x.b What key results, outputs or characteristics of the model are emerging from the individuals? (Emergence)	The decreasing trend in diversion (learning adaptive agents)
Details	II.i Implementation Details	III.i.a How has the model been implemented?	We coded the model in python and ran it on the Windows system.
		III.i.b Is the model accessible and if so where?	No.
	III.ii Initialization	III.ii.a What is the initial state of the model world, i.e. at time t=0 of a simulation run?	The historical values of the time previous to the beginning of the simulation.
		III.ii.b Is initialization always the same, or is it allowed to vary among simulations?	Yes, it is the same.
		III.ii.c Are the initial values chosen arbitrarily or based on data?	Based on the historical data.

	III.iii Input Data	III.iii.a Does the model use input from external sources such as data files or other models to represent processes that change over time?	Yes. The input data includes precipitation forecast, reservoir releases, and streamflow.
	III.iv Submodels	III.iv.a What, in detail, are the submodels that represent the processes listed in 'Process overview and scheduling?	Please see section 3.2 in the main text.
		III.iv.b What are the model parameters, their dimensions and reference values?	The model dimension varies with different model types (Table 4-2).
		III.iv.c How were submodels designed or chosen, and how were they parameterized and then tested?	We designed different components to capture the historical diversion pattern empirically. Parameters are calibrated by a genetic algorithm.

Table C5. Calibrated minor diversions during the growing season (April to October) above Parker gauge.

Month	1	2	3	4	5	6	7	8	9	10	11	12
Minor diversion above Parker (m^3/sec)	0	0	0	56.0	42.0	11.2	44.1	43.9	23.8	14.2	0	0

Table C6. Genetic algorithm calibration statistics of reservoir inflow models, hydrological models, and ABM models.

Model		The best objective value	Calibration objective values (Table C3)	Average improve rate[a]	Average within-population objective values standard deviation[a]
S1		0.85	(0.812, 0.842, 0.85)	(0.0, 0.001, 0.0)	(0.068, 0.096, 0.101)
S2		0.894	(0.894, 0.886, 0.838)	(0.0, 0.0, 0.001)	(0.084, 0.066, 0.052)
S3		0.818	(0.577, 0.795, 0.818)	(0.002, 0.0, 0.0)	(0.059, 0.139, 0.139)
Hydrological model		10.666	(9.945, 10.212, 10.666)	(0.0, 0.0, 0.002)	(1.873, 2.618, 4.921)
HydroEMR1[b]	M_S	1.302	(1.302, 1.302, 1.294)	(0.0, 0.0, 0.0)	(0.036, 0.037, 0.043)
	$M_{A,L}$	1.351	(1.351, 1.334, 1.312)	(0.0, 0.003, 0.0)	(0.047, 0.052, 0.056)
	$M_{A,Q}$	1.387	(1.387, 1.366, 1.385)	(0.004, 0.0, 0.007)	(0.095, 0.081, 0.101)
	$M_{L,L}$	1.445	(1.445, 1.408, 1.362)	(0.005, 0.001, 0.0)	(0.071, 0.069, 0.083)
	$M_{L,Q}$	1.327	(1.327, 1.267, 1.287)	(0.0, 0.001, 0.0)	(0.088, 0.085, 0.107)
HydroEMR2[b]	M_S	1.307	(1.307, 1.292, 1.287)	(0.0, 0.0, 0.0)	(0.056, 0.041, 0.044)
	$M_{A,L}$	1.312	(1.311, 1.312, 1.312)	(0.0, 0.003, 0.0)	(0.048, 0.047, 0.05)
	$M_{A,Q}$	1.4	(1.337, 1.345, 1.4)	(0.002, 0.002, 0.0)	(0.096, 0.08, 0.116)
	$M_{L,L}$	1.4	(1.4, 1.388, 1.371)	(0.0, 0.0, 0.0)	(0.073, 0.067, 0.094)
	$M_{L,Q}$	1.328	(1.326, 1.328, 1.316)	(0.005, 0.001, 0.0)	(0.087, 0.099, 0.107)

Three values in a bracket represent the statistics corresponding to three random seeds, 9, 28, and 83, respectively.

In the adaptive model, quadratic functions can better capture the dynamics that learning behavior captures (higher objective value in $M_{A,Q}$). However, quadratic functions become noised to the learning behavior in the learning adaptive models, where the objective value of $M_{L,Q}$ is lower than $M_{L,L}$.

[a] The statistics are averaged over the last five generations.

[b] HydroEMR1 and HydroEMR2 are identified from the hydrological model calibration.

Appendix D: Supplementary Materials for Chapter 5

D.1 Construction of a state-space model for a given pond network

A state-space model can linearly describe state (e.g., water level) dynamics, as shown in Equations D-1 and D-2.

$$\boldsymbol{x_t} = A \cdot \boldsymbol{x_{t-1}} + B_u \cdot \boldsymbol{u_{t-1}} + B_w \cdot \boldsymbol{w_{t-1}} \quad \text{(D-1)}$$

$$\boldsymbol{y_t} = C \cdot \boldsymbol{x_t} \quad \text{(D-2)}$$

where $\boldsymbol{x_t}$ is a state vector, and $\boldsymbol{y_t}$ is an output vector at the time step t. $\boldsymbol{u_{t-1}}$ is a control vector, and $\boldsymbol{w_{t-1}}$ is a disturbance vector, respectively. A, B_u, B_w, and C are state matrix, control matrix, disturbance matrix, and output matrix, respectively.

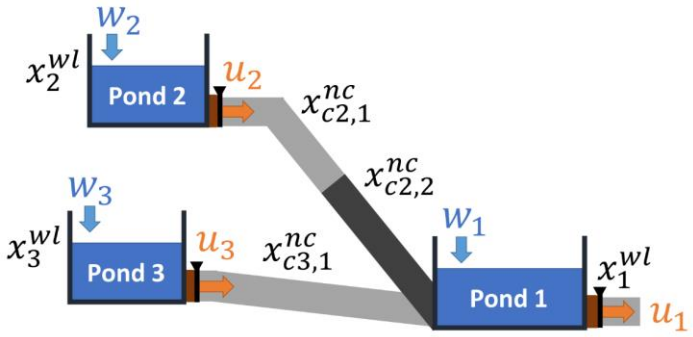

Figure D1. A three-pond stormwater system for state-space model construction demonstration. $\boldsymbol{w}$ and $\boldsymbol{u}$ are runoffs and outflows, respectively. $\boldsymbol{x}$ are states including water level (with wl superscript) and water quantities in segments of a conduit (with nc superscript).

In a smart stormwater system context, as shown in a three-pond stormwater system in Figure D1, $\boldsymbol{x}$ consists of pond water level states (x^{wl}) and water quantity states of segments of a conduct c (x_c^{nc}). Terms $\boldsymbol{w}$ and $\boldsymbol{u}$ are runoffs and outflows of each pond,

respectively. A, B_u, and B_w describe the topology of a given pond network. C is a matrix to collect x^{wl} from $\boldsymbol{x}$ (contain x^{wl} and x_c^{nc}), where $\boldsymbol{y}$ is defined as the water level measurements acquired from sensors (ignoring sensor noises). We demonstrate a state-space model construction for a given stormwater system below, where Equation D-1 can be rewritten into Equation D-3 for the stormwater system shown in Figure D1.

$$\boldsymbol{x_t} = \begin{bmatrix} x_2^{wl} \\ x_{c2,1}^{nc} \\ x_{c2,2}^{nc} \\ x_3^{wl} \\ x_{c3,1}^{nc} \\ x_1^{wl} \end{bmatrix}_{\mathrm{t}} = \overbrace{\begin{bmatrix} 1 & 0 & 0 & 0 & 0 & 0 \\ 0 & 0 & 0 & 0 & 0 & 0 \\ 0 & 1 & 0 & 0 & 0 & 0 \\ 0 & 0 & 0 & 1 & 0 & 0 \\ 0 & 0 & 0 & 0 & 0 & 0 \\ 0 & \frac{a_{s,2}}{n_{c2}a_{s,1}} & \frac{a_{s,2}}{n_{c2}a_{s,1}} & 0 & \frac{a_{s,3}}{n_{c3}a_{s,1}} & 1 \end{bmatrix}}^{A} \cdot \begin{bmatrix} x_2^{wl} \\ x_{c2,1}^{nc} \\ x_{c2,2}^{nc} \\ x_3^{wl} \\ x_{c3,1}^{nc} \\ x_1^{wl} \end{bmatrix}_{\mathrm{t-1}}$$

$$+ \overbrace{\begin{bmatrix} 0 & 1 & 0 \\ 0 & -1 & 0 \\ 0 & 0 & 0 \\ 0 & 0 & 1 \\ 0 & 0 & -1 \\ 1 & 0 & 0 \end{bmatrix}}^{B_u} \cdot \begin{bmatrix} u_1 \\ u_2 \\ u_3 \end{bmatrix}_{\mathrm{t-1}} + \overbrace{\begin{bmatrix} 0 & 1 & 0 \\ 0 & 0 & 0 \\ 0 & 0 & 0 \\ 0 & 0 & 1 \\ 0 & 0 & 0 \\ 1 & 0 & 0 \end{bmatrix}}^{B_w} \cdot \begin{bmatrix} w_1 \\ w_2 \\ w_3 \end{bmatrix}_{t-1} \quad \text{(D-3)}$$

Note that $\boldsymbol{x_t}$, $\boldsymbol{u_{t-1}}$, and $\boldsymbol{w_{t-1}}$ are represented in the water level change of their corresponding ponds in a length unit (i.e., cm). For example, $w_{1,t}$ is expressed in the water level change of Pond 1 caused by the runoff at time t. x_{c2}^{nc} is depicted by the water level change of Pond 2. Therefore, we have conversion factors $\frac{a_{s,2}}{a_{s,1}}$ and $\frac{a_{s,3}}{a_{s,1}}$ in the last row of matrix A to convert the water level change of Pond 2 and 3 to the water level change of Pond 1 when calculating the inflow of Pond 1 from conduits 2 and 3. The term $\frac{1}{n_c}$ is for a linear routing process (Equation D-4):

$$I_{c,t} = \frac{1}{n_c}\sum_{i=1}^{n_c} x_{c_i,t} \tag{D-4}$$

where I_c is the inflow from the conduit c, presented in the water level change of the destination pond. To provide a more intuitive presentation of the water level dynamics of a pond, we show $x_{1,t}^{wl}$ calculation in Equation D-5.

$$x_{1,t}^{wl} = x_{1,t-1}^{wl} + \underbrace{\overbrace{\frac{a_{s,2}}{n_{c2}a_{s,1}}\left(x_{c2,1,t-1}^{nc} + x_{c2,2,t-1}^{nc}\right)}^{\text{Conduit inflow from Pond 2}} + \overbrace{\frac{a_{s,3}}{n_{c3}a_{s,1}}\left(x_{c3,1}^{nc}\right)}^{\text{Conduit inflow from Pond 3}} + \overbrace{u_{1,t-1}}^{\text{Outflow}} + \overbrace{w_{1,t-1}}^{\text{Runoff}}}_{\text{Water level change of Pond 1 from different sources}} \tag{D-5}$$

where outflow $u_{1,t-1}$ is a nonpositive value. Equation D-2 is expanded for Figure D1 as shown below.

$$\boldsymbol{y_t} = \begin{bmatrix} x_1^{wl} \\ x_2^{wl} \\ x_3^{wl} \end{bmatrix}_t = \begin{bmatrix} 0 & 0 & 0 & 0 & 0 & 1 \\ 1 & 0 & 0 & 0 & 0 & 0 \\ 0 & 0 & 1 & 0 & 0 & 0 \end{bmatrix} \cdot \begin{bmatrix} x_2^{wl} \\ x_{c2,1}^{nc} \\ x_{c2,2}^{nc} \\ x_3^{wl} \\ x_{c3,1}^{nc} \\ x_1^{wl} \end{bmatrix}_t$$

D.2 Time-invariant linear quadratic gaussian (LQG) controller

The LQG controller that we used in this study is formulated as the following.

$$\hat{\boldsymbol{x}}_{\boldsymbol{t}} = A \cdot \hat{\boldsymbol{x}}_{\boldsymbol{t-1}} + B_u \cdot \boldsymbol{u}_{\boldsymbol{t-1}} + B_w \cdot \boldsymbol{w}_{\boldsymbol{t-1}} + L \cdot \boldsymbol{z}_{\boldsymbol{t-1}} \quad \text{(D-6)}$$

$$\hat{\boldsymbol{y}}_{\boldsymbol{t}} = C \cdot \hat{\boldsymbol{x}}_{\boldsymbol{t}} \quad \text{(D-7)}$$

$$\hat{\boldsymbol{u}}_{\boldsymbol{t}} = -K \cdot \hat{\boldsymbol{x}}_{\boldsymbol{t}} + K_r \cdot \boldsymbol{r}_{\boldsymbol{t}} + K_w \cdot \tilde{\boldsymbol{w}}_{\boldsymbol{t}} \quad \text{(D-8)}$$

$$\boldsymbol{z}_{\boldsymbol{t}} = \boldsymbol{y}_{\boldsymbol{t}} - \hat{\boldsymbol{y}}_{\boldsymbol{t}} \quad \text{(D-9)}$$

The LQG controller consists of a linear quadratic estimator (LQE; Equation D-6) and a linear quadratic regulator (LQR; Equation D-8). Terms $\hat{\boldsymbol{x}}_{\boldsymbol{t}}$ and $\hat{\boldsymbol{y}}_{\boldsymbol{t}}$ are model estimates for $\boldsymbol{x}_{\boldsymbol{t}}$ and $\boldsymbol{y}_{\boldsymbol{t}}$, respectively. $\hat{\boldsymbol{u}}_{\boldsymbol{t}}$ is the optimal control of outflows given the objective function, J:

$$J = \hat{\boldsymbol{x}}_{\boldsymbol{T}}^{\mathrm{T}} Q \hat{\boldsymbol{x}}_{\boldsymbol{T}} + \sum_{t=1}^{T-1} (\hat{\boldsymbol{x}}_{\boldsymbol{t}}^{\mathrm{T}} Q \hat{\boldsymbol{x}}_{\boldsymbol{t}} + \hat{\boldsymbol{u}}_{\boldsymbol{t}}^{\mathrm{T}} R \hat{\boldsymbol{u}}_{\boldsymbol{t}}) \quad \text{(D-10)}$$

In this study, the weight matrixes of the control error (Q) and the control cost (R) are manually tuned to the control needs and defined as:

$$Q = diag([1,\ 1,\ 1,\ 100,\ 100,\ 900,\ 250,\ 1,\ 10]) \quad \text{(D-11)}$$

$$R = diag([1,\ 3,\ 50,\ 30,\ 15,\ 120,\ 50,\ 20000,\ 10]) \quad \text{(D-12)}$$

where $diag$ stands for diagonal matrix.

In the following sections, we will show the equations for Kalman gain (L), feedback gain (K), feedforward gain of reference tracking (K_r), and feedforward gain of disturbance cancelation (K_w).

D.2.1 LQE and Kalman gain (L):

The core of LQE is the Kalman filter, which can assimilate measurements into model prediction, as shown in Equation D-6. This study solves Kalman gain (L) for a steady-state time-invariant system:

$$L = \xi_X C^{\mathrm{T}}(C\xi_X C^{\mathrm{T}} + Cov_V)^{-1} \tag{D-13}$$

where Cov_V is the covariance matrix for sensor noises. In our case, Cov_V is equal to $I_n \cdot \boldsymbol{\sigma_s^2}$, where I_n is the identity matrix with size equal to the number of sensors (n) and $\boldsymbol{\sigma_s}$ is a vector of the standard deviation of sensor white noises. ξ_X is computed by a discrete time algebraic Riccati equation:

$$\xi_X = A[\xi_X - \xi_X C^{\mathrm{T}}(C\xi_X C^{\mathrm{T}} + Cov_V)^{-1} C\xi_X]A^{\mathrm{T}} + B_w Cov_w B_w^{\mathrm{T}}$$

where Cov_W is the covariance matrix for weather forecast uncertainties. We define it as

$$Cov_W = diag([\sigma_{w,1}, \sigma_{w,2}, \dots, \sigma_{w,8}, \sigma_{w,9}]) \tag{D-14}$$

where $\boldsymbol{\sigma_w}$ is a vector of the forecast uncertainties at ponds.

D.2.2 LQR and *K*

LQR is a closed-loop feedback control method that will use $\hat{\boldsymbol{x}}_{\boldsymbol{t}}$ from LQE to determine the optimal control given J (Equation D-10). The analytical solution for this optimal control is:

$$\hat{\mathbf{u}}_{\mathbf{t}} = -K\hat{\boldsymbol{x}}_{\boldsymbol{t}} \tag{D-15}$$

where K is solved by a discrete time algebraic Riccati equation shown below.

$$K = (B_u^{\mathrm{T}}\xi_P B_u + R)^{-1} B_u^{\mathrm{T}}\xi_P A \tag{D-16}$$

$$\xi_P = A^{\mathrm{T}}[\xi_P - \xi_P B_u(B_u^{\mathrm{T}}\xi_P B_u + R)^{-1} B_u^{\mathrm{T}}\xi_P]A + Q \tag{D-17}$$

D.2.3 Feedforward control for reference tracking, K_r

In our problem, instead of controlling $\boldsymbol{x_t}$ to be 0, we want to control the water levels of ponds to desired reference values $\boldsymbol{r_t}$ (tracking $\boldsymbol{r_t}$). We called this reference tracking, in which we approach it by a feedforward control. A control that uses the reference value at the next time step to inform the current control decision. Now the optimal control becomes:

$$\widehat{\boldsymbol{u}}_{\mathbf{t}} = -K\widehat{\boldsymbol{x}}_{\boldsymbol{t}} + K_r\boldsymbol{r_t} \tag{D-18}$$

where K_r is equal to

$$K_r = [C(I - A + B_uK)^{-1}B_u]^{-1} \tag{D-19}$$

in a discrete system under a stability assumption. We show the derivation in the following.

First, we plug Equation D-18 into a state-space model (without the disturbance term) and solve Equation D-21 for the steady-state, where $\boldsymbol{x_t} = \boldsymbol{x_{t-1}} = \boldsymbol{x}$, $\boldsymbol{y_t} = \boldsymbol{y_{t-1}} = \boldsymbol{y}$, and $\boldsymbol{r_t} = \boldsymbol{r}$. We got

$$\begin{aligned} \boldsymbol{x} &= A\boldsymbol{x} + B_u\boldsymbol{u} \\ &= A\boldsymbol{x} + B_u(-K\boldsymbol{x} + K_r\boldsymbol{r}) \\ &= (A - B_uK)\boldsymbol{x} + B_uK_r\boldsymbol{r} \end{aligned} \tag{D-20}$$

where we assume a perfect prediction model ($\widehat{\boldsymbol{x}} = \boldsymbol{x}$ and $\widehat{\boldsymbol{u}} = \boldsymbol{u}$). Next, we collect $\boldsymbol{x}$-related terms and put them together, we have

$$(I - A + B_uK)\boldsymbol{x} = B_uK_r\boldsymbol{r} \tag{D-21}$$

$$\boldsymbol{x} = (I - A + B_uK)^{-1}B_uK_r\boldsymbol{r} \tag{D-22}$$

Next, we plug $\boldsymbol{x}$ back into Equation D-2, we have

$$\boldsymbol{y} = C\boldsymbol{x} = C(I - A + B_uK)^{-1}B_uK_r\boldsymbol{r} \tag{D-23}$$

Since $\boldsymbol{r}$ is the control target, $\boldsymbol{y}_\infty$ is equal to $\boldsymbol{r}$ in the steady state in a stable system; hence, we got

$$\boldsymbol{y}_\infty = \boldsymbol{r} = C(I - A + B_u K)^{-1} B_u K_r \boldsymbol{r} \tag{D-24}$$

$$K_r = [C(I - A + B_u K)^{-1} B_u]^{-1} \tag{D-25}$$

Done.

D.2.4 Feedforward control for disturbance cancelation, $\boldsymbol{K_w}$

This section illustrates a feedforward control method to incorporate weather forecasts ($\widetilde{\boldsymbol{w}}_{\boldsymbol{t}}$) into the optimal control. This is called disturbance cancelation in control theory, in which runoffs ($\boldsymbol{w_t}$) are viewed as disturbances to the control system. Now the optimal control becomes:

$$\widehat{\boldsymbol{u}}_{\mathbf{t}} = -K\widehat{\boldsymbol{x}}_{\boldsymbol{t}} + K_w \widetilde{\boldsymbol{w}}_{\boldsymbol{t}} \tag{D-26}$$

where K_W is equal to

$$K_W = -[C(I - A + B_u K)^{-1} B_u]^{-1} C(I - A + B_u K)^{-1} B_w \tag{D-27}$$

in a discrete system under a stability assumption. We show the derivation in the following.

First, we plug Equation D-26 into the state-space model (Equation D-1) and solve Equation D-21 for the steady-state, where $\boldsymbol{x_t} = \boldsymbol{x_{t-1}} = \boldsymbol{x}$ and $\boldsymbol{y_t} = \boldsymbol{y_{t-1}} = \boldsymbol{y}$. We got

$$\begin{aligned} \boldsymbol{x} &= A\boldsymbol{x} + B_u \boldsymbol{u} + B_w \boldsymbol{w} \\ &= A\boldsymbol{x} + B_u(-K\boldsymbol{x} + K_w \boldsymbol{w}) + B_w \boldsymbol{w} \\ &= (A - B_u K)\boldsymbol{x} + B_u K_w \boldsymbol{w} + B_w \boldsymbol{w} \end{aligned} \tag{D-28}$$

where we assume a perfect forecast ($\widetilde{\boldsymbol{w}}_{\boldsymbol{t}} = \boldsymbol{w}_{\boldsymbol{t}} = \boldsymbol{w}$) and a perfect prediction model ($\widehat{\boldsymbol{x}}_{\boldsymbol{t}} = \boldsymbol{x}_{\boldsymbol{t}} = \boldsymbol{x}$ and $\widehat{\boldsymbol{u}}_{\boldsymbol{t}} = \boldsymbol{u}_{\boldsymbol{t}} = \boldsymbol{u}$). Next, we collect $\boldsymbol{x}$-related terms and put them together, we have

$$(I - A + B_u K)\boldsymbol{x} = B_u K_w \boldsymbol{w} + B_w \boldsymbol{w} \tag{D-29}$$

$$\boldsymbol{x} = (I - A + B_u K)^{-1} B_u K_w \boldsymbol{w} + (I - A + B_u K)^{-1} B_w \boldsymbol{w} \tag{D-30}$$

Next, we plug $\boldsymbol{x}$ back into Equation D-2, we have

$$\boldsymbol{y} = C\boldsymbol{x} = C(I - A + B_u K)^{-1} B_u K_w \boldsymbol{w} + C(I - A + B_u K)^{-1} B_w \boldsymbol{w} \tag{D-31}$$

Since we want to cancel $\boldsymbol{w}$ using K_w and $\boldsymbol{y}_\infty$ is zero in the steady state, we got

$$\boldsymbol{y}_\infty = 0 = C(I - A + B_u K)^{-1} B_u K_w \boldsymbol{w} + C(I - A + B_u K)^{-1} B_w \boldsymbol{w} \tag{D-32}$$

$$K_W = -[C(I - A + B_u K)^{-1} B_u]^{-1} C(I - A + B_u K)^{-1} B_w \tag{D-33}$$

Done.

D.2.5 Linear combination of $\boldsymbol{K}$, $\boldsymbol{K_r}$, and $\boldsymbol{K_w}$

From the above subsection, we derive K_r and K_w independently. In our study, we applied feedback control (i.e., K) with both feedforward controls (i.e., K_r and K_w). Here, we want to show that it is mathematically correct for this linear combination of optimal control as one might notice that K_r is based on the assumption of $\boldsymbol{y}_\infty = \boldsymbol{r}$ and K_w is based on the assumption of $\boldsymbol{y}_\infty = 0$. To prove the correctness, we can solve $K_w{}'$ given $\boldsymbol{y}_\infty = \boldsymbol{r}$ and compare

$$\boldsymbol{u}' = -K\boldsymbol{x} + K_w{}'\boldsymbol{w} \tag{D-34}$$

with

$$\boldsymbol{u} = -K\mathbf{x} + K_r\boldsymbol{r} + K_w\boldsymbol{w} \tag{D-35}$$

Following the similar procedure from Equation D-28 to D-31, we have

$$\boldsymbol{y} = C\boldsymbol{x} = C(I - A + B_u K)^{-1} B_u K_w{}'\boldsymbol{w} + C(I - A + B_u K)^{-1} B_w \boldsymbol{w} \tag{D-36}$$

Now, instead of $\boldsymbol{y}_\infty = 0$, we solve $K_w{}'$ with $\boldsymbol{y}_\infty = \boldsymbol{r}$. We got

$$\boldsymbol{y}_\infty = \boldsymbol{r} = C(I - A + B_u K)^{-1} B_u K_w{}' \boldsymbol{w} + C(I - A + B_u K)^{-1} B_w \boldsymbol{w} \quad \text{(D-37)}$$

$$K_w' \boldsymbol{w} = [C(I - A + B_u K)^{-1} B_u]^{-1} [\boldsymbol{r} - C(I - A + B_u K)^{-1} B_w \boldsymbol{w}] \quad \text{(D-38)}$$

Next, we plug Equation D-38 back into Equation D-34, we have

$$\boldsymbol{u}' = -K\boldsymbol{x} + [C(I - A + B_u K)^{-1} B_u]^{-1} [\boldsymbol{r} - C(I - A + B_u K)^{-1} B_w \boldsymbol{w}] \quad \text{(D-39)}$$

Also, we can compute Equation D-35 by plugging in K_r and K_w from Equations D-25 and D-33, respectively, where we got

$$\begin{aligned} \boldsymbol{u} = &-K\boldsymbol{x} + [C(I - A + B_u K)^{-1} B_u]^{-1} \boldsymbol{r} \\ &-[C(I - A + B_u K)^{-1} B_u]^{-1} C(I - A + B_u K)^{-1} B_w \boldsymbol{w} \end{aligned} \quad \text{(D-40)}$$

$$\boldsymbol{u} = -K\boldsymbol{x} + [C(I - A + B_u K)^{-1} B_u]^{-1} [\boldsymbol{r} - C(I - A + B_u K)^{-1} B_w \boldsymbol{w}] \quad \text{(D-41)}$$

We found that $\boldsymbol{u}'$ and $\boldsymbol{u}$ are equivalent to each other. Therefore, we have shown that we can linearly combine feedback control (i.e., K) with both feedforward controls (i.e., K_r and K_w).

D.3 MIQCP problem for solving FDI in a smart stormwater system

Objective:

$$Obj = Max\left\{\sum y_{s_{\text{target}},t}^{sim}\right\} \tag{D-42}$$

Subject to:

$$\boldsymbol{x_t} = A \cdot \boldsymbol{x_{t-1}} + B_u \cdot \boldsymbol{u_{t-1}} + B_w \cdot \boldsymbol{w_{t-1}} \tag{D-43}$$

$$\boldsymbol{y_t^{sim}} = C \cdot \boldsymbol{x_t} \tag{D-44}$$

$$\boldsymbol{y_t} = \Gamma_t^{\mathrm{h}} \cdot (\boldsymbol{y_t^{sim}}) + \Gamma_t^{a} \cdot \boldsymbol{y_t^{a}} \tag{D-45}$$

$$\widehat{\boldsymbol{x}}_{\boldsymbol{t}} = A \cdot \widehat{\boldsymbol{x}}_{\boldsymbol{t-1}} + B_u \cdot \boldsymbol{u_{t-1}} + B_w \cdot \boldsymbol{w_{t-1}} + L \cdot \boldsymbol{z_{t-1}} \tag{D-46}$$

$$\boldsymbol{z_t} = \boldsymbol{y_t} - \widehat{\boldsymbol{y}}_{\boldsymbol{t}} \tag{D-47}$$

$$\widehat{\boldsymbol{y}}_{\boldsymbol{t}} = C \cdot \widehat{\boldsymbol{x}}_{\boldsymbol{t}} \tag{D-48}$$

$$\widehat{\boldsymbol{u}}_{\boldsymbol{t}} = -K \cdot \widehat{\boldsymbol{x}}_{\boldsymbol{t}} + K_r \cdot \boldsymbol{r_t} + K_w \cdot \widetilde{\boldsymbol{w}}_{\boldsymbol{t}} \tag{D-49}$$

$$\boldsymbol{u_t} = \max(min(0, \widehat{\boldsymbol{u}}_{\boldsymbol{t}}), -\boldsymbol{u_t^{aw}}, -\boldsymbol{u_t^{uc}}) \tag{D-50}$$

$$\boldsymbol{u_t^{aw}} = \boldsymbol{y_t^{sim}} \tag{D-51}$$

$$\boldsymbol{u_t^{uc}} = \boldsymbol{c_g} \times \boldsymbol{\mu} \times \boldsymbol{a_g} \times \sqrt{2g\boldsymbol{y_t^{act}}} \times \left(\frac{dt}{\boldsymbol{a_s}}\right) \tag{D-52}$$

$$\boldsymbol{y_t^{act}} = \min\left(\boldsymbol{y^{max}}, max\left(0, \boldsymbol{y_t^{sim}}\right)\right) \tag{D-53}$$

$$\boldsymbol{z_t}^{\mathrm{T}} \cdot \mathcal{G}^{-1} \cdot \boldsymbol{z_t} \leq Err^{a} \tag{D-54}$$

$$\boldsymbol{x}_{\mathbf{t_s}} = \widehat{\boldsymbol{x}}_{\mathbf{t_s}} = \boldsymbol{x}_{\mathbf{t_s}}^{\boldsymbol{h}}, \boldsymbol{u}_{\mathbf{t_s}} = \boldsymbol{u}_{\mathbf{t_s}}^{\boldsymbol{h}}, t \in \mathcal{T}^{\mathrm{a}} = \{t_s + 1, t_s + 2, \dots, t_s + T^{a}\} \tag{D-55}$$

D.4 Supplementary figures and tables

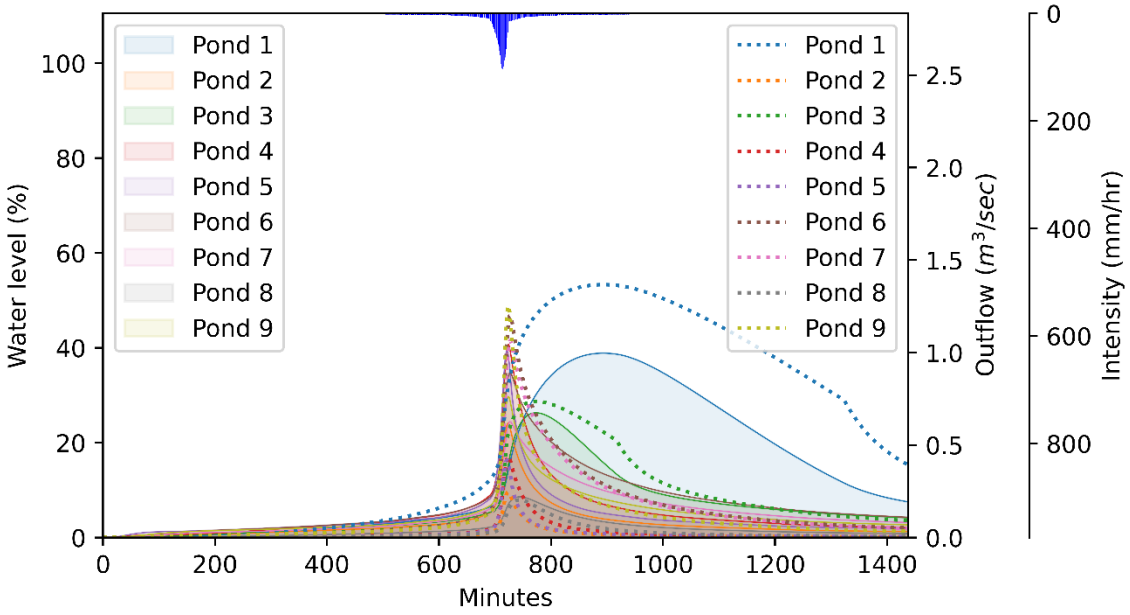

Figure D2. SWMM model simulated water levels (solid lines filled with color) and outflows (dotted lines) of each pond with a 2-year-24-hour design storm (blue bars).

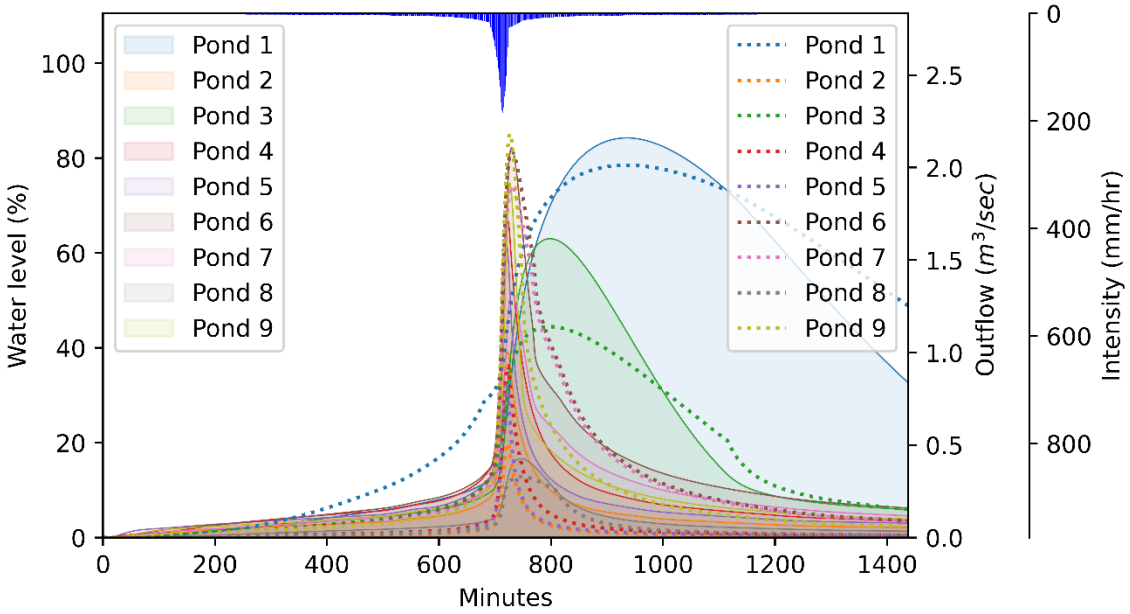

Figure D3. SWMM model simulated water levels (solid lines filled with color) and outflows (dotted lines) of each pond with a 25-year-24-hour design storm (blue bars).

Table D1. The design stormwater system configurations.

Item	Storage capacity [m^3]	Maximum depth [m]	Pond surface area [m^2]	Inverted elevation [m]	Outflow conduit diameter [m]	Subcatch-ment area [ha]	Subcatch-ment slope [%]
Pond 1	46843.00	2.40	19517.92	108.50	0.70	19.86	2.40
Pond 2	378.00	0.60	630.00	111.00	0.61	1.78	2.43
Pond 3	12310.00	1.80	6838.89	119.00	0.61	22.26	3.31
Pond 4	320.00	0.40	800.00	122.50	0.91	3.37	3.17
Pond 5	300.00	0.40	750.00	112.20	0.91	2.39	2.45
Pond 6	320.04	0.91	350.00	111.00	0.91	1.15	3.14
Pond 7	2262.00	1.20	1885.00	112.00	0.91	14.22	3.11
Pond 8	6927.00	1.80	3848.33	115.00	0.46	3.15	3.71
Pond 9	1100.00	1.10	1000.00	112.20	0.91	12.84	2.83

Vita

Chung-Yi Lin

Biographical Information

Ph.D.
Water Resources Engineering
Department of Civil and Environmental Engineering
Lehigh University

1) EDUCATION

Lehigh University (LU), Bethlehem, PA, USA

- Ph.D. in Civil & Environmental Engineering (CEE) *Aug 2019 – Jan 2023*

National Taiwan University (NTU), Taipei, Taiwan

- M.S. in Bioenvironmental Systems Engineering (BSE) *Sep 2017 – Feb 2019*
- B.S. in Bioenvironmental Systems Engineering (BSE) *Sep 2014 – Jun 2017*

2) RESEARCH EXPERIENCES

Themes

Cyber-Physical Systems & Infrastructure Resilience

- IoT-based stormwater infrastructures, false data injection, optimization, control

Coupled Natural-Human System

- Agent-based modeling, software development, uncertainty characterization

Risk Assessment in Complex Adaptive Water Systems

- Climate risks, food-water nexus, cyber-physical risks

Research Assistant

- Complex Adaptive Water Systems (CAWS) Lab., LU *Sep 2020 – Jan 2022*

Intern

- Institute for Global Environmental Strategies (IGES), Hayama, Japan *Jun 2019 – Jul 2019*
- Microsoft Student Partner, Taipei, Taiwan *Jun 2017 – Jun 2018*

Publications and Creative Activities

Peer-reviewed Journals

1. **Lin, C. Y.**, Yang, Y. C. E., & Wi S. (2022). HydroCNHS: A Python Package of Hydrological Model for Coupled Natural Human Systems, *Journal of Water Resources Planning and Management*.
2. Jhong, B. C., **Lin, C. Y.**, Jhong, Y. D., Chang, H. K., Chu, J. L., Fang, H. T. (2022) Assessing effective spatial characteristics of input features by physics-informed machine learning in inundation forecasting during typhoons, *Hydrological Sciences Journal*, 1-19.
3. **Lin, C. Y.**, Yang, Y. C. E., Malekc, K., & Adam, J. C. (2022). An investigation of coupled natural human systems using a two-way coupled agent-based modeling framework, *Environmental Modelling & Software*, *155*, 105451
4. **Lin, C. Y.**, & Yang, Y. C. E. (2022). The effects of model complexity on model output uncertainty in co-evolved coupled natural–human systems, *Earth's Future, 10,* e2021EF002403.
5. Tung, C. P., Tsao, J. H., Tien, Y. C., **Lin, C. Y.**, & Jhong, B. C. (2019). Development of a Novel Climate Adaptation Algorithm for Climate Risk Assessment. *Water*, 11(3), 497.

Preparation & Revision

6. **Lin, C. Y.**, Yang, Y. C. E., & Moazeni, F. (2022). Compounding risks of natural hazards and human interventions in smart stormwater systems, *Water Resources Research.*
7. **Lin, C. Y.**, & Yang, Y. C. E. (2022). Analyzing the Role of Social-Economic Factors in Water Quality Management through Agent-Based Modeling ─ Susquehanna River Basin, US, *Journal of Hydrology*.

Software (citable without journal publication)

8. **Lin, C. Y.** (2021). MultiWG: Multi-site stochastic Weather Generator (MultiWG) (v1.0.0). *Zenodo*. https://doi.org/10.5281/zenodo.5147575

Conferences

9. **Lin, C. Y.**, Yang, Y. C. E. (2022). Risk assessment of compound disturbances in coupled natural human systems. Oral [1107573] presented at 2022 EWRI Congress, Atlanta, GA, 5-8 Jun.
10. **Lin, C. Y.**, Yang, Y. C. E. (2021). Uncertainty decomposition of coupled natural human systems with differing model parameter complexity. Abstract [H25U-1267] presented at 2021 Fall Meeting, AGU, New Orleans, LA, 13-17 Dec.
11. Tung, C. P., Tsao, J. H., Jhong, B. C., Li, M. H., Perng, P. W., Huang, J., Tien, Y. C., & **Lin, C. Y.** (2019) Enable Climate Intelligent Assistant for Resilient Cities. ECCA International Conference Abstracts, Lisbon, Portugal.
12. Takeda, T. & **Lin, C. Y.** (2019) Japan's Challenges and Opportunities Regarding Nitrogen Management. Water and Environment Technology Conference 2019, Suita, Osaka, Japan.
13. **Lin, C. Y.**, Wang, Z. L., Huang, J., Jhong, B. C., & Tung, C. P. (2018). Development of a cross-scale and cross-sector adaptation assessment model integrating agriculture and water resources fields: A case study of regional to local scale. Abstract [H21Q-1953] presented at 2018 Fall Meeting, AGU, Washington, D.C., 10-14 Dec.
14. Wang, Z. L., Tung, C. P., **Lin, C. Y.**, Jhong, B. C., & Huang, J. (2018). Investigating the Feasibility of Water Market in Water Reallocation by Virtual Gaming Simulation during

Drought Periods: A Case Study of the Taoyuan Area, Taiwan. Abstract [H21Q-1938] presented at 2018 Fall Meeting, AGU, Washington, D.C., 10-14 Dec.

15. Jhong, B. C., Tung, C. P., Tsao, J. H., **Lin, C. Y.**, & Li, M. H. (2018). Interdisciplinary assessment of climate risk for water resources and agriculture and flood disaster. PAWEES & INWEPF International Conference 2018 Abstracts, Nara, Japan.
16. **Lin, C. Y.**, Jhong, B. C., Chen, P. Y., & Tung, C. P. (2017). Development of surrogate model for the hydrological module of SWAT. PAWEES International Conference 2017 Abstracts, Taichung, Taiwan. (**Award for Excellent Oral Presentation**)
17. **Lin, C. Y.**, Li, Y. H., Li, M. H., & Tung, C. P. (2015). Analysis of the water-food nexus under climate change: A case study of thousand-ponds-city in Taiwan. ECCA International Conference Abstracts, Glasgow, Scotland.

Book, Report & Thesis

18. Tung, C. P., Li, M. H., Liu, T. M., Sung, R. T., Hong, N. M., Hsu, S. Y., Lee, T. Y., Tsao, J. H., Li, Y. H., Jhong, B. C., & **Lin, C. Y.** (2020) Climate Adaptation Advanced Training – Water Resources (translated), Ministry of Education, Taiwan. (Mandarin)
19. **Lin, C. Y.** (2019). Development of Interdisciplinary AgriHydro Model and Application with Climate Smart Adaptation Algorithm - A Case Study in Taoyuan, The Graduated Thesis of Graduate Institute of Bioenvironmental Systems Engineering, NTU, Taiwan. (Mandarin with English abstract)

Honors and Awards

- Gibson Teaching Fellowship, LU *Aug 2022*
- Certificate of Teacher Development Program, LU *Dec 2019*
- Lehigh University Fellowship, LU *Sep 2019*
- Summer Institute Programme Scholarship *Jul 2018*
  (at IMK-IFU, Garmisch-Partenkirchen, Germany),
  Ministry of Science and Technology-German Academic Exchange Service (MOST-DAAD)
- Award for Excellent Oral Presentation, PAWEES International Conference *Nov 2017*
- Chi-Seng Water Management Research & Development Foundation Scholarship, NTU *Sep 2017*
- Water Youth Ambassador (to Netherlands), Water Resources Agency (WRA), Taiwan *Aug 2017*
- Award of Academic Research Thesis in Bachelor, NTU *Jun 2017*
- College Student Research Scholarship, MOST, Taiwan *Jul 2016*
- Taiwan Water Youth Camp & Wetskills First price, WRA, Taiwan, *Jul 2016*
- Exchanged to Purdue University, NTU *Jan 2016*
- Agricultural Engineering Research Center Scholarship, *Dec 2015*
  Agricultural Engineering Research Center, NTU
- Academic Excellence Award (4 times), BSE, NTU *Apr 2014, Oct 2014, Apr 2015, Apr 2016*

Research Funding and Training Grants

- Contributor, 2023-2025, *"Understanding the drivers of interbasin water transfers to identify and mitigate future conflict,"* PI Landon Marston with Co-PI Kathryn Powlen

(USGS), Agency: United States Geological Survey and National Institutes for Water Resources, **$248,458**.
(contribute to the contextualization of modeling approach and visualization)

Professional Presentations

Invited Presenter *Aug 2022*
2022 CUAHSI Making Waves in Water Science: Open Source Tools for Water Science Webinar, USA
Presented a developed open-source software, HydroCNHS.

Convener *Aug 2022*
2022 AGU-H3S Navigating Academic Waters: Succeeding as a Postdoc webinar, USA
Moderated the virtual panel discussion on "Navigating Academic Waters: Succeeding as a Postdoc."

Presenter *Jun 2022*
2022 EWRI Congress, Atlanta, USA
Presented a research topic about risk assessment of compound disturbances in coupled natural human systems.

Invited Presenter *Jul 2019*
Institute for Global Environmental Strategies (IGES), Japan
Presented a topic about exploring challenges & opportunities of nitrogen management in Japan & Taiwan.

Invited Presenter *Aug 2018*
Institute of Meteorology and Climate Research Atmospheric Environmental Research (IMK-IFU) in Garmisch-Partenkirchen, Germany
Presented a research topic about a stochastic weather generator and climate risk assessment in the water-food nexus.

Invited Presenter *Jun 2018*
National Science and Technology Center for Disaster Reduction (NCDR), Taiwan
Presented a research topic about climate scenario downscaling and a stochastic weather generator.

Presenter *Sep 2017*
PAWEES International Conference 2017, Taichung, Taiwan
Presented a research topic about the water-food nexus under climate change for Taoyuan, Taiwan.

Teaching and Mentoring

Course Design and Teaching

- *Co-instructor/co-developer, CEE 497 Applications of Catastrophe Modeling, LU (with Prof. Yang)* *F'22*

Teaching Assistant

- *CEE 122 Fluid Mechanics, LU* *F'22*
- *CEE 222 Water Resources Engineering, LU* *Sp'22*
- *BSE 5071 Climate Change and Environmental Ecology, NTU* *Sp'17, Sp'18*

- *BSE 5091 Environmental Systems Analysis, NTU* *F'17*

Mentor

- *Mentored two mentees (Tanumoy Banerjee & Jasreen Kaur), Mentor Collective at Lehigh, LU* *Aug – Dec 2020*

Tutor

- *Taught Python lectures at NCDR, Taiwan* *Feb – Mar 2018*

Service

Professional Service

- AGU, Water and Society Technical Committee, Student Representatives *2022 – present*
- AGU, Hydrology Section Student Subcommittee (H3S), Prof. Dev. Subcommittee Co-chair *2022 – present*
- ASCE, EWRI, Environmental and Water Resources System (EWRS) Committee *2021 – present*

Lehigh University

- CEE Department Representatives for the Graduate Students Recruitment Program *2021 – present*
- CEE Department Representatives for the Graduate Senate Meeting *2021*
- Lehigh Graduate Open House CEE Representatives *2021*
- Lehigh Mentor Collective, Mentor *2021*

National Taiwan University

- Charter President of Climate Action Club, NTU *Sep 2014 – Dec 2015*

Ad Hoc Reviewer – Journals

- Journal of Water Resources Planning and Management – ASCE
- Science of the Total Environment – ELSEVIER
- Environmental Modeling & Software – ScienceDirect
- Ecology & Society – Resilience Alliance